

**AUTOMATED TRAJECTORY CONTROL FOR PROXIMITY
OPERATIONS USING RELATIVE ORBITAL ELEMENTS**

A Dissertation
Presented to
The Academic Faculty

by

David A. Spencer

In Partial Fulfillment
of the Requirements for the Degree
Doctor of Philosophy in the
Daniel Guggenheim School of Aerospace Engineering

Georgia Institute of Technology
May 2015

COPYRIGHT © 2015 BY DAVID A. SPENCER

AUTOMATED TRAJECTORY CONTROL FOR PROXIMITY OPERATIONS USING RELATIVE ORBITAL ELEMENTS

Approved by:

Dr. Robert Braun, Advisor
Daniel Guggenheim School of
Aerospace Engineering
Georgia Institute of Technology

Dr. Panagiotis Tsiotras
Daniel Guggenheim School of
Aerospace Engineering
Georgia Institute of Technology

Dr. Mark Costello
Daniel Guggenheim School of
Aerospace Engineering
Georgia Institute of Technology

Dr. T. Alan Lovell
SpaceVehicles Directorate
U.S. Air Force Research Laboratory

Dr. R. Scott Erwin
SpaceVehicles Directorate
U.S. Air Force Research Laboratory

Date Approved: March 6, 2015

To my wife Sallie

ACKNOWLEDGEMENTS

I would like to thank my advisor, Dr. Robert Braun, for his guidance and support throughout my PhD program. He has been a close friend and colleague since our collaboration on Mars Pathfinder beginning in 1993, and he has had a major influence on my career and academic pursuits.

I would also like to acknowledge Dr. Alan Lovell for providing the foundational work upon which much of my research is based. Our collaboration on relative orbital elements has been both fruitful and enjoyable. Dr. Lovell's insights and feedback have been invaluable in preparing this dissertation.

I would like to thank the other members of my PhD committee, Dr. Panagiotis Tsiotras, Dr. Mark Costello, and Dr. Scott Erwin. Your guidance has been greatly appreciated.

Finally, I would like to thank my wife, Sallie, whose support has been unwavering throughout all of my endeavors.

TABLE OF CONTENTS

	Page
ACKNOWLEDGEMENTS	iv
LIST OF TABLES	viii
LIST OF FIGURES	ix
LIST OF SYMBOLS	xi
LIST OF ABBREVIATIONS	xvi
SUMMARY	xviii
 <u>CHAPTER</u>	
1 Motivation, Background and Contributions of this Investigation	1
1.1 Introduction and Motivation	1
1.2 Background	3
1.2.1 A Brief History of Relative Proximity Operations	3
1.2.2 Trend Toward Autonomy	12
1.2.3 Relative Orbital Elements	14
1.2.4 Artificial Potential Functions	16
1.3 Contributions of this Investigation	19
2 Relative Orbital Elements	21
2.1 Clohessy-Wiltshire Equations for Relative Motion	21
2.2 Definition of Relative Orbital Elements	29
2.2.1 Derivation of Relative Orbital Elements	30
2.2.2 Transformation from Relative Orbital Elements to LVLH Cartesian State	38
2.2.3 Evolution of Relative Orbital Elements with Time	40

2.2.4	Additional Parameters Related to Relative Orbital Elements	42
2.3	Characteristics of the Unforced Motion	52
2.3.1	Evolution of Relative Orbital Elements with Time	42
2.3.2	Characteristics of the Unforced Motion	45
2.4	Changes in Relative Orbital Elements Due to a Single Impulsive Maneuver	59
2.5	Relative Orbital Element Control Strategies	75
2.5.1	Rendezvous	75
2.4.4	Natural Motion Circumnavigation	81
2.4.5	Station-Keeping in a Leading or Trailing Orbit	84
3	Artificial Potential Function Trajectory Control Formulation Using Relative Orbital Elements	99
3.1	Artificial Potential Function Control Methodology	99
3.2	Artificial Potential Functions Using Relative Orbital Elements	115
3.2.1	Targeting a Single Relative Orbital Element: x_r	118
3.2.2	Targeting a Single Relative Orbital Element: y_r	123
3.2.3	Targeting a Single Relative Orbital Element: a_r	128
3.2.4	Targeting a Single Relative Orbital Element: A_z	133
3.2.5	Targeting Multiple Relative Orbital Elements: $x_r, y_r, a_r,$ and A_z	137
3.2.6	Combining Attractive and Repulsive Potentials	146
3.2.7	Monte Carlo Analysis	155
4	Automated Trajectory Control in a Simulated Environment	164
4.1	Guidance, Navigation and Control Six Degree-of-Freedom Simulation Environment	164
4.2	Relative Orbital Elements Station-Keeping	166
4.3	Relative Orbital Elements Transfer	176

4.4 Relative Orbital Elements Transfer with Artificial Potential Function Obstacle Avoidance	184
4.5 Artificial Potential Function Targeting of Relative Orbital Elements	193
4.5 Artificial Potential Function Targeting of Relative Orbital Elements with Obstacle Avoidance	193
5 Conclusions and Future Work	207
5.1 Conclusions	207
5.2 Suggestions for Future Work	209
APPENDIX A: Application of the Harmonic Addition Theorem to the Solution of the Clohessy-Wiltshire Equations	212
REFERENCES	235

LIST OF TABLES

	Page
Table 1: Summary of RPO approaches used for U.S. and international missions.	11
Table 2: Expressions for ROEs in terms of LVLH Cartesian state elements.	38
Table 3: Expressions for LVLH Cartesian state elements in terms of ROEs.	40
Table 4: Expressions for ROEs in terms of ROE initial conditions.	42
Table 5: Expressions for useful parameters related to ROEs.	52
Table 6: Modes of unforced relative motion.	54
Table 7: x_r, y_r, a_r variations based upon impulsive maneuver components, $0 \leq E_r^- < \pi$.	66
Table 8: x_r, y_r, a_r variations based upon impulsive maneuver components, $\pi \leq E_r^- < 2\pi$.	67
Table 9: E_r variations based upon impulsive maneuver components, $0 \leq E_r^- < \frac{\pi}{2}$.	68
Table 10: E_r variations based upon impulsive maneuver components, $\frac{\pi}{2} \leq E_r^- < \pi$.	69
Table 11: E_r variations based upon impulsive maneuver components, $\pi \leq E_r^- < \frac{3\pi}{2}$.	70
Table 12: E_r variations based upon impulsive maneuver components, $\frac{3\pi}{2} \leq E_r^- < 2\pi$.	71
Table 13: A_z variations based upon impulsive maneuver components.	72
Table 14: ψ variations based upon impulsive maneuver components.	73
Table 15: ψ variations based upon impulsive maneuver components.	74
Table 16: Rendezvous problem formulation in terms of ROE's.	75

Table 17: Rendezvous problem example.	78
Table 18: Natural motion circumnavigation problem formulation.	81
Table 19: Example of transition from leading orbit to NMC motion.	83
Table 20: Station-keeping problem formulation for a leading or trailing orbit.	85
Table 21: Station-keeping maneuver sequence summary.	95
Table 22: Station-keeping example.	96
Table 23: Station-keeping example maneuver summary.	97
Table 24: Conditions for APF control example.	105
Table 25: APF control example, attractive and repulsive fields.	112
Table 26: APF control example, targeting ROE x_r .	121
Table 27: APF control example, targeting ROE y_r .	126
Table 28: APF control example, targeting ROE a_r .	131
Table 29: APF control example, targeting ROE A_z .	135
Table 30: APF control example, targeting ROEs x_r, y_r, a_r, A_z .	143
Table 31: APF control example, targeting ROEs x_r, y_r, a_r, A_z with repulsive obstacle.	150
Table 32: Attractive APF Monte Carlo evaluation parameters.	156
Table 33: Attractive APF Monte Carlo results.	157
Table 34: Comparison of ΔV utilization between the APF formulation and the two-impulse STM approach.	160
Table 35: Attractive APF with obstacle Monte Carlo evaluation parameters.	162
Table 36: Attractive APF with obstacle Monte Carlo results.	163
Table 37: Orbit perturbations for a 720 km circular orbit.	166
Table 38: ROE station-keeping scenario.	169
Table 39: ROE station-keeping maneuvers 1A, 2A.	170
Table 40: ROE station-keeping maneuvers 3A, 4A.	171

Table 41: ROE station-keeping, maneuvers 1B, 2B.	172
Table 42: ROE station-keeping maneuver 3B.	173
Table 43: ROE transfer scenario.	179
Table 44: ROE transfer maneuvers 1 and 2.	180
Table 45: ROE transfer maneuvers 3 and 4.	181
Table 46: ROE transfer with APF obstacle avoidance scenario.	187
Table 47: ROE transfer with APF obstacle avoidance, maneuvers 1A and 2A.	188
Table 48: ROE transfer with APF obstacle avoidance, maneuvers 3-APF and 1B.	189
Table 49: ROE transfer with APF obstacle avoidance, maneuvers 2B and 3B.	190
Table 50: APF targeting of ROEs x_d, y_d, a_r, A_z .	196
Table 51: APF targeting of ROEs x_d, y_d, a_r, A_z , with obstacle avoidance.	202

LIST OF FIGURES

	Page
Figure 1: NEXTSat as imaged from ASTRO during Orbital Express proximity operations. Image credit: DARPA.	8
Figure 2: In 2016, Prox-1 will perform automated relative proximity operations for on-orbit inspection of the LightSail spacecraft using ROEs and APFs for trajectory guidance.	10
Figure 3: Coordinate system definition for LVLH frame.	21
Figure 4: Relative orbit geometry in the LVLH $\hat{x} - \hat{y}$ plane.	34
Figure 5: Cross-track motion phase angle geometry, projected onto the $\hat{x} - \hat{z}$ plane.	36
Figure 6: Secular along-track drift in the $\hat{x} - \hat{y}$ plane.	44
Figure 7: Geometry of relative eccentric anomaly and relative true anomaly.	45
Figure 8: Geometry of relative inclination.	48
Figure 9: Four types of relative drifting motion in the $\hat{x} - \hat{y}$ plane. Mode 1B, 2A: solid line, $a_r = 0$. Mode 1B, 2B: dashed quasi-sinusoidal curve, $a_r < \frac{3}{2} x_r $; bolded cycloid-like curve with cusp, $a_r = \frac{3}{2} x_r $; bold-dashed cycloid-like curve with curl, $a_r > \frac{3}{2} x_r $. In all cases, motion is from right to left.	55
Figure 10: Mode 1A, 2B, 3B motion with varying phase difference, γ . Bold solid line: $\gamma = 0$; dashed line: $\gamma = \frac{\pi}{2}$; solid line: $\gamma = \pi$; dotted line: $\gamma = \frac{3\pi}{2}$. (a) $\hat{y} - \hat{x}$ projection, (b) $\hat{z} - \hat{x}$ projection, (c) $\hat{y} - \hat{z}$ projection, (d) 3D plot.	58
Figure 11: Mode 1B, 2B, 3B motion. (a) $\hat{y} - \hat{x}$ projection, (b) $\hat{z} - \hat{x}$ projection, (c) $\hat{y} - \hat{z}$ projection, (d) 3D plot.	59
Figure 12: Function value from Eq. (176) versus maneuver epoch.	79

Figure 13: Trajectory propagation with rendezvous maneuver targeting a stationary relative ellipse. (a) $\hat{y} - \hat{x}$ projection, (b) $\hat{z} - \hat{x}$ projection, (c) $\hat{y} - \hat{z}$ projection, (d) Three-dimensional trajectory plot.	80
Figure 14: Natural motion circumnavigation circular orbit initiated from a leading orbit. (a) $\hat{y} - \hat{x}$ projection, (b) $\hat{z} - \hat{x}$ projection, (c) $\hat{y} - \hat{z}$ projection, (d) Three-dimensional trajectory plot.	84
Figure 15: The second maneuver initiates a secular drift designed to reach the station-keeping target s orbital periods after the maneuver epoch.	91
Figure 16: Station-keeping example. (a) $\hat{y} - \hat{x}$ projection, (b) $\hat{z} - \hat{x}$ projection, (c) $\hat{y} - \hat{z}$ projection, (d) Three-dimensional trajectory plot.	98
Figure 17: Attractive potential as a function of position relative to the goal. (a) $k_a = 1$, $\bar{\bar{Q}}_a = \bar{\bar{I}}_{2 \times 2}$, (b) $k_a = 3$, $\bar{\bar{Q}}_a = \bar{\bar{I}}_{2 \times 2}$, (c) $k_a = 1$, $\bar{\bar{Q}}_a = \begin{bmatrix} 10 & 0 \\ 0 & 1 \end{bmatrix}$, (d) $k_a = 1$, $\bar{\bar{Q}}_a = \begin{bmatrix} 1 & 0 \\ 0 & 10 \end{bmatrix}$.	102
Figure 18: APF trajectory control to a target using an attractive potential.	106
Figure 19: APF attractive control maneuver magnitudes.	106
Figure 20: Repulsive potential as a function of position relative to the goal. (a) $k_r = 1$, $\bar{\bar{Q}}_r = \bar{\bar{I}}_{2 \times 2}$, $\sigma = 500$, (b) $k_r = 2$, $\bar{\bar{Q}}_r = \bar{\bar{I}}_{2 \times 2}$, $\sigma = 500$, (c) $k_r = 1$, $\bar{\bar{Q}}_r = \begin{bmatrix} 10 & 0 \\ 0 & 1 \end{bmatrix}$, $\sigma = 500$, (d) $k_r = 1$, $\bar{\bar{Q}}_r = \bar{\bar{I}}_{2 \times 2}$, $\sigma = 5000$.	108
Figure 21: Total potential field with attractive potential centered at $x = 0$ km, $y = 0.100$ km, repulsive potential centered at $x = -0.040$ km, $y = 0.130$ km.	113
Figure 22: APF trajectory control influence by attractive and repulsive potential fields.	114
Figure 23: APF repulsive control maneuver magnitudes.	114
Figure 24: APF targeting of single ROE x_r . (a) Unforced motion, 10,000 s propagation from initial conditions, (b) APF targeting of $x_r = 0$, $\hat{y} - \hat{x}$ projection, (c) Value of x_r as a function of time.	122

Figure 25: APF x_r targeting maneuver magnitudes.	123
Figure 26: APF targeting of single ROE y_r . (a) Unforced motion, 10,000 s propagation from initial conditions, (b) APF targeting of $y_r = 0$, $\hat{y} - \hat{x}$ projection, (c) Value of y_r as a function of time.	127
Figure 27: APF y_r targeting maneuver magnitudes.	128
Figure 28: APF targeting of single ROE a_r . (a) Unforced motion, 10,000 s propagation from initial conditions, (b) APF targeting of $a_r = 0$, $\hat{y} - \hat{x}$ projection, (c) Value of a_r as a function of time.	132
Figure 29: APF a_r targeting maneuver magnitudes.	133
Figure 30: APF targeting of single ROE A_z . (a) Unforced motion, 20,000 s propagation from initial conditions, (b) APF targeting of $A_z = 0$, $\hat{z} - \hat{x}$ projection, (c) Value of A_z as a function of time.	136
Figure 31: APF A_z targeting maneuver magnitudes.	137
Figure 32: APF targeting of ROEs x_d, y_d, a_r , and A_z , 250,000 sec propagation. (a) $\hat{y} - \hat{x}$ projection, (b) $\hat{z} - \hat{x}$ projection, (c) $\hat{z} - \hat{y}$ projection, (d) 3D trajectory plot.	144
Figure 33: APF targeting of ROEs x_d, y_d, a_r , and A_z , 25,000 sec propagation. (a) x_r time history, (b) y_r time history, (c) a_r time history, (d) A_z time history.	145
Figure 34: Maneuver components as a function of time for APF targeting of ROEs x_d, y_d, a_r , and A_z . Blue: ΔV_x , Green: ΔV_y , Red: ΔV_z .	146
Figure 35: APF targeting of ROEs x_r, y_r , and a_r , 250,000 sec propagation, (a) Trajectory with no obstacle, attractive potential only, $\hat{y} - \hat{x}$ projection, (b) Trajectory with obstacle, attractive and repulsive potentials, $\hat{y} - \hat{x}$ projection.	151
Figure 36: APF targeting of ROEs x_d, y_d , and a_r , with obstacle, 250,000 sec propagation. (a) x_r time history, (b) y_r time history, (c) a_r time history.	152
Figure 37: Maneuver magnitudes for attractive ROE targeting (blue) and repulsive obstacle avoidance (red).	153
Figure 38: The effect of repulsive maneuvers is to shape the trajectory to avoid the obstacle sphere of influence. (a) No repulsive maneuvers performed, (b) Repulsive maneuvers performed in response to 20 m obstacle sphere of influence.	154

Figure 39: Attractive APF Monte Carlo simulation relative Cartesian state initial conditions.	157
Figure 40: Attractive APF with obstacle Monte Carlo simulation relative Cartesian state initial conditions.	163
Figure 41: Guidance, navigation and control simulation block diagram.	166
Figure 42: ROE station-keeping scenario, (a) Relative position components as a function of time, (b) Relative velocity components as a function of time.	174
Figure 43: ROE station-keeping scenario, (a) $\hat{y} - \hat{x}$ projection, (b) $\hat{z} - \hat{x}$ projection, (c) $\hat{z} - \hat{y}$ projection, (d) 3D trajectory plot.	175
Figure 44: ROE station-keeping scenario, (a) x_r as a function of time, (b) y_r as a function of time, (c) a_r as a function of time, (d) A_z as a function of time.	176
Figure 45: ROE station-keeping scenario, maneuver magnitudes.	177
Figure 46: ROE transfer scenario, (a) Relative position components as a function of time, (b) Relative velocity components as a function of time.	182
Figure 47: ROE transfer scenario, (a) $\hat{y} - \hat{x}$ projection, (b) $\hat{z} - \hat{x}$ projection, (c) $\hat{z} - \hat{y}$ projection, (d) 3D trajectory plot.	183
Figure 48: ROE transfer scenario, (a) x_r as a function of time, (b) y_r as a function of time, (c) a_r as a function of time, (d) A_z as a function of time.	184
Figure 49: ROE transfer scenario, maneuver magnitudes.	185
Figure 50: ROE transfer scenario with APF obstacle avoidance, (a) Relative position components as a function of time, (b) Relative velocity components as a function of time.	191
Figure 51: ROE transfer scenario with APF obstacle avoidance, (a) $\hat{y} - \hat{x}$ projection, (b) $\hat{z} - \hat{x}$ projection, (c) $\hat{z} - \hat{y}$ projection, (d) 3D trajectory plot.	192
Figure 52: ROE transfer scenario with APF obstacle avoidance, (a) x_r as a function of time, (b) y_r as a function of time, (c) a_r as a function of time, (d) A_z as a function of time.	193

Figure 53: ROE transfer scenario with APF obstacle avoidance, maneuver magnitudes.	194
Figure 54: APF targeting of relative orbital elements, (a) Relative position components as a function of time, (b) Relative velocity components as a function of time.	197
Figure 55: APF targeting of relative orbital elements, (a) $\hat{y} - \hat{x}$ projection, (b) $\hat{z} - \hat{x}$ projection, (c) $\hat{z} - \hat{y}$ projection, (d) 3D trajectory plot.	198
Figure 56: APF targeting of relative orbital elements, (a) x_r as a function of time, (b) y_r as a function of time, (c) a_r as a function of time, (d) A_z as a function of time.	199
Figure 57: APF targeting of relative orbital elements, maneuver magnitudes.	200
Figure 58: APF targeting of ROEs x_d, y_d, a_r, A_z , with obstacle avoidance, (a) Relative position components as a function of time, (b) Relative velocity components as a function of time.	203
Figure 59: APF targeting of ROEs x_d, y_d, a_r, A_z , with obstacle avoidance, $\hat{y} - \hat{x}$ projection.	204
Figure 60: APF targeting of ROEs x_d, y_d, a_r, A_z , with obstacle avoidance, (a) x_r as a function of time, (b) y_r as a function of time, (c) a_r as a function of time.	205
Figure 61: APF targeting of ROEs x_d, y_d, a_r, A_z , with obstacle avoidance, maneuver magnitudes.	206

LIST OF SYMBOLS

a_e	semi-major axis of the instantaneous relative ellipse (Lovell notation)
a_r	semi-major axis of the instantaneous relative ellipse
$\bar{\mathbf{a}}_T$	acceleration vector resulting from external forces
a_{T_x}	x -component of acceleration resulting from external forces
a_{T_y}	y -component of acceleration resulting from external forces
a_{T_z}	z -component of acceleration resulting from external forces
A_x	amplitude of the motion in the LVLH x -direction
A_y	amplitude of the motion in the LVLH y -direction
A_z	amplitude of the motion in the LVLH z -direction
E_r	relative eccentric anomaly
$\bar{\mathbf{g}}$	gravitational acceleration vector
i_r	relative inclination
$\bar{\mathbf{I}}$	identity matrix
k_a	scaling parameter for attractive potential
k_r	scaling parameter for repulsive potential
n	mean motion of the chief's orbit
$\bar{\mathbf{n}}_r$	vector normal to the instantaneous relative orbit plane
$\hat{\mathbf{n}}_r$	unit vector normal to the instantaneous relative orbit plane
P	period of the chief's orbit
q	shaping matrix element

$\bar{\bar{Q}}_a$	shaping matrix for attractive potential
$\bar{\bar{Q}}_r$	shaping matrix for repulsive potential
r	magnitude of deputy position vector with respect to center of central body
r_{obs_soi}	radius of obstacle sphere of influence
$\bar{\mathbf{r}}$	deputy position vector with respect to center of central body
${}^I\dot{\bar{\mathbf{r}}}$	derivative with respect to time of deputy position vector, taken in inertial frame
${}^I\ddot{\bar{\mathbf{r}}}$	second derivative with respect to time of deputy position vector, taken in inertial frame
r^C	magnitude of chief position vector with respect to center of central body
$\bar{\mathbf{r}}^C$	chief position vector with respect to center of central body
${}^I\dot{\bar{\mathbf{r}}}^C$	derivative with respect to time of chief position vector, taken in inertial frame
${}^I\ddot{\bar{\mathbf{r}}}^C$	second derivative with respect to time of chief position vector, taken in inertial frame
s	integer number of orbits for station-keeping drift to target location
t	time
t_b	time at which maneuver is executed
tgt	subscript indicating target
T	relative orbital element error matrix component
$\bar{\mathbf{T}}$	relative orbital element error vector
$\bar{\mathbf{v}}$	relative velocity vector in LVLH frame
x	relative position vector component in LVLH x -direction
\dot{x}	derivative with respect to time of relative position vector component in LVLH x -direction, taken in LVLH frame
\ddot{x}	second derivative with respect to time of relative position vector component in LVLH x -direction, taken in LVLH frame

\hat{x}	LVLH coordinate unit vector in radial direction
\hat{x}'	unit vector parallel to LVLH coordinate unit vector in radial direction
x_d	coordinate of instantaneous center of motion in radial direction (Lovell notation)
x_r	coordinate of instantaneous center of motion in radial direction
x_{max}	maximum constraint in LVLH x -direction
x_{min}	minimum constraint in LVLH x -direction
x_q	x -coordinate of point Q on circle that circumscribes instantaneous relative orbit ellipse
y	relative position vector component in LVLH y -direction
y_d	y -coordinate of instantaneous center of motion (Lovell notation)
y_r	y -coordinate of instantaneous center of motion
y_q	y -coordinate of point Q on circle that circumscribes instantaneous relative orbit ellipse
\dot{y}	derivative with respect to time of relative position vector component in LVLH y -direction, taken in LVLH frame
\ddot{y}	second derivative with respect to time of relative position vector component in along-track direction, taken in LVLH frame
\hat{y}	LVLH coordinate unit vector in along-track direction
\hat{y}'	unit vector parallel to LVLH coordinate unit vector in along-track direction
y_{max}	maximum constraint in LVLH y -direction
y_{min}	minimum constraint in LVLH y -direction
y_s	secular drift in LVLH y -direction
y_{tgt}	target position component in LVLH y -direction
\dot{y}_s	secular drift rate in LVLH y -direction
z	relative position vector component in LVLH z -direction
\dot{z}	derivative with respect to time of relative position vector component in LVLH z -direction, taken in LVLH frame

\ddot{z}	second derivative with respect to time of relative position vector component in LVLH z -direction, taken in LVLH frame
\hat{z}	LVLH coordinate unit vector in angular momentum direction
\hat{z}'	unit vector parallel to LVLH coordinate unit vector in cross-track direction
z_{max}	maximum constraint in LVLH z -direction
z_{min}	minimum constraint in LVLH z -direction
${}^I\bar{\alpha}^R$	angular acceleration vector of LVLH frame with respect to inertial frame
$\bar{\tau}$	vector containing the set of relative orbital elements
$\bar{\tau}_{tgt}$	vector containing the set of targeted relative orbital elements
β	x - y motion phase angle (Lovell notation)
γ	constant phase difference between relative eccentric anomaly and z -motion phase angle
ΔV	change in velocity
$\Delta\bar{V}$	change in velocity vector
$\Delta\bar{V}_a$	change in velocity vector due to attractive APF
$\Delta\bar{V}_r$	change in velocity vector due to repulsive APF
$\Delta\bar{V}_{TOTAL}$	total change in velocity vector due to attractive and repulsive APFs
ΔV_x	change in velocity in LVLH x -direction
ΔV_y	change in velocity in LVLH y -direction
ΔV_z	change in velocity in LVLH z -direction
ϕ	scalar potential function
ϕ_a	attractive artificial potential function
$\dot{\phi}_a$	time rate of change of attractive artificial potential function

ϕ_r	repulsive artificial potential function
ϕ_{rr}	state transition matrix 3x3 element
ϕ_{rv}	state transition matrix 3x3 element
ϕ_{vr}	state transition matrix 3x3 element
ϕ_{vv}	state transition matrix 3x3 element
$\dot{\phi}_r$	time rate of change of repulsive artificial potential function
ϕ_{TOT}	total artificial potential function
$\dot{\phi}_{TOT}$	time rate of change of total artificial potential function
μ	gravitational parameter of central body
v_r	relative true anomaly
ρ	magnitude of deputy relative position vector with respect to chief
$\bar{\rho}$	deputy relative position vector with respect to chief
${}^I \dot{\bar{\rho}}$	derivative with respect to time of deputy relative position vector with respect to chief, taken in inertial frame
${}^R \dot{\bar{\rho}}$	derivative with respect to time of deputy relative position vector with respect to chief, taken in LVLH frame
${}^I \ddot{\bar{\rho}}$	second derivative with respect to time of deputy relative position vector with respect to chief, taken in inertial frame
${}^R \ddot{\bar{\rho}}$	second derivative with respect to time of deputy relative position vector with respect to chief, taken in LVLH frame
$\bar{\rho}^{IC}$	position vector of relative orbit instantaneous center with respect to chief
$\bar{\rho}_{obs}$	position vector of obstacle with respect to chief
$\bar{\rho}_{tgt}$	target deputy position vector with respect to chief
σ	potential field broadening parameter
$\bar{\tau}$	vector containing relative orbital elements

$\bar{\tau}_{igt}$	vector containing relative orbital element targets
ψ	cross-track phase angle
ω	magnitude of angular velocity of LVLH frame with respect to inertial frame
$\dot{\omega}$	magnitude of angular acceleration of LVLH frame with respect to inertial frame
${}^I\bar{\omega}^R$	angular velocity vector of LVLH frame with respect to inertial frame
∇_{ρ}	gradient with respect to relative position vector
$\nabla_{\dot{\rho}}$	gradient with respect to relative velocity vector
0	subscript indicating initial condition
-	superscript indicating pre-maneuver condition
+	superscript indicating post-maneuver condition

LIST OF ABBREVIATIONS

AERCam	Autonomous Extravehicular Robotic Camera
AFRL	U.S. Air Force Research Laboratory
APF	artificial potential function
ARCSS	Autonomous Rendezvous and Capture Sensor System
ASTRO	Autonomous Space Transport Robotic Operations
ATV	Automated Transfer Vehicle
AVGS	Advanced Video Guidance Sensor
BAA	Broad Agency Announcement
CPOD	CubeSat Proximity Operations Demonstration
CSM	Command/Service Module
DARPA	Defense Advanced Research Projects Agency
DART	Demonstration of Autonomous Rendezvous Technology
DOF	degrees of freedom
ETS	Engineering Test Satellite
GN&C	guidance, navigation and control
GPS	Global Positioning System
HCW	Hills-Clohessy-Wiltshire
HTV	H-II Transfer Vehicle
ISS	International Space Station
JSC	Johnson Space Center
KMP	key maneuver point
LLC	limited liability company

LEM	Lunar Excursion Module
LIDAR	Laser Imaging Detection and Ranging
LVLH	local-vertical local-horizontal
MUBLCOM	Multiple Paths, Beyond-Line-of-Sight Communications
NASA	National Aeronautics and Space Administration
NASDA	National Space Development Agency
NEXTSat	Next Generation Satellite
PRISMA	Prototype Research Instruments and Space Mission Technology Advancement
RADAR	radio detection and ranging
ROE	relative orbital element
RPO	relative proximity operations
RSS	root sum square
RVS	Rendezvous Sensor
SpaceX	Space Exploration Technologies Corporation
SPHERES	Synchronized Position Hold Engage and Reorient Experimental Satellites
STM	state transition matrix
STS	Space Transportation System
TriDAR	Triangulation and LIDAR Automated Rendezvous and Docking
USSR	Union of Soviet Socialist Republics
XSS	Experimental Small Satellite
3U	three-unit

SUMMARY

This dissertation develops a methodology for automated trajectory control of a spacecraft about a non-maneuvering target. The methodology utilizes relative orbital elements (ROEs), combined with guidance laws based upon artificial potential functions (APFs), to perform automated trajectory planning and maneuver design.

The investigation provides a definitive reference on the definition and use of ROEs for relative proximity operations. The detailed derivation of ROEs is provided, along with transformations between ROEs and relative Cartesian state elements, characteristics of unforced motion in terms of ROEs, and the effect of impulsive maneuvers on ROEs. Through this work, the geometric interpretations of the angular ROEs have been clarified, leading to a stronger analogy between ROEs and classical orbital elements. New parameters, relative true anomaly and relative inclination, are defined. In addition, operationally useful guidance algorithms utilizing ROEs are developed and demonstrated. These ROE-based algorithms for rendezvous, circumnavigation and station-keeping provide a toolkit for relative proximity operations mission planning.

A new approach for APF formulation using ROEs as the target variables is developed. While previous approaches allowed targeting of a specified relative position, the present approach allows the targeting of a relative orbit geometry. The approach capitalizes upon the orbital dynamics represented through the ROEs, and retains the computational simplicity offered by the APFs. Formulations for the APF targeting of individual ROEs, as well as simultaneous targeting of a set of ROEs, are established. An approach for combining ROE targeting using APFs with obstacle avoidance is presented.

The trajectory guidance algorithm performance is evaluated using a flight-like guidance, navigation and control simulation environment, including orbital perturbations. Algorithm performance is established through a set of operationally relevant scenarios. The guidance algorithms are shown to be capable of correcting for environmental disturbances, while meeting the targeted relative orbits in an automated fashion.

CHAPTER 1

MOTIVATION, BACKGROUND AND CONTRIBUTIONS OF THIS INVESTIGATION

1.1 Introduction and Motivation

The close relative proximity operation (RPO) of two or more spacecraft in orbit is increasingly utilized in order to achieve mission objectives spanning on-orbit inspection [1], formation flight [2, 3], space station resupply [4], and satellite servicing [5, 6], for commercial and defense applications. The increasing prevalence of nano- and micro-spacecraft and emerging architectures including fractionated spacecraft have added to the priority of robust close proximity trajectory design and control [7, 8].

While the mission objectives related to RPO are diverse, there exists a set of relative trajectory control behaviors that are common to most RPO mission architectures, including rendezvous and station-keeping. Cooperative formation missions often have a stringent requirement on the relative spacing of the satellites in the cluster. For on-orbit inspection applications, circumnavigation of the space object may be desired. For satellite servicing or resupply missions, close approach and mating must occur. Underlying all of these behaviors is the requirement to maintain safe relative trajectories, where collision avoidance is assured [9, 10, 11, 12, 13].

A clear understanding of the relative motion between close proximity spacecraft on orbit is critical to the design of safe, robust mission plans [14]. To this end, this investigation advances the development of relative orbital elements (ROEs) for RPO mission planning. Analogous to classical orbital elements, ROEs provide a geometric interpretation of the relative motion of a deputy spacecraft with respect to a chief spacecraft that is in a circular orbit. ROEs allow the characterization of the deputy

spacecraft relative motion in a free-drift (unforced) trajectory, and ROEs provide a direct visualization of the maneuver effects on the relative motion geometry. The ROE formulation gives rise to straightforward control strategies that can be utilized to establish desired RPO behaviors [15, 16].

The common RPO requirement to ensure the avoidance of unintended contact between vehicles can be addressed, in part, by the utilization of a control methodology that is based upon artificial potential functions (APFs). APFs are widely utilized in robotics applications to establish relative control of vehicles [17, 18]. Attractive and repulsive potentials can be utilized to establish vehicle behaviors, including formation control and impact avoidance. This work advances the application of APFs to RPO missions, with the objective of providing a guidance formulation using ROEs to target the desired orbit geometry and ensure persistent collision avoidance. To date, ROEs have not been utilized for automated on-orbit mission planning. Limited testing of APF formulations for relative path planning has been conducted (as discussed in Section 1.2), but APFs have not been utilized for a flight mission to date. This work represents the first presentation of an APF formulation for targeting ROEs, allowing the targeting of a relative orbit geometry.

The work developed through this investigation is directly relevant to a number of mission applications, including the Georgia Institute of Technology's Prox-1 small satellite mission, sponsored by the United States Air Force Office of Scientific Research/Air Force Research Laboratory. Planned for launch in 2016, the Prox-1 mission will demonstrate automated trajectory control relative to a deployed CubeSat, for on-orbit inspection purposes. The trajectory guidance approaches developed through this work are validated within the Prox-1 guidance, navigation and control simulation environment, leading to implementation for the flight mission [19].

1.2 Background

1.2.1 A Brief History of Relative Proximity Operations

There is a rich history of relative proximity operations, dating back to the early years of human spaceflight. In the mid-1960's, the United States' Gemini program, and the Soviet Union's Soyuz program, had parallel goals to develop and demonstrate the systems, operational concepts, and techniques for orbital rendezvous and docking [20]. On December 16, 1965, U.S. astronauts Walter Schirra and Thomas Stafford navigated the Gemini VI spacecraft to rendezvous with Gemini VII, carrying astronauts Frank Borman and James Lovell. With an initial range following rendezvous of 40 m, over the next three orbits the two spacecraft stayed within ranges from 30 cm to 90 m. The first docking of two spacecraft occurred on March 16, 1966, when Neil Armstrong and David Scott docked Gemini VIII with the Agena target vehicle.

Following the failed Soyuz 1 mission in April 1967 that resulted in the catastrophic loss of the spacecraft and cosmonaut Vladimir Komarov, two unmanned Soviet Soyuz prototype spacecraft performed the first automated spacecraft rendezvous and docking. This automated approach was repeated in early 1968, paving the way for additional manned Soyuz missions beginning in October 1968. In January 1969, Soyuz 4 and 5 completed orbital rendezvous, docking, and crew transfer.

Two distinct methods arose from the rival space programs. The approach for orbital rendezvous and docking that was developed by the United States' National Aeronautics and Space Administration (NASA) favored a manual method for rendezvous and docking missions, with a priority placed upon operational flexibility with a pilot-in-the-loop. This approach reduced the need for hardware redundancy and complexity, and relied upon the astronauts' expertise for both nominal operations and anomaly response. The Soviet Union's approach to rendezvous and docking was centered on autonomy. The

stringent reliability requirements mandated by this approach added complexity to the system, resulting in longer development times and higher development costs, but over time the automated approach became highly efficient and repeatable [20].

NASA's Apollo mission architecture for the human exploration of the lunar surface depended upon the successful rendezvous and docking of the ascent stage of the lunar excursion vehicle (LEM) with the orbiting command/service module (CSM). Based upon technology demonstrated in the Gemini program, the LEM was equipped with a digital guidance computer, an inertial measurement unit, optical equipment, and a rendezvous radar system. The geometry of the LEM/CSM rendezvous scenario was defined such that the LEM was initially placed in a co-elliptic orbit 28 km below the CSM. When the "look angle" (the angle from the local horizontal in the LEM's orbit to the CSM) reached 26.6 deg, the terminal-phase burn was initiated to place the LEM on a rendezvous transfer. Astronauts actively controlled the terminal docking maneuvers.

The U.S. Skylab space station was launched in 1973. Three manned missions to Skylab were conducted, using the Apollo CSM for rendezvous and docking, and crew transfer. An Apollo CSM also docked with a Soviet Soyuz vehicle in July 1975, marking the first on-orbit docking of spacecraft from different nations.

In the three decades of NASA's Space Transportation System (STS, also known as the Space Shuttle) program, the Shuttle flew over sixty missions that involved close proximity operations [21]. With missions involving resupply and crew transport to Mir and the International Space Station (ISS), satellite servicing, payload deployment and retrieval, the Shuttle program demonstrated RPO capability that was highly flexible over a broad range of applications. Similar to Gemini and Apollo, the core systems of the Shuttle's RPO capability consisted of digital guidance computers, inertial measurement units, optical equipment, and a rendezvous radar. For rendezvous and docking, the Shuttle utilized a laser ranging device mounted in the payload bay, that provided range, range rate, and bearing to the target within 1.5 km. A visible camera was used to provide

the crew with visual aids during terminal docking. Shuttle RPO differed from Gemini and Apollo in that many of the RPO targets were not equipped with navigation aids (transponders or lights), nor were they designed to support rendezvous, retrieval, and on-orbit servicing. However, the Shuttle systems combined with skilled astronauts resulted in a highly successful RPO track record.

Automated RPO for robotic spacecraft has advanced significantly in the past 15 years. NASA Johnson Space Center (JSC) developed and flew the Autonomous Extravehicular Robotic Camera (AERCam) Sprint vehicle during the STS-87 mission in December 1997 [22]. The free-flying microsatellite demonstrated technologies necessary for external inspection and remote viewing of human spaceflight activities. Equipped with 12 cold-gas thrusters and gyros for maneuvering and angular rate sensing, the Sprint spacecraft employed a variable focal length video camera with a light source to provide illumination. The 16 kg flight system was 36 cm in diameter. Sprint was released and retrieved in the Space Shuttle Orbiter Payload Bay by astronaut Winston Scott during an extra-vehicular activity, and operated for approximately 75 minutes. JSC is currently developing Mini AERCam, a successor to AERCam Sprint. Mini AERCam development began in 2000, with the goal of reducing the free-flyer size (5 kg, 19 cm diameter) while adding additional cameras and relative navigation capability using GPS. Automatic position hold and point-to-point maneuvering capability are being developed, although the Mini AERCam will primarily be remotely piloted by astronauts.

The National Space Development Agency (NASDA) of Japan ETS-VII mission successfully performed the first fully autonomous rendezvous and docking of robotic satellites in July 1998 [23, 24]. The two satellites were launched together, and the chaser satellite was equipped with global positioning system (GPS) receivers, laser radar for ranging and bearing angles data, and a visible camera to measure relative position and attitude. The target satellite was cooperative, with passive laser radar reflectors and markings to assist the vision-based navigation. It was also equipped with GPS, and

transmitted its orbital state to the chaser. GPS measurements were used for relative navigation to a range of 500 m, laser ranging was used during approach from 500 m to 2 m, and the visible proximity sensing system was used for the final docking phase.

The United States Air Force Research Laboratory (AFRL) Experimental Small Satellite-10 (XSS-10) was launched in 2003, and demonstrated automated mission planning and trajectory control to provide rendezvous and on-orbit inspection relative to a spent launch vehicle upper stage [25]. A visible camera system was used for identification and relative tracking of the upper stage. The 20-hour mission was fully successful. AFRL followed with XSS-11 in 2005, a more capable flight system that conducted an 18-month mission, also demonstrating on-orbit inspection of a launch vehicle upper stage and other resident space objects. Details of the XSS-10 and XSS-11 guidance, navigation and control system architecture are not publicly available.

The Demonstration of Autonomous Rendezvous Technology (DART) mission, managed by NASA Marshall Spaceflight Center with Orbital Sciences Corporation as the system contractor, was designed to demonstrate autonomous close proximity operations of a small satellite (363 kg) relative to an experimental communications satellite, Multiple Paths, Beyond-Line-of-Sight Communications (MUBLCOM) [26, 27]. DART's primary sensor was the Advanced Video Guidance Sensor (AVGS), which derived from the Video Guidance Sensor that flew successfully onboard two Space Shuttle missions (STS-87 and STS-95). AVGS provided bearing measurements for ranges from 200-500 m, and provided range, bearing, and relative attitude within 200 m of the target. Additionally, GPS receivers on DART and MUBLCOM were used cooperatively to determine relative position and velocity. GPS data was used for relative navigation over large ranges; close-range relative navigation incorporated AVGS data as the primary data type. DART was not designed to receive ground commands, and the intent of the mission was to demonstrate that a pre-programmed spacecraft could autonomously rendezvous with a cooperative satellite. The flight of DART occurred on

April 15, 2005. A problem occurred in the transition from GPS to AVGS navigation that prevented the full capability of the AVGS system from being utilized [28]. With AVGS bearing data but without ranging data, DART was able to steer towards MUBLCOM, but was not able to accurately estimate range. Less than 11 hours into the mission, DART collided with MUBLCOM. Shortly thereafter, with little fuel remaining, DART autonomously initiated its pre-programmed departure and retirement maneuver, which ended the mission.

In 2007, the Defense Advanced Research Projects Agency (DARPA) Orbital Express mission demonstrated the technical feasibility and operational utility of autonomous techniques for on-orbit satellite servicing [29, 30]. Following autonomous rendezvous, proximity operations, and capture, propellant was transferred from the servicing satellite, ASTRO, to the chief satellite, NEXTSat (Figure 1). A flight hardware component was installed by the ASTRO onto NEXTSat, and the operation of the component was verified. The Orbital Express Autonomous Rendezvous and Capture Sensor System (ARCSS) consisted of visible and infrared sensors, and a laser rangefinder. On-board vision-based flight software performed relative orbit estimation and determined the attitude of the chief, while guidance and relative navigation software provided mission planning capability to enable fully automated relative proximity operations. While the chief spacecraft was passive, apriori knowledge of the chief configuration was utilized in the relative navigation algorithms.

The Massachusetts Institute of Technology Space Systems Laboratory developed a system called “Synchronized Position Hold Engage and Reorient Experimental Satellites” (SPHERES), that has been used in ground testing and on-board the ISS to validate navigation and control algorithms for RPO applications. In 2007 and 2008, a series of six tests were performed on the ISS using the SPHERES platforms [31, 32]. The initial tests involved three SPHERES satellites: a chaser, a target, and an obstacle. The test to demonstrate automated obstacle avoidance and rendezvous were not

successfully completed due to incorrect deployment by the crew. A subsequent test with a single satellite maneuvering about a virtual obstacle, and conducting rendezvous with a virtual target, was successful.



Figure 1: NEXTSat as imaged from ASTRO during Orbital Express proximity operations. Image credit: DARPA.

The European Space Agency's Jules Verne automated transfer vehicle (ATV) mated with the International Space Station (ISS) in April 2008 using an automated rendezvous and docking control system, along with automated collision avoidance software [33]. The European Prototype Research Instruments and Space Mission Technology Advancement (PRISMA) mission was launched in 2010, to demonstrate autonomous rendezvous and formation flying of two collaborative spacecraft, Mango and Tango [34, 35]. The chaser spacecraft, Mango, had a mass of 150 kg. Several different relative navigation techniques were utilized during the 10-month primary mission, including differential GPS measurements, spacecraft-to-spacecraft radio frequency

crosslink, and vision-based navigation. Long-range rendezvous and formation flight with as close as 1 m separation between spacecraft was tested.

The Georgia Institute of Technology's Prox-1 mission is designed to demonstrate automated trajectory control in low-Earth orbit relative to a deployed three-unit (3U) CubeSat, for an on-orbit inspection application [36]. The spacecraft is designed, fabricated and tested by a team of Georgia Tech undergraduate and graduate students who will also be responsible for mission operations. As shown in Figure 2, the 50 kg Prox-1 flight system will deploy The Planetary Society's LightSail 3U CubeSat. Prox-1 will then rendezvous with LightSail, and demonstrate automated station-keeping and range targeting based upon relative orbit determination using passive infrared and visible imaging. Prox-1 will circumnavigate LightSail, and conduct on-orbit inspection for LightSail's solar sail deployment event. The central system-level technology advancement of the Prox-1 mission is the vision-based autonomous navigation system. This system applies automated image processing algorithms to detect the CubeSat against the background of space. Relative orbit determination is performed based upon filtered angles and range estimates. Automated trajectory control maneuvers are calculated using a guidance methodology that applies ROEs to provide station-keeping, range targeting, and natural motion circumnavigation behaviors while APFs provide persistent collision avoidance. Prox-1 will be the first flight mission to utilize ROEs and APFs for automated mission planning. In addition, Prox-1 will provide flight validation of advanced micro-sun sensor technology, a micro-satellite propulsion system, and a lightweight thermal imager for small satellite applications.

A summary of the space flight systems that have performed relative proximity operations is provided in Table 1. The sensors and navigation aids used for guidance and control during rendezvous and proximity operations are indicated. While it is difficult to determine from the literature the level of autonomy that has been achieved by each system, it is clear that increased autonomy has been a trend since the XSS-10 mission in

2003. Large spacecraft with precise ranging requirements have increasingly utilized LIDAR rather than RADAR systems for range measurements. Since the late 1990s, differential GPS has been utilized by several missions for relative orbit determination. As flight systems decrease in size and cost, passive sensing (visible and infrared imaging), RF crosslink, and differential GPS are often used as an alternative to the resource-intensive active systems (LIDAR and RADAR).

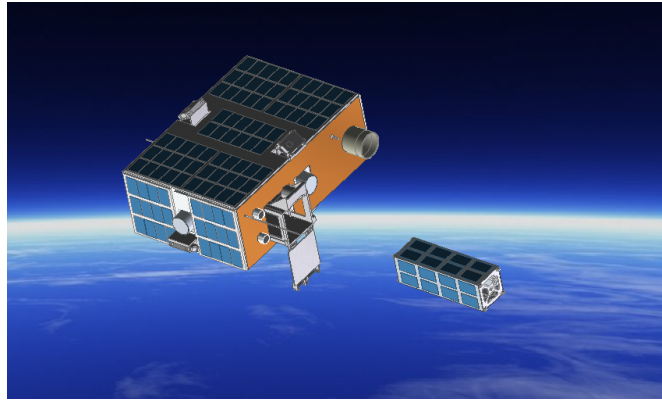


Figure 2: In 2016, Prox-1 will perform automated relative proximity operations for on-orbit inspection of the LightSail spacecraft using ROEs and APFs for trajectory guidance.

Table 1: Summary of RPO approaches used for U.S. and international missions.

Program/ Project	Implementing Organization	Operational Period	Instrumentation							Operability			Behaviors			
			Optical Markings	Acquisition Lighting	Visible Imaging	Infrared Imaging	RF Crosslink	Differential GPS	RADAR	LIDAR	Pilot-in-the-Loop	Ground-in-the-Loop	Telerobotic Operation	Rendezvous	Station Keeping	Docking/Berthing
Gemini	NASA	1962-1966	X	X	X		X		X		X	X		X	X	X
Soyuz	USSR	1967-			X		X				X	X		X	X	X
Apollo	NASA	1966-1972	X	X	X		X		X		X	X		X	X	X
STS	NASA	1981-2011			X		X		X	X	X	X		X	X	X
AERCam Sprint	NASA	1997			X								X		X	
ETS-VII	NASDA	1997-1999			X		X	X		X		X	X	X	X	
XSS-10	AFRL	2003			X							X		X	X	
XSS-11	AFRL	2005-2006			X					X		X		X	X	
DART	NASA	2005			X			X						X	X	
Orbital Express	DARPA	2007			X	X				X		X		X	X	X
SPHERES	MIT	2006-2008			X										X	
ATV	ESA	2008 -			X		X	X				X		X	X	X
PRISMA	ESA	2010 -			X		X	X				X		X	X	
CPOD	Tyvak	2015 (plan)			X		X	X				X		X	X	X
Prox-1	Georgia Tech	2015 (plan)			X	X						X		X	X	

1.2.2 Trend Toward Autonomy

Based upon missions in the recent past, and priorities for technology advancement related to proximity operations, there is a clear trend toward increasing autonomy in RPO applications. Future concepts for many RPO missions are centered on small spacecraft, without the capacity to operate power-intensive navigational systems. RPO is to be achieved without sophisticated collaboration schemes between spacecraft, and human-in-the-loop operation is not practical for most small satellite missions.

In the 2012 NASA Broad Agency Announcement (BAA) for the Edison Small Satellite Flight Demonstration Missions within the Office of the Chief Technologist, a Technology Focus Area was established for “Demonstration of Close Proximity Operations Technologies Utilizing Small Spacecraft Systems” [37]. The goal of the focus area was to demonstrate the ability of one or more small spacecraft to rendezvous and dock with other space objects, to advance technologies related to on-orbit inspection and satellite servicing. The Edison BAA noted: “Large and small spacecraft have demonstrated limited proximity operations, but more work is needed to develop highly reliable autonomous formation flight and rendezvous systems, especially for approaching uncooperative objects...” Through this opportunity, Tyvak Nano-Satellite Systems LLC, in partnership with California Polytechnic State University of San Luis Obispo, was selected to implement a space flight project to demonstrate automated rendezvous and docking of two three-unit CubeSats in orbit. The CubeSat Proximity Operations Demonstration (CPOD) mission is scheduled to launch in 2015.

The Office of the United States Air Force Chief Scientist describes a potential capability area related to fractionated/distributed space systems: “Constellations of smaller satellites operating cooperatively to perform a given mission set can provide greater survivability and greater ease of systematic upgrade. Architectures based on fractionation involve several functionally different satellite elements that cooperate to act

as a single system, while distributed architectures involve many copies of identical elements that operate coherently to produce greater capability than each element could individually” [38]. Such a vision will require significant autonomy to be achieved, including automated path planning and safe trajectory control. The United States Air Force Space Command is examining disaggregated space architectures to increase the resilience and affordability of critical space systems, as an alternative to traditional monolithic assets. Disaggregated systems distribute the capabilities of the system across multiple platforms. The Air Force Space Command white paper entitled “Resiliency and Disaggregated Space Architectures” states: “A disaggregated system design offers a means to avoid threats, ensure survivable capabilities despite hostile action, and develop the capacity to reconstitute, recover or operate through adverse events should robustness fail. Carefully pursued, disaggregation can lead to less costly and more resilient space architectures in the face of a rapidly evolving security environment” [39]. A key advantage of the fractionation approach is the capability to upgrade or replace a subcomponent without having to replace an entire system. Unit development costs and launch costs can be significantly reduced through fractionation. The fractionation approach requires automated collaborative operation between dispersed systems operating in a relative proximity operations domain.

Building upon the technical advancements of the past five decades in RPO, new tools and techniques are required to meet the demanding mission objectives of the future. Presently, close proximity operations generally require significant cooperation between vehicles, resource-intensive navigation instrumentation, or a human-in-the-loop to provide interactive control. Future RPO systems will become increasingly automated, with limited or no human involvement during critical mission operations. Increasingly, resource-constrained small spacecraft will be called upon to perform automated RPO tasks utilizing light-weight, low-power navigation sensors without reliance upon active cooperation from the chief vehicle.

1.2.3 Relative Orbital Elements

For RPO applications where two or more spacecraft are flying in close proximity, it is often convenient to apply the Clohessy-Wiltshire differential relative motion equations (discussed in Section 2.1), in order to calculate the relative motion of a deputy spacecraft about a chief spacecraft that is assumed to be in a circular orbit [40, 41]. Under these assumptions, the solutions to the Clohessy-Wiltshire equations can be re-parameterized as a set of relative orbital elements that fully characterize the relative motion of the deputy about the chief. In contrast to the position and velocity state elements expressed in a local-vertical, local-horizontal (LVLH) frame, ROEs provide a clear geometric interpretation of the relative motion. They also yield an intuitive understanding of how the unforced relative motion will evolve with time, and how the relative orbit will change in response to impulsive maneuvers with components in the LVLH unit directions.

Previous works have defined and utilized geometric parameterizations of the relative motion. Schaub and Junkins [42] and Vallado [43] defined scalar offsets in the orbit radial and downtrack directions, consistent with the relative orbital elements representing the instantaneous center of the motion in the plane of the chief's motion. Vallado describes the magnitude of the oscillatory motion in the chief's orbital plane. He also defines a constant that is consistent with the amplitude of the motion in the out-of-plane direction. Numerous works have evaluated relative motion and control algorithms associated with small variations in classical orbital elements between the deputy and chief [42, 44]. A relative parameter set that has been used extensively for mission applications is that developed by D'Amico and Montenbruck [45, 46, 47]. These relative parameters consist of either orbital element differences, or nonlinear combinations thereof. Han and Yin [48] put forward a set of geometric relative coordinates and demonstrate their use for elliptical chief relative motion.

This investigation advances the development of a parameterization of ROEs for close proximity mission planning. ROEs are a direct re-parameterization of the solutions to the Clohessy-Wiltshire equations. Lovell, Tragesser and Tollefson initially formulated ROEs in 2004 [15, 16], defining six elements that fully characterize the Clohessy-Wiltshire relative motion, and establishing the transformation between ROEs and LVLH Cartesian coordinates. They also showed the effect of one or more instantaneous maneuvers on ROEs, and developed a multiple-impulse guidance methodology for relative trajectory control. These advancements provide a useful framework for relative orbit mission planning. Analogous to classical orbital elements, ROEs provide a geometric interpretation of the relative motion of a deputy spacecraft with respect to a chief spacecraft that is in a circular orbit. ROEs allow the characterization of the deputy spacecraft relative motion in an unforced (free-motion) trajectory, and provide a direct visualization of the effects of maneuvers on the relative motion geometry.

Since the introduction of ROEs in 2004, the formulation has been used for the development of several analytical guidance strategies. Bevilacqua and Lovell [49] developed relative motion guidance solutions applying continuous, on-off thrust, and utilizing ROEs as a geometrical representation of the dynamics. Phillips [50] utilized ROEs for determination of satellite collision probability. Aubin [51] employed ROEs to generate solution vectors for a particle swarm evolutionary algorithm. Schwartz et al [52, 53] developed an ROE-based controller for station-keeping of a cluster of spacecraft as part of the DARPA System F6 flight program. Estimation of ROEs from relative angles and range data has been studied by the Air Force Research Laboratory's Space Vehicles Directorate, as described in Doolittle, Chavez and Lovell [54]. Johnson [55] derived ROEs for spacecraft on elliptical orbits in close proximity to a virtual chief on a known circular orbit. The Prox-1 small satellite mission will apply impulsive control strategies based upon ROEs to implement formation flight and circumnavigation maneuvers [56].

This work formally documents the derivation of the ROE parameterization in Section 2.1. A geometric interpretation of the ROEs is provided, leading to a strong analogy between ROEs and classical orbital elements. Additional parameters related to ROEs are described, including the newly-defined parameters relative true anomaly and relative inclination. The transformation between the LVLH Cartesian state elements and ROEs is provided in Section 2.2, and the evolution of ROEs with time is evaluated. Characteristics of the unforced motion are described in terms of ROEs in Section 2.3, including discussion of the three primary modes of the motion that are determined based upon the values of the ROEs. The formulation of this canonical set of ROEs is a recent advancement that provides a framework for mission planning within the context of the circular chief problem. This investigation seeks to utilize this framework to develop operationally-useful algorithms for RPO mission planning, described in Chapter 4.

It is noted that the notation for the ROEs used in this dissertation differs for some elements from that previously presented in References [15, 16]. Specifically, the coordinates for the instantaneous center of the relative motion, x_r and y_r , are changed from the notation previously used by Lovell et al, x_d and y_d . The notation for the semi-major axis of the instantaneous relative ellipse, a_r , is changed from a_e . The notation for relative eccentric anomaly, E_r , is changed from β . The subscript r denotes “relative.” The notation for the amplitude of the motion in the z -direction, A_z , is changed from the notation used by Lovell et al, z_{max} . These notation changes are intended to strengthen the analogy to classical orbital elements; the geometric interpretation of these ROEs is quite similar to their counterparts in classical orbital elements.

1.2.4 Artificial Potential Functions

Artificial potential function (APF) guidance formulations have been used since the 1980s for robotic control, beginning with Khatib [17], and continuing to the present time with a broad array of terrestrial applications [57]. Similar to potential fields that

occur in nature, such as gravitational and electromagnetic fields, artificial potential fields can be defined to shape the interaction of a robotic vehicle with the environment. Force vectors for vehicle control are found by taking the gradient of the APF. Trajectories based upon APF control are not planned explicitly, but rather, are shaped by the potential field in reaction to the changing environment.

The control forces resulting from an APF may be used to guide the robotic vehicle to a goal, at the minimum of the scalar potential function, along a path of steepest descent. Obstacles may be represented as areas of high potential in the APF, with the resultant repulsive control forces to enable obstacle avoidance. The attractive potential associated with the goal and repulsive potentials associated with obstacles can be superposed to provide a three-dimensional potential field that governs robot motion to the goal along a collision-free path [58]. The continuous nature of guidance based upon APFs, along with its computational simplicity, makes it an appealing approach for sustained robotic control applications where computational capability is limited. APFs may also be used to guide formations of vehicles [18].

Difficulties associated with APF formulation include the possible existence of local minima, where the total force acting on the vehicle is summed to zero at a point other than the goal. A second issue is oscillatory behavior, where the control forces acting on the vehicle result in an unstable, but bounded, motion. Lyapunov's second method for stability is often applied to APFs to demonstrate asymptotic stability about the goal [59].

In 1993, McInnes developed an APF control approach for orbital vehicles [60], and he later extended the algorithm to enable distributed control of multiple vehicles [61], and applied the approach to autonomous rendezvous [62]. McQuade [63] developed an APF-based controller for station-keeping and on-orbit assembly, and Tatsch and Xu described an approach for utilizing APFs for spacecraft attitude control [64]. Tatsch and Fitz-Coy developed a controller that applies APFs for on-orbit inspection and satellite

servicing [65]. Formulations for spacecraft swarm navigation and control using APFs were demonstrated by Saaj, Lappas and Gazi [66].

In 2007 and 2008, tests of a multiple-spacecraft close-proximity control algorithm were performed on board the International Space Station, using the SPHERES facility developed by the Massachusetts Institute of Technology Space Systems Laboratory [67]. The control algorithm, provided by the United States Naval Postgraduate School [68], combined a linear quadratic regulator for attraction to goal positions with artificial potential functions for collision avoidance. A total of six flight tests were implemented on board the ISS, demonstrating the capability to avoid obstacles and control an approach trajectory to enable soft docking.

Common APF formulations operate upon the range vector from the goal, and/or obstacle, to the vehicle. Lopez and McInnes [62] presented a guidance law that exerts control forces to align the velocity vector with the negative gradient of the potential field. While these methods will generally allow the vehicle to reach the goal, provided that the available thrust levels and propellant are great enough, the control strategy does not take advantage of the dynamics associated with the orbital environment.

This investigation seeks to develop APFs that operate upon ROEs, rather than range or velocity vectors, to control spacecraft motion in a manner that capitalizes upon the relative motion dynamics as expressed in the solutions to the Clohessy-Wiltshire equations. As such, this approach has the potential to enable spacecraft guidance with reduced thrust and propellant requirements relative to traditional methods, while retaining the computational simplicity that is inherent in the APF approach.

The general APF control methodology is described in Section 3.1, and applied to orbital trajectory guidance. An APF formulation for targeting ROEs is developed in Section 3.2. Targeting of individual ROE parameters is shown, and then the simultaneous targeting of multiple ROEs is demonstrated. An approach for combining attractive APFs for ROE targeting and repulsive APFs for obstacle avoidance is given.

The performance of the APF formulation is evaluated through a Monte Carlo simulation, and propellant utilization is compared with that for traditional maneuver design methods.

1.3 Contributions of this Investigation

This dissertation develops a methodology for automated trajectory guidance of a deputy spacecraft about a non-maneuvering target spacecraft designated the chief. The methodology utilizes relative orbital elements (ROEs), combined with guidance laws based upon artificial potential functions, to perform automated trajectory planning and maneuver design. The performance of the formulation is evaluated in a simulated flight environment, using the Prox-1 mission as a test case.

This investigation results in three key contributions that, together, advance the state of the art in relative proximity operations:

1. *Advancement of Relative Orbital Elements*

This investigation provides the detailed derivation of ROEs, transformations between ROEs and LVLH relative Cartesian state elements, establishes characteristics of unforced motion in terms of ROEs, and defines the effect of impulsive maneuvers on ROEs. While ROEs have been previously defined and their utility illustrated, this dissertation represents a definitive reference on the definition and application of ROEs for relative proximity operations. Through this work, the geometric interpretations of relative eccentric anomaly and the crosstrack-motion phase angle have been clarified, leading to a stronger analogy between ROEs and classical orbital elements. New parameters, relative true anomaly and relative inclination, are defined. The unforced relative motion trajectory is characterized in terms of ROEs, and three primary modes of the motion are described in terms of the values for ROEs. In addition, operationally useful control algorithms utilizing ROEs are developed and demonstrated; these algorithms for ROE-based rendezvous, natural motion circumnavigation, and station-keeping, represent a toolkit for relative proximity operations maneuver planning.

2. *Artificial Potential Function Control Formulation Using Relative Orbital Elements*

This work develops a new approach for APF formulation using ROEs as the targeted variables. Previous investigations of APFs for on-orbit trajectory control have utilized LVLH relative Cartesian state elements as input variables from which control forces are computed. Through the present approach, the APFs are constructed such that the derived control forces take advantage of the orbital dynamics that are embedded within the ROEs. This represents a significant advancement relative to prior formulations of APFs for on-orbit trajectory control, which often must work against orbital dynamics in order to achieve the desired behaviors. Formulations for the APF targeting of individual ROEs, as well as simultaneous targeting of a set of ROEs, are established. Through this formulation, the targeting of a full relative orbit geometry is accomplished. An approach for combining ROE targeting using APFs with obstacle avoidance is presented. Convergence of the APF algorithms to the targeted ROE values is evaluated.

3. *Evaluation of Trajectory Control Algorithms in a Realistic Environment*

This investigation evaluates the performance of the ROE and APF-based trajectory control approaches within the framework of a realistic guidance, navigation and control simulation environment. Flight-like scenarios are evaluated, including ROE station-keeping, ROE transfers to leading or trailing orbits, ROE transfers with APF-based obstacle avoidance, and APF targeting of ROEs with and without APF-based obstacle avoidance. It is shown that the automated trajectory control algorithms developed through this investigation are effective in correcting for environmental disturbances, and are suitable for application in flight missions.

CHAPTER 2

RELATIVE ORBITAL ELEMENTS

2.1 Clohessy-Wiltshire Equations for Relative Motion

The solutions to the Clohessy-Wiltshire equations [41] are often used to approximate the relative motion of one spacecraft with respect to another. Figure 3 shows the vector positions of two spacecraft in orbit about the same central body. For the derivation of the classical Clohessy-Wiltshire differential relative motion equations, it is assumed that the “chief” spacecraft travels in circular two-body motion about the central body, and the “deputy” also travels in two-body motion about the central body; the central body, chief, and deputy are treated as point masses, and all perturbations are neglected. The relative motion of the deputy about the chief is desired. The derivation of the HCW relative motion equations is included in numerous works, including Vallado [43].

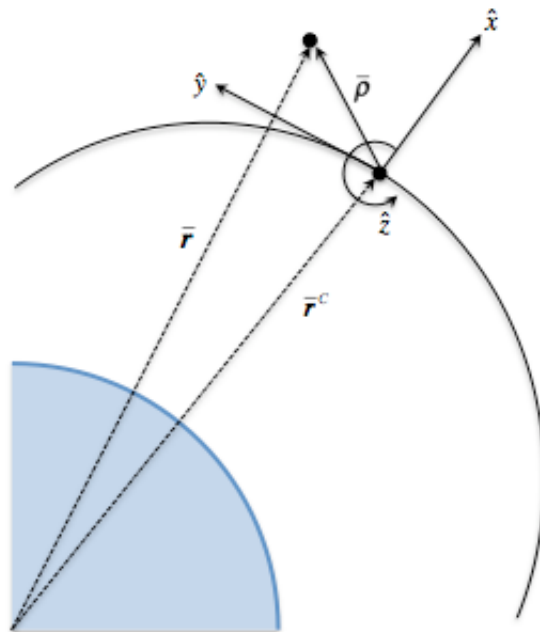


Figure 3: Coordinate system definition for LVLH frame.

The vector from the central body to the deputy is $\bar{\mathbf{r}}$, and the vector from the central body to the chief is $\bar{\mathbf{r}}^C$. The vector from the chief to the deputy is $\bar{\boldsymbol{\rho}}$.

$$\bar{\mathbf{r}} + \bar{\mathbf{r}}^C = \bar{\boldsymbol{\rho}} \quad (1)$$

Differentiating twice with respect to time in an inertial reference frame yields:

$${}^I\ddot{\bar{\mathbf{r}}} + {}^I\ddot{\bar{\mathbf{r}}^C} = {}^I\ddot{\bar{\boldsymbol{\rho}}} \quad (2)$$

The left superscript I indicates that the derivative is taken with respect to the inertial frame. The acceleration of the chief spacecraft due to two-body gravity in the inertial frame, is given by:

$${}^I\ddot{\bar{\mathbf{r}}^C} = -\frac{\mu}{(r^C)^3}\bar{\mathbf{r}}^C \quad (3)$$

The acceleration of the deputy spacecraft with respect to the chief expressed in the inertial reference frame is:

$${}^I\ddot{\bar{\boldsymbol{\rho}}} = {}^R\ddot{\bar{\boldsymbol{\rho}}} + 2({}^I\bar{\boldsymbol{\omega}}^R \times {}^R\dot{\bar{\boldsymbol{\rho}}}) + {}^I\bar{\boldsymbol{\alpha}}^R \times \bar{\boldsymbol{\rho}} + {}^I\bar{\boldsymbol{\omega}}^R \times ({}^I\bar{\boldsymbol{\omega}}^R \times {}^R\bar{\boldsymbol{\rho}}) \quad (4)$$

The left superscript R indicates that the derivative is taken with respect to the rotating reference frame. The rotating reference frame, commonly known as the local-vertical, local-horizontal (LVLH) frame, is shown in Figure 3. It is defined such that the \hat{x} -axis is aligned with the radial vector from the central body to the chief, the \hat{y} -axis is in the chief's along-track direction, and the \hat{z} -axis is orthogonal to \hat{x} and \hat{y} , in the direction of the chief's angular momentum vector. The angular velocity of the rotating frame with respect to the inertial frame is given by ${}^I\bar{\boldsymbol{\omega}}^R$, and the angular acceleration of the rotating frame with respect to the inertial frame is ${}^I\bar{\boldsymbol{\alpha}}^R$. Substituting Eqs. (3) and (4) into (2) gives:

$${}^I\ddot{\mathbf{r}} = -\frac{\mu}{(r^C)^3}\bar{\mathbf{r}}^C + {}^R\ddot{\boldsymbol{\rho}} + 2({}^I\bar{\boldsymbol{\omega}}^R \times {}^R\dot{\boldsymbol{\rho}}) + {}^I\bar{\boldsymbol{\alpha}}^R \times \bar{\boldsymbol{\rho}} + {}^I\bar{\boldsymbol{\omega}}^R \times ({}^I\bar{\boldsymbol{\omega}}^R \times {}^R\bar{\boldsymbol{\rho}}) \quad (5)$$

The acceleration of the deputy spacecraft in the inertial frame, ${}^I\ddot{\mathbf{r}}$, is due to the gravitational acceleration from the central body, $\bar{\mathbf{g}}$, plus any acceleration resulting from external forces (thrust, drag, etc.), $\bar{\mathbf{a}}_T$:

$${}^I\ddot{\mathbf{r}} = \bar{\mathbf{g}} + \bar{\mathbf{a}}_T \quad (6)$$

Expanding the two-body gravitational acceleration term, treating the central body as spherically symmetric, and neglecting the mass of the deputy spacecraft:

$${}^I\ddot{\mathbf{r}} = -\frac{\mu}{r^3}\bar{\mathbf{r}} + \bar{\mathbf{a}}_T \quad (7)$$

Substituting Eq. (1) into (7) gives:

$${}^I\ddot{\mathbf{r}} = -\frac{\mu}{|\bar{\mathbf{r}}^C + \bar{\boldsymbol{\rho}}|^3}(\bar{\mathbf{r}}^C + \bar{\boldsymbol{\rho}}) + \bar{\mathbf{a}}_T \quad (8)$$

The absolute value in the denominator of Eq. (8) can be expanded as:

$$|\bar{\mathbf{r}}^C + \bar{\boldsymbol{\rho}}| = [(\bar{\mathbf{r}}^C + \bar{\boldsymbol{\rho}}) \cdot (\bar{\mathbf{r}}^C + \bar{\boldsymbol{\rho}})]^{1/2} \quad (9)$$

Carrying out the dot product gives:

$$|\bar{\mathbf{r}}^C + \bar{\boldsymbol{\rho}}| = \bar{r}^C \left[1 + \frac{2(\bar{\mathbf{r}}^C \cdot \bar{\boldsymbol{\rho}})}{(r^C)^2} + \frac{\rho^2}{(r^C)^2} \right]^{1/2} \quad (10)$$

and

$$|\bar{\mathbf{r}}^C + \bar{\boldsymbol{\rho}}|^{-3} = \frac{1}{(r^C)^3} \left[1 + \frac{2(\bar{\mathbf{r}}^C \cdot \bar{\boldsymbol{\rho}})}{(r^C)^2} + \frac{\rho^2}{(r^C)^2} \right]^{-3/2} \quad (11)$$

The Binomial Theorem is employed to simplify Eq. (11). Neglecting terms of second order and higher, Eq. (11) can be rewritten as:

$$|\bar{\mathbf{r}}^C + \bar{\boldsymbol{\rho}}|^{-3} = \frac{1}{(r^C)^3} \left\{ 1 - \frac{3}{2} \left[\frac{2(\bar{\mathbf{r}}^C \cdot \bar{\boldsymbol{\rho}})}{(r^C)^2} + \frac{\rho^2}{(r^C)^2} \right] \right\} \quad (12)$$

It is assumed that the distance from the chief to the deputy is much less than the radial distance from the central body to the chief (i.e., $\rho \ll r^C$), allowing Eq. (12) to be further simplified as:

$$|\bar{\mathbf{r}}^C + \bar{\boldsymbol{\rho}}|^{-3} = \frac{1}{(r^C)^3} \left[1 - \frac{3(\bar{\mathbf{r}}^C \cdot \bar{\boldsymbol{\rho}})}{(r^C)^2} \right] \quad (13)$$

Substituting Eq. (13) into Eq. (8) gives:

$${}^I \ddot{\bar{\mathbf{r}}} = -\frac{\mu}{(r^C)^3} (\bar{\mathbf{r}}^C + \bar{\boldsymbol{\rho}}) \left[1 - \frac{3(\bar{\mathbf{r}}^C \cdot \bar{\boldsymbol{\rho}})}{(r^C)^2} \right] + \bar{\mathbf{a}}_r \quad (14)$$

Eqs. (5) and (14) can be combined to yield:

$$-\frac{\mu}{(r^C)^3} \bar{\mathbf{r}}^C + {}^R \ddot{\bar{\boldsymbol{\rho}}} + 2({}^I \bar{\boldsymbol{\omega}}^R \times {}^R \dot{\bar{\boldsymbol{\rho}}}) + {}^I \bar{\boldsymbol{\alpha}}^R \times \bar{\boldsymbol{\rho}} + {}^I \bar{\boldsymbol{\omega}}^R \times ({}^I \bar{\boldsymbol{\omega}}^R \times {}^R \bar{\boldsymbol{\rho}}) =$$

$$-\frac{\mu}{(r^C)^3} (\bar{\mathbf{r}}^C + \bar{\boldsymbol{\rho}}) \left[1 - \frac{3(\bar{\mathbf{r}}^C \cdot \bar{\boldsymbol{\rho}})}{(r^C)^2} \right] + \bar{\mathbf{a}}_r \quad (15)$$

Expanding the right-hand side of Eq. (15) and simplifying gives:

$${}^R\ddot{\bar{\rho}} + 2({}^I\bar{\omega}^R \times {}^R\dot{\bar{\rho}}) + {}^I\bar{\alpha}^R \times \bar{\rho} + {}^I\bar{\omega}^R \times ({}^I\bar{\omega}^R \times {}^R\bar{\rho}) = -\frac{\mu}{(r^C)^3} \left[\bar{\rho} - \frac{3\bar{r}^C(\bar{r}^C \cdot \bar{\rho})}{(r^C)^2} - \frac{3\bar{\rho}(\bar{r}^C \cdot \bar{\rho})}{(r^C)^2} \right] + \bar{a}_T \quad (16)$$

Each term in Eq. (2.1-16) will now be written in terms of Cartesian coordinates expressed in the LVLH rotating frame. The position vector from the chief to the deputy is written:

$$\bar{\rho} = x\hat{x} + y\hat{y} + z\hat{z} \quad (17)$$

so the relative velocity of the deputy with respect to the chief in the LVLH frame is:

$${}^R\dot{\bar{\rho}} = \dot{x}\hat{x} + \dot{y}\hat{y} + \dot{z}\hat{z} \quad (18)$$

and the relative acceleration of the deputy expressed in the LVLH frame is:

$${}^R\ddot{\bar{\rho}} = \ddot{x}\hat{x} + \ddot{y}\hat{y} + \ddot{z}\hat{z} \quad (19)$$

The angular velocity of the LVLH frame with respect to the inertial frame is:

$${}^I\bar{\omega}^R = \omega\hat{z} \quad (20)$$

and the angular acceleration of the LVLH frame with respect to the inertial frame is:

$${}^I\bar{\alpha}^R = \dot{\omega}\hat{z} \quad (21)$$

The second term on the left-hand side of Eq. (16) can be expanded as:

$$2({}^I\bar{\omega}^R \times {}^R\dot{\bar{\rho}}) = 2[\omega\hat{z} \times (\dot{x}\hat{x} + \dot{y}\hat{y} + \dot{z}\hat{z})] \quad (22)$$

Carrying out the cross product gives:

$$2({}^I\bar{\omega}^R \times {}^R\dot{\bar{\rho}}) = -2\omega\dot{y}\hat{x} + 2\omega\dot{x}\hat{y} \quad (23)$$

The third term on the left-hand side of Eq. (16) can be expanded as:

$${}^I\bar{\alpha}^R \times \bar{\rho} = \dot{\omega}\hat{z} \times (x\hat{x} + y\hat{y} + z\hat{z}) \quad (24)$$

Carrying out the cross product gives:

$${}^I\bar{\alpha}^R \times \bar{\rho} = -\dot{\omega}y\hat{x} + \dot{\omega}x\hat{y} \quad (25)$$

The fourth term on the left-hand side of Eq. (16) can be expanded as:

$${}^I\bar{\omega}^R \times ({}^I\bar{\omega}^R \times {}^R\bar{\rho}) = \omega\hat{z} \times [\omega\hat{z} \times (x\hat{x} + y\hat{y} + z\hat{z})] \quad (26)$$

Carrying out the cross products gives:

$${}^I\bar{\omega}^R \times ({}^I\bar{\omega}^R \times {}^R\bar{\rho}) = -\omega^2x\hat{x} - \omega^2y\hat{y} \quad (27)$$

On the right-hand side of Eq. (16), the mean motion of the chief's orbit, representing the average angular rate of the orbit, is defined as:

$$n = \sqrt{\frac{\mu}{(r^C)^3}} \quad (28)$$

Squaring both sides,

$$n^2 = \frac{\mu}{(r^C)^3} \quad (29)$$

The dot product that appears twice on the right-hand side of Eq. (16) can be expanded as:

$$\bar{r}^C \cdot \bar{\rho} = (r^C\hat{x}) \cdot (x\hat{x} + y\hat{y} + z\hat{z}) \quad (30)$$

Carrying out the dot product gives:

$$\bar{r}^C \cdot \bar{\rho} = r^C x \quad (31)$$

Evaluating the second term on the right-hand side of Eq. (16),

$$-\frac{3\bar{r}^c(\bar{r}^c \cdot \bar{\rho})}{(r^c)^2} = -3x\hat{x} \quad (32)$$

and the third term on the right-hand side of Eq. (16) is evaluated as:

$$-\frac{3\bar{\rho}(\bar{r}^c \cdot \bar{\rho})}{(r^c)^2} = \frac{-3x}{r^c}(x\hat{x} + y\hat{y} + z\hat{z}) \quad (33)$$

Substituting Eqs. (17), (19), (22), (25), (27), (29), (32) and (33) into Eq. (16) yields:

$$\begin{aligned} \ddot{x}\hat{x} + \ddot{y}\hat{y} + \ddot{z}\hat{z} - 2\omega\dot{y}\hat{x} + 2\omega\dot{x}\hat{y} - \dot{\omega}y\hat{x} + \dot{\omega}x\hat{y} - \omega^2x\hat{x} - \omega^2y\hat{y} = \\ -n^2 \left[x\hat{x} + y\hat{y} + z\hat{z} - 3x\hat{x} - 3\frac{x}{r^c}(x\hat{x} + y\hat{y} + z\hat{z}) \right] + \bar{a}_T \end{aligned} \quad (34)$$

Collecting terms in each of the LVLH frame unit directions,

$$\hat{x}: \quad \ddot{x} - 2\omega\dot{y} - (\omega^2 + 2n^2)x - \dot{\omega}y - \frac{3n^2x^2}{r^c} = a_{T_x} \quad (35)$$

$$\hat{y}: \quad \ddot{y} + 2\omega\dot{x} - (\omega^2 - n^2)y + \dot{\omega}x - \frac{3n^2xy}{r^c} = a_{T_y} \quad (36)$$

$$\hat{z}: \quad \ddot{z} + n^2z - \frac{3n^2xz}{r^c} = a_{T_z} \quad (37)$$

At this point, simplifying assumptions are made to obtain the HCW equations. For a circular orbit, the orbit angular velocity is equal to the mean motion, i.e.,

$$\omega = \sqrt{\frac{\mu}{(r^c)^3}} \quad (38)$$

and the angular acceleration for a circular orbit is zero,

$$\dot{\omega} = 0 \quad (39)$$

If, as before, it is assumed that $\rho \ll r^c$, then the following terms are negligible and can be neglected:

$$\frac{3n^2 x^2}{r^c} \approx 0 \quad (40)$$

$$\frac{3n^2 xy}{r^c} \approx 0 \quad (41)$$

$$\frac{3n^2 xz}{r^c} \approx 0 \quad (42)$$

Note that each of these terms arises from the term $\frac{3\bar{\rho}(\bar{r}^c \cdot \bar{\rho})}{(r^c)^2}$ in Eq. (16).

With these assumptions, Eqs. (35), (36) and (37) can be simplified to the Clohessy-Wiltshire equations:

$$\ddot{x} - 2n\dot{y} - 3n^2 x = a_{T_x} \quad (43)$$

$$\ddot{y} + 2n\dot{x} = a_{T_y} \quad (44)$$

$$\ddot{z} + n^2 z = a_{T_z} \quad (45)$$

For unforced motion, where no thrust is applied to the deputy spacecraft, the Clohessy-Wiltshire equations reduce to:

$$\ddot{x} - 2n\dot{y} - 3n^2 x = 0 \quad (46)$$

$$\ddot{y} + 2n\dot{x} = 0 \quad (47)$$

$$\ddot{z} + n^2 z = 0 \quad (48)$$

A detailed derivation of the solutions to the Clohessy-Wiltshire equations using Laplace transforms is given in Vallado [43]. If the initial conditions for the relative Cartesian state are denoted by the subscript 0, then the position and velocity solutions to the Clohessy-Wiltshire equations are given by:

$$x = \frac{\dot{x}_0}{n} \sin[n(t-t_0)] - \left(3x_0 + \frac{2\dot{y}_0}{n}\right) \cos[n(t-t_0)] + 4x_0 + \frac{2\dot{y}_0}{n} \quad (49)$$

$$y = \frac{2\dot{x}_0}{n} \cos[n(t-t_0)] + \left(6x_0 + \frac{4\dot{y}_0}{n}\right) \sin[n(t-t_0)] - (6nx_0 + 3\dot{y}_0)(t-t_0) - \frac{2\dot{x}_0}{n} + y_0 \quad (50)$$

$$z = \frac{\dot{z}_0}{n} \sin[n(t-t_0)] + z_0 \cos[n(t-t_0)] \quad (51)$$

$$\dot{x} = \dot{x}_0 \cos[n(t-t_0)] + (3nx_0 + 2\dot{y}_0) \sin[n(t-t_0)] \quad (52)$$

$$\dot{y} = -2\dot{x}_0 \sin[n(t-t_0)] + (6nx_0 + 4\dot{y}_0) \cos[n(t-t_0)] - 6nx_0 + 3\dot{y}_0 \quad (53)$$

$$\dot{z} = \dot{z}_0 \cos[n(t-t_0)] - nz_0 \sin[n(t-t_0)] \quad (54)$$

From Eqs. (49) and (52), the radial motion oscillates about a fixed offset, while Eqs. (50) and (53) show that the along-track motion has a similar oscillation, but with a secular drift at a constant rate. From Eqs. (51) and (54), it is seen that the motion in the cross-track direction is a simple harmonic oscillator, and the cross-track motion is decoupled from the motion in the chief's orbit plane.

2.2 Definition of Relative Orbital Elements

Similar to classical orbital elements that convey the orbit geometry in an inertially fixed reference frame, ROEs provide a geometric interpretation of the relative orbit expressed in the LVLH frame. The six ROE parameters fully define the relative orbital

state, and there is a clear transformation between the Cartesian state expressed in the LVLH frame and ROE's.

2.2.1 Derivation of Relative Orbital Elements

The ROEs are derived from the solution to the Clohessy-Wiltshire equations. The application of the Harmonic Addition Theorem to Eqs. (49-51), detailed in Appendix A, results in the equations:

$$x(t) = \begin{cases} 4x_0 + \frac{2\dot{y}_0}{n} + \frac{1}{2} \operatorname{sgn} \left[- \left(3x_0 + \frac{2\dot{y}_0}{n} \right) \right] \left[\left(6x_0 + \frac{4\dot{y}_0}{n} \right)^2 + \left(\frac{2\dot{x}_0}{n} \right)^2 \right]^{1/2} \\ \cos \left[n(t-t_0) + \tan^{-1} \left(\frac{\dot{x}_0/n}{3x_0 + \frac{2\dot{y}_0}{n}} \right) \right], 3x_0 + \frac{2\dot{y}_0}{n} \neq 0 \\ 4x_0 + \frac{2\dot{y}_0}{n} + \frac{\dot{x}_0}{n} \sin [n(t-t_0)], 3x_0 + \frac{2\dot{y}_0}{n} = 0 \end{cases} \quad (55)$$

$$y(t) = \begin{cases} y_0 - \frac{2\dot{x}_0}{n} - (6nx_0 + 3\dot{y}_0)(t-t_0) + \operatorname{sgn} \left(\frac{2\dot{x}_0}{n} \right) \\ \cos [n(t-t_0)] + \tan^{-1} \left(-\frac{6\dot{x}_0 + 4\dot{y}_0/n}{2\dot{x}_0/n} \right), \dot{x}_0 \neq 0 \\ y_0 - \frac{2\dot{x}_0}{n} - (6nx_0 + 3\dot{y}_0)(t-t_0) + \left(6\dot{x}_0 + \frac{4\dot{y}_0}{n} \right) \sin [n(t-t_0)], \dot{x}_0 = 0 \end{cases} \quad (56)$$

$$z(t) = \begin{cases} \operatorname{sgn}(z_0) \left[z_0^2 + \left(\frac{\dot{z}_0}{n} \right)^2 \right]^{1/2} \cos \left[n(t-t_0) + \tan^{-1} \left(-\frac{\dot{z}_0/n}{z_0} \right) \right], z_0 \neq 0 \\ \frac{\dot{z}_0}{n} \sin [n(t-t_0)], z_0 = 0 \end{cases} \quad (57)$$

Through introduction of the atan2 function, it can be shown that Equations (55-57) may be expressed as:

$$x(t) = 4x_0 + \frac{2\dot{y}_0}{n} - \frac{1}{2} \sqrt{\left(6x_0 + \frac{4\dot{y}_0}{n}\right)^2 + \left(\frac{2\dot{x}_0}{n}\right)^2} \cos\left[n(t-t_0) + \text{atan2}\left(\frac{2\dot{x}_0}{n}, 6x_0 + \frac{4\dot{y}_0}{n}\right)\right] \quad (58)$$

$$y(t) = y_0 - \frac{2\dot{x}_0}{n} - (6nx_0 + 3\dot{y}_0)(t-t_0) +$$

$$\sqrt{\left(6x_0 + \frac{4\dot{y}_0}{n}\right)^2 + \left(\frac{2\dot{x}_0}{n}\right)^2} \sin\left[n(t-t_0) + \text{atan2}\left(\frac{2\dot{x}_0}{n}, 6x_0 + \frac{4\dot{y}_0}{n}\right)\right] \quad (59)$$

$$z(t) = \sqrt{z_0^2 + \left(\frac{\dot{z}_0}{n}\right)^2} \sin\left[n(t-t_0) + \text{atan2}\left(z_0, \frac{\dot{z}_0}{n}\right)\right] \quad (60)$$

In Eqs. (58-60), the $\text{atan2}(a,b)$ function is related to the arctangent function $\tan^{-1}\left(\frac{a}{b}\right)$,

where $-\pi < \text{atan2}(a,b) \leq \pi$ based upon which quadrant contains the two arguments a and b . The $\text{atan2}(a,b)$ function eliminates the need for the sgn function, as well as the need to account for two different cases that appear in each of Eqs. (55-57). Note that for each equation, if both arguments of the $\text{atan2}(a,b)$ function are equal to zero, the coefficient of the sinusoid also equates to zero, resulting in a zero value for the periodic term.

The expressions for the deputy spacecraft position in the orbital plane of the chief spacecraft, Eqs. (58-59), each have periodic terms and constant terms. The along-track expression (59) also has a term that varies linearly with time, resulting in a secular drift motion. The first two ROEs describe the deputy spacecraft's instantaneous center of motion relative to the chief, encompassing the constant and linear time-varying terms in Eqs. (58-59). Expressed in terms of the LVLH Cartesian state initial conditions, the instantaneous center of motion ROEs are defined as:

$$x_r = 4x_0 + \frac{2\dot{y}_0}{n} \quad (61)$$

$$y_r = y_0 - \frac{2\dot{x}_0}{n} - (6nx_0 + 3\dot{y}_0)(t - t_0) \quad (62)$$

From Eq. (59), the amplitude of the sinusoidal motion in the along-track direction is given by:

$$A_y = \sqrt{\left(6x_0 + \frac{4\dot{y}_0}{n}\right)^2 + \left(\frac{2\dot{x}_0}{n}\right)^2} \quad (63)$$

From Eq. (58), the amplitude of the sinusoidal motion in the radial direction is:

$$A_x = \frac{1}{2} \sqrt{\left(6x_0 + \frac{4\dot{y}_0}{n}\right)^2 + \left(\frac{2\dot{x}_0}{n}\right)^2} \quad (64)$$

Note that the amplitude of the sinusoidal motion in the radial direction is half of that in the along-track direction. Thus, the motion in the $\hat{x} - \hat{y}$ plane is always along an “instantaneous ellipse” with the major axis in the along-track direction and with a length that is twice that of the minor axis in the radial direction. Therefore, a single parameter can specify the shape of the instantaneous ellipse in the $\hat{x} - \hat{y}$ plane. This parameter, a_r , is the ROE representing the semi-major axis of the instantaneous relative orbit ellipse, equal to the along-track amplitude of the sinusoidal motion, A_y :

$$a_r = \sqrt{\left(6x_0 + \frac{4\dot{y}_0}{n}\right)^2 + \left(\frac{2\dot{x}_0}{n}\right)^2} \quad (65)$$

The fourth ROE parameterizes the angular position of the chaser spacecraft as it moves along the instantaneous relative orbit ellipse in the $\hat{x} - \hat{y}$ plane. This ROE is

termed the relative eccentric anomaly, E_r . It represents the argument of the sine and cosine functions in Eqs. (58) and (59), and can be written:

$$E_r = E_{r_0} + n(t - t_0) \quad (66)$$

where

$$E_{r_0} = \text{atan2}\left(\frac{2\dot{x}_0}{n}, 6x_0 + \frac{4\dot{y}_0}{n}\right) \quad (67)$$

A geometric interpretation of the first four ROE's is shown on an instantaneous relative motion ellipse in Figure 4. The semi-major axis of the ellipse is given by a_r . The instantaneous center of the ellipse is given by x_r and y_r , and the deputy's periapsis is annotated as point P. The instantaneous deputy position along the ellipse is annotated as point D, with coordinates (x, y) . A circle of radius a_r is circumscribed about the ellipse, and a dashed line, perpendicular to the major axis, is extended through point D, intersecting with the circumscribed circle at point Q. Relative eccentric anomaly, E_r , measures the angle centered on (x_r, y_r) , between the periapsis point P and point Q. Relative eccentric anomaly increases from zero at periapsis with motion in the counter-clockwise direction.

A geometric interpretation of A_z and ψ is shown in Figure 5, where the three-dimensional relative motion is projected onto the $\hat{x} - \hat{z}$ plane. The deputy position along the relative motion ellipse is annotated as initial condition D_0 at time t_0 and as point D at time t . A circle of radius A_z is drawn, with the center of the circle coincident with the center of the ellipse at point C. A dashed line, perpendicular to the \hat{z} -axis, is extended through point D_0 , intersecting with the circumscribed circle at point F_0 . Point G_0 is shown where a line parallel to the \hat{z} -axis through point F_0 intersects the \hat{x} -axis. The angle ψ then represents the angle, centered on point C with coordinates $(x_r, y_r, 0)$, between the $-\hat{x}$ -axis and the segment CF on the circle. The deputy's relative motion intersects the chief's orbit plane at $\psi = 0$ and $\psi = \pi$. These points are referred to as the relative ascending and descending nodes, respectively [15, 16]. The relative ascending node is the point where the deputy spacecraft passes through $z = 0$ with $\dot{z} = 0$; the direction of the deputy's motion is indicated by an arrow in Figure 5. At $t = t_0$, the cross-track motion phase angle is ψ_0 . As the deputy progresses in its relative motion about the chief, the cross-track motion phase angle changes according to Eq. (69) as point F progresses at a constant rate (equal to the chief's mean motion) about the circle. At the point in the ellipse where $z = A_z$, $\psi = \frac{\pi}{2}$. The relative descending node occurs at $\psi = \pi$, and

$$z = -A_z \text{ at } \psi = -\frac{\pi}{2}.$$

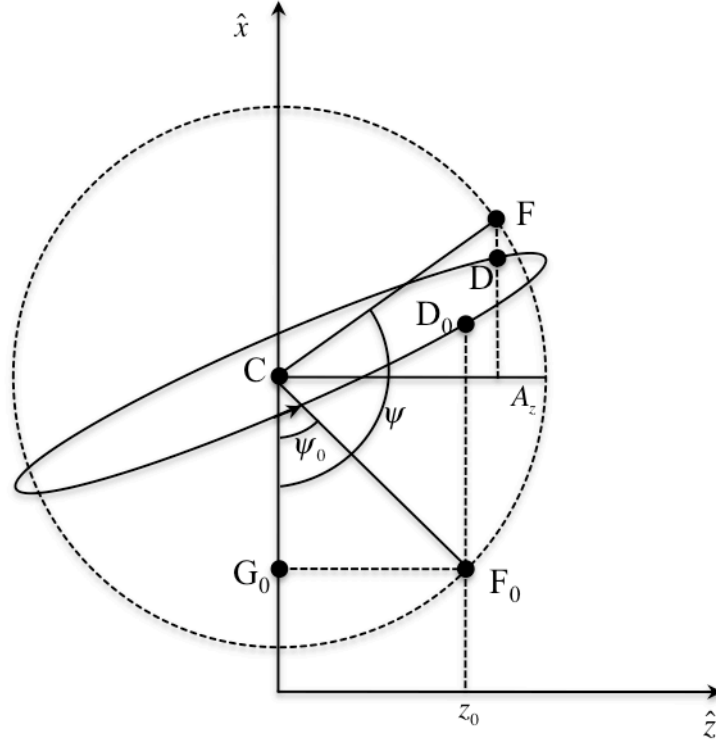


Figure 5: Cross-track motion phase angle geometry, projected onto the $\hat{x} - \hat{z}$ plane.

Expressions for ROEs in terms of the time-varying Cartesian state elements may be found as follows. Eq. (61) may be combined with Eqs. (49) and (53) to show that:

$$x_r = 4x + \frac{2\dot{y}}{n} \quad (71)$$

(For Cartesian state elements without the subscript 0, time dependence is implied.)

Likewise, Eq. (62) may be combined with Eqs. (50) and (52) to give:

$$y_r = y - \frac{2\dot{x}}{n} \quad (72)$$

For unforced motion, the time derivative of x_r may be taken using Eq. (71), and by substituting for the \ddot{y} acceleration term using Eq. (47), \dot{x}_r is shown to be equal to zero.

Therefore, x_r is invariant with time. However, taking the time derivative of y_r in Eq. (72)

and substituting for the \ddot{x} acceleration term using Eq. (46) shows that y_r has a secular drift that varies linearly with time.

Eq. (65) may be combined with Eqs. (49), (52), and (53) to show that:

$$a_r = \sqrt{\left(6x + \frac{4\dot{y}}{n}\right)^2 + \left(\frac{2\dot{x}}{n}\right)^2} \quad (73)$$

Taking the time derivative of a_r as expressed in Eq. (73) and substituting for \ddot{x} using Eq. (46) and for \ddot{y} using Eq. (47), it is shown that \dot{a}_r is equal to zero. Therefore, a_r is constant for unforced motion. Eqs. (71) – (73) indicate that while the instantaneous center of the motion in the $\hat{x} - \hat{y}$ plane may drift in the along-track direction, its radial component and size are invariant with time.

Eqs. (66) and (67) may be combined with Eqs. (49), (52) and (53) to show that:

$$E_r = \text{atan2}\left(\frac{2\dot{x}}{n}, 6x + \frac{4\dot{y}}{n}\right) \quad (74)$$

From Eq. (66), it is seen that the time derivative of E_r is equal to n .

Eq. (68) may be combined with Eqs. (51) and (54) to show that:

$$A_z = \sqrt{\dot{z}^2 + \left(\frac{\dot{z}}{n}\right)^2} \quad (75)$$

Taking the time derivative of A_z as expressed in Eq. (75), and substituting for the \ddot{z} term using Eq. (48), it is shown that \dot{A}_z is equal to zero. Therefore, A_z is a constant of the unforced motion.

Eqs. (69) and (70) may be combined with Eqs. (51) and (54) to show that:

$$\psi = \text{atan2}\left(z, \frac{\dot{z}}{n}\right) \quad (76)$$

From Eq. (69), it is seen that the time derivative of ψ is equal to n .

Table 2 summarizes the expressions for the six ROEs as a function of time in terms of the LVLH Cartesian state initial conditions, and in terms of the instantaneous LVLH Cartesian state elements.

Table 2: Expressions for ROEs in terms of LVLH Cartesian state elements.

Relative Orbital Element	Expressed in terms of LVLH Cartesian State Initial Conditions	Expressed in terms of Instantaneous LVLH Cartesian State Elements
x_r	$4x_0 + \frac{2\dot{y}_0}{n}$	$4x + \frac{2\dot{y}}{n}$
y_r	$y_0 - \frac{2\dot{x}_0}{n} - (6nx_0 + 3\dot{y}_0)(t - t_0)$	$y - \frac{2\dot{x}}{n}$
a_r	$\sqrt{\left(6x_0 + \frac{4\dot{y}_0}{n}\right)^2 + \left(\frac{2\dot{x}_0}{n}\right)^2}$	$\sqrt{\left(6x + \frac{4\dot{y}}{n}\right)^2 + \left(\frac{2\dot{x}}{n}\right)^2}$
E_r	$\text{atan2}\left(\frac{2\dot{x}_0}{n}, 6x_0 + \frac{4\dot{y}_0}{n}\right) + n(t - t_0)$	$\text{atan2}\left(\frac{2\dot{x}}{n}, 6x + \frac{4\dot{y}}{n}\right)$
A_z	$\sqrt{z_0^2 + \left(\frac{\dot{z}_0}{n}\right)^2}$	$\sqrt{z^2 + \left(\frac{\dot{z}}{n}\right)^2}$
ψ	$\text{atan2}\left(z_0, \frac{\dot{z}_0}{n}\right) + n(t - t_0)$	$\text{atan2}\left(z, \frac{\dot{z}}{n}\right)$

2.2.2 Transformation from Relative Orbital Elements to LVLH Cartesian State

It is frequently desirable to transform from ROEs to LVLH Cartesian states.

These transformations are developed here. The position components of the LVLH Cartesian state can be found as follows: Eqs. (61, 65, 66, 67) may be substituted into Eq. (58) to yield:

$$x = x_r - \frac{1}{2}a_r \cos E_r \quad (77)$$

Similarly, Eqs. (62, 65, 66, 67) may be substituted into Eq. (59) to give:

$$y = y_r + a_r \sin E_r \quad (78)$$

Eqs. (68, 69, 70) may be substituted into Eq. (60) to give:

$$z = A_z \sin \psi \quad (79)$$

The velocity LVLH state components can be found as follows. Eq. (72) may be substituted into Eq. (78) and rearranged to yield:

$$\dot{x} = \frac{n}{2} a_r \sin E_r \quad (80)$$

Eq. (71) may be substituted into Eq. (77) and rearranged to give:

$$\dot{y} = -\frac{3}{2} nx + \frac{1}{4} na_r \cos E_r \quad (81)$$

Eq. (71) can be rewritten as:

$$x = \frac{x_r}{4} - \frac{\dot{y}}{2n} \quad (82)$$

Substituting (82) into (81) and solving for \dot{y} gives:

$$\dot{y} = -\frac{3}{2} nx_r + na_r \cos E_r \quad (83)$$

Rearranging Eq. (75) gives:

$$\dot{z}^2 = n^2 (A_z^2 - z^2) \quad (84)$$

Substituting Eq. (79) into (84) gives:

$$\dot{z}^2 = n^2 A_z^2 \cos^2 \psi \quad (85)$$

Taking the square root of both sides of Eq. (43) gives:

$$\dot{z} = \pm n A_z \cos \psi \quad (86)$$

Referencing Fig. 6, because $\dot{z} > 0$ when $\psi = 0$, then

$$\dot{z} = n A_z \cos \psi \quad (87)$$

A summary of the transformation from ROEs to LVLH Cartesian state elements is given in Table 3.

Table 3: Expressions for LVLH Cartesian state elements in terms of ROEs.

LVLH Cartesian State Element	Expressed in Terms of ROEs
x	$x_r - \frac{1}{2} a_r \cos E_r$
y	$y_r + a_r \sin E_r$
z	$A_z \sin \psi$
\dot{x}	$\frac{n}{2} a_r \sin E_r$
\dot{y}	$-\frac{3}{2} n x_r + n a_r \cos E_r$
\dot{z}	$n A_z \cos \psi$

2.2.3 Evolution of Relative Orbital Elements with Time

Previously, expressions for the time variation of ROEs were developed in terms of LVLH Cartesian state elements. In this section, expressions for the time variation of each ROE are developed in terms of initial ROE values. The initial condition for each ROE at time t_0 is denoted with a subscript 0.

Eqs. (61) and (62) express the variation of the instantaneous center of motion with time, given initial conditions expressed in terms of the LVLH Cartesian state. From Eq. (61), it is clear that at $t = t_0$:

$$x_{r_0} = 4x_0 + \frac{2\dot{y}_0}{n} \quad (88)$$

As described in Section 2.2.1, the radial coordinate of the instantaneous center of the motion is shown to be constant for unforced motion:

$$x_r = x_{r_0} \quad (89)$$

Evaluating Eq. (62) at $t = t_0$ yields:

$$y_{r_0} = y_0 - \frac{2\dot{x}_0}{n} \quad (90)$$

Multiplying Eq. (61) by a factor of $\frac{3n}{2}$, and substituting with Eqs. (89) and (90) into Eq.

(62) gives:

$$y_r = y_{r_0} - \frac{3}{2}nx_{r_0}(t - t_0) \quad (91)$$

As discussed in Section 2.2.1, for unforced motion a_r does not vary as a function of time:

$$a_r = a_{r_0} \quad (92)$$

Relative eccentric anomaly varies with time as expressed in Eq. (66), and repeated here:

$$E_r = E_{r_0} + n(t - t_0) \quad (93)$$

The amplitude of the cross-track motion, A_z , is given by Eq. (68) as a function of the LVLH Cartesian state initial conditions. Once established by the initial conditions, A_z does not vary with time, therefore:

$$A_z = A_{z_0} \quad (94)$$

Finally, the phase angle in the cross-track harmonic motion is given by Eq. (69), repeated here:

$$\psi = \psi_0 + n(t - t_0) \quad (95)$$

In summary, for unforced motion the ROEs x_r , a_r and A_z remain constant, y_r varies linearly with time proportional to the secular drift rate, while the angular ROEs E_r and ψ vary at a constant angular rate equal to the chief's mean motion, n . A summary of the expressions for ROEs in terms of the ROE initial conditions is provided in Table 4.

Table 4: Expressions for ROEs in terms of ROE initial conditions.

Relative Orbital Element	Expressed in terms of ROE Initial Conditions
x_r	x_{r_0}
y_r	$y_{r_0} - \frac{3}{2}nx_{r_0}(t - t_0)$
a_r	a_{r_0}
E_r	$E_{r_0} + n(t - t_0)$
A_z	A_{z_0}
ψ	$\psi_0 + n(t - t_0)$

2.2.4 Additional Parameters Related to Relative Orbital Elements

In addition to the ROEs summarized in Table 2, there are several related parameters that provide insight into the relative motion. The additional parameters described here include along-track secular drift and drift rate, relative true anomaly, phase angle difference, and relative inclination.

Along-Track Secular Drift and Drift Rate

The linear time-varying along-track secular drift term in Eq. (59) indicates the direction and rate of the instantaneous center of motion in the $\hat{x} - \hat{y}$ plane. The secular drift parameter, y_s , is defined as:

$$y_s = -(6nx_0 + 3\dot{y}_0)(t - t_0) \quad (96)$$

In Eq. (96), y_s equals the distance in the along-track direction that the instantaneous center of motion has moved during the time period $t - t_0$. At a given time, the secular drift rate can be written as:

$$\dot{y}_s = -(6nx_0 + 3\dot{y}_0) \quad (97)$$

For unforced motion, the secular drift rate is a constant. By taking the time derivative of Eq. (62), it is clear that \dot{y}_s is equivalent to \dot{y}_r . From Eqs. (61) and (97), it is apparent that:

$$\dot{y}_s = -\frac{3}{2}nx_r \quad (98)$$

Thus, the secular drift rate of the instantaneous ellipse in the $\hat{x} - \hat{y}$ plane is negatively proportional to the radial coordinate of the instantaneous center of motion; if x_r is greater than zero, the secular drift is in the negative along-track direction, and vice-versa. If x_r equals zero, there is no drift. From Eqs. (62) and (97) it can be seen that:

$$y_r = y_0 + \dot{y}_s(t - t_0) \quad (99)$$

where

$$y_0 = y_0 - \frac{2\dot{x}_0}{n} \quad (100)$$

An example is shown in Fig. 6. The initial coordinates of the instantaneous center of motion in the $\hat{x} - \hat{y}$ plane at $t = t_0$ are (x_{r_0}, y_{r_0}) . Three orbit periods later, the instantaneous center coordinates are (x_r, y_r) . In this case, $x_{r_0} > 0$, so \dot{y}_s is negative, and

the secular drift is from right to left, in the negative along-track direction. Secular drift rate may be used as an alternative to x_r within the set of ROEs.

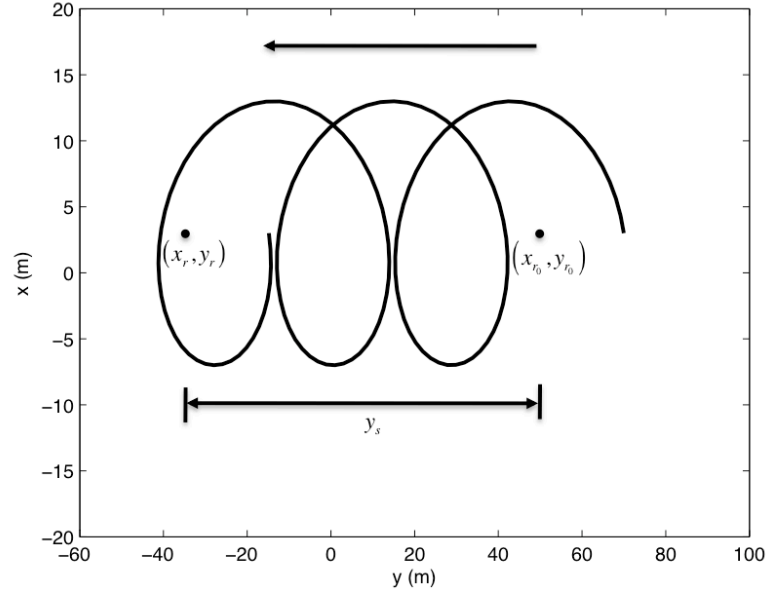


Figure 6: Secular along-track drift in the $\hat{x} - \hat{y}$ plane.

Relative True Anomaly

An angle termed relative true anomaly may be defined that is analogous to the classical orbital element true anomaly, except that it is defined strictly in the $\hat{x} - \hat{y}$ plane. As shown in Figure 7, relative true anomaly, ν_r , is the angle, centered on (x_r, y_r) , between the periapsis point P and point D, the instantaneous deputy position along the ellipse. Point Q on the circumscribed circle is always twice as far as point D from the semi-major axis of the instantaneous relative motion ellipse. This can be shown as follows. From the standard equation of an ellipse, the instantaneous relative motion ellipse equation is:

$$\frac{(y - y_r)^2}{a_r^2} + \frac{(x - x_r)^2}{\left(\frac{a_r}{2}\right)^2} = 1 \quad (101)$$

Solving Eq. (80) for $x - x_r$ gives:

$$x - x_r = \frac{1}{2} \sqrt{a_r^2 - (y - y_r)^2} \quad (102)$$

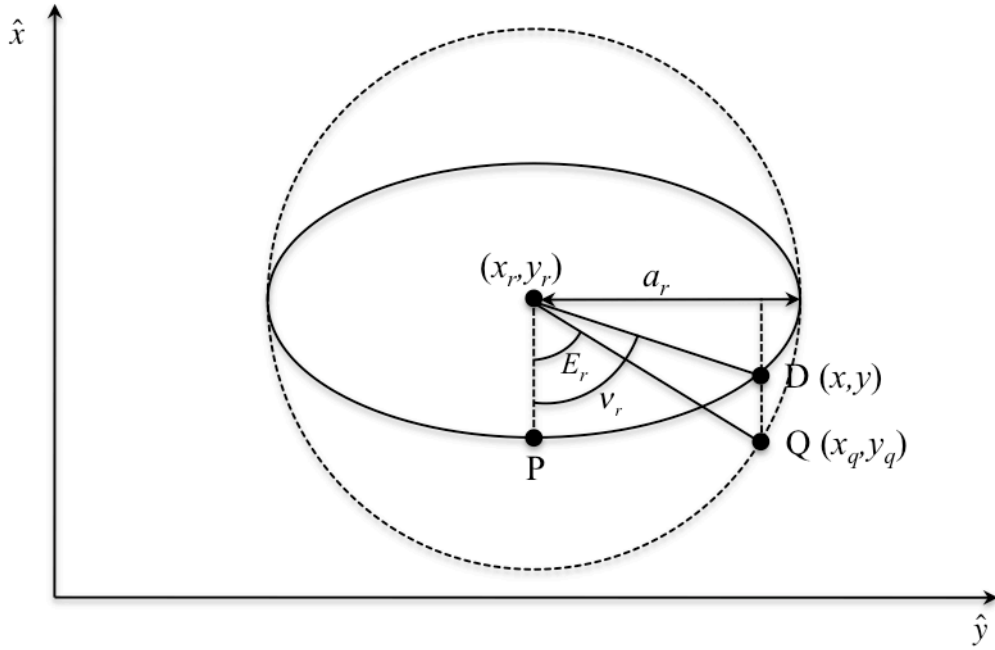


Figure 7: Geometry of relative eccentric anomaly and relative true anomaly.

From the standard equation for a circle, the equation for the circumscribed circle can be written as:

$$\frac{(y_q - y_r)^2}{a_r^2} + \frac{(x_q - x_r)^2}{a_r^2} = 1 \quad (103)$$

Solving Eq. (103) for $x_q - x_r$, and noting that $y_q = y$, gives:

$$x_q - x_r = \sqrt{a_r^2 - (y - y_r)^2} \quad (104)$$

From Eqs. (102) and (104), the desired result is obtained:

$$x - x_r = \frac{1}{2} (x_q - x_r) \quad (105)$$

From Fig. 8, it is clear that:

$$\tan E_r = \frac{y - y_r}{2(x_r - x)} \quad (106)$$

Substituting for x_r and y_r in Eq. (106) using Eqs. (71) and (72) and simplifying gives:

$$\tan E_r = \frac{\dot{x}}{3nx + 2\dot{y}} \quad (107)$$

From Fig. 8, it is apparent that:

$$\tan v_r = \frac{y - y_r}{x_r - x} \quad (108)$$

Substituting for x_r and y_r in Eq. (108) using Eqs. (71) and (72) and simplifying gives:

$$\tan v_r = \frac{2\dot{x}}{3nx + 2\dot{y}} \quad (109)$$

Therefore, relative true anomaly may be expressed as:

$$v_r = \tan^{-1} \left(\frac{2\dot{x}}{3nx + 2\dot{y}} \right) \quad (110)$$

Comparing Eq. (110) with Eq. (107), the relationship between relative eccentric anomaly and relative true anomaly is then:

$$v_r = \tan^{-1} (2 \tan E_r) \quad (111)$$

Relative true anomaly may be used as an alternative to relative eccentric anomaly within the set of ROEs.

Phase Angle Difference

The phase angle difference between the relative eccentric anomaly, E_r , and the cross-track motion phase angle, ψ , can be expressed as:

$$\gamma = \psi - E_r \quad (112)$$

The cross-track motion phase angle and relative eccentric anomaly both change at a rate that is equal to the chief's mean motion, as seen in Eqs. (66) and (69). Therefore, the phase difference γ is a constant, equal to the difference between the two angles at any chosen instant in time. Eq. (112) may be used to replace ψ with $\gamma + E_r$. The advantage of this approach is that four of the six ROEs are then constant, with y_r and E_r being the only time-varying ROEs. (Note that one could alternatively replace E_r with $\psi - \gamma$ and also achieve four constant ROEs.) The phase difference may be written in terms of LVLH Cartesian state elements as:

$$\gamma = \text{atan2}\left(z, \frac{\dot{z}}{n}\right) - \text{atan2}\left(\frac{2\dot{x}}{n}, 6x + \frac{4\dot{y}}{n}\right) \quad (113)$$

Relative Inclination

An important parameter related to the three-dimensional relative motion is the relative inclination, the angle between the relative orbit plane and the chief's orbit plane (i.e., the $\hat{x} - \hat{y}$ plane). As shown in Figure 8, the normal vector to the instantaneous relative orbit plane, \bar{n}_r , is found by taking the cross-product of two position vectors on the relative orbit, corresponding to $E_r = 0$ and $E_r = \frac{\pi}{2}$. In Figure 8, the LVLH $\hat{x} - \hat{y} - \hat{z}$

coordinate system is translated to parallel axes $\hat{x}'-\hat{y}'-\hat{z}'$ with the origin at $(x_r, y_r, 0)$.

The relative inclination is the angle between the relative orbit normal, \hat{n}_r and the \hat{z}' axis.

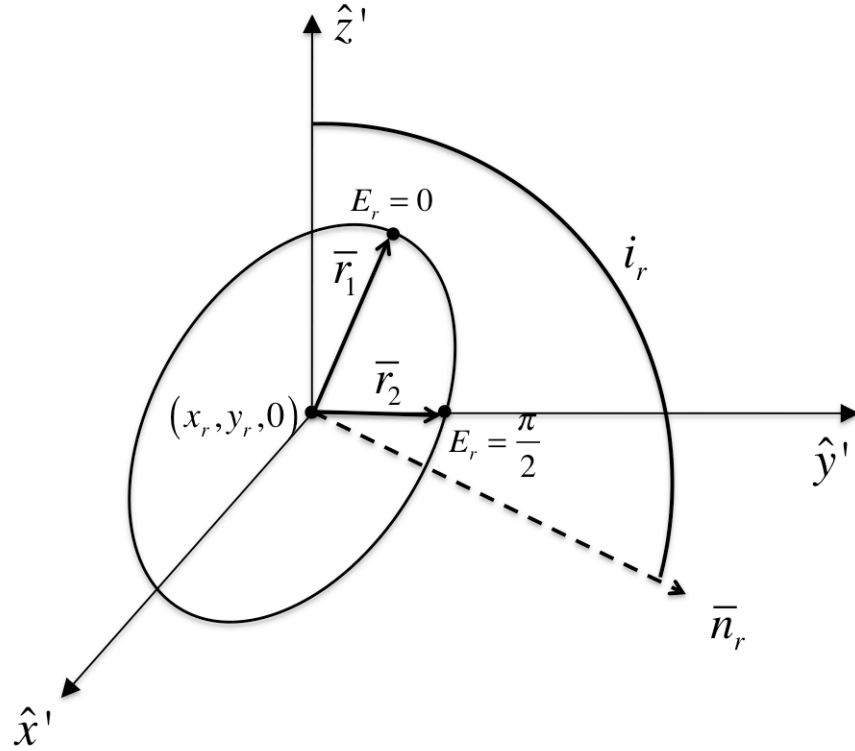


Figure 8: Geometry of relative inclination.

The position of the instantaneous center (IC) of the relative motion with respect to the origin of the LVLH coordinate system is given by the vector:

$$\bar{\rho}^{IC} = [x_r, y_r, 0]^T \quad (114)$$

The vector from the origin of the LVLH coordinate system to the relative orbit position corresponding to $E_r = 0$ (periastron) is given by Eqs. (77) – (79) as:

$$\bar{\rho}_1 = \begin{bmatrix} x_r - \frac{1}{2}a_r \\ y_r \\ A_z \sin \gamma \end{bmatrix} \quad (115)$$

where, from Eq. (112), γ is equal to ψ for $E_r = 0$. The position vector from the instantaneous center to the location on the relative orbit corresponding to $E_r = 0$ is given by:

$$\bar{\mathbf{r}}_1 = \bar{\boldsymbol{\rho}}_1 - \bar{\boldsymbol{\rho}}^{IC} \quad (116)$$

From Eqs. (114) – (116), $\bar{\mathbf{r}}_1$ can be evaluated as:

$$\bar{\mathbf{r}}_1 = \begin{bmatrix} -\frac{1}{2}a_r \\ 0 \\ A_z \sin \gamma \end{bmatrix} \quad (117)$$

The vector from the origin of the LVLH coordinate system to the relative orbit position

corresponding to $E_r = \frac{\pi}{2}$ is:

$$\bar{\boldsymbol{\rho}}_2 = \begin{bmatrix} x_r \\ y_r + a_r \\ A_z \cos \gamma \end{bmatrix} \quad (118)$$

Note that for $E_r = \frac{\pi}{2}$, $\gamma = \psi - \frac{\pi}{2}$. From Eq. (79), the cross-track component of the

position vector is equal to $A_z \sin \psi$, which equates to $A_z \sin \left(\gamma + \frac{\pi}{2} \right)$ for $E_r = \frac{\pi}{2}$. This is

simplified to $A_z \cos \gamma$ in Eq. (118). The position vector from the instantaneous center to

the deputy at $E_r = \frac{\pi}{2}$ is given by:

$$\bar{\mathbf{r}}_2 = \bar{\boldsymbol{\rho}}_2 - \bar{\boldsymbol{\rho}}^{IC} \quad (119)$$

From Eqs. (114), (118) and (119), $\bar{\mathbf{r}}_2$ can be evaluated as:

$$\bar{\mathbf{r}}_2 = \begin{bmatrix} 0 \\ a_r \\ A_z \cos \gamma \end{bmatrix} \quad (120)$$

Using the two position vectors on the instantaneous relative orbit, the cross-product can be taken to find the relative orbit normal, $\bar{\mathbf{n}}_r$:

$$\bar{\mathbf{n}}_r = \bar{\mathbf{r}}_1 \times \bar{\mathbf{r}}_2 \quad (121)$$

Using Eqs. (117) and (120), the relative orbit normal vector can be evaluated as:

$$\bar{\mathbf{n}}_r = \begin{bmatrix} -a_r A_z \sin \gamma \\ \frac{1}{2} a_r A_z \cos \gamma \\ -\frac{1}{2} a_r^2 \end{bmatrix} \quad (122)$$

The unit vector in the direction of the relative orbit normal is given by:

$$\hat{\mathbf{n}}_r = \frac{\bar{\mathbf{n}}_r}{|\bar{\mathbf{n}}_r|} \quad (123)$$

The relative inclination, i_r , is the angle between the instantaneous relative orbit plane and the chief orbit plane. The angle between the relative orbit normal and the chief's orbit normal can be found through the dot product of the two normal unit vectors:

$$\hat{\mathbf{n}}_r \cdot \hat{\mathbf{z}} = \cos i_r \quad (124)$$

The relative inclination is given by:

$$i_r = \cos^{-1}(\hat{\mathbf{n}}_r \cdot \hat{\mathbf{z}}) \quad (125)$$

Substituting Eqs. (122) and (123) into Eq. (125) and simplifying yields:

$$i_r = \cos^{-1} \left(\frac{-a_r}{\sqrt{3A_z^2 \sin^2 \gamma + A_z^2 \cos^2 \gamma + a_r^2}} \right) \quad (126)$$

From Eq. (126), it is seen that relative inclination is a function of the semi-major axis of the instantaneous relative ellipse in the $\hat{x} - \hat{y}$ plane, a_r , the amplitude of the cross-track motion, A_z , and the phase difference, γ . For unforced motion, each of these parameters is constant, so relative inclination is a constant as well. If the relative ellipse has a secular along-track drift rate due to a non-zero value for x_r , the instantaneous relative ellipse lies in a plane that is translating in the along-track direction, with a constant relative inclination angle. Note that for relative motion constrained to the $\hat{x} - \hat{y}$ plane ($A_z = 0$), the relative orbit normal is in the $-\hat{z}$ direction, resulting in a relative inclination of 180 deg. Because i_r is a function of a_r , A_z , and γ , it may be used to replace any of these three quantities within the set of ROEs.

To express relative inclination in terms of LVLH Cartesian state elements, Eqs. (73), (75) and (113) are substituted into Eq. (126) to give:

$$i_r = \cos^{-1} \left\{ \frac{-\sqrt{\left(6x + \frac{4\dot{y}}{n}\right)^2 + \left(\frac{2\dot{x}}{n}\right)^2}}{\sqrt{3 \left[z^2 + \left(\frac{\dot{z}}{n}\right)^2 \right] \sin^2 \left[\text{atan2} \left(z, \frac{\dot{z}}{n} \right) - \text{atan2} \left(\frac{2\dot{x}}{n}, 6x + \frac{4\dot{y}}{n} \right) \right] + z^2 + \left(\frac{\dot{z}}{n}\right)^2 + \left(6x + \frac{4\dot{y}}{n}\right)^2 + \left(\frac{2\dot{x}}{n}\right)^2}} \right\} \quad (127)$$

A summary of the useful parameters related to ROEs is provided in Table 5.

Table 5: Expressions for useful parameters related to ROEs.

Parameter	Expressed in terms of LVLH Cartesian State Elements	Expressed in terms of ROEs
y_s	$-(6nx_0 + 3\dot{y}_0)(t - t_0)$	$-\frac{3}{2}nx_r(t - t_0)$
\dot{y}_s	$-(6nx + 3\dot{y})$	$-\frac{3}{2}nx_r$
v_r	$\tan^{-1}\left(\frac{2\dot{x}}{3nx + 2\dot{y}}\right)$	$\tan^{-1}(2 \tan E_r)$
γ	$\text{atan2}\left(z, \frac{\dot{z}}{n}\right) - \text{atan2}\left(\frac{2\dot{x}}{n}, 6x + \frac{4\dot{y}}{n}\right)$	$\psi - E_r$
i_r	See Eq. (127)	$\cos^{-1}\left(\frac{-a_r}{\sqrt{3A_z^2 \sin^2 \gamma + A_z^2 \cos^2 \gamma + a_r^2}}\right)$

2.3 Characteristics of the Unforced Motion

Utilizing the ROEs defined in Section 2.2, the unforced “free drift” deputy spacecraft trajectory relative to the chief can be readily characterized. Similar to classical orbital elements, ROEs provide a physical understanding of the relative motion that is not obvious from the relative Cartesian state.

The relative motion is characterized in terms of three primary modes of the motion, based upon the values of the ROEs x_r , a_r , and A_z . As seen in Table 5, the first mode of the relative motion is dependent upon the value for x_r . If $x_r = 0$ (Mode 1A), then there is no secular drift of the relative motion in the along-track direction. If $x_r \neq 0$ (Mode 1B), then the instantaneous relative ellipse in the $\hat{x} - \hat{y}$ plane will have a secular drift with a rate that is dependent upon the value for x_r : a negative value for x_r results in a positive secular drift rate in the along-track direction, and a positive value for x_r results in a negative rate for secular along-track drift. Note that this behavior makes physical sense when one considers that $x_r = 0$ implies that the chief and deputy possess the same orbit

period, $x_r > 0$ implies that the deputy is on a larger inertial orbit (longer period) than the chief, and $x_r < 0$ implies that the deputy is on a smaller orbit (shorter period) than the chief.

The second mode of the relative motion depends upon the value for a_r . If $a_r = 0$ (Mode 2A), then there is no instantaneous relative ellipse in the $\hat{x} - \hat{y}$ plane. Stated differently, the instantaneous relative ellipse devolves to a point. If $a_r > 0$ (Mode 2B), then the instantaneous relative ellipse in the $\hat{x} - \hat{y}$ plane has the typical 2:1 ratio of semi-major axis in the along-track direction to semi-minor axis in the radial direction. This behavior makes physical sense when one considers that $a_r = 0$ implies that the chief and deputy are both on circular orbits, whereas $a_r > 0$ implies that the deputy is on an elliptical inertial orbit.

The third mode of the relative motion is dependent upon the value for A_z . If $A_z = 0$ (Mode 3A), then there is no cross-track motion. If $A_z > 0$ (Mode 3B), then there is simple harmonic oscillatory motion in the cross-track direction. It is noted that the initial value for y_r does not define a primary mode for the relative motion; y_r simply gives the initial along-track coordinate of the instantaneous relative ellipse in the $\hat{x} - \hat{y}$ plane. The angular ROEs E_r and ψ are used to define the location of the deputy on the relative orbit in-plane and out-of-plane of the chief's orbit, respectively. The phasing between these angles impacts the three-dimensional shape of the relative orbit, and determines the locations of the relative ascending and descending nodes where the deputy's inertial trajectory intersects the chief's orbit plane.

Table 6: Modes of unforced relative motion.

Mode		Initial Condition	Description
1	1A	$x_r = 0$	No secular along-track drift of instantaneous ellipse
	1B	$x_r \neq 0$	Secular along-track drift of instantaneous ellipse: $x_r > 0 \Rightarrow \dot{y}_s < 0$ $x_r < 0 \Rightarrow \dot{y}_s > 0$
2	2A	$a_r = 0$	No instantaneous ellipse in the $\hat{x} - \hat{y}$ plane
	2B	$a_r > 0$	Instantaneous ellipse in the $\hat{x} - \hat{y}$ plane
3	3A	$A_z = 0$	No cross-track motion
	3B	$A_z > 0$	Simple harmonic oscillatory cross-track motion

Each of the three primary modes of relative motion can be superposed to capture the full motion of the deputy spacecraft relative to the chief. For Mode 1A, there is no secular drift in the along-track direction, so the motion in the $\hat{x} - \hat{y}$ plane is either a stationary point with $x = 0$ (Mode 1A, 2A), or a stationary ellipse (Mode 1A, 2B) with the characteristic 2:1 ratio of the major-axis to minor-axis length in the $\hat{x} - \hat{y}$ plane.

For Mode 1B, where there is a secular drift of the instantaneous ellipse in the along-track direction, the $\hat{x} - \hat{y}$ projection of the deputy's motion will take on one of four different shapes. Figure 9 shows an example of each of these relative motion shapes, for a case where the chief's circular orbit altitude is 500 km, the initial along-track coordinate for the deputy is 100 m, and x_r for the deputy is 5 m, resulting in a negative secular drift rate in the along-track direction. One orbit period is shown. The shape of the relative drifting motion in the $\hat{x} - \hat{y}$ plane is determined by the value of a_r relative to x_r . For $a_r = 0$ (Mode 1B, 2A), the deputy is on a circular orbit, and the motion with respect to the chief is a straight line in the LVLH frame, with a fixed radial component. For $a_r > 0$ (Mode 1B, 2B), the relative motion may be a quasi-sinusoidal curve, a cycloid-

like curve that cusps at the extrema, or a cycloid-like curve that curls at the extrema. For all three of the cases in Mode 1B, 2B, the minimum radial coordinate occurs at perigee in the deputy's orbit, and the maximum radial coordinate occurs at apogee. The quasi-sinusoidal curve is produced when the along-track component of the LVLH Cartesian state increases or decreases monotonically.

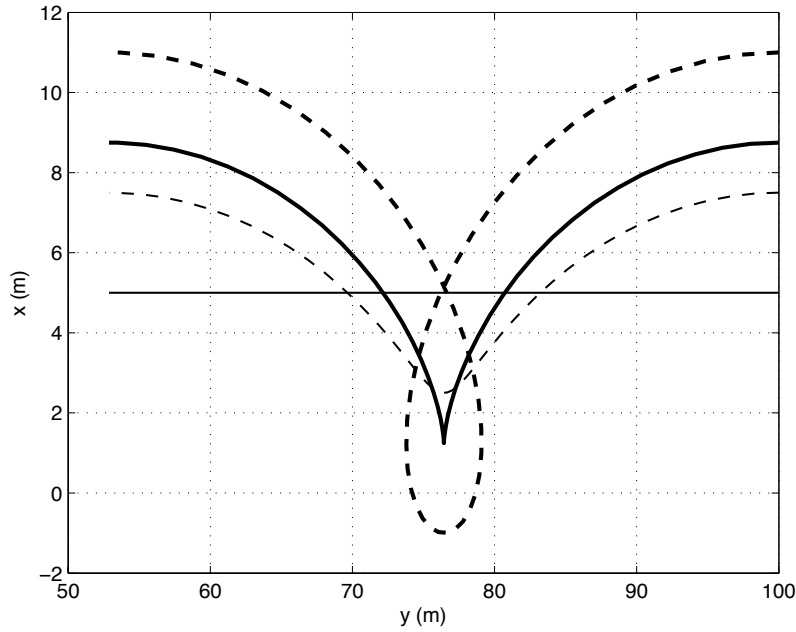


Figure 9: Four types of relative drifting motion in the $\hat{x} - \hat{y}$ plane. Mode 1B, 2A: solid line, $a_r = 0$. Mode 1B, 2B: dashed quasi-sinusoidal curve, $a_r < \frac{3}{2}|x_r|$; bolded cycloid-like curve with cusp, $a_r = \frac{3}{2}|x_r|$; bold-dashed cycloid-like curve with curl, $a_r > \frac{3}{2}|x_r|$. In all cases, motion is from right to left.

Substituting Eq. (77) into Eq. (81), and using Eq. (98) it is found that:

$$\dot{y} = \dot{y}_s + na_r \cos E_r \quad (128)$$

For the case where the along-track component is monotonically decreasing (as shown by the dashed curve in Fig. 10),

$$\dot{y}_s + na_r < 0 \quad (129)$$

Substituting for \dot{y}_s with Eq. (98) gives:

$$a_r < \frac{3}{2}x_r \quad (130)$$

Written generally, to account for both the monotonically increasing and decreasing cases, the condition for a quasi-sinusoidal curve can be written as:

$$a_r < \frac{3}{2}|x_r| \quad (131)$$

For a cycloid-like curve that cusps, $\dot{y} = 0$ at either periapsis or apoapsis in the deputy's orbit (i.e., at $E_r = 0$ or $E_r = \pi$). From Eq. (128), it is found that the condition reduces to:

$$a_r = \frac{3}{2}|x_r| \quad (132)$$

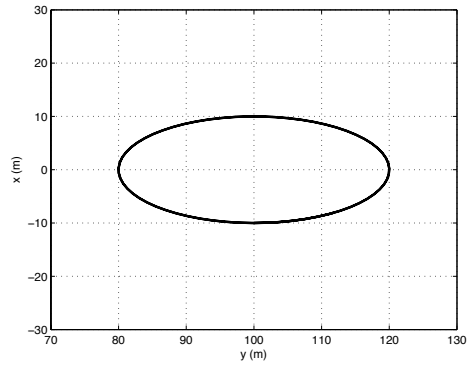
It is noted that for the case where the secular drift rate in the along-track direction is negative, cusps occur at perigee (as shown by the bolded curve in Fig. 10), while for a positive secular drift rate cusps occur at apogee. Finally, cycloid-like curves that curl occur for all other values of a_r , when:

$$a_r > \frac{3}{2}|x_r| \quad (133)$$

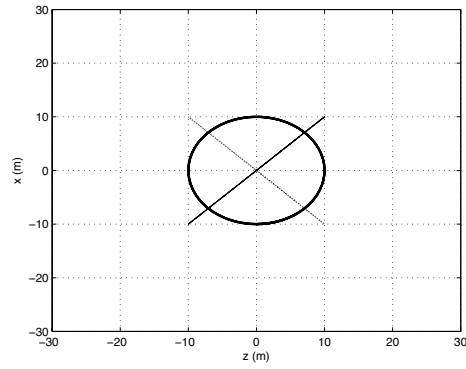
For Mode 3A, there is no cross-track motion and $z = 0$. For the combination of Modes 1A, 2A, 3B, the motion is a simple oscillation in the cross-track direction, and there is no motion in the $\hat{x} - \hat{y}$ plane.

For Mode 1A, 2B, 3B, the relative orbit is stationary and in a fixed plane. The angular difference between the relative eccentric anomaly and cross-track phase angle (equal to the parameter γ defined in Section 2.1) determines the shape and orientation of the projection of the motion in the $\hat{x}-\hat{z}$ and $\hat{y}-\hat{z}$ planes. The motion in the $\hat{x}-\hat{z}$ plane is an ellipse centered on $x = 0, z = 0$. The motion in the $\hat{y}-\hat{z}$ plane is an ellipse centered on $y = y_r, z = 0$. Figure 10 shows an example where $x_r = 0, y_r = 100$ m, $a_r = 20$ m, and $A_z = 10$ m. Relative orbits associated with four different values for γ are shown: $0, \pi/2, \pi,$ and $3\pi/2$. While the motion in the $\hat{x}-\hat{y}$ plane is unchanged for each case, the shape and orientation of the ellipses in the $\hat{x}-\hat{z}$ and $\hat{y}-\hat{z}$ planes are determined by the value of γ . Note that for $\gamma = \pi/2$ and $\gamma = 3\pi/2$, the projection of the motion onto the $\hat{x}-\hat{z}$ and $\hat{y}-\hat{z}$ planes are straight lines.

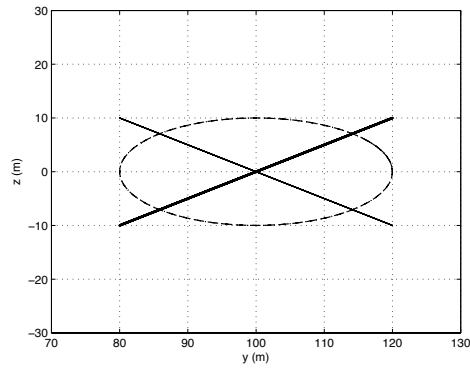
For Mode 1B, 2B, 3B, a secular along-track drift is superimposed upon the three-dimensional relative motion. Figure 11 shows an example where $x_r = 1$ m, $y_r = 100$ m, $a_r = 20$ m, $A_z = 10$ m, and $\gamma = 0$. The “corkscrew” motion apparent in the three-dimensional plot, Figure 11(d), results from the translation of the instantaneous plane of the motion in the along-track direction.



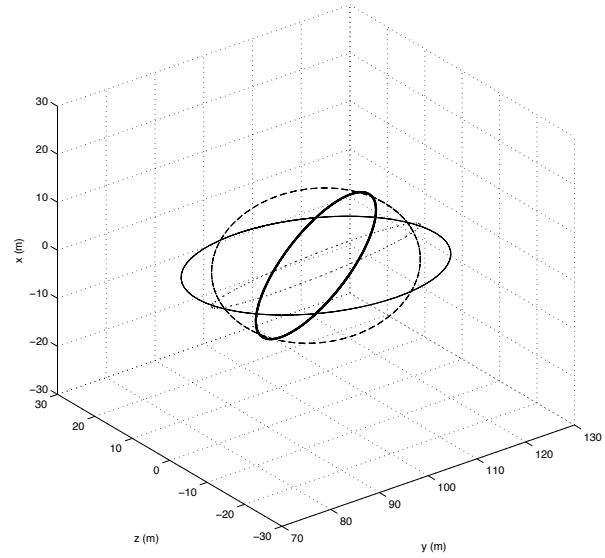
(a)



(b)

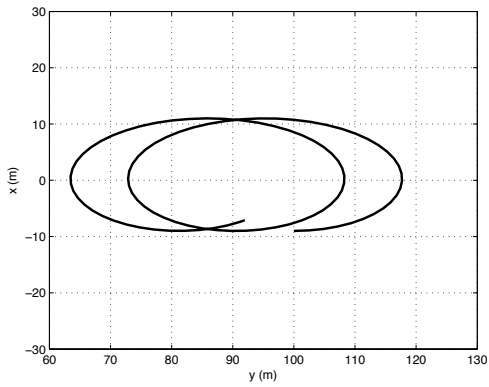


(c)

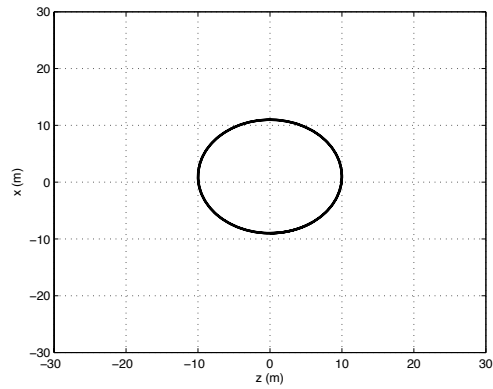


(d)

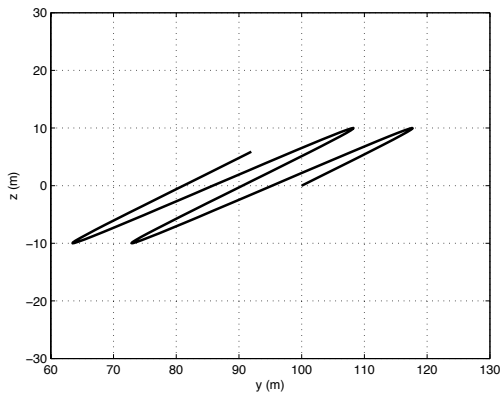
Figure 10: Mode 1A, 2B, 3B motion with varying phase difference, γ . Bold solid line: $\gamma = 0$; dashed line: $\gamma = \pi/2$; solid line: $\gamma = \pi$; dotted line: $\gamma = 3\pi/2$. (a) $\hat{y} - \hat{x}$ projection, (b) $\hat{z} - \hat{x}$ projection, (c) $\hat{y} - \hat{z}$ projection, (d) 3D plot.



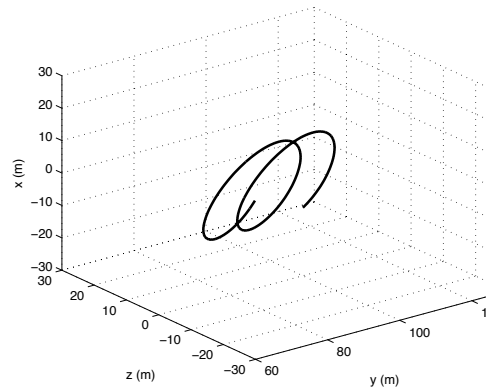
(a)



(b)



(c)



(d)

Figure 11: Mode 1B, 2B, 3B motion. (a) $\hat{y}-\hat{x}$ projection, (b) $\hat{z}-\hat{x}$ projection, (c) $\hat{y}-\hat{z}$ projection, (d) 3D plot.

2.4 Changes in Relative Orbital Elements Due to a Single Impulsive Maneuver

In addition to providing insight into the unforced relative motion, ROEs also provide a direct visualization of the effects of impulsive maneuvers on the relative motion geometry. A single impulsive maneuver will instantaneously increment the

relative velocity vector by the maneuver component in each coordinate direction of the LVLH frame: ΔV_x , ΔV_y , ΔV_z . The relative position vector is unchanged by the impulsive maneuver. Using the superscript “-” to denote state elements prior to the impulsive maneuver, and the superscript “+” for state elements following the maneuver, the following expressions can be written from Eqs. (77), (78), (79), (80), (83), and (87):

$$x^+ = x_r^- - \frac{1}{2}a_r^- \cos E_r^- \quad (134)$$

$$y^+ = y_r^- + a_r^- \sin E_r^- \quad (135)$$

$$z^+ = A_z^- \sin \psi^- \quad (136)$$

$$\dot{x}^+ = \frac{n}{2}a_r^- \sin E_r^- + \Delta V_x \quad (137)$$

$$\dot{y}^+ = -\frac{3}{2}nx_r^- + na_r^- \cos E_r^- + \Delta V_y \quad (138)$$

$$\dot{z}^+ = nA_z^- \cos \psi^- + \Delta V_z \quad (139)$$

The ROEs following an impulsive maneuver can be expressed in terms of Cartesian state elements by substituting Eqs. (134) – (139) into Eqs. (71) – (76), giving:

$$x_r^+ = 4x^+ + \frac{2\dot{y}^+}{n} \quad (140)$$

$$y_r^+ = y^+ - \frac{2\dot{x}^+}{n} \quad (141)$$

$$a_r^+ = \sqrt{\left(6x^+ + \frac{4\dot{y}^+}{n}\right)^2 + \left(\frac{2\dot{x}^+}{n}\right)^2} \quad (142)$$

$$E_r^+ = \text{atan2}\left(\dot{x}^+, 3nx^+ + 2\dot{y}^+\right) \quad (143)$$

$$A_z^+ = \sqrt{(z^+)^2 + \left(\frac{\dot{z}^+}{n}\right)^2} \quad (144)$$

$$\psi^+ = \text{atan2}\left(z^+, \frac{\dot{z}^+}{n}\right) \quad (145)$$

Substitution of Eqs. (134) – (139) into Eqs. (140) – (145) allows the post-maneuver ROEs to be expressed in terms of the pre-maneuver ROEs and the impulsive maneuver components. Specifically, substituting Eqs. (134) and (138) into Eq. (140) gives:

$$x_r^+ = x_r^- + \frac{2}{n} \Delta V_y \quad (146)$$

Substituting Eqs. (135) and (137) into Eq. (141) gives:

$$y_r^+ = y_r^- - \frac{2}{n} \Delta V_x \quad (147)$$

Substituting Eqs. (134), (137), and (138) into Eq. (142) gives:

$$a_r^+ = \sqrt{\left(a_r^- \cos E_r^- + \frac{4}{n} \Delta V_y\right)^2 + \left(a_r^- \sin E_r^- + \frac{2}{n} \Delta V_x\right)^2} \quad (148)$$

Substituting Eqs. (134), (137), and (138) into Eq. (143) gives:

$$E_r^+ = \text{atan2}\left(a_r^- \sin E_r^- + \frac{2}{n} \Delta V_x, a_r^- \cos E_r^- + \frac{4}{n} \Delta V_y\right) \quad (149)$$

Substituting Eqs. (136) and (139) into Eq. (144) gives:

$$A_z^+ = \sqrt{\left(A_z^- \sin \psi^-\right)^2 + \left(A_z^- \cos \psi^- + \frac{1}{n} \Delta V_z\right)^2} \quad (150)$$

Substituting Eqs. (136) and (139) into Eq. (145) gives:

$$\psi^+ = \text{atan2}\left(A_z^- \sin \psi^-, A_z^- \cos \psi^- + \frac{1}{n} \Delta V_z\right) \quad (151)$$

Introducing a parameter that represents the maneuver time, t_b , the post-maneuver ROEs can be expressed in terms of the relative Cartesian state initial conditions, the epoch for the initial conditions, given by t_0 , the maneuver time, t_b , and the maneuver components ΔV_x , ΔV_y , ΔV_z . Substituting Eqs. (61), (62), (65), (66), (67), (68), (69) and (70) into Eqs. (146) – (151), gives:

$$x_r^+ = 4x_0 + \frac{2\dot{y}_0}{n} + \frac{2}{n} \Delta V_y \quad (152)$$

$$y_r^+ = y_0 - \frac{2\dot{x}_0}{n} - (6nx_0 + 3\dot{y}_0)(t - t_0) - \frac{2}{n} \Delta V_x \quad (153)$$

$$a_r^+ = \left\{ \left[\left[\left(6x_0 + \frac{4\dot{y}_0}{n} \right)^2 + \left(\frac{2\dot{x}_0}{n} \right)^2 \right]^{1/2} \cos \left[\text{atan2}(\dot{x}_0, 3nx_0 + 2\dot{y}_0) + n(t_b - t_0) \right] + \frac{4}{n} \Delta V_y \right]^2 + \left[\left[\left(6x_0 + \frac{4\dot{y}_0}{n} \right)^2 + \left(\frac{2\dot{x}_0}{n} \right)^2 \right]^{1/2} \sin \left[\text{atan2}(\dot{x}_0, 3nx_0 + 2\dot{y}_0) + n(t_b - t_0) \right] + \frac{2}{n} \Delta V_x \right]^2 \right\}^{1/2} \quad (154)$$

$$E_r^+ = \text{atan2} \left\{ \left[\left[\left(6x_0 + \frac{4\dot{y}_0}{n} \right)^2 + \left(\frac{2\dot{x}_0}{n} \right)^2 \right]^{1/2} \sin \left[\text{atan2}(\dot{x}_0, 3nx_0 + 2\dot{y}_0) + n(t_b - t_0) \right] + \frac{2}{n} \Delta V_x, \left[\left(6x_0 + \frac{4\dot{y}_0}{n} \right)^2 + \left(\frac{2\dot{x}_0}{n} \right)^2 \right]^{1/2} \cos \left[\text{atan2}(\dot{x}_0, 3nx_0 + 2\dot{y}_0) + n(t_b - t_0) \right] + \frac{4}{n} \Delta V_y \right\} \quad (155)$$

$$A_z^+ = \left\{ \left(\left[z_0^2 + \left(\frac{\dot{z}_0}{n} \right)^2 \right]^{1/2} \sin \left[\text{atan2}(nz_0, \dot{z}_0) + n(t_b - t_0) \right] \right)^2 + \left(\left[z_0^2 + \left(\frac{\dot{z}_0}{n} \right)^2 \right]^{1/2} \cos \left[\text{atan2}(nz_0, \dot{z}_0) + n(t_b - t_0) \right] + \frac{1}{n} \Delta V_z \right)^2 \right\}^{1/2} \quad (156)$$

$$\psi^+ = \text{atan2} \left\{ \left[z_0^2 + \left(\frac{\dot{z}_0}{n} \right)^2 \right]^{1/2} \sin \left[\text{atan2}(nz_0, \dot{z}_0) + n(t_b - t_0) \right], \left[z_0^2 + \left(\frac{\dot{z}_0}{n} \right)^2 \right]^{1/2} \cos \left[\text{atan2}(nz_0, \dot{z}_0) + n(t_b - t_0) \right] + \frac{1}{n} \Delta V_z \right\} \quad (157)$$

Considerable simplifications can be achieved by writing the above expressions in terms of ROE initial conditions rather than Cartesian state initial conditions. Returning to Eqs. (61), (62), (65), (67), (68), and (70), we can express the ROE initial conditions at $t = t_0$ as:

$$x_{r_0} = 4x_0 + \frac{2\dot{y}_0}{n} \quad (158)$$

$$y_{r_0} = y_0 - \frac{2\dot{x}_0}{n} \quad (159)$$

$$a_{r_0} = \sqrt{\left(6x_0 + \frac{4\dot{y}_0}{n} \right)^2 + \left(\frac{2\dot{x}_0}{n} \right)^2} \quad (160)$$

$$E_{r_0} = \text{atan2} \left(\frac{2\dot{x}_0}{n}, 6x_0 + \frac{4\dot{y}_0}{n} \right) \quad (161)$$

$$A_{z_0} = \sqrt{z_0^2 + \left(\frac{\dot{z}_0}{n} \right)^2} \quad (162)$$

$$\psi_0 = \text{atan2}\left(z_0, \frac{\dot{z}_0}{n}\right) \quad (163)$$

Substituting Eqs. (158) – (163) into Eqs. (152) – (157) and simplifying yields:

$$x_r^+ = x_{r_0} + \frac{2}{n} \Delta V_y \quad (164)$$

$$y_r^+ = y_{r_0} - \frac{3}{2} n x_{r_0} (t_b - t_0) - \frac{2}{n} \Delta V_x \quad (165)$$

$$a_r^+ = \left(\left\{ a_{r_0} \cos[E_{r_0} + n(t_b - t_0)] + \frac{4}{n} \Delta V_y \right\}^2 + \left\{ a_{r_0} \sin[E_{r_0} + n(t_b - t_0)] + \frac{2}{n} \Delta V_x \right\}^2 \right)^{1/2} \quad (166)$$

$$E_r^+ = \text{atan2}\left\{ a_{r_0} \sin[E_{r_0} + n(t_b - t_0)] + \frac{2}{n} \Delta V_x, a_{r_0} \cos[E_{r_0} + n(t_b - t_0)] + \frac{4}{n} \Delta V_y \right\} \quad (167)$$

$$A_z^+ = \left\{ \left(A_z \sin[\psi_0 + n(t_b - t_0)] \right)^2 + \left(A_z \cos[\psi_0 + n(t_b - t_0)] + \frac{1}{n} \Delta V_z \right)^2 \right\}^{1/2} \quad (168)$$

$$\psi^+ = \text{atan2}\left\{ A_{z_0} \sin[\psi_0 + n(t_b - t_0)], A_{z_0} \cos[\psi_0 + n(t_b - t_0)] + \frac{1}{n} \Delta V_z \right\} \quad (169)$$

Through evaluation of Eqs. (164) – (169), the variation of ROEs as a function of the impulsive maneuver components in each LVLH coordinate direction may be established. Tables 7 and 8 show the direction of change (“+” representing a positive change, “-” representing a negative change) for ROEs x_r , y_r , and a_r , resulting from an impulse in the \hat{x} or \hat{y} coordinate directions, shown as ΔV_x and ΔV_y , respectively. The

location of the maneuver on the instantaneous relative orbit ellipse in the $\hat{x} - \hat{y}$ plane is parameterized by E_r^- , the relative eccentric anomaly at the maneuver epoch prior to the impulsive maneuver; Table 7 shows the variations based upon impulsive maneuvers performed within $0 \leq E_r^- < \pi$, and Table 8 shows the ROE variations for maneuver locations within the range of $\pi \leq E_r^- < 2\pi$. Tables 9 – 12 show the effect of impulsive maneuvers in the \hat{x} and \hat{y} directions on the value of E_r . Table 13 shows the variation of A_z based upon the sign of the maneuver component ΔV_z , where the maneuver location is parameterized by ψ^- . Tables 14 – 15 show the effect of maneuvers in the \hat{z} direction on the value of ψ . Collectively, Tables 7 – 15 represent a logic structure that captures the effect of an impulsive maneuver on the ROEs, as a function of maneuver component values and maneuver placement in the relative orbit.

Table 7: x_r, y_r, a_r variations based upon impulsive maneuver components, $0 \leq E_r^- < \pi$.

E_r^-	ΔV_x	ΔV_y	Δx_r	Δy_r	Δa_r
$E_r^- = 0$	+	0	0	-	+
	-	0	0	+	+
	0	+	+	0	+
	0	-	-	0	$0, \Delta V_y = -\frac{n}{2}a_r^-$ $+, \Delta V_y < -\frac{n}{2}a_r^-$ $-, -\frac{n}{2}a_r^- < \Delta V_y < 0$
$0 < E_r^- < \frac{\pi}{2}$	+	0	0	-	+
	-	0	0	+	$0, \Delta V_x = -na_r^- \sin E_r^-$ $+, \Delta V_x < -na_r^- \sin E_r^-$ $-, -na_r^- \sin E_r^- < \Delta V_x < 0$
	0	+	+	0	+
	0	-	-	0	$0, \Delta V_y = -\frac{n}{2}a_r^- \cos E_r^-$ $+, \Delta V_y < -\frac{n}{2}a_r^- \cos E_r^-$ $-, -\frac{n}{2}a_r^- \cos E_r^- < \Delta V_y < 0$
$E_r^- = \frac{\pi}{2}$	+	0	0	-	+
	-	0	0	+	$0, \Delta V_x = -na_r^-$ $+, \Delta V_x < -na_r^-$ $-, -na_r^- < \Delta V_x < 0$
	0	+	+	0	+
	0	-	-	0	+
$\frac{\pi}{2} < E_r^- < \pi$	+	0	0	-	+
	-	0	0	+	$0, \Delta V_x = -na_r^- \sin E_r^-$ $+, \Delta V_x < -na_r^- \sin E_r^-$ $-, -na_r^- \sin E_r^- < \Delta V_x < 0$
	0	+	+	0	$0, \Delta V_y = -\frac{n}{2}a_r^- \cos E_r^-$ $+, \Delta V_y > -\frac{n}{2}a_r^- \cos E_r^-$ $-, 0 < \Delta V_y < -\frac{n}{2}a_r^- \cos E_r^-$
	0	-	-	0	+

Table 8: x_r, y_r, a_r variations based upon impulsive maneuver components, $\pi \leq E_r^- < 2\pi$.

E_r^-	ΔV_x	ΔV_y	Δx_r	Δy_r	Δa_r
$E_r^- = \pi$	+	0	0	-	+
	-	0	0	+	+
	0	+	+	0	$0, \Delta V_y = \frac{n}{2} a_r^-$ $+, \Delta V_y > \frac{n}{2} a_r^-$ $-, 0 < \Delta V_y < \frac{n}{2} a_r^-$
	0	-	-	0	+
$\pi < E_r^- < \frac{3\pi}{2}$	+	0	0	-	$0, \Delta V_x = -n a_r^- \sin E_r^-$ $+, \Delta V_x > -n a_r^- \sin E_r^-$ $-, 0 < \Delta V_x < -n a_r^- \sin E_r^-$
	-	0	0	+	+
	0	+	+	0	$0, \Delta V_y = -\frac{n}{2} a_r^- \cos E_r^-$ $+, \Delta V_y > -\frac{n}{2} a_r^- \cos E_r^-$ $-, 0 < \Delta V_y < -\frac{n}{2} a_r^- \cos E_r^-$
	0	-	-	0	+
$E_r^- = \frac{3\pi}{2}$	+	0	0	-	$0, \Delta V_x = n a_r^-$ $+, \Delta V_x > n a_r^-$ $-, 0 < \Delta V_x < n a_r^-$
	-	0	0	+	+
	0	+	+	0	+
	0	-	-	0	+
$\frac{3\pi}{2} < E_r^- < 2\pi$	+	0	0	-	$0, \Delta V_x = -n a_r^- \sin E_r^-$ $+, \Delta V_x > -n a_r^- \sin E_r^-$ $-, 0 < \Delta V_x < -n a_r^- \sin E_r^-$
	-	0	0	+	+
	0	+	+	0	+
	0	-	-	0	$0, \Delta V_y = -\frac{n}{2} a_r^- \cos E_r^-$ $+, \Delta V_y < -\frac{n}{2} a_r^- \cos E_r^-$ $-, -\frac{n}{2} a_r^- \cos E_r^- < \Delta V_y < 0$

Table 9: E_r variations based upon impulsive maneuver components, $0 \leq E_r^- < \frac{\pi}{2}$.

E_r^-	ΔV_x	ΔV_y	E_r^+
$E_r^- = 0$	+	0	$0 < E_r^+ \leq \frac{\pi}{2}$
	-	0	$\frac{3\pi}{2} \leq E_r^+ < 2\pi$
	0	+	$E_r^+ = 0$
	0	-	$\Delta V_y < -\frac{n}{4}a_r^- < 0 \Rightarrow E_r^+ = \pi$ $\Delta V_y \geq -\frac{n}{4}a_r^- \Rightarrow E_r^+ = 0$
$0 < E_r^- < \frac{\pi}{2}$	+	0	$0 < E_r^+ \leq \frac{\pi}{2}$
	-	0	$\Delta V_x < -\frac{n}{2}a_r^- \sin E_r^- \Rightarrow \frac{3\pi}{2} \leq E_r^+ < 2\pi$ $\Delta V_x = -\frac{n}{2}a_r^- \sin E_r^- \Rightarrow E_r^+ = 0$ $-\frac{n}{2}a_r^- \sin E_r^- < \Delta V_x < 0 \Rightarrow 0 < E_r^+ \leq \frac{\pi}{2}$
	0	+	$0 \leq E_r^+ < \frac{\pi}{2}$
	0	-	$-\frac{n}{4}a_r^- \cos E_r^- < \Delta V_y < 0 \Rightarrow 0 \leq E_r^+ < \frac{\pi}{2}$ $\Delta V_y = -\frac{n}{4}a_r^- \cos E_r^- \Rightarrow \begin{cases} a_r^- = 0 \Rightarrow E_r^+ = 0 \\ a_r^- > 0 \Rightarrow E_r^+ = \frac{\pi}{2} \end{cases}$ $\Delta V_y < -\frac{n}{4}a_r^- \cos E_r^- \Rightarrow \frac{\pi}{2} < E_r^+ \leq \pi$

Table 10: E_r variations based upon impulsive maneuver components, $\frac{\pi}{2} \leq E_r^- < \pi$.

E_r^-	ΔV_x	ΔV_y	E_r^+
$E_r^- = \frac{\pi}{2}$	+	0	$E_r^+ = \frac{\pi}{2}$
	-	0	$\Delta V_x < -\frac{n}{2}a_r^- \Rightarrow E_r^+ = \frac{3\pi}{2}$
			$\Delta V_x = -\frac{n}{2}a_r^- \Rightarrow E_r^+ = 0$
			$\Delta V_x > -\frac{n}{2}a_r^- \Rightarrow E_r^+ = \frac{\pi}{2}$
0	+	$0 < E_r^+ \leq \frac{\pi}{2}$	
0	-	$\frac{\pi}{2} < E_r^+ \leq \pi$	
$\frac{\pi}{2} < E_r^- < \pi$	+	0	$\frac{\pi}{2} \leq E_r^+ < \pi$
	-	0	$-\frac{n}{2}a_r^- \sin E_r^- < \Delta V_x < 0 \Rightarrow \frac{\pi}{2} \leq E_r^+ < \pi$
			$\Delta V_x = -\frac{n}{2}a_r^- \sin E_r^- \Rightarrow \begin{cases} a_r^- = 0 \Rightarrow E_r^+ = 0 \\ a_r^- > 0 \Rightarrow E_r^+ = \pi \end{cases}$
			$\Delta V_x < -\frac{n}{2}a_r^- \sin E_r^- \Rightarrow \pi < E_r^+ \leq \frac{3\pi}{2}$
0	+	$0 < \Delta V_y < -\frac{n}{4}a_r^- \cos E_r^- \Rightarrow \frac{\pi}{2} < E_r^+ \leq \pi$	
		$\Delta V_y = -\frac{n}{4}a_r^- \cos E_r^- \Rightarrow E_r^+ < 0$	
0	-	$\Delta V_y > -\frac{n}{4}a_r^- \cos E_r^- \Rightarrow 0 < E_r^+ \leq \frac{\pi}{2}$	
0	-	$\frac{\pi}{2} < E_r^+ \leq \pi$	

Table 11: E_r variations based upon impulsive maneuver components, $\pi \leq E_r^- < \frac{3\pi}{2}$.

E_r^-	ΔV_x	ΔV_y	E_r^+
$E_r^- = \pi$	+	0	$0 < \Delta V_x < \frac{n}{2}a_r^- \Rightarrow E_r^+ = \frac{3\pi}{2}$
			$\Delta V_x = \frac{n}{2}a_r^- \Rightarrow E_r^+ = 0$
			$\Delta V_x > \frac{n}{2}a_r^- \Rightarrow E_r^+ = \frac{\pi}{2}$
	-	0	$E_r^+ = \frac{3\pi}{2}$
0	+	$\frac{3\pi}{2} < E_r^+ \leq 2\pi$	
0	-	$\pi < E_r^+ \leq \frac{3\pi}{2}$	
$\pi < E_r^- < \frac{3\pi}{2}$	+	0	$0 < \Delta V_x < -\frac{n}{2}a_r^- \sin E_r^- \Rightarrow \pi < E_r^+ \leq \frac{3\pi}{2}$
			$\Delta V_x = -\frac{n}{2}a_r^- \sin E_r^- \Rightarrow \begin{cases} a_r^- = 0 \Rightarrow E_r^+ = 0 \\ a_r^- > 0 \Rightarrow E_r^+ = \pi \end{cases}$
			$\Delta V_x > -\frac{n}{2}a_r^- \sin E_r^- \Rightarrow \frac{\pi}{2} \leq E_r^+ < \pi$
	-	0	$\pi < E_r^+ \leq \frac{3\pi}{2}$
0	+	0	$0 < \Delta V_y < -\frac{n}{4}a_r^- \cos E_r^- \Rightarrow \pi \leq E_r^+ < \frac{3\pi}{2}$
			$\Delta V_y = -\frac{n}{4}a_r^- \cos E_r^- \Rightarrow \begin{cases} a_r^- = 0 \Rightarrow E_r^+ = 0 \\ a_r^- > 0 \Rightarrow E_r^+ = \frac{3\pi}{2} \end{cases}$
			$\Delta V_y > -\frac{n}{4}a_r^- \cos E_r^- \Rightarrow \frac{3\pi}{2} < E_r^+ < 2\pi$
0	-	$\pi \leq E_r^+ < \frac{3\pi}{2}$	

Table 12: E_r variations based upon impulsive maneuver components, $\frac{3\pi}{2} \leq E_r^- < 2\pi$.

E_r^-	ΔV_x	ΔV_y	E_r^+
$E_r^- = \frac{3\pi}{2}$	+	0	$0 < \Delta V_x < \frac{n}{2} a_r^- \Rightarrow E_r^+ = \frac{3\pi}{2}$
			$\Delta V_x = \frac{n}{2} a_r^- \Rightarrow E_r^+ = 0$
			$\Delta V_x > \frac{n}{2} a_r^- \Rightarrow E_r^+ = \frac{\pi}{2}$
	-	0	$E_r^+ = \frac{3\pi}{2}$
0	+	$\frac{3\pi}{2} < E_r^+ \leq 2\pi$	
0	-	$\pi \leq E_r^+ < \frac{3\pi}{2}$	
$\frac{3\pi}{2} < E_r^- < 2\pi$	+	0	$0 < \Delta V_x < -\frac{n}{2} a_r^- \sin E_r^- \Rightarrow \frac{3\pi}{2} \leq E_r^+ < 2\pi$
			$\Delta V_x = -\frac{n}{2} a_r^- \sin E_r^- \Rightarrow E_r^+ = 0$
			$\Delta V_x > -\frac{n}{2} a_r^- \sin E_r^- \Rightarrow 0 < E_r^+ \leq \frac{\pi}{2}$
	-	0	$\frac{3\pi}{2} \leq E_r^+ < 2\pi$
0	+	$\frac{3\pi}{2} < E_r^+ \leq 2\pi$	
0	-	-	$-\frac{n}{4} a_r^- \cos E_r^- < \Delta V_y < 0 \Rightarrow \frac{3\pi}{2} \leq E_r^+ < 2\pi$
			$\Delta V_y = -\frac{n}{4} a_r^- \cos E_r^- \Rightarrow E_r^+ = 0$
			$\Delta V_y < -\frac{n}{4} a_r^- \cos E_r^- \Rightarrow \pi \leq E_r^+ < \frac{3\pi}{2}$

Table 13: A_z variations based upon impulsive maneuver components.

ψ^-	ΔV_z	ΔA_z
$\psi^- = 0$	+	+
	-	-
$0 < \psi^- < \frac{\pi}{2}$	+	+
	-	0, $\Delta V_z = -2nA_z^- \cos \psi^-$ +, $\Delta V_z < -2nA_z^- \cos \psi^-$ -, $-2nA_z^- \cos \psi^- < \Delta V_z < 0$
$\psi^- = \frac{\pi}{2}$	+	+
	-	+
$\frac{\pi}{2} < \psi^- < \pi$	+	0, $\Delta V_z = -2nA_z^- \cos \psi^-$ +, $\Delta V_z > -2nA_z^- \cos \psi^-$ -, $0 < \Delta V_z < -2nA_z^- \cos \psi^-$
	-	+
$\psi^- = \pi$	+	0, $\Delta V_z = 2nA_z^-$ +, $\Delta V_z > 2nA_z^-$ -, $0 < \Delta V_z < 2nA_z^-$
	-	+
$\pi < \psi^- < \frac{3\pi}{2}$	+	0, $\Delta V_z = -2nA_z^- \cos \psi^-$ +, $\Delta V_z > -2nA_z^- \cos \psi^-$ -, $0 < \Delta V_z < -2nA_z^- \cos \psi^-$
	-	+
$\psi^- = \frac{3\pi}{2}$	+	+
	-	+
$\frac{3\pi}{2} < \psi^- < 2\pi$	+	+
	-	0, $\Delta V_z = -2nA_z^- \cos \psi^-$ +, $\Delta V_z < -2nA_z^- \cos \psi^-$ -, $-2nA_z^- \cos \psi^- < \Delta V_z < 0$

Table 14: ψ variations based upon impulsive maneuver component.

ψ^-	ΔV_z	ψ^+
$\psi^- = 0$	+	$\psi^+ = \pi$
	-	$\Delta V_z < -nA_z^- \Rightarrow \psi^+ = \pi$ $\Delta V_z = -nA_z^- \Rightarrow \psi^+ = 0$ $-nA_z^- < \Delta V_z < 0 \Rightarrow \psi^+ = 0$
$0 < \psi^- < \frac{\pi}{2}$	+	$0 \leq \psi^+ < \frac{\pi}{2}$
	-	$\Delta V_z < -nA_z^- \cos \psi^- \Rightarrow \frac{\pi}{2} < \psi^+ \leq \pi$ $\Delta V_z = -nA_z^- \cos \psi^- \Rightarrow \begin{cases} A_z^- = 0 \Rightarrow \psi^+ = 0 \\ A_z^- > 0 \Rightarrow \psi^+ = \frac{\pi}{2} \end{cases}$ $-nA_z^- \cos \psi^- < \Delta V_z < 0 \Rightarrow 0 \leq \psi^+ < \frac{\pi}{2}$
$\psi^- = \frac{\pi}{2}$	+	$0 \leq \psi^+ < \frac{\pi}{2}$
	-	$\frac{\pi}{2} < \psi^+ \leq \pi$
$\frac{\pi}{2} < \psi^- < \pi$	+	$0 < \Delta V_z < -nA_z^- \cos \psi^- \Rightarrow \frac{\pi}{2} < \psi^+ \leq \pi$ $\Delta V_z = -nA_z^- \cos \psi^- \Rightarrow \begin{cases} A_z^- = 0 \Rightarrow \psi^+ = 0 \\ A_z^- > 0 \Rightarrow \psi^+ = \frac{\pi}{2} \end{cases}$ $\Delta V_z > -nA_z^- \cos \psi^- \Rightarrow 0 \leq \psi^+ < \frac{\pi}{2}$
	-	$\frac{\pi}{2} < \psi^+ \leq \pi$

Table 15: ψ variations based upon impulsive maneuver component.

ψ^-	ΔV_z	ψ^+
$\psi^- = \pi$	+	$0 < \Delta V_z < nA_z^- \Rightarrow \psi^+ = \pi$ $\Delta V_z \geq nA_z^- \Rightarrow \psi^+ = 0$
	-	$\psi^+ = \pi$
$\pi < \psi^- < \frac{3\pi}{2}$	+	$0 < \Delta V_z < -nA_z^- \cos \psi^- \Rightarrow \pi \leq \psi^+ < \frac{3\pi}{2}$ $\Delta V_z = -nA_z^- \cos \psi^- \Rightarrow \begin{cases} A_z^- = 0 \Rightarrow \psi^+ = 0 \\ A_z^- > 0 \Rightarrow \psi^+ = \frac{3\pi}{2} \end{cases}$ $\Delta V_z > -nA_z^- \cos \psi^- \Rightarrow \frac{3\pi}{2} < \psi^+ \leq 2\pi$
	-	$\pi \leq \psi^+ < \frac{3\pi}{2}$
$\psi^- = \frac{3\pi}{2}$	+	$\frac{3\pi}{2} < \psi^+ \leq 2\pi$
	-	$\pi \leq \psi^+ < \frac{3\pi}{2}$
$\frac{3\pi}{2} < \psi^- < 2\pi$	+	$\frac{3\pi}{2} < \psi^+ \leq 2\pi$
	-	$\Delta V_z < -nA_z^- \cos \psi^- \Rightarrow \pi \leq \psi^+ < \frac{3\pi}{2}$ $\Delta V_z = -nA_z^- \cos \psi^- \Rightarrow \begin{cases} A_z^- = 0 \Rightarrow \psi^+ = 0 \\ A_z^- > 0 \Rightarrow \psi^+ = \frac{3\pi}{2} \end{cases}$ $-nA_z^- \cos \psi^- < \Delta V_z < 0 \Rightarrow \frac{3\pi}{2} < \psi^+ \leq 2\pi$

2.5 Relative Orbital Element Control Strategies

If the initial conditions are known, Eqs. (164) through (169) represent six equations with ten unknown variables: t_b , ΔV_x , ΔV_y , ΔV_z , x_r^+ , y_r^+ , a_r^+ , E_r^+ , A_z^+ and ψ^+ . If four of the unknown variables are specified, then the six equations can be used to solve for the six remaining unknowns, assuming a solution exists. Three different scenarios demonstrating impulsive control strategies in terms of ROEs will be described herein: rendezvous, natural motion circumnavigation, and station-keeping.

2.5.1 Rendezvous

Rendezvous is defined to occur when the deputy spacecraft attains a desired stationary relative orbit with respect to the chief. The targeted rendezvous distance from the chief to the deputy can range from zero (necessary for docking or capture) up to several kilometers. The stationary relative orbit implies that there is no secular drift of the instantaneous relative ellipse; in terms of ROE's, x_r is zero upon the completion of rendezvous. The initial conditions, target conditions, and unknown variables for the rendezvous problem in terms of ROE's are summarized in Table 16. The initial conditions are known, and the maneuver epoch, maneuver vector, and the post-maneuver angular ROE's are to be found, while targeting a specific post-maneuver relative orbit geometry with zero secular drift.

Table 16: Rendezvous problem formulation in terms of ROE's.

Initial Conditions	$t_0, x_{r_0}, y_{r_0}, a_{r_0}, E_{r_0}, A_{z_0}, \psi_0$
Target Conditions	$x_r^+ = 0, y_r^+, a_r^+, A_z^+$
Unknown Variables	$t_b, \Delta V_x, \Delta V_y, \Delta V_z, E_r^+, \psi^+$

The unknown variables in Table 16 may be solved through the system of Eqs. (164) – (169). Eq. (164) may be solved directly to find ΔV_y . With the target condition $x_r^+ = 0$, Eq. (164) yields:

$$\Delta V_y = -\frac{n}{2}x_{r_0} \quad (170)$$

Solving Eq. (165) for ΔV_x yields:

$$\Delta V_x = \frac{n}{2}(y_{r_0} - y_r^+) - \frac{3}{4}n^2x_{r_0}(t_b - t_0) \quad (171)$$

Substituting Eqs. (170) and (171) into Eq. (166) gives:

$$a_r^+ = \left(\left\{ a_{r_0} \cos[E_{r_0} + n(t_b - t_0)] - 2x_{r_0} \right\}^2 + \left\{ a_{r_0} \sin[E_{r_0} + n(t_b - t_0)] + y_{r_0} - y_r^+ - \frac{3}{2}nx_{r_0}(t_b - t_0) \right\}^2 \right)^{1/2} \quad (172)$$

The only unknown in Eq. (172) is the maneuver time, t_b , and this can be solved for using a root finder, provided a solution exists. The solution for t_b is then substituted into Eq. (171) to solve for ΔV_x . Eq. (167) then allows E_r^+ to be found, as:

$$E_r^+ = \text{atan2} \left\{ a_{r_0} \sin[E_{r_0} + n(t_b - t_0)] + y_{r_0} - y_r^+ - \frac{3}{2}nx_{r_0}(t_b - t_0), \right. \\ \left. a_{r_0} \cos[E_{r_0} + n(t_b - t_0)] - 2x_{r_0} \right\} \quad (173)$$

Eqs. (168) and (169) are used as a system of equations to solve for the unknown variables ΔV_z and ψ^+ . Solving Eq. (168) for ΔV_z gives:

$$\Delta V_z = -nA_{z_0} \cos[\psi_0 + n(t_b - t_0)] \pm n\sqrt{(A_z^+)^2 - \{A_{z_0} \sin[\psi_0 + n(t_b - t_0)]\}^2}$$

(174)

Substituting into Eqs. (169) yields:

$$\psi^+ = \text{atan2} \left\{ A_{z_0} \sin[\psi_0 + n(t_b - t_0)], \pm \sqrt{(A_z^+)^2 - \{A_{z_0} \sin[\psi_0 + n(t_b - t_0)]\}^2} \right\}$$

(175)

As an example, consider a rendezvous problem where the deputy spacecraft and the chief are initially docked, but then the two spacecraft are separated such that the deputy initial conditions with respect to the chief at the time of separation are as shown in Table 17. For this example, the chief spacecraft is in a circular orbit at an altitude of 720 km, with a mean motion about the Earth of 0.0010557 rad/s and an orbital period of 5,951.5 s. The desired relative orbit target at rendezvous has a semi-major axis of the ellipse in the $\hat{x} - \hat{y}$ plane of 0.5 km centered on $x_r^+ = 0$, $y_r^+ = 2$ km, and cross-track motion with an amplitude of 0.433 km. The problem is to find the maneuver epoch and component magnitudes of the maneuver vector to achieve the targeted rendezvous conditions, and to find the resulting angular ROE's E_r^+ and ψ^+ immediately following the impulsive maneuver.

Table 17: Rendezvous problem example.

Initial Conditions	$t_0 = 0$ $x_{r_0} = 0.3168 \text{ km}$ $y_{r_0} = 3.0137 \text{ km}$ $a_{r_0} = 3.0796 \text{ km}$ $E_{r_0} = -1.3636 \text{ km}$ $A_{z_0} = 0$ $\psi_0 = 0$
Target Conditions	$x_r^+ = 0$ $y_r^+ = 2 \text{ km}$ $a_r^+ = 0.5 \text{ km}$ $A_z^+ = 0.433 \text{ km}$
Find	$t_b, \Delta V_x, \Delta V_y, \Delta V_z, E_r^+, \psi^+$

From Eq. (170), $\Delta V_y = -0.16725 \text{ m/s}$. Eq. (172) may be rewritten as a function equal to zero, and solved for the maneuver epoch t_b , using a root-finding routine:

$$a_r^+ - \left(\left\{ a_{r_0} \cos [E_{r_0} + n(t_b - t_0)] - 2x_{r_0} \right\}^2 + \left\{ a_{r_0} \sin [E_{r_0} + n(t_b - t_0)] + y_{r_0} - y_r^+ - \frac{3}{2}nx_{r_0}(t_b - t_0) \right\}^2 \right)^{1/2} = 0 \quad (176)$$

The value of the function on the left-hand side of Eq. (176) is plotted versus the maneuver epoch in Figure 12, over a maneuver epoch range from 0 to 20,000 s. It is seen that two roots of the function exist during this time period, at $t_b = 8,407.28 \text{ s}$ and at $t_b = 8,667.27 \text{ s}$.

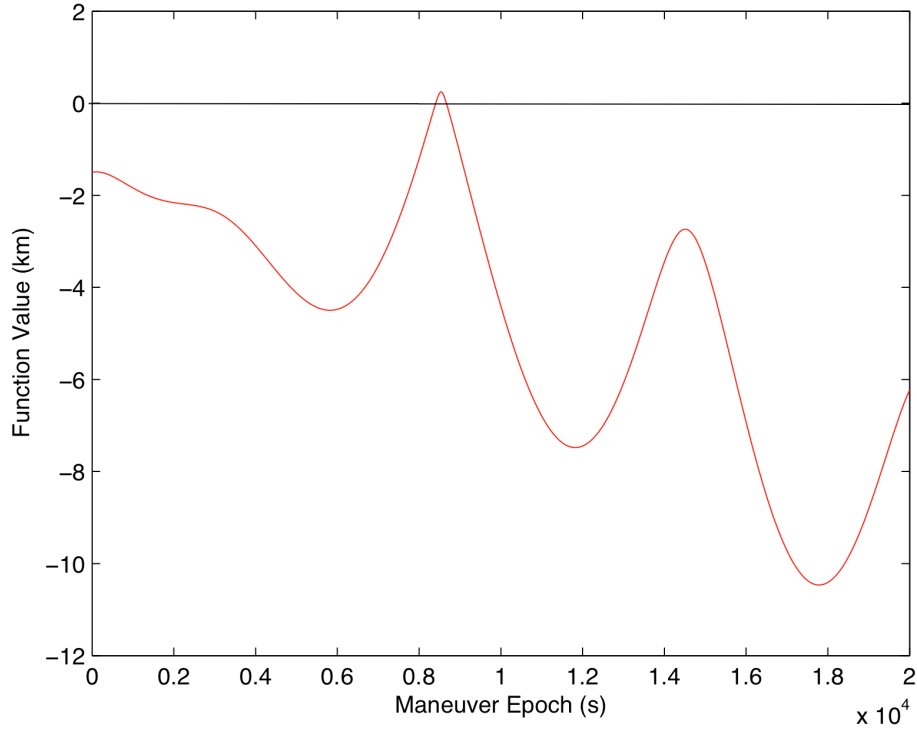
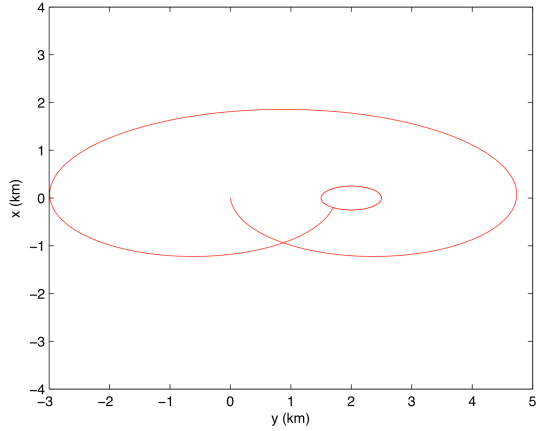


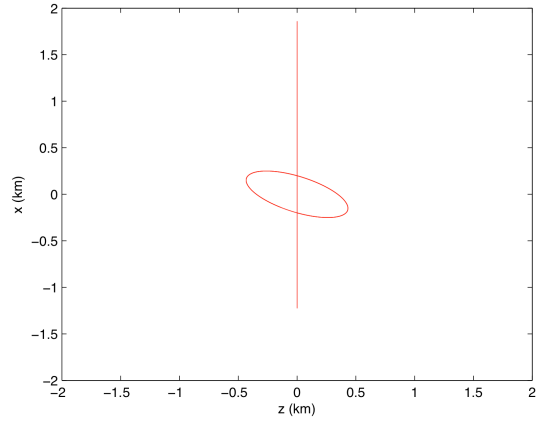
Figure 12: Function value from Eq. (176) versus maneuver epoch.

Taking the first root, at $t_b = 8,407.28$ s, Eq. (171) gives $\Delta V_x = -1.69120$ m/s . Eq. (174) yields $\Delta V_z = \pm 0.45713$ m/s . Physically, the two solutions for ΔV_z result in opposite directions for the initial cross-track motion immediately following the impulsive maneuver, and different orientations of the post-maneuver ellipse projections onto the $\hat{x} - \hat{z}$ and $\hat{y} - \hat{z}$ planes. Eq. (173) gives $E_r^+ = -0.64766$ rad, and Eq. (175) results in two potential values for ψ^+ : $\psi^+ = 0$ and $\psi^+ = \pi$ rad. The trajectory for this case is propagated using the Clohessy-Wiltshire equations, and is shown in Figure 13. Inspection of Figure 13 (a) and (b) shows that the maneuver occurs when x has a negative value at $z = 0$, corresponding to $\psi^+ = 0$ rad. The second maneuver opportunity at $t_b =$

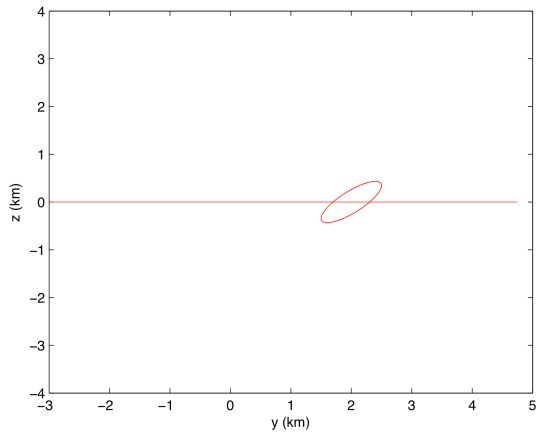
8,667.27 s occurs where free-drift trajectory would intersect the target post-maneuver ellipse with a positive \hat{x} -component, corresponding to $\psi^+ = \pi$ rad. At the maneuver opportunity corresponding to the second root, $\Delta V_x = -1.76006$ m/s, and the values for ΔV_y and ΔV_z are unchanged.



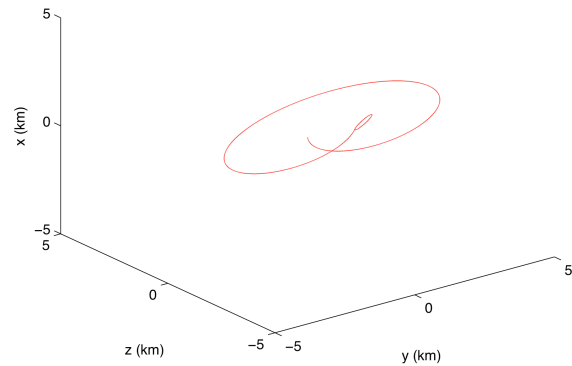
(a)



(b)



(c)



(d)

Figure 13: Trajectory propagation with rendezvous maneuver targeting a stationary relative ellipse. (a) $\hat{y} - \hat{x}$ projection, (b) $\hat{z} - \hat{x}$ projection, (c) $\hat{y} - \hat{z}$ projection, (d) Three-dimensional trajectory plot.

2.5.2 Natural Motion Circumnavigation

A natural-motion circumnavigation (NMC) relative orbit about the chief can be obtained with a single impulsive maneuver, starting from a leading or trailing orbit where the deputy is in the same orbit as the chief, but either ahead of or behind the chief in the direction of motion. Transfer to an orbit where the chief is at the geometric center of the NMC relative orbit ($x_r^+ = 0$, $y_r^+ = 0$) is often desired, although it is noted that an NMC orbit can be established about a “virtual” center, with an offset of y_r^+ away from zero. The problem formulation for establishing a NMC from a leading or trailing orbit, with the chief at the geometric center of the NMC, is provided in Table 18. Because the deputy is initially stationary relative to the chief, E_{r_0} and ψ_0 are undefined. We desire to find the $\Delta\bar{V}$ components and the resulting ROEs necessary to establish the chief at the center of the NMC, with the motion having an amplitude in the along-track direction of $a_r^+ = y_{r_0}$ and amplitude in the cross-track direction of $A_z^+ = A_{z_{tgt}}$.

Table 18: Natural motion circumnavigation problem formulation.

Initial Conditions	$t_0 = 0, x_{r_0} = 0, y_{r_0}, a_{r_0} = 0, E_{r_0}$ undefined, $A_{z_0} = 0, \psi_0$ undefined
Target Conditions	$x_r^+ = 0$ $y_r^+ = 0$ $a_r^+ = y_{r_0}$ $A_z^+ = A_{z_{tgt}}$
Unknown Variables	$\Delta V_x, \Delta V_y, \Delta V_z, E_r^+, \psi^+$

The solution to the NMC problem proceeds as follows. Eq. (165) is solved for ΔV_x with the initial conditions shown in Table 18, resulting in:

$$\Delta V_x = \frac{n}{2} y_{r_0} \quad (177)$$

Eq. (164) is solved for ΔV_y . With $x_{r_0} = 0$ and $x_r^+ = 0$ it is found that there is no along-track component for the maneuver to initiate an NMC orbit from a leading or trailing orbit:

$$\Delta V_y = 0 \quad (178)$$

Eq. (168) is used to find ΔV_z , giving:

$$\Delta V_z = \pm n A_{z_{tgt}} \quad (179)$$

Substituting Eqs. (177) and (178) into Eq. (166), it is seen that:

$$a_r^+ = \pm y_{r_0} \quad (180)$$

If $y_{r_0} < 0$, then $a_r^+ = -y_{r_0}$, and if $y_{r_0} > 0$, then $a_r^+ = y_{r_0}$, since the parameter a_r is always positive. Therefore, Eq. (180) can be expressed as:

$$a_r^+ = |y_{r_0}| \quad (181)$$

Eq. (167) results in $E_r^+ = \frac{\pi}{2}$ if $\Delta V_x > 0$, and $E_r^+ = \frac{3\pi}{2}$ if $\Delta V_x < 0$. Eq. (169) with

$A_{z_0} = 0$ yields:

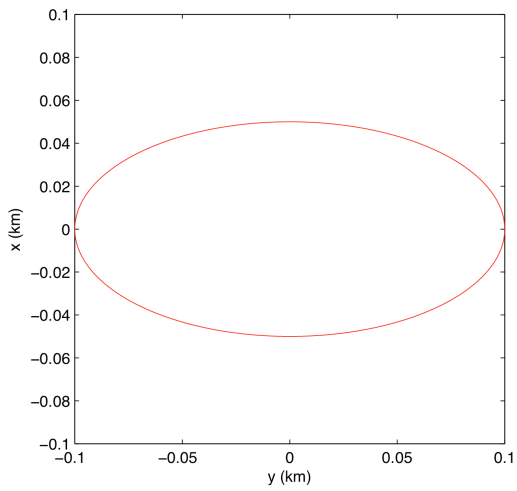
$$\psi^+ = \text{atan2}\left(0, \frac{1}{n} \Delta V_z\right) \quad (182)$$

If $\Delta V_z > 0$ then $\psi^+ = 0$, and if $\Delta V_z < 0$ then $\psi^+ = \pi$. If $\Delta V_z = 0$ then there is no cross-track motion and ψ^+ is undefined.

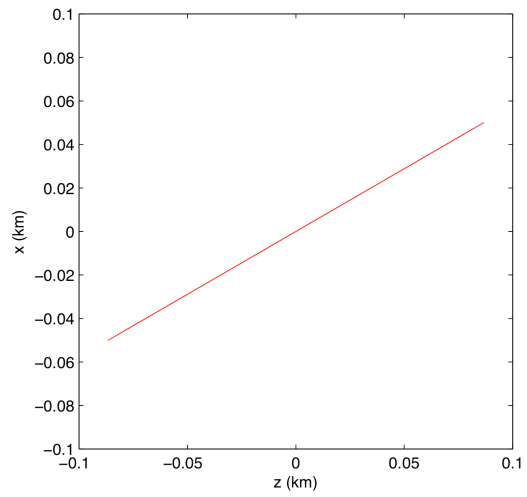
An example of the transition from a leading orbit to a circular NMC orbit is summarized in Table 19. From the initial leading orbit position 100 m along-track from the chief, the targeted NMC is a circular orbit with a radius of 100 m about the chief, including cross-track motion to establish the circular orbit geometry (i.e., the targeted deputy relative orbit about the chief has a constant radius). It is also given that the NMC maneuver is designed to have a positive ΔV_x component and a positive ΔV_z component, resulting in $E_r^+ = \frac{\pi}{2}$ and $\psi^+ = 0$. The NMC maneuver is performed at t_0 . The maneuver components resulting from Eqs. (177) – (179) are shown in Table 19. The resulting NMC orbit is shown in Figure 14. As designed, the deputy maintains a constant 100 m radius about the chief throughout the NMC orbit.

Table 19: Example of transition from leading orbit to NMC motion.

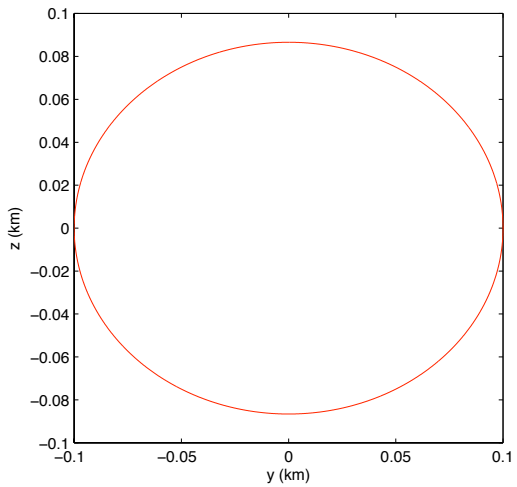
Initial Conditions	$t_0, x_{r_0} = 0, y_{y_0} = 0.100 \text{ km}, a_{r_0} = 0, A_{z_0} = 0$
Target Conditions	$x_r^+ = 0, y_r^+ = 0, a_r^+ = 0.100 \text{ km}, A_z^+ = \sqrt{\frac{3}{4}}a_r^+ = 0.0866 \text{ km}$
Solutions	$\Delta V_x = 5.5339E - 02 \text{ m/s}$ $\Delta V_y = 0$ $\Delta V_z = 9.3847E - 05 \text{ m/s}$ $E_r^+ = \frac{\pi}{2} \text{ rad}$ $\psi^+ = 0$



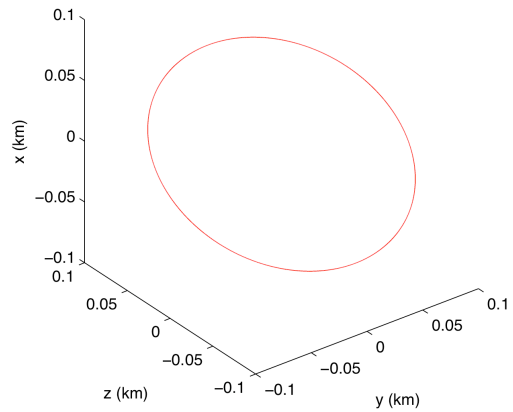
(a)



(b)



(c)



(d)

Figure 14: Natural motion circumnavigation circular orbit initiated from a leading orbit.

(a) $\hat{y} - \hat{x}$ projection, (b) $\hat{z} - \hat{x}$ projection, (c) $\hat{y} - \hat{z}$ projection, (d) Three-dimensional trajectory plot.

2.5.3 Station-Keeping in a Leading or Trailing Orbit

In terms of ROEs, the deputy spacecraft is in a stationary leading or trailing orbit when $x_r = 0$, $a_r = 0$, and $A_z = 0$. If the previous conditions are met and $y_r > 0$, the

deputy is in a leading orbit relative to the chief, and if $y_r < 0$, the deputy is in a trailing orbit. If $y_r = 0$, the deputy is coincident with the chief. Within the HCW assumptions, in the absence of disturbance forces, there is no secular drift with $x_r = 0$, and the deputy position relative to the chief in the LVLH frame will not change with time in a leading or trailing orbit. In practice, however, variations from a leading or trailing orbit will occur due to disturbances such as outgassing, atmospheric drag, solar pressure, etc. It is often desirable to perform station-keeping maneuvers to counteract disturbance forces, and maintain the desired leading or trailing orbit. The station-keeping problem for a leading or trailing orbit is summarized in Table 20.

Table 20: Station-keeping problem formulation for a leading or trailing orbit.

Initial Conditions	$t_0, x_{r_0}, y_{r_0}, a_{r_0}, E_{r_0}, A_{z_0}, \psi_0$
Target Conditions	$x_r^+ = 0, y_r^+ = y_{tgt}, a_r^+ = 0, A_z^+ = 0$

A station-keeping strategy based upon the geometric insights provided by ROEs is summarized below. The strategy applies a sequence of four impulsive maneuvers in order to station-keep to the desired leading or trailing orbit:

- 1) Perform ΔV_y to establish $x_r^+ = 0$ and stop the secular drift in the along-track direction.
- 2) At a \hat{y} -axis crossing, perform ΔV_y to establish a secular drift in the along-track direction that will cause the trajectory to cross the \hat{y} -axis at $y = y_{tgt}$ an integer number of orbits later.

3) At the point where the trajectory crosses the \hat{y} -axis at $y = y_{igt}$, perform ΔV_x , ΔV_y to establish $x_r^+ = 0$, $a_r^+ = 0$. Following this maneuver, the relative position is “fixed” in the $\hat{x} - \hat{y}$ plane at $x = 0$, $y = y_{igt}$.

4) Perform ΔV_z at a crossing of the $\hat{x} - \hat{y}$ plane at $z = 0$ to establish $A_z^+ = 0$.

Following this sequence of maneuvers, absent any additional disturbance forces, the relative position of the deputy is “fixed” relative to the chief in a leading or trailing orbit at $x = 0$, $y = y_{igt}$, $z = 0$. Each maneuver in the station-keeping strategy will now be examined in detail.

Maneuver 1: Stop Secular Along-Track Drift

The first maneuver in the station-keeping sequence is designed to stop the secular drift in the along-track direction. This requires that following the maneuver, $x_r^+ = 0$. From Eq. (164), setting $x_r^+ = 0$, the required maneuver can be found as:

$$\Delta V_y = -\frac{n}{2}x_{r_0} \quad (183)$$

It is noted that this maneuver can be performed at any point in the relative orbit; the secular drift in the along-track direction can be arrested at any time by applying an appropriately sized ΔV_y . However, from Eq. (166), the point in the relative orbit at which the ΔV_y is applied impacts the magnitude of the semi-major axis of the instantaneous relative ellipse following the maneuver, a_r^+ . To reduce the magnitude of subsequent maneuvers in the station-keeping sequence (specifically, the third maneuver), it may be desirable to minimize the magnitude of the a_r^+ resulting from the first

maneuver. Eq. (166) can be written in terms of eccentric relative anomaly at the maneuver epoch, as:

$$a_r^+ = \sqrt{\left(a_{r_0} \cos E_r^- + \frac{4}{n} \Delta V_y\right)^2 + \left(a_{r_0} \sin E_r^- + \frac{2}{n} \Delta V_x\right)^2} \quad (184)$$

Differentiating Eq. (184) with respect to E_r^- , where $\Delta V_x = 0$ gives:

$$\frac{\partial a_r^+}{\partial E_r^-} = \frac{-2a_{r_0} \sin E_r^- \left(a_{r_0} \cos E_r^- + \frac{4}{n} \Delta V_y\right) + 2a_{r_0}^2 \sin E_r^- \cos E_r^-}{2\sqrt{\left(a_{r_0} \cos E_r^- + \frac{4}{n} \Delta V_y\right)^2 + \left(a_{r_0} \sin E_r^-\right)^2}} \quad (185)$$

Setting Eq. (186) equal to zero and solving for E_r^- allows the maneuver locations in terms of relative eccentric anomaly to be found that result in extrema for a_r^+ . The resulting values for E_r^- are 0 and π . The second partial derivative of a_r^+ with respect to E_r^- where $\Delta V_x = 0$ is:

$$\begin{aligned} \frac{\partial^2 a_r^+}{\partial E_r^{-2}} = & \frac{-\left[2a_{r_0}^2 \cos E_r^- \sin E_r^- - 2a_{r_0} \sin E_r^- \left(a_{r_0} \cos E_r^- + \frac{4}{n} \Delta V_y\right)\right]^2}{4\left[\left(a_{r_0} \cos E_r^- + \frac{4}{n} \Delta V_y\right)^2 + \left(a_{r_0} \sin E_r^-\right)^2\right]^{3/2}} + \\ & \frac{2a_{r_0}^2 \cos E_r^- - 2a_{r_0} \cos E_r^- \left(a_{r_0} \cos E_r^- + \frac{4}{n} \Delta V_y\right)}{2\left[\left(a_{r_0} \cos E_r^- + \frac{4}{n} \Delta V_y\right)^2 + \left(a_{r_0} \sin E_r^-\right)^2\right]^{1/2}} \end{aligned} \quad (186)$$

Evaluating Eq. (186) for $E_r^- = 0$ gives:

$$\frac{\partial^2 a_r^+}{\partial E_r^{-2}} = a_{r_0} \left(\frac{a_{r_0}}{a_{r_0} + \frac{4}{n} \Delta V_y} - 1 \right) \quad (187)$$

and evaluating Eq. (186) for $E_r^- = \pi$ gives:

$$\frac{\partial^2 a_r^+}{\partial E_r^{-2}} = a_{r_0} \left(\frac{a_{r_0}}{-a_{r_0} + \frac{4}{n} \Delta V_y} + 1 \right) \quad (188)$$

Eqs. (187) and (188) can be evaluated to determine which value for E_r^- results in the minimum value for a_r^+ ; the second partial derivative of a_r^+ with respect to E_r^- will be positive at the minimum. Once the relative eccentric anomaly for the maneuver is known, the maneuver time, t_b , can be found from:

$$E_r^- = E_{r_0} + n(t_b - t_0) \quad (189)$$

Solving Eq. (189) for t_b gives:

$$t_b = t_0 + \frac{E_r^- - E_{r_0}}{n} \quad (190)$$

Maneuver 2: Initiate Secular Drift to Target Location

The second maneuver in the station-keeping sequence is designed to initiate a secular drift in the along-track direction toward the targeted station-keeping location. However, in order to achieve the targeted \hat{y} -coordinate, y_{tgt} , it is necessary to design the second maneuver such that the resulting secular drift will establish a \hat{y} -axis crossing at y_{tgt} . From the stationary relative ellipse established by the first maneuver in the sequence, the second maneuver is designed to be performed at a \hat{y} -axis crossing, where $E_r^- = \frac{\pi}{2}$ or

$E_r^- = \frac{3\pi}{2}$. As shown in Figure 15, this maneuver is designed to initiate a secular drift rate such that an integer number s orbits after the maneuver, the relative orbit crosses $x = 0$ at $y = y_{igt}$. In Fig. 15, the initial stationary relative ellipse with $x_r^- = 0$, shown in blue, is centered on y_r^- . The maneuver occurs at the \hat{y} -axis crossing labeled “0,” where $E_r^- = \frac{\pi}{2}$. Following the maneuver, the relative trajectory drifts in the positive along-track direction, with ascending crossings of the \hat{y} -axis labeled in numerical order. The trajectory crosses the \hat{y} -axis at Point 4 with $y = y_{igt}$ exactly four orbit periods after the maneuver epoch ($s = 4$). From Figure 15, it is apparent that Point 0 is located at $y = y_r^- + a_r^-$. The maneuver results in a change to the relative orbit geometry such that $x_r^+ < 0$, initiating a secular drift. Each subsequent \hat{y} -axis crossing occurs at the same relative eccentric anomaly. The time interval between \hat{y} -axis crossings is equal to the orbital period of the chief, P , where:

$$P = \frac{2\pi}{n} \quad (191)$$

From the geometry in Figure 15, the following equation may be written:

$$y_{igt} = (y_r^- + a_r^-) + sP\dot{y}_s^+ \quad (192)$$

In Eq. (192), the term $sP\dot{y}_s^+$ represents the distance that the instantaneous center of the relative orbit moves during s orbit periods, as a result of the post-maneuver secular drift rate \dot{y}_s^+ . The secular drift rate following the maneuver may be written as:

$$\dot{y}_s^+ = -\frac{3}{2}nx_r^+ \quad (193)$$

Combining Eqs. (146) and (193) gives:

$$\dot{y}_s^+ = -\frac{3}{2}n\left(x_r^- + \frac{2}{n}\Delta V_y\right) \quad (194)$$

Since $x_r^- = 0$ as a result of the first maneuver in the station-keeping sequence, Eq. (194)

simplifies to:

$$\dot{y}_s^+ = -3\Delta V_y \quad (195)$$

Substituting Eqs. (191) and (195) into Eq. (192) and solving for ΔV_y gives:

$$\Delta V_y = \frac{n(y_r^- + a_r^- - y_{tgt})}{6\pi s} \quad (196)$$

It is emphasized that the integer number of relative orbits s is an important design variable for the second maneuver, dictating the secular drift rate for the station-keeping segment, and the transit time to the target location. If a slow drift is acceptable and it is desired to minimize total station-keeping ΔV , then s can be given a larger value. For a rapid return to the targeted location, or if the maneuver magnitude must be increased to comply with thruster capabilities, then s can be reduced to a small positive integer.

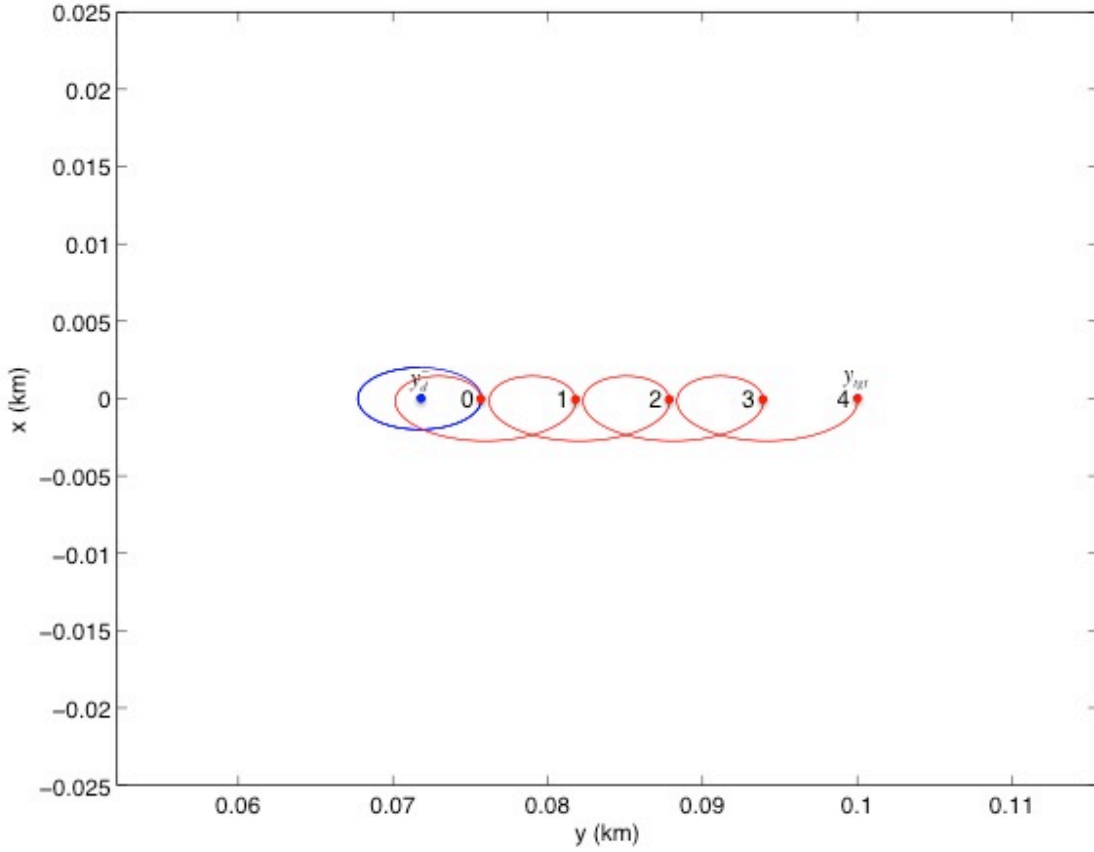


Figure 15: The second maneuver initiates a secular drift designed to reach the station-keeping target s orbital periods after the maneuver epoch.

Maneuver 3: Fix Motion in the Plane at the Targeted Location

The third maneuver in the station-keeping sequence is performed at the \hat{y} -axis crossing s orbit periods after the second maneuver, and is designed to fix the motion in the $\hat{x} - \hat{y}$ plane at the targeted location, y_{tgt} . In terms of ROEs, the desired conditions following the third maneuver are: $x_r^+ = 0, y_r^+ = y_{tgt}, a_r^+ = 0$. Geometrically, the $y_r^+ = y_{tgt}$ condition can only be met if the instantaneous ellipse resulting from the maneuver is reduced to a point (i.e., $a_r^+ = 0$).

Taking the relative orbit state immediately following the second maneuver as the initial conditions, ΔV_y for the third maneuver can be found from Eq. (164), setting

$$x_r^+ = 0 :$$

$$\Delta V_y = -\frac{n}{2}x_{r_0} \quad (197)$$

Eq. (165) can be used to find ΔV_x :

$$\Delta V_x = -\frac{n}{2} \left[y_r^+ - y_{r_0} + \frac{3}{2}nx_{r_0}(t_b - t_0) \right] \quad (198)$$

The quantity $t_b - t_0$ is the time difference between the second and third maneuvers, which is equal to s times the chief's orbital period. From Eq. (91) we can write:

$$y_r^- = y_{r_0} - \frac{3}{2}nx_{r_0}(t_b - t_0) \quad (199)$$

Substituting Eq. (199) into Eq. (198), setting $y_r^+ = y_{igt}$ and solving for ΔV_x yields:

$$\Delta V_x = -\frac{n}{2}(y_{igt} - y_r^-) \quad (200)$$

Performing an impulsive maneuver composed of the maneuver components as shown in Eqs. (197) and (200) results in a relative orbit with $x_r^+ = 0$ and $y_r^+ = y_{igt}$. The values for ΔV_x and ΔV_y calculated from Eqs. (200) and (197) drive a_r^+ to zero. Referring to Fig. 15, it is clear that the relative eccentric anomaly at each of the numbered ascending \hat{y} -axis crossings is equal to the relative eccentric anomaly immediately following the second station-keeping maneuver. The geometry repeats each orbit period. Therefore, it is seen that:

$$E_r^- = E_{r_0} + n(t_b - t_0) = E_{r_0} \quad (201)$$

Also, applying the geometry for relative eccentric anomaly shown in Fig. 5 to the problem, it may be shown that:

$$\sin E_{r_0} = \frac{y_{tgt} - y_{r_0} + 3\pi s x_{r_0}}{a_{r_0}} \quad (202)$$

and

$$\cos E_{r_0} = \frac{2x_{r_0}}{a_{r_0}} \quad (203)$$

Using Eq. (191) we can write:

$$t_b - t_0 = \frac{2\pi s}{n} \quad (204)$$

Substitution of Eqs. (197), (200), (201), (202), (203) and (204) into Eq. (166) shows that

$$a_r^+ = 0.$$

Maneuver 4: Zero-Out Cross-Track Motion

The fourth maneuver in the station-keeping sequence is designed to zero-out the cross-track motion. This maneuver must be performed at a crossing of the $\hat{x} - \hat{y}$ plane, where $z = 0$ and $\psi^- = 0$ or $\psi^- = \pi$. The burn time for the fourth maneuver can be found from:

$$\psi^- = \psi_0 + n(t_b - t_0) \quad (205)$$

Solving for t_b ,

$$t_b = \frac{\psi^- - \psi_0}{n} + t_0 \quad (206)$$

where the initial conditions are specified immediately following the previous maneuver.

Eq. (168) can be written as:

$$A_z^+ = \sqrt{(A_z \sin \psi^-)^2 \left(A_z \cos \psi^- + \frac{1}{n} \Delta V_z \right)^2} \quad (207)$$

The first term under the radical in Eq. (207) equals zero, since $\psi^- = 0$ or $\psi^- = \pi$.

Setting A_z^+ and solving for ΔV_z gives:

$$\Delta V_z = -nA_{z_0} \cos \psi^- \quad (208)$$

The direction (sign) of the maneuver will change, depending upon whether the maneuver is performed at $\psi^- = 0$ or $\psi^- = \pi$. It is noted that the maneuver to zero-out the cross-track motion can be performed at *any* $\hat{x} - \hat{y}$ plane crossing. It is therefore not required that this maneuver be the fourth in the station-keeping sequence; it is represented as the fourth maneuver in the sequence only for clarity, since the \hat{z} -motion is decoupled from the $\hat{x} - \hat{y}$ motion controlled by the first three maneuvers in the sequence.

The station-keeping maneuver sequence is summarized in Table 21. The initial conditions for each trajectory segment in the station-keeping sequence are indicated by a subscript 0. For example, y_{i_0} appears in the ΔV_x component for the third maneuver; this term represents the value for y_i immediately following the second maneuver in the station-keeping sequence.

Table 21: Station-keeping maneuver sequence summary.

Maneuver #	Maneuver Location	$\Delta\bar{V}$ Components	Purpose
1	Any	$\Delta V_y = -\frac{n}{2}x_{r_0}$	Stop secular along-track drift.
2	$x = 0$	$\Delta V_y = \frac{n(y_r^- + a_r^- - y_{tgt})}{6\pi s}$	Initiate secular drift along-track drift such that s orbits after maneuver, orbit crosses $x = 0, y = y_{tgt}$.
3	$x = 0, y = y_{tgt}$	$\Delta V_x = -\frac{n}{2}(y_{tgt} - y_r^-)$ $\Delta V_y = -\frac{n}{2}x_{r_0}$	Fix motion in $\hat{x} - \hat{y}$ plane at $x = 0, y = y_{tgt}$.
4	$z = 0$	$\Delta V_z = -nA_{z_0} \cos\psi^-$	Zero-out cross-track motion.

The station-keeping strategy will now be illustrated within the context of an example scenario. The initial conditions, target conditions, and constraints for the example are shown in Table 22. The targeted station-keeping position is a leading orbit, 100 m ahead of the chief in the $+\hat{y}$ -direction. The initial conditions show that the instantaneous center of the deputy's orbit is 3 m higher than the chief's orbit, resulting in a relative drift in the $-\hat{y}$ -direction.

Table 22: Station-keeping example.

Initial Conditions	$t_0 = 0$ s $x_{r_0} = 3$ m $y_{r_0} = 100$ m $a_{r_0} = 2$ m $E_{r_0} = 0$ rad $A_{z_0} = 1$ m $\psi_0 = \frac{\pi}{2}$ rad
Target Conditions	$x_r = 0$ m $y_r = y_{tgt} = 100$ m $a_r = 0$ m $A_z = 0$ m

The deputy spacecraft trajectory relative to the chief is shown in Fig. 16. The initial trajectory is shown in black. Left unchecked, the unforced motion would continually drift in the negative along-track direction. The first maneuver in the station-keeping sequence occurs when $E_r^- = 0$, at $y = 70$ m. This maneuver halts the secular along-track drift, resulting in the motion shown in blue in Fig. 16.

The second maneuver in the station-keeping sequence is performed at the \hat{y} -axis crossing where $E_r^- = \frac{\pi}{2}$. The maneuver initiates a secular drift in the $+\hat{y}$ -direction such that the resulting motion will cross the \hat{y} -axis at the targeted location of $y = 100$ m exactly four revs after the maneuver ($s = 4$). The motion following the second maneuver is shown in red in Figure 16.

The third maneuver in the sequence is performed at the targeted $\hat{x} - \hat{y}$ location: $x = 0, y = 100$ m. The maneuver has both \hat{x} - and \hat{y} -components in order to

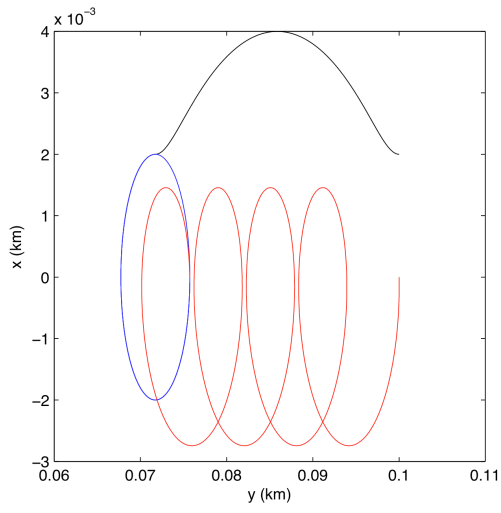
simultaneously arrest the secular along-track drift, and reduce the magnitude of a_r^+ to zero. The motion following the third maneuver is shown in green in Figure 16. It is seen that there is no further motion in the $\hat{x} - \hat{y}$ plane; the subsequent motion is solely in the cross-track direction.

The final maneuver in the station-keeping sequence is performed at $z = 0$, where $\psi^- = \pi$. This maneuver nulls the cross-track motion, resulting in a fixed position for the deputy relative to the chief at the targeted location. Barring additional thrusting or disturbance forces, the deputy will remain in this relative position within the Clohessy-Wiltshire assumptions.

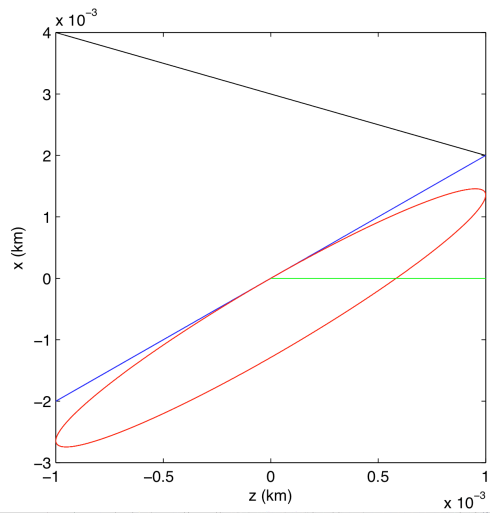
The station-keeping maneuver timing and component magnitudes are given in Table 23. The total ΔV magnitude associated with the station-keeping sequence for this example is 5.3654E-03 m/s.

Table 23: Station-keeping example maneuver summary.

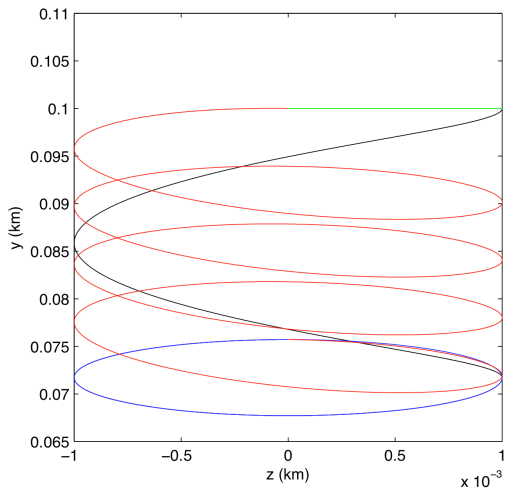
Maneuver	Time from Initial State (s)	ΔV_x (m/s)	ΔV_y (m/s)	ΔV_z (m/s)
1	5,676.981	0	-1.6602E-03	0
2	15,611.699	0	-3.5632E-04	0
3	38,319.624	-2.2136E-03	3.5633E-04	0
4	41,158.115	0	0	1.1068E-03



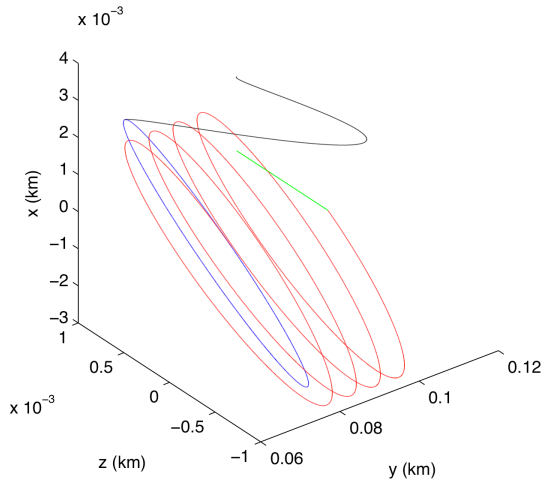
(a)



(b)



(c)



(d)

Figure 16: Station-keeping example. (a) $\hat{y}-\hat{x}$ projection, (b) $\hat{z}-\hat{x}$ projection, (c) $\hat{y}-\hat{z}$ projection, (d) Three-dimensional trajectory plot.

CHAPTER 3

ARTIFICIAL POTENTIAL FUNCTION TRAJECTORY CONTROL FORMULATION USING RELATIVE ORBITAL ELEMENTS

3.1 Artificial Potential Function Control Methodology

Persistent knowledge and control of the relative orbit is often required for missions involving proximity operations. Maneuvering of the deputy spacecraft for station-keeping, formation flight, collision avoidance, and close approach for docking or berthing are activities that may require persistent trajectory control. An approach that is often used in terrestrial robotics applications is motion control based upon artificial potential fields. Similar to potential fields found in nature, such as gravitational or electromagnetic fields, artificial potential fields may be defined by an operator to shape the interaction of a robotic vehicle with the environment. Vehicle control forces are computed by taking the gradient of the scalar potential function: for motion towards a goal at the minimum of the potential field, control forces act in the direction of steepest descent. Obstacles may be represented as regions of high potential in the field, with the resultant repulsive control forces to enable obstacle avoidance. Attractive and repulsive potentials may be superposed to create a “total” potential field that can govern robotic motion to reach the goal while avoiding obstacles. The continuous nature of guidance using APFs, along with the inherent computational simplicity of the approach, provides an efficient methodology for robotic motion control where computational capability is limited and persistent control is required.

APF guidance is based upon the Second Method of Lyapunov [59] for assessing the stability of equilibrium points of a dynamical system. The Second Method states that

the following conditions must be met for a globally stable attractive equilibrium point at the target location, $\bar{\rho}_{tgt}$:

$$\phi(\bar{\rho}) \geq 0 \quad \forall \bar{\rho}, \text{ where } \phi(\bar{\rho}) = 0 \text{ if and only if } \bar{\rho} = \bar{\rho}_{tgt} \quad (209)$$

$$\dot{\phi}(\bar{\rho}) \leq 0 \quad \forall \bar{\rho}, \text{ where } \dot{\phi}(\bar{\rho}) = 0 \text{ if and only if } \bar{\rho} = \bar{\rho}_{tgt} \quad (210)$$

The condition in Eq. (209) is met by choosing ϕ_a to be a positive semi-definite function of $\bar{\rho}$. The condition expressed in Eq. (210) is met through defining control input such that the motion of the robotic vehicle following an impulse is tangent to the local gradient of the potential field, in the direction of steepest descent. This ensures that the derivative of the potential function after a control impulse is negative definite. Under these conditions, ϕ is considered to be a Lyapunov function, and the system is asymptotically stable about the globally attractive point $\bar{\rho}_{tgt}$.

An example of an attractive artificial potential function is shown in Eq. (211). The attractive potential, ϕ_a , is a scalar function of the relative position vector of the robotic vehicle with respect to the target location, $\bar{\rho} - \bar{\rho}_{tgt}$, the positive-definite diagonal shaping matrix $\bar{\bar{Q}}_a$, and the scaling parameter k_a :

$$\phi_a = \frac{1}{2} k_a (\bar{\rho} - \bar{\rho}_{tgt})^T \bar{\bar{Q}}_a (\bar{\rho} - \bar{\rho}_{tgt}) \quad (211)$$

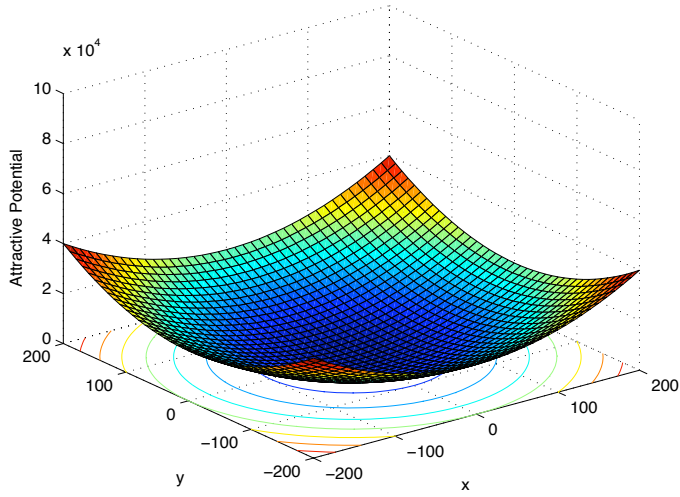
Figure 17 shows the attractive potential as a function of the position relative to the target location \bar{r}_{tgt} , where the target is located at the origin of the coordinate system. In the top left figure, the scaling parameter is equal to one, and the shaping matrix is set to

the 2x2 identity matrix. In the top right figure, the scaling parameter is increased to a value of three, while the shaping matrix is maintained as the 2x2 identity matrix. It is seen that the effect of increasing the scaling parameter is to steepen the gradient of the potential field at every point other than the goal. In the bottom left figure, the scaling parameter is set equal to one, and the shaping matrix is of the form $\bar{\bar{Q}}_a = \begin{bmatrix} 10 & 0 \\ 0 & 1 \end{bmatrix}$.

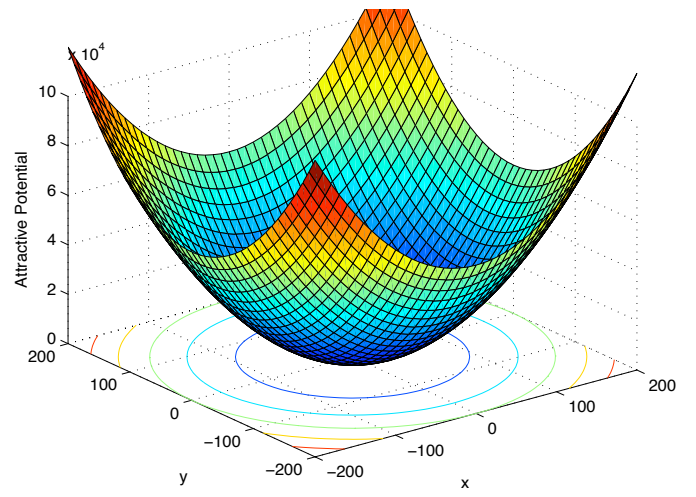
This shaping matrix results in a potential field that has steep gradients toward the goal for deviations from the target in the \hat{x} -direction, and shallow gradients toward the goal for deviations in the \hat{y} -direction. In the bottom right figure, the scaling parameter is set

equal to one, and the shaping matrix is of the form $\bar{\bar{Q}}_a = \begin{bmatrix} 1 & 0 \\ 0 & 10 \end{bmatrix}$. Here, the shaping

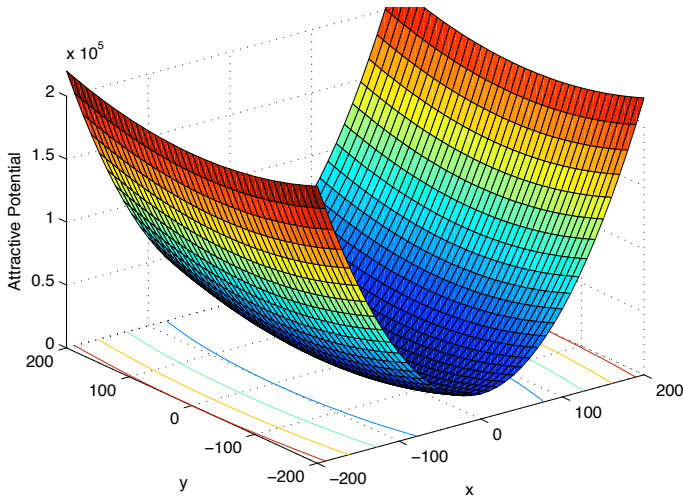
matrix results in a potential field that has steep gradients in the \hat{y} -direction, and shallow gradients in the \hat{x} -direction.



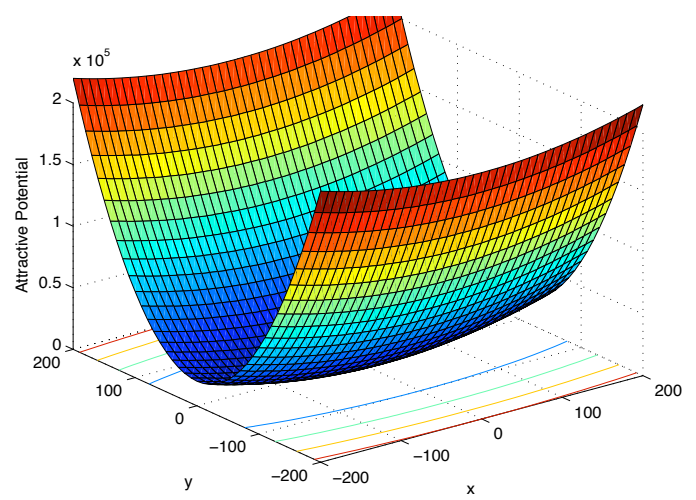
(a)



(b)



(c)



(d)

Figure 17: Attractive potential as a function of position relative to the goal. (a) $k_a = 1$,

$$\bar{\bar{Q}}_a = \bar{\bar{I}}_{2 \times 2}, \text{ (b) } k_a = 3, \bar{\bar{Q}}_a = \bar{\bar{I}}_{2 \times 2}, \text{ (c) } k_a = 1, \bar{\bar{Q}}_a = \begin{bmatrix} 10 & 0 \\ 0 & 1 \end{bmatrix}, \text{ (d) } k_a = 1, \bar{\bar{Q}}_a = \begin{bmatrix} 1 & 0 \\ 0 & 10 \end{bmatrix}.$$

The potential function in Eq. (211) can be expanded as:

$$\phi_a = \frac{1}{2} k_a \left(\bar{\rho}^T \bar{\mathcal{Q}}_a \bar{\rho} - \bar{\rho}^T \bar{\mathcal{Q}}_a \bar{\rho}_{igt} - \bar{\rho}_{igt}^T \bar{\mathcal{Q}}_a \bar{\rho} + \bar{\rho}_{igt}^T \bar{\mathcal{Q}}_a \bar{\rho}_{igt} \right) \quad (212)$$

Taking the gradient of ϕ_a with respect to $\bar{\rho}$,

$$\nabla_{\rho} \phi_a = \frac{\partial \phi_a}{\partial \bar{\rho}} \quad (213)$$

The gradient is evaluated as follows:

$$\nabla_{\rho} \phi_a = \frac{\partial \phi_a}{\partial \bar{\rho}} = \frac{1}{2} k_a \left[\frac{\partial}{\partial \bar{\rho}} \left(\bar{\rho}^T \bar{\mathcal{Q}}_a \bar{\rho} \right) - \frac{\partial}{\partial \bar{\rho}} \left(\bar{\rho}^T \bar{\mathcal{Q}}_a \bar{\rho}_{igt} \right) - \frac{\partial}{\partial \bar{\rho}} \left(\bar{\rho}_{igt}^T \bar{\mathcal{Q}}_a \bar{\rho} \right) + \frac{\partial}{\partial \bar{\rho}} \left(\bar{\rho}_{igt}^T \bar{\mathcal{Q}}_a \bar{\rho}_{igt} \right) \right] \quad (214)$$

Carrying out the partial derivatives, where $\bar{\mathcal{Q}}_a$ is assumed to be a diagonal matrix, and simplifying yields:

$$\nabla_{\rho} \phi_a = k_a \bar{\mathcal{Q}}_a \left(\bar{\rho} - \bar{\rho}_{igt} \right) \quad (215)$$

The APF control law dictates that immediately following the application of a control force (i.e., a maneuver), the relative velocity of the spacecraft, \bar{v}^+ , should be in the negative gradient direction, that is,

$$\bar{v}^+ = -\nabla_{\rho} \phi_a = -k_a \bar{\mathcal{Q}}_a \left(\bar{\rho} - \bar{\rho}_{igt} \right) \quad (216)$$

A maneuver is commanded when the natural motion of the spacecraft is such that, in the absence of a maneuver, the potential function would increase with time. The total derivative of the potential function in Eq. (212) is found as:

$$\dot{\phi}_a = \frac{d\phi}{dt} = \frac{1}{2}k_a \left[\frac{d(\bar{\rho}^T \bar{Q}_a \bar{\rho})}{dt} - \frac{d(\bar{\rho}^T \bar{Q}_a \bar{\rho}_{tgt})}{dt} - \frac{d(\bar{\rho}_{tgt}^T \bar{Q}_a \bar{\rho})}{dt} + \frac{d(\bar{\rho}_{tgt}^T \bar{Q}_a \bar{\rho}_{tgt})}{dt} \right] \quad (217)$$

Carrying out the derivatives under the assumption that \bar{Q}_a is a diagonal matrix and $\bar{\rho}_{tgt}$ is fixed gives:

$$\dot{\phi}_a = k_a \dot{\bar{\rho}}^T \bar{Q}_a (\bar{\rho} - \bar{\rho}_{tgt}) \quad (218)$$

The total derivative given by Eq. (218) is utilized as a switching condition for the control action:

$$\Delta \bar{V} = \begin{cases} 0 & , \quad \dot{\phi}_a \leq 0 \\ -\nabla_{\rho} \phi_a - \dot{\bar{\rho}} & , \quad \dot{\phi}_a > 0 \end{cases} \quad (219)$$

The control action is taken when the value of the potential function is increasing; a maneuver is defined such that the relative velocity following the impulse is in the negative gradient direction of the potential field.

Consider an example where the initial relative state of the deputy spacecraft is as shown in Table 24: at $t = 0$, the deputy is at a position 200 m ahead of the chief in the along-track direction, with an initial velocity of 0.020 m/s in the radial direction. The

chief spacecraft is assumed to be in a circular orbit about Earth, with a radius of 7098.14 km (720 km orbit altitude).

Table 24: Conditions for APF control example.

Initial Conditions	$x = 0.000 \text{ km}$ $\dot{x} = 2E - 05 \text{ km/s}$ $y = 0.200 \text{ km}$ $\dot{y} = 0 \text{ km/s}$ $z = 0.000 \text{ km}$ $\dot{z} = 0 \text{ km/s}$
Target Location	$x = 0.000 \text{ km}$ $y = 0.100 \text{ km}$ $z = 0.000 \text{ km}$
APF Parameters	$k_a = 1E - 03$ $\bar{\bar{Q}}_a = \bar{\bar{I}}_{3 \times 3}$

The attractive potential function is defined per Eq. (211), with $\bar{\rho}_{tgt}^T = \begin{bmatrix} 0 & 0.100 & 0 \end{bmatrix}$ km. The scaling parameter k_a is set equal to 1E-03, and the shaping matrix $\bar{\bar{Q}}_a$ is set equal to $\bar{\bar{I}}_{3 \times 3}$. The switching condition, Eq. (219) is queried every 60 sec along the trajectory. Examination of the switching condition shows that when the range to the target is increasing, a maneuver is commanded to drive the relative velocity of the spacecraft directly toward the target. The resulting behavior is shown in Figure 18. During the 10,000 sec simulation, 25 maneuvers are performed, with a total ΔV magnitude of 0.687 m/s. In general, the maneuver magnitudes become progressively smaller as the target is approached, as shown in Figure 19. At the conclusion of the simulation, the spacecraft is within 0.5 m of the target position.

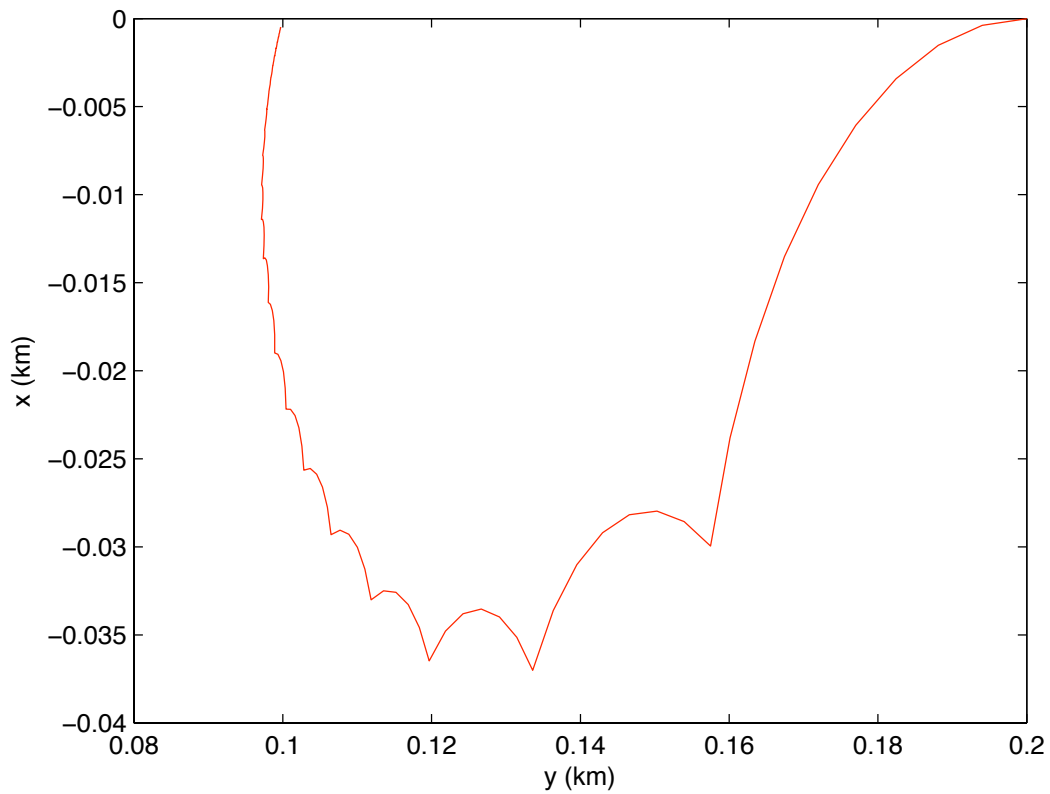


Figure 18: APF trajectory control to a target using an attractive potential.

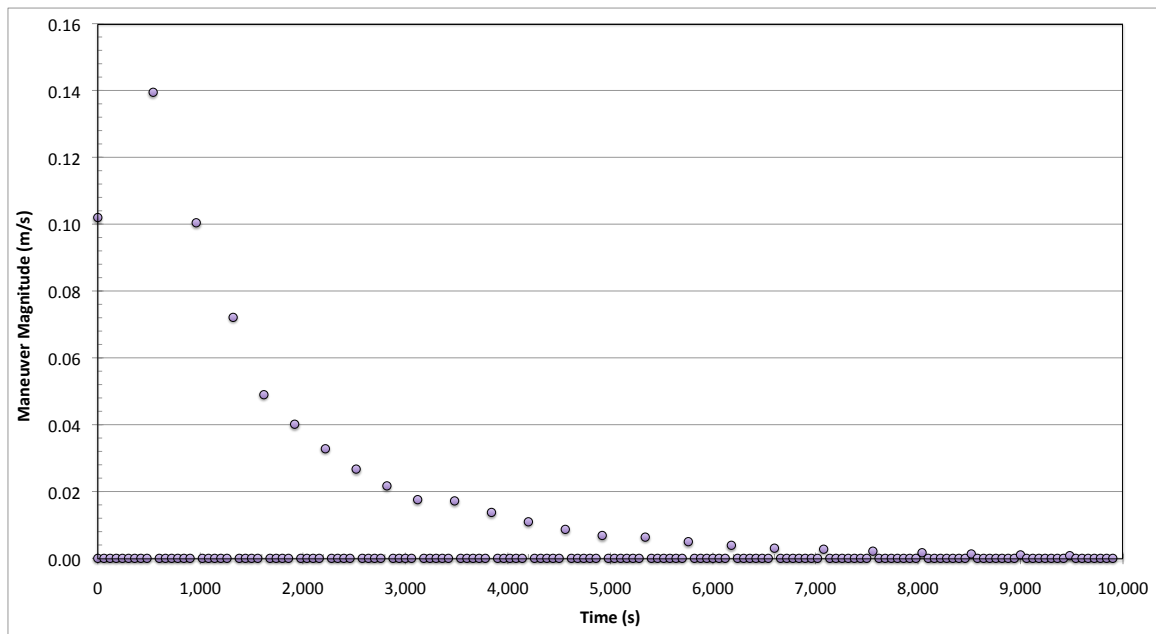


Figure 19: APF attractive control maneuver magnitudes.

An obstacle, or region to avoid, may be represented in the potential field as a region of high potential, resulting in the vehicle being repulsed from the obstacle. An example of a repulsive artificial potential function is given in Eq. (220). The repulsive potential, ϕ_r , is a scalar function of the relative position vector of the robotic vehicle with respect to the obstacle location, $\bar{\rho} - \bar{\rho}_{obs}$, the positive-definite diagonal shaping matrix, $\bar{\bar{Q}}_r$, the scaling parameter, k_r , and the broadening parameter, σ :

$$\phi_r = k_r \exp \left[- \frac{(\bar{\rho} - \bar{\rho}_{obs})^T \bar{\bar{Q}}_r (\bar{\rho} - \bar{\rho}_{obs})}{\sigma} \right] \quad (220)$$

Figure 20 shows the repulsive potential as a function of the position relative to the obstacle location, where the obstacle is located at the origin of the coordinate system. In the top left figure, the scaling parameter is equal to one, the shaping matrix is set to the 3x3 identity matrix, and the broadening parameter is set equal to 500. In the top right figure, the scaling parameter is increased to a value of two, while the other parameters remain unchanged. It is seen that the effect of increasing the scaling parameter is to increase the peak of the potential field at the obstacle location, thus increasing the gradients near the obstacle. In the bottom left figure, the scaling parameter is set equal to one, the shaping matrix is of the form $\bar{\bar{Q}}_r = \begin{bmatrix} 10 & 0 \\ 0 & 1 \end{bmatrix}$, and the broadening parameter

remains at 500. The increase to the $\bar{\bar{Q}}_r(1,1)$ shaping matrix element results in a

narrowing of the potential field in the \hat{x} -direction. In the bottom right figure, the shaping matrix is set to the 3x3 identity matrix, and the broadening parameter is increased by an

order of magnitude to 5000. Here, the broadening parameter results in a broadening of the base of the potential field, and shallower gradients overall.

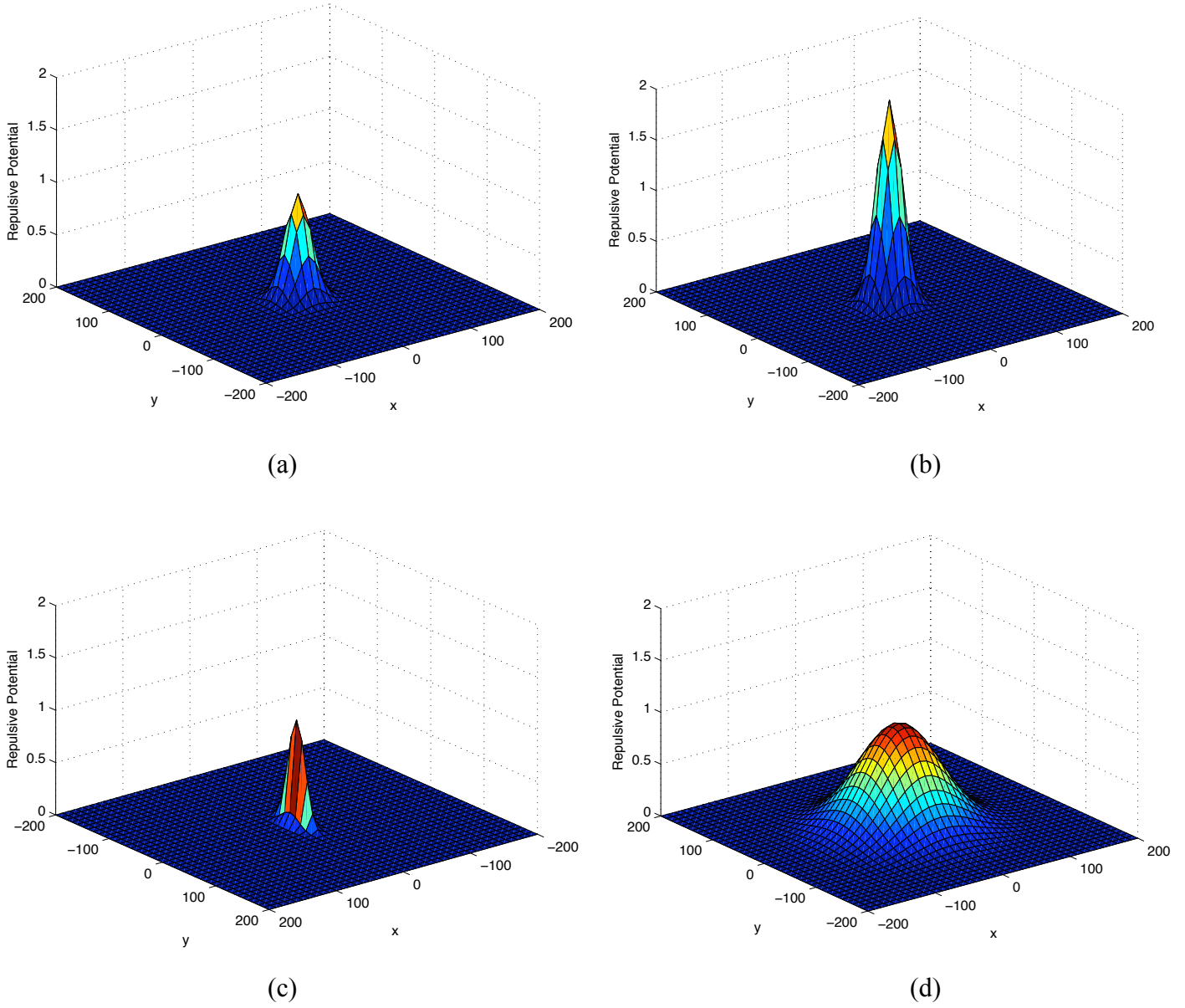


Figure 20: Repulsive potential as a function of position relative to the goal. (a) $k_r = 1$,

$$\bar{\bar{Q}}_r = \bar{\bar{I}}_{2 \times 2}, \sigma = 500, \text{ (b) } k_r = 2, \bar{\bar{Q}}_r = \bar{\bar{I}}_{2 \times 2}, \sigma = 500, \text{ (c) } k_r = 1, \bar{\bar{Q}}_r = \begin{bmatrix} 10 & 0 \\ 0 & 1 \end{bmatrix},$$

$$\sigma = 500, \text{ (d) } k_r = 1, \bar{\bar{Q}}_r = \bar{\bar{I}}_{2 \times 2}, \sigma = 5000.$$

The potential function in Eq. (220) can be expanded as:

$$\phi_r = k_r \exp \left[\frac{-\bar{\rho}^T \bar{\bar{Q}}_r \bar{\rho} + \bar{\rho}^T \bar{\bar{Q}}_r \bar{\rho}_{obs} + \bar{\rho}_{obs}^T \bar{\bar{Q}}_r \bar{\rho} - \bar{\rho}_{obs}^T \bar{\bar{Q}}_r \bar{\rho}_{obs}}{\sigma} \right] \quad (221)$$

Taking the gradient of ϕ_r with respect to $\bar{\rho}$,

$$\nabla_{\rho} \phi_r = \frac{\partial \phi_r}{\partial \bar{\rho}} \quad (222)$$

The gradient is evaluated as follows:

$$\begin{aligned} \nabla_{\rho} \phi_r = \frac{k_r}{\sigma} & \left[-\frac{\partial(\bar{\rho}^T \bar{\bar{Q}}_r \bar{\rho})}{\partial \bar{\rho}} + \frac{\partial(\bar{\rho}^T \bar{\bar{Q}}_r \bar{\rho}_{obs})}{\partial \bar{\rho}} + \frac{\partial(\bar{\rho}_{obs}^T \bar{\bar{Q}}_r \bar{\rho})}{\partial \bar{\rho}} - \frac{\partial(\bar{\rho}_{obs}^T \bar{\bar{Q}}_r \bar{\rho}_{obs})}{\partial \bar{\rho}} \right] \cdot \\ & \exp \left[\frac{-\bar{\rho}^T \bar{\bar{Q}}_r \bar{\rho} + \bar{\rho}^T \bar{\bar{Q}}_r \bar{\rho}_{obs} + \bar{\rho}_{obs}^T \bar{\bar{Q}}_r \bar{\rho} - \bar{\rho}_{obs}^T \bar{\bar{Q}}_r \bar{\rho}_{obs}}{\sigma} \right] \end{aligned} \quad (223)$$

If $\bar{\bar{Q}}_r$ is assumed to be a diagonal matrix, Eq. (223) can be evaluated and simplified as:

$$\nabla_{\rho} \phi_r = \frac{-2k_r}{\sigma} \left[\bar{\bar{Q}}_r (\bar{\rho} - \bar{\rho}_{obs}) \right] \cdot \exp \left[\frac{-\bar{\rho}^T \bar{\bar{Q}}_r \bar{\rho} + 2\bar{\rho}^T \bar{\bar{Q}}_r \bar{\rho}_{obs} - \bar{\rho}_{obs}^T \bar{\bar{Q}}_r \bar{\rho}_{obs}}{\sigma} \right] \quad (224)$$

Similar to an attractive APF, the control law for a repulsive field dictates that immediately following the application of a control force, the relative velocity of the

spacecraft should be in the negative gradient direction (i.e., the direction of steepest descent) with respect to the repulsive potential field:

$$\bar{\mathbf{v}}^+ = -\nabla_{\rho} \phi_r = \frac{2k_r}{\sigma} \left[\bar{\mathbf{Q}}_r (\bar{\rho} - \bar{\rho}_{obs}) \right] \cdot \exp \left[\frac{-\bar{\rho}^T \bar{\mathbf{Q}}_r \bar{\rho} + 2\bar{\rho}^T \bar{\mathbf{Q}}_r \bar{\rho}_{obs} - \bar{\rho}_{obs}^T \bar{\mathbf{Q}}_r \bar{\rho}_{obs}}{\sigma} \right] \quad (225)$$

The total derivative of the potential function in Eq. (221) is found as:

$$\dot{\phi}_r = \frac{d\phi_r}{dt} = \frac{k_r}{\sigma} \exp \left[\frac{-\bar{\rho}^T \bar{\mathbf{Q}}_r \bar{\rho} + 2\bar{\rho}^T \bar{\mathbf{Q}}_r \bar{\rho}_{obs} - \bar{\rho}_{obs}^T \bar{\mathbf{Q}}_r \bar{\rho}_{obs}}{\sigma} \right] \cdot \frac{d}{dt} \left(-\bar{\rho}^T \bar{\mathbf{Q}}_r \bar{\rho} + 2\bar{\rho}^T \bar{\mathbf{Q}}_r \bar{\rho}_{obs} - \bar{\rho}_{obs}^T \bar{\mathbf{Q}}_r \bar{\rho}_{obs} \right) \quad (226)$$

Carrying out the time derivatives, where $\bar{\rho}_{obs}$ is assumed to be stationary:

$$\dot{\phi}_r = \frac{k_r}{\sigma} \left(-\dot{\bar{\rho}}^T \bar{\mathbf{Q}}_r \bar{\rho} - \bar{\rho}^T \bar{\mathbf{Q}}_r \dot{\bar{\rho}} + 2\dot{\bar{\rho}}^T \bar{\mathbf{Q}}_r \bar{\rho}_{obs} \right) \exp \left[\frac{-\bar{\rho}^T \bar{\mathbf{Q}}_r \bar{\rho} + 2\bar{\rho}^T \bar{\mathbf{Q}}_r \bar{\rho}_{obs} - \bar{\rho}_{obs}^T \bar{\mathbf{Q}}_r \bar{\rho}_{obs}}{\sigma} \right] \quad (227)$$

The total derivative given by Eq. (227) is utilized as a switching condition for the control action:

$$\Delta \bar{\mathbf{V}} = \begin{cases} 0 & , \quad \dot{\phi}_r \leq 0 \\ -\nabla_{\rho} \phi_r - \dot{\bar{\rho}} & , \quad \dot{\phi}_r > 0 \end{cases} \quad (228)$$

Similar to the attractive potential, the control action in response to a repulsive potential field is taken when the value of the potential function is increasing; a maneuver is defined such that the relative velocity following the impulse is in the negative gradient direction of the potential field.

A potential field that combines attractive and repulsive potentials can be constructed by superposing the scalar potentials into a total potential field, ϕ_{TOT} :

$$\phi_{TOT} = \phi_a + \phi_r \quad (229)$$

The gradient of the total potential is simply the sum of the gradients of the attractive and repulsive fields,

$$\nabla_{\rho} \phi_{TOT} = \nabla_{\rho} \phi_a + \nabla_{\rho} \phi_r \quad (230)$$

The time derivative of the total potential is given by:

$$\dot{\phi}_{TOT} = \dot{\phi}_a + \dot{\phi}_r \quad (231)$$

The control action is defined as:

$$\Delta \bar{V} = \begin{cases} 0 & , \quad \dot{\phi}_{TOT} \leq 0 \\ -\nabla_{\rho} \phi_{TOT} - \dot{\bar{\rho}} & , \quad \dot{\phi}_{TOT} > 0 \end{cases} \quad (232)$$

The previous example is now considered with the addition of a repulsive potential field, centered on $\bar{\rho}_{obs}^T = [-0.040 \quad 0.130 \quad 0]$ km; the attractive potential field remains centered on the target location $\bar{\rho}_{tgt}^T = [0.000 \quad 0.100 \quad 0.000]$ km. The initial conditions and APF parameters are given in Table 25. The total potential field formed by

superposing the attractive and repulsive potentials is illustrated in Figure 21. The values for the APF scaling parameters, k_a and k_r , and the value for the repulsive field broadening parameter, σ , are selected iteratively to limit the size of the control maneuvers such that the trajectory behavior is as desired. It is noted that the scaling parameter for the repulsive field is selected to be three orders of magnitude smaller than that for the attractive field, in order to size the repulsive ΔV s such that the trajectory converges to the target.

Table 25: APF control example, attractive and repulsive fields.

Initial Conditions	$x = 0.000 \text{ km}$ $\dot{x} = 2E - 05 \text{ km/s}$ $y = 0.200 \text{ km}$ $\dot{y} = 0 \text{ km/s}$ $z = 0.000 \text{ km}$ $\dot{z} = 0 \text{ km/s}$
Target Location	$x = 0.000 \text{ km}$ $y = 0.100 \text{ km}$ $z = 0.000 \text{ km}$
Obstacle Location	$x = -0.040 \text{ km}$ $y = 0.130 \text{ km}$ $z = 0.000 \text{ km}$
APF Parameters	$k_a = 1E - 03$ $k_r = 2E - 06$ $\bar{\bar{Q}}_a = \bar{\bar{I}}_{3 \times 3}$ $\bar{\bar{Q}}_r = \bar{\bar{I}}_{3 \times 3}$ $\sigma = 1E - 04$

The resulting trajectory is shown in Figure 22. The effect of the repulsive potential field is clearly evident through comparison with Figure 18. As the vehicle enters the influence of the repulsive field, a ΔV is commanded to redirect the velocity vector in the negative gradient direction, away from the obstacle. The trajectory is then influenced primarily by the attractive potential, leading to convergence to the targeted location.

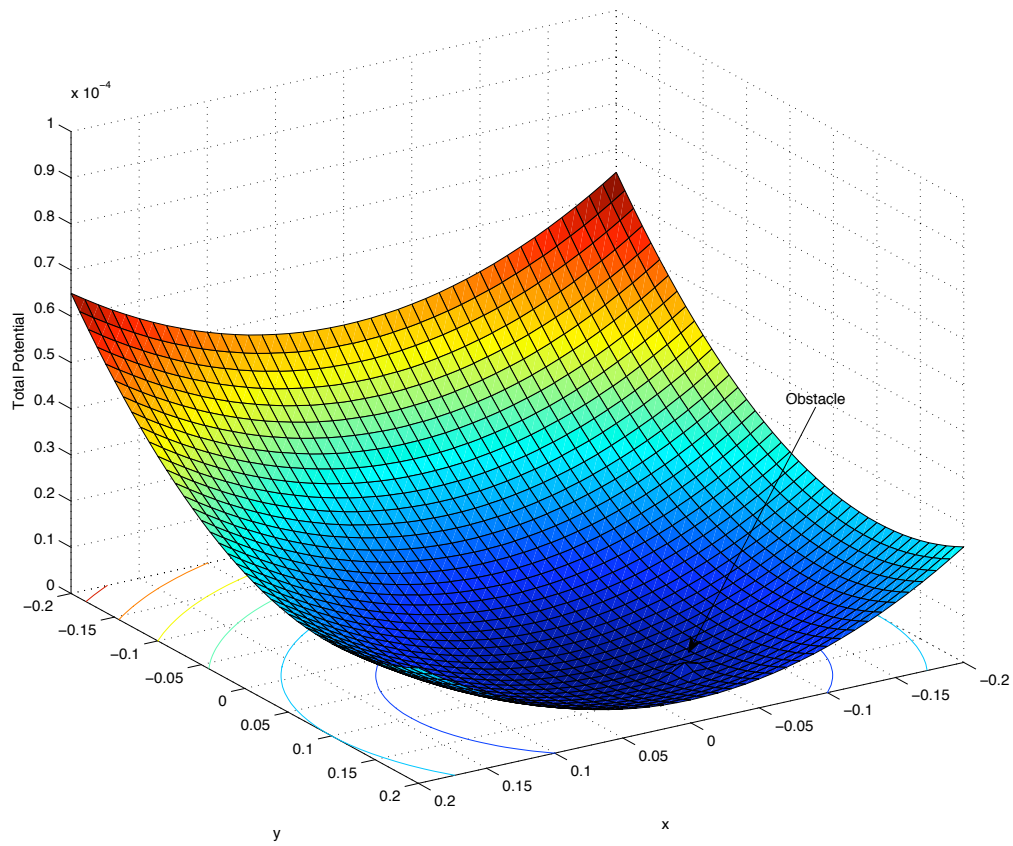


Figure 21: Total potential field with attractive potential centered at $x = 0$ km, $y = 0.100$ km, repulsive potential centered at $x = -0.040$ km, $y = 0.130$ km.

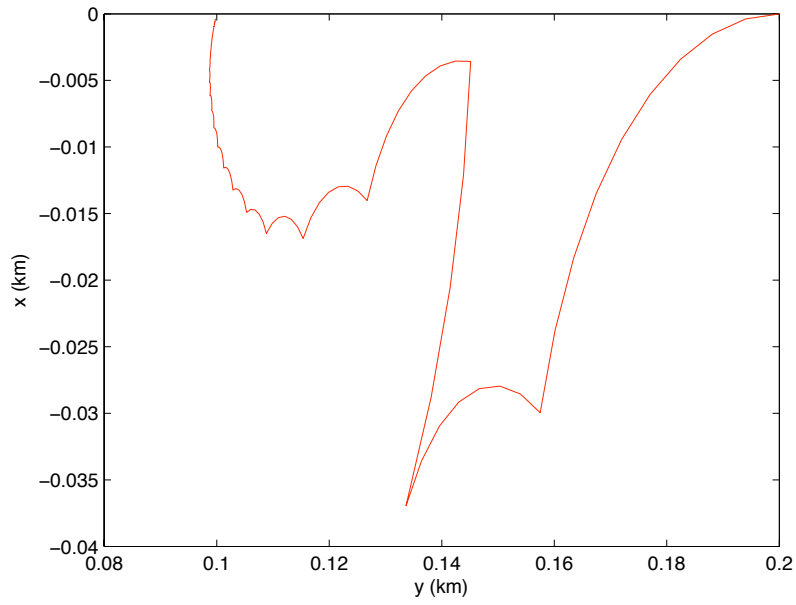


Figure 22: APF trajectory control influence by attractive and repulsive potential fields.

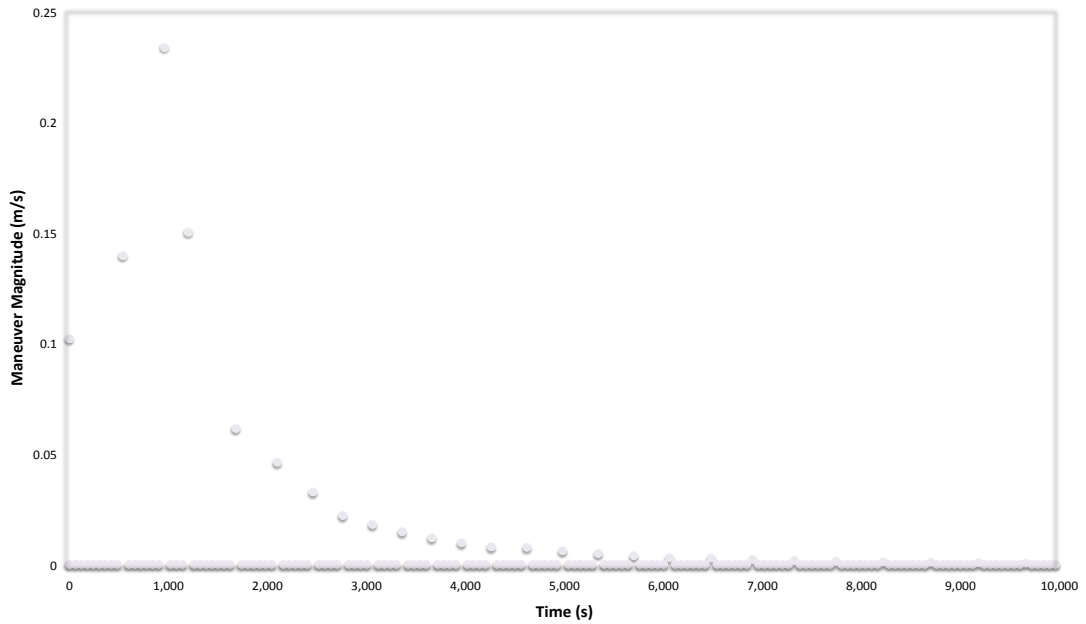


Figure 23: APF repulsive control maneuver magnitudes.

3.2 Artificial Potential Functions Using Relative Orbital Elements

Current APF formulations similar to those described in Section 3.1 are operationally useful due to their computational simplicity and the flexible, continuous nature of the APF control approach. An attractive APF of the form shown in Figure 17 results in a potential field with a global minimum at the target location. Provided the vehicle has adequate thrust and propellant to achieve the commanded ΔV s, the control strategy will successfully guide the vehicle to the target. However, this control strategy does not utilize any knowledge of orbital dynamics, so it is inherently inefficient. The control methodology is such that impulsive maneuvers are commanded whenever the value of the scalar potential is increasing; that is, whenever the range from the target to the vehicle is increasing. Maneuvers are performed to redirect the velocity vector of the vehicle in the direction of steepest descent of the potential field at the current position. In the case of an attractive potential field, all ΔV s are commanded such that the relative velocity vector immediately following a maneuver is directed toward the target location. The applied ΔV ensures that the motion immediately following the maneuver will result in a decreasing value for the scalar potential function. If maneuvers are initiated whenever the value of the time derivative of the scalar potential is greater than or equal to zero, convergence to the goal position is ensured.

In this investigation, a strategy is sought that retains the simplicity of the APF approach, but capitalizes upon orbital dynamics to provide trajectory control capability with fewer commanded maneuvers and reduced fuel utilization, while meeting the objective. The relative orbital element formulation succinctly captures relative motion with a set of algebraic expressions, within the framework of the HCW assumptions. As

such, ROEs offer the potential of achieving an APF control strategy that capitalizes upon orbital dynamics, as an alternative to the approach described in Section 3.1. This work investigates artificial potential functions that are expressed in terms of relative orbital elements, in order to shape the trajectory along paths that utilize the natural motion established by the relative orbital dynamics, while targeting the desired relative orbit. Through defining a scalar potential function in terms of ROEs, the resulting potential field may be shaped such that the path of steepest descent lies in the direction of the desired ROEs, where the natural motion of the trajectory leads to the goal. A major advantage of the ROE-based approach is that the APFs allow targeting of a specified relative *orbit*, whereas the previous approach only allowed targeting of a relative position. The ROE-based approach can target a fixed position if desired (with targets for a_r and A_z set to zero), however, the formulation also allows targeting of orbit geometries relative to the chief.

When targeting a set of relative orbital elements, the artificial potential function is defined in terms of the full relative Cartesian state, including position and velocity elements. As a result, establishing the post-maneuver velocity vector in the negative gradient direction of the potential function with respect to the position vector does not ensure that subsequent unforced motion will reduce the value of the scalar potential. The velocity derivatives may be such that the post-maneuver motion results in an increase in the scalar potential. Convergence to the goal is not ensured.

An alternative formulation is needed for ROE targeting. It is noted that three of the ROEs, x_r , a_r , and A_z , are constant for unforced motion. These ROES can be controlled to their target values only through the application of maneuvers. A fourth

ROE, y_r , varies with time at a constant rate in unforced motion. A maneuver can instantaneously change the value for y_r , and can also change the time rate of change of y_r .

A control law for ROE targeting may be established whereby impulsive maneuvers are defined to control each ROE in the direction of its targeted value, if such a ΔV exists. In this formulation, the gradient of the potential function with respect to velocity is determined, and the control ΔV is defined to be in the negative gradient direction. The maneuver is constrained such that it ensures that each ROE value moves in the direction of the targeted value as a result of the ΔV . The applied ΔV therefore results in an instantaneous decrease of the scalar potential value. If a maneuver is performed whenever the value for the scalar potential would otherwise increase or remain constant, provided a suitable ΔV exists, the control law will result in convergence to the goal.

An attractive artificial potential may be written in terms of ROEs as:

$$\phi_a = \frac{1}{2} k_a (\bar{\tau} - \bar{\tau}_{igt})^T \bar{Q}_a (\bar{\tau} - \bar{\tau}_{igt}) \quad (233)$$

where $\bar{\tau}$ is a vector composed of a set of ROEs and $\bar{\tau}_{igt}$ is composed of the target values for those ROEs. For brevity, we can replace the vector difference $\bar{\tau} - \bar{\tau}_{igt}$ with the vector \bar{T} , where

$$\bar{T} = \bar{\tau} - \bar{\tau}_{igt} \quad (234)$$

such that

$$\phi_a = \frac{1}{2} k_a \bar{\mathbf{T}}^T \bar{\mathbf{Q}}_a \bar{\mathbf{T}} \quad (235)$$

Targeting of ROEs using this attractive potential function will be demonstrated initially for target vectors with a single element: x_r , y_r , a_r , or A_z . The targeting of a vector composed of multiple ROEs will then be addressed. It is noted that the targeting of fixed values for the angular ROEs, E_r and ψ , is not practical with impulsive ΔV s and will not be considered here.

The negative gradient of the potential function, or path of steepest descent, defines the control direction in which a maneuver should be performed. The control equation can be written:

$$\Delta \bar{\mathbf{V}} = -\nabla_{\dot{\rho}} \phi_a \quad (236)$$

The control action may be initiated based upon the maneuver constraints shown in Tables 7, 8, and 13. Through utilizing these constraints, a maneuver may be initiated only when a maneuver exists that can drive each of the ROEs contained within the target vector toward their targeted values.

3.2.1 Targeting a Single Relative Orbital Element: x_r

For targeting the single ROE x_r , the ROE vector then becomes:

$$\bar{\boldsymbol{\tau}} = [x_r] \quad (237)$$

and the vector difference of the ROE with respect to the target is:

$$\bar{\mathbf{T}} = \begin{bmatrix} x_r - x_{r_{tgt}} \end{bmatrix} = [T_1] \quad (238)$$

Based upon Eq. (71), we can evaluate T_1 in Eq. (238) as:

$$T_1 = 4x + \frac{2\dot{y}}{n} - x_{r_{tgt}} \quad (239)$$

With a single element in the target vector, Eq. (235) can be written as:

$$\phi_a = \frac{1}{2} k_a q_{11} T_1^2 \quad (240)$$

Taking the partial derivative of the potential function shown in Eq. (240) with respect to the relative velocity vector yields:

$$\frac{\partial \phi_a}{\partial \dot{x}} = k_a q_{11} T_1 \frac{\partial T_1}{\partial \dot{x}} \quad (241)$$

$$\frac{\partial \phi_a}{\partial \dot{y}} = k_a q_{11} T_1 \frac{\partial T_1}{\partial \dot{y}} \quad (242)$$

$$\frac{\partial \phi_a}{\partial \dot{z}} = k_a q_{11} T_1 \frac{\partial T_1}{\partial \dot{z}} \quad (243)$$

Evaluating the partial derivative of T_1 with respect to each component of the relative velocity gives:

$$\frac{\partial T_1}{\partial \dot{x}} = 0 \quad (244)$$

$$\frac{\partial T_1}{\partial \dot{y}} = \frac{2}{n} \quad (245)$$

$$\frac{\partial T_1}{\partial \dot{z}} = 0 \quad (246)$$

Eqs. (244) – (246) establish the gradient vector as:

$$\nabla_{\rho} \phi_a = \begin{bmatrix} 0 \\ \frac{2}{n} k_a q_{11} T_1 \\ 0 \end{bmatrix} \quad (247)$$

Based upon Eq. (236), the control strategy gives:

$$\Delta V = -\nabla_{\rho} \phi_a = \begin{bmatrix} 0 \\ -\frac{2}{n} k_a q_{11} T_1 \\ 0 \end{bmatrix} \quad (248)$$

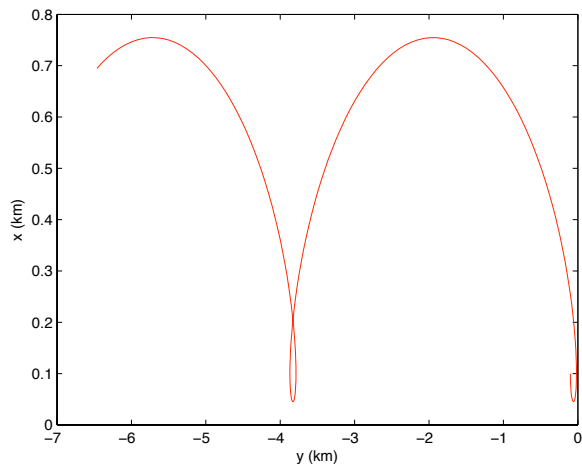
As noted previously, because x_r is a constant of the relative motion, the potential function based upon x_r is constant for unforced motion. Therefore, $\dot{\phi}_a = 0$, and $\dot{\phi}_a$ is not useful as a control switching condition. However, per Tables 7 - 8, a ΔV may be implemented in the \hat{y} -direction at any point in the orbit, to increase or decrease the value of x_r . Thus, the control action shown in Eq. (248) may be taken at each time step in the orbit, until the target conditions are met to the desired tolerance level.

An example of x_r targeting is summarized in Table 26. The initial value for x_r is 0.400 km, and the targeted value for x_r is zero. Figure 24(a) shows a 10,000 s propagation of the unforced motion, starting with the initial conditions shown in Table 26. With no maneuvers, the trajectory drifts in the negative along-track direction due to the positive value of x_r . Figure 24(b) shows the effect of APF control, with the control

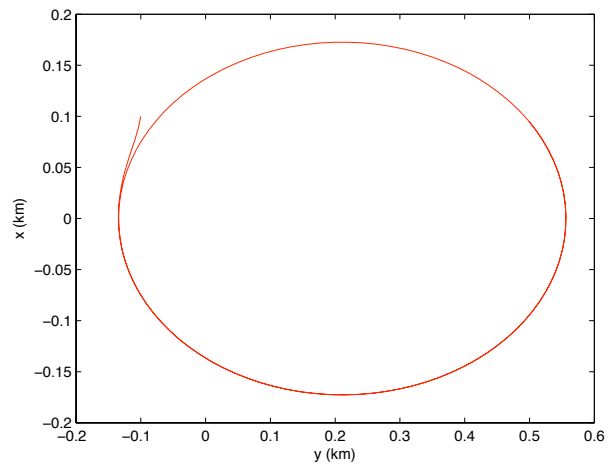
impulse calculated every 60 s. The control forces shape the relative orbit into a stationary ellipse centered on $x = 0$. The value of x_r as a function of time is shown in Figure 24(c). It is seen that the desired condition, $x_r = 0$, is reached within 1,000 s. Maneuver magnitudes as a function of time are shown in Figure 25. The total ΔV expended for trajectory control is 0.211 m/s.

Table 26: APF control example, targeting ROE x_r .

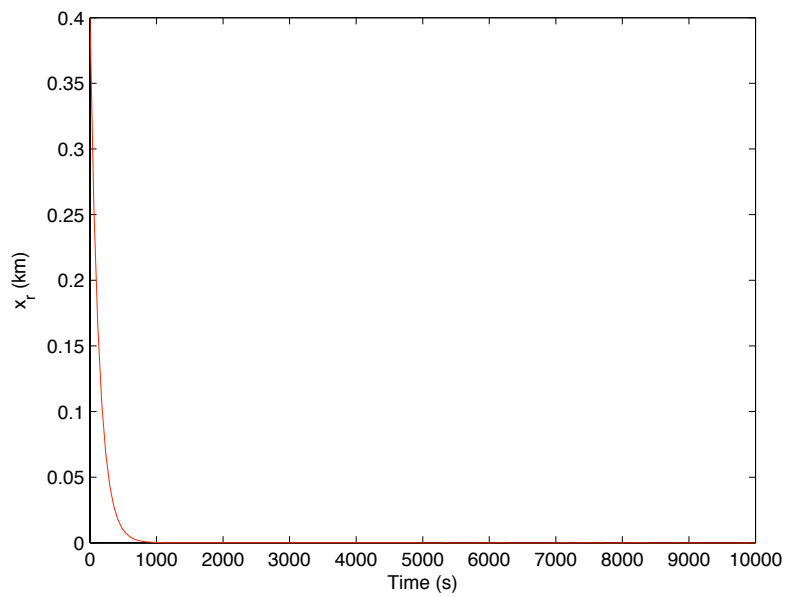
Initial Conditions	Cartesian	$x = 0.100 \text{ km}$ $\dot{x} = -0.0002 \text{ km/s}$ $y = -0.100 \text{ km}$ $\dot{y} = 0.0000 \text{ km/s}$ $z = 0.000 \text{ km}$ $\dot{z} = 0.0000 \text{ km/s}$
	ROEs	$x_r = 0.4000 \text{ km}$ $E_r = 5.7199 \text{ rad}$ $y_r = 0.2789 \text{ km}$ $A_z = 0.0000 \text{ km}$ $a_r = 0.7096 \text{ km}$ $\psi = 0.0000 \text{ rad}$
Target ROEs		$x_r = 0.0000 \text{ km}$
APF Parameters		$k_a = 1E - 07$ $\bar{\bar{Q}}_a = \bar{\bar{I}}_{1 \times 1}$



(a)



(b)



(c)

Figure 24: APF targeting of single ROE x_r . (a) Unforced motion, 10,000 s propagation from initial conditions, (b) APF targeting of $x_r = 0$, $\hat{y} - \hat{x}$ projection, (c) Value of x_r as a function of time.

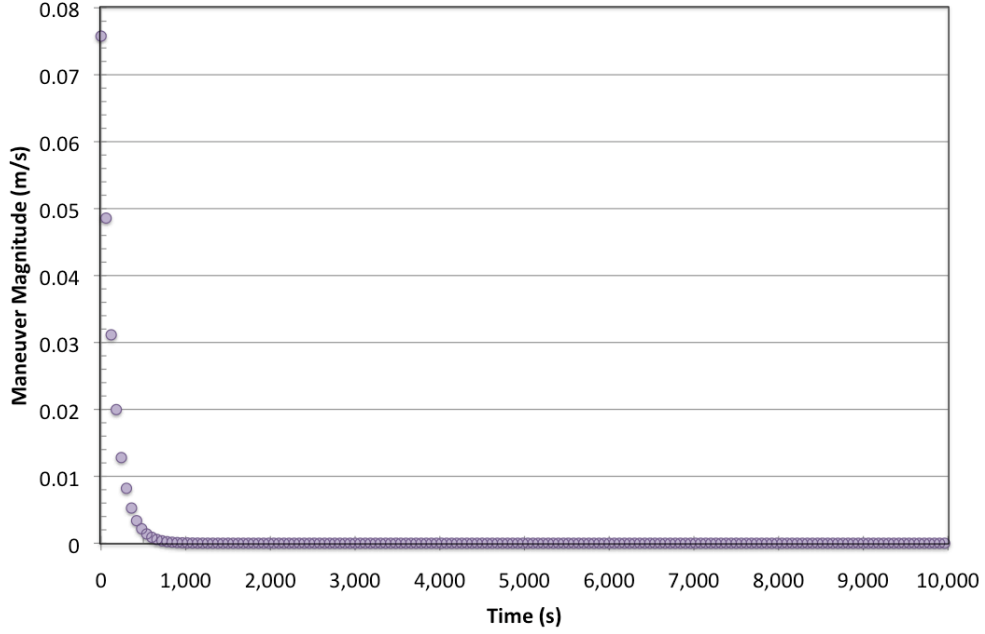


Figure 25: APF x_r targeting maneuver magnitudes.

3.2.2 Targeting a Single Relative Orbital Element: y_r

Targeting the single ROE y_r , the ROE vector becomes:

$$\bar{\tau} = [y_r] \quad (249)$$

and the vector difference of the ROE with respect to the target is:

$$\bar{T} = [y_r - y_{r_{tgt}}] = [T_1] \quad (250)$$

Based upon Eq. (72), we can evaluate T_1 in Eq. (250) as:

$$T_1 = y - \frac{2\dot{x}}{n} - y_{r_{tgt}} \quad (251)$$

The potential function and its partial derivatives remain as written in Eqs. (240) – (243). Evaluating the partial derivative of T_I with respect to each component of the relative velocity gives:

$$\frac{\partial T_I}{\partial \dot{x}} = -\frac{2}{n} \quad (252)$$

$$\frac{\partial T_I}{\partial \dot{y}} = 0 \quad (253)$$

$$\frac{\partial T_I}{\partial \dot{z}} = 0 \quad (254)$$

Eqs. (252) – (254) establish the gradient vector as:

$$\nabla_{\rho} \phi_a = \begin{bmatrix} -\frac{2}{n} k_a q_{11} T_I \\ 0 \\ 0 \end{bmatrix} \quad (255)$$

Based upon Eq. (236), the control strategy gives:

$$\Delta \bar{V} = -\nabla_{\rho} \phi_a = \begin{bmatrix} \frac{2}{n} k_a q_{11} T_I \\ 0 \\ 0 \end{bmatrix} \quad (256)$$

The control switching condition is defined as:

$$\Delta \bar{V} = \begin{cases} 0 & , \dot{\phi}_a \leq 0 \\ -\nabla_{\rho} \phi_a & , \dot{\phi}_a > 0 \end{cases} \quad (257)$$

where

$$\dot{\phi}_a = k_a q_{11} T_1 \dot{T}_1 \quad (258)$$

and the time derivative of T_1 is found by differentiating Eq. (251):

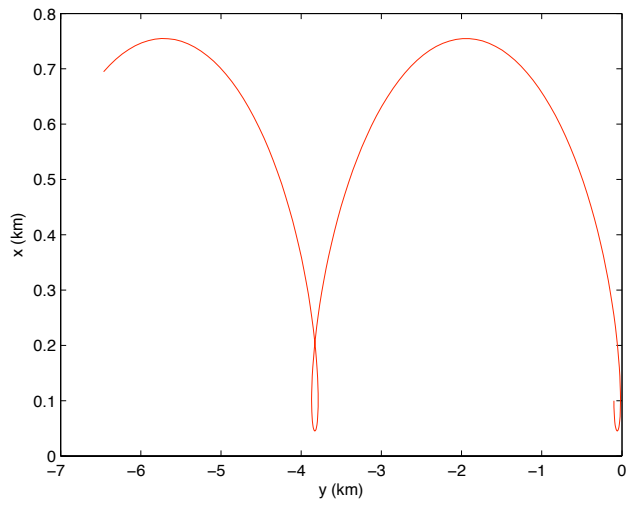
$$\dot{T}_1 = -3\dot{y} - 6nx \quad (259)$$

An example of y_r targeting is summarized in Table 27. The initial conditions are the same as in the previous example. The initial value for y_r is 0.2789 km, and the targeted value for y_r is zero. Figure 26(a) shows a 10,000 s propagation of the unforced motion, which is unchanged from the previous example. Figure 26(b) shows the effect of APF control using y_r targeting. It is seen that the control forces shape the relative orbit into a stationary ellipse centered on $y = 0$. The value of y_r as a function of time is shown in Figure 26(c). The desired condition $y_r = 0$ is quickly reached, however there is some jitter about the targeted value. The jitter occurs because the untargeted ROE x_r remains at the initial condition value of 0.400 km. With a positive value for x_r , the APF control effectively exerts a near-continuous thrust (commanding an impulse at each opportunity) once the targeted value of y_r is reached. Impulses are performed in the $-\hat{x}$ -direction to offset the secular drift in the along-track direction and maintain y_r at the targeted value. It is noted that the resulting stationary ellipse shown in Figure 26(b) is centered on $x = 0.1$ km. This is not consistent with x_r , because the ellipse shown is a forced trajectory based upon the control impulses; if the impulses were stopped, the unforced instantaneous ellipse would be centered on $x = 0.400$ km. Maneuver magnitudes as a function of time

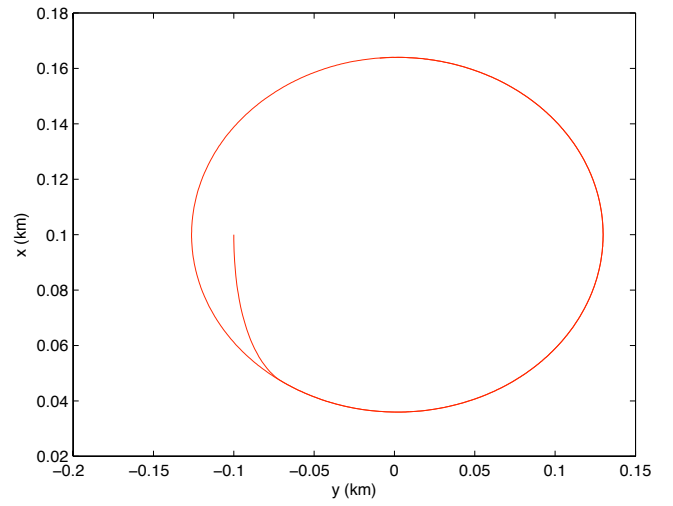
are shown in Figure 27. The total ΔV expended for trajectory control during the 10,000 s simulation is 3.201 m/s.

Table 27: APF control example, targeting ROE y_r .

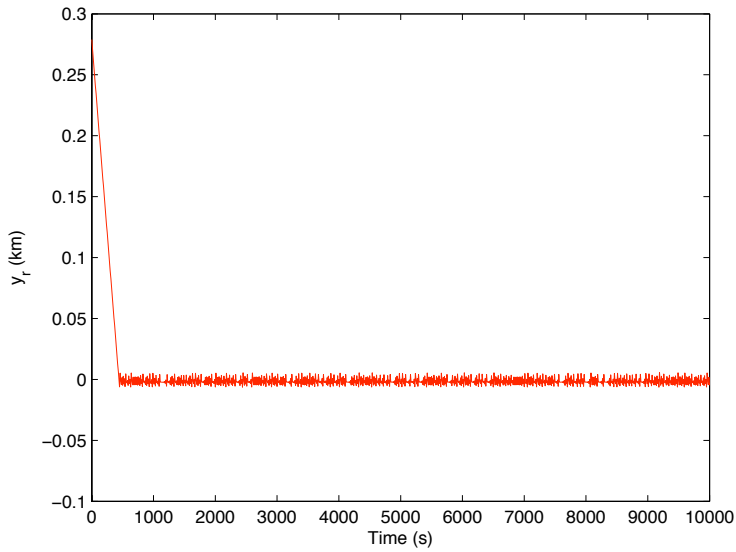
Initial Conditions	Cartesian	$x = 0.100 \text{ km}$ $\dot{x} = -0.0002 \text{ km/s}$ $y = -0.100 \text{ km}$ $\dot{y} = 0.0000 \text{ km/s}$ $z = 0.000 \text{ km}$ $\dot{z} = 0.0000 \text{ km/s}$
	ROEs	$x_r = 0.4000 \text{ km}$ $E_r = 5.7199 \text{ rad}$ $y_r = 0.2789 \text{ km}$ $A_z = 0.0000 \text{ km}$ $a_r = 0.7096 \text{ km}$ $\psi = 0.0000 \text{ rad}$
Target ROEs		$x_r = 0.0000 \text{ km}$
APF Parameters		$k_a = 1E - 07$ $\bar{\bar{Q}}_a = \bar{\bar{I}}_{1 \times 1}$



(a)



(b)



(c)

Figure 26: APF targeting of single ROE y_r . (a) Unforced motion, 10,000 s propagation from initial conditions, (b) APF targeting of $y_r = 0$, $\hat{y} - \hat{x}$ projection, (c) Value of y_r as a function of time.

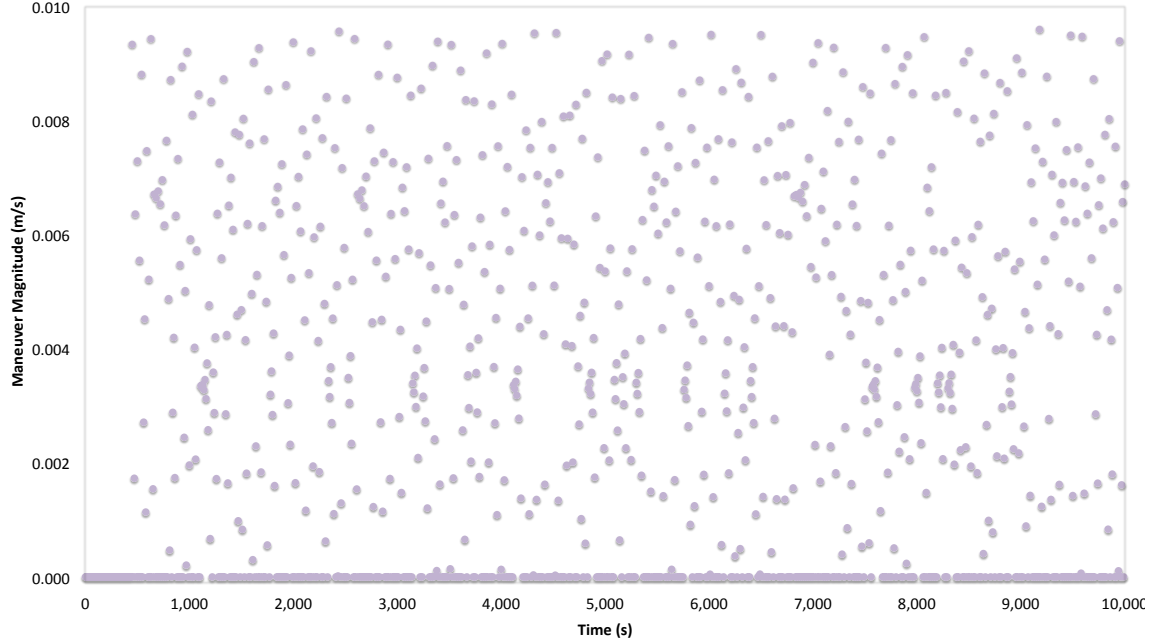


Figure 27: APF y_r targeting maneuver magnitudes.

3.2.3 Targeting a Single Relative Orbital Element: a_r

Targeting the single ROE a_r , the ROE vector becomes:

$$\bar{\tau} = [a_r] \quad (260)$$

and the vector difference of the ROE with respect to the target is:

$$\bar{T} = [a_r - a_{r_{tgt}}] = [T_1] \quad (260)$$

Based upon Eq. (73), we can evaluate T_1 in Eq. (260) as:

$$T_1 = \left[\left(6x + \frac{4\dot{y}}{n} \right)^2 + \left(\frac{2\dot{x}}{n} \right)^2 \right] - a_{r_{tgt}} \quad (262)$$

The potential function and its partial derivatives remain as written in Eqs. (240) – (243).

Evaluating the partial derivative of T_1 with respect to each component of the relative velocity gives:

$$\frac{\partial T_1}{\partial \dot{x}} = \frac{4\dot{x}/n}{\left[\left(6x + \frac{4\dot{y}}{n} \right)^2 + \left(\frac{2\dot{x}}{n} \right)^2 \right]^{1/2}} \quad (263)$$

$$\frac{\partial T_1}{\partial \dot{y}} = \frac{24x + 16\dot{y}/n}{n \left[\left(6x + \frac{4\dot{y}}{n} \right)^2 + \left(\frac{2\dot{x}}{n} \right)^2 \right]^{1/2}} \quad (264)$$

$$\frac{\partial T_1}{\partial \dot{z}} = 0 \quad (265)$$

Eqs. (263) – (265) establish the gradient vector as:

$$\nabla_{\dot{\rho}} \phi_a = \begin{bmatrix} \frac{4\dot{x}/n}{\left[\left(6x + \frac{4\dot{y}}{n} \right)^2 + \left(\frac{2\dot{x}}{n} \right)^2 \right]^{1/2}} \\ \frac{24x + 16\dot{y}/n}{n \left[\left(6x + \frac{4\dot{y}}{n} \right)^2 + \left(\frac{2\dot{x}}{n} \right)^2 \right]^{1/2}} \\ 0 \end{bmatrix} \quad (266)$$

Based upon Eq. (236), the control strategy gives:

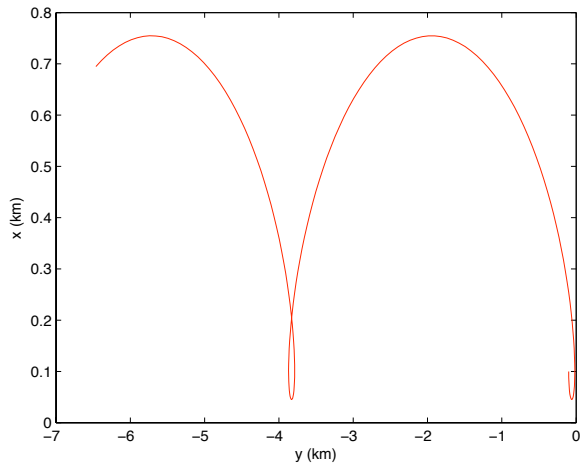
$$\Delta \bar{V} = -\nabla_{\rho} \phi_a = \begin{bmatrix} -\frac{4\dot{x}/n}{\left[\left(6x + \frac{4\dot{y}}{n} \right)^2 + \left(\frac{2\dot{x}}{n} \right)^2 \right]^{1/2}} \\ -\frac{24x + 16\dot{y}/n}{n \left[\left(6x + \frac{4\dot{y}}{n} \right)^2 + \left(\frac{2\dot{x}}{n} \right)^2 \right]^{1/2}} \\ 0 \end{bmatrix} \quad (267)$$

Because a_r is a constant of the relative motion, the potential function based upon a_r is invariant for the unforced motion. Therefore, $\dot{\phi}_a = 0$, and $\dot{\phi}_a$ is not useful as a control switching condition. However, the maneuver logic structure contained in Tables 7 - 8 may be utilized to determine the locations in the relative orbit where an impulsive maneuver may drive a_r in the desired direction. The information in Tables 7 – 8, expressed in terms of the ROE E_r , is utilized as the switching condition for control implementation.

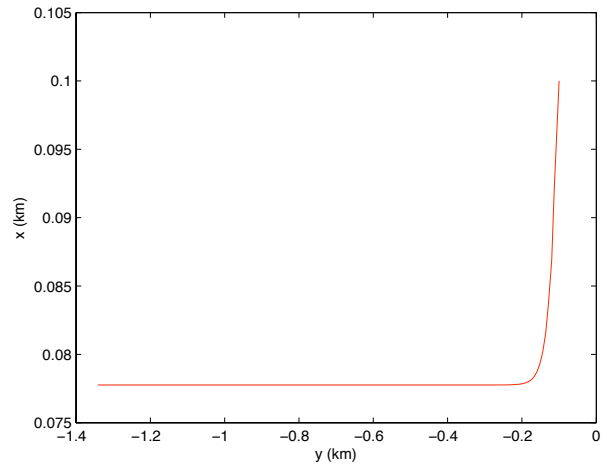
An example of a_r targeting is summarized in Table 28. The initial conditions are unchanged from the previous examples. The initial value for a_r is 0.7096 km, and the targeted value for a_r is zero. Figure 28(a) shows a 10,000 s propagation of the unforced motion, which is unchanged from the previous examples. Figure 28(b) shows the effect of APF control using a_r targeting. It is seen that the control forces result in a circular deputy orbit with a value for x_r of 0.0776 km. With the resulting positive value for x_r , the deputy spacecraft has a secular drift in the negative along-track direction. The value of a_r as a function of time is shown in Figure 28(c). The desired condition $a_r = 0$ is reached within 1,000 s. Maneuver magnitudes as a function of time are shown in Figure 29. The total ΔV expended for trajectory control during the 10,000 s simulation is 0.462 m/s.

Table 28: APF control example, targeting ROE a_r .

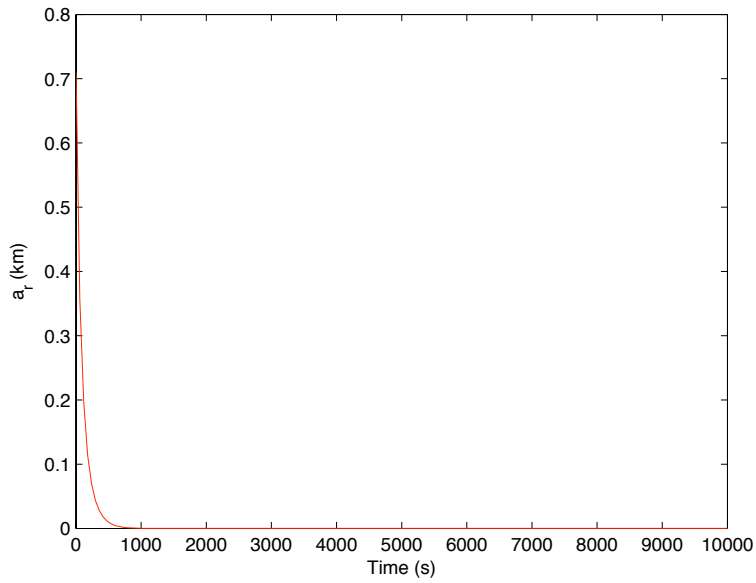
Initial Conditions	Cartesian	$x = 0.100 \text{ km}$ $\dot{x} = -0.0002 \text{ km/s}$ $y = -0.100 \text{ km}$ $\dot{y} = 0.0000 \text{ km/s}$ $z = 0.000 \text{ km}$ $\dot{z} = 0.0000 \text{ km/s}$
	ROEs	$x_r = 0.4000 \text{ km}$ $E_r = 5.7199 \text{ rad}$ $y_r = 0.2789 \text{ km}$ $A_z = 0.0000 \text{ km}$ $a_r = 0.7096 \text{ km}$ $\psi = 0.0000 \text{ rad}$
Target ROEs		$a_r = 0.0000 \text{ km}$
APF Parameters		$k_a = 1E - 07$ $\bar{\bar{Q}}_a = \bar{\bar{I}}_{1 \times 1}$



(a)



(b)



(c)

Figure 28: APF targeting of single ROE a_r . (a) Unforced motion, 10,000 s propagation from initial conditions, (b) APF targeting of $a_r = 0$, $\hat{y} - \hat{x}$ projection, (c) Value of a_r as a function of time.

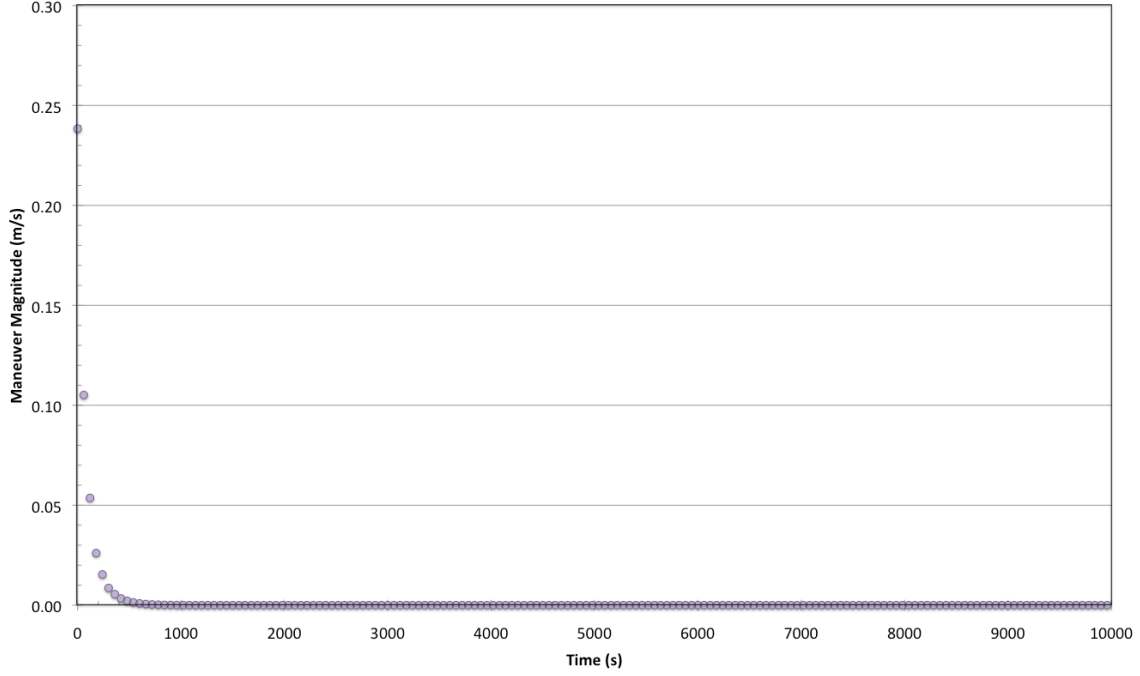


Figure 29: APF a_r targeting maneuver magnitudes.

3.2.4 Targeting a Single Relative Orbital Element: A_z

Targeting the single ROE A_z , the ROE vector becomes:

$$\bar{\mathbf{r}} = [A_z] \quad (268)$$

and the vector difference of the ROE with respect to the target is:

$$\bar{\mathbf{T}} = [A_z - A_{z_{tgt}}] = [T_1] \quad (269)$$

Based upon Eq. (75), we can evaluate T_1 in Eq. (268) as:

$$T_1 = \left[z^2 + \left(\frac{\dot{z}}{n} \right)^2 \right] - A_{z_{tgt}} \quad (270)$$

The potential function and its partial derivatives remain as written in Eqs. (240) – (243).

Evaluating the partial derivative of T_I with respect to each component of the relative velocity gives:

$$\frac{\partial T_I}{\partial \dot{x}} = 0 \quad (271)$$

$$\frac{\partial T_I}{\partial \dot{y}} = 0 \quad (272)$$

$$\frac{\partial T_I}{\partial \dot{z}} = \frac{\dot{z}/n}{\left[z^2 + \left(\frac{\dot{z}}{n} \right)^2 \right]^{1/2}} \quad (273)$$

Eqs. (271) – (273) establish the gradient vector as:

$$\nabla_{\dot{\rho}} \phi_a = \begin{bmatrix} 0 \\ 0 \\ \frac{\dot{z}/n}{\left[z^2 + \left(\frac{\dot{z}}{n} \right)^2 \right]^{1/2}} \end{bmatrix} \quad (274)$$

Based upon Eq. (236), the control strategy gives:

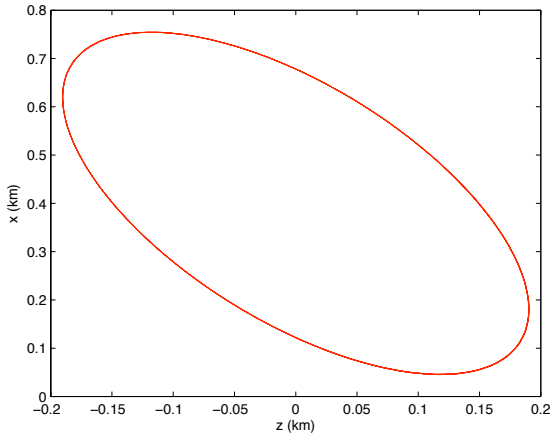
$$\Delta \bar{V} = -\nabla_{\dot{\rho}} \phi_a = \begin{bmatrix} 0 \\ 0 \\ -\frac{\dot{z}/n}{\left[z^2 + \left(\frac{\dot{z}}{n} \right)^2 \right]^{1/2}} \end{bmatrix} \quad (275)$$

Because A_z is a constant of the relative motion, the potential function based upon A_z is invariant for the unforced motion. Therefore, $\dot{\phi}_a = 0$, and $\dot{\phi}_a$ is not useful as a control switching condition. However, the maneuver logic structure contained in Tables 13 – 14 may be utilized to determine the locations in the relative orbit where an impulsive maneuver may drive A_z in the desired direction. The information in Tables 13 – 14, expressed in terms of the ROE ψ , is utilized as the switching condition for control implementation.

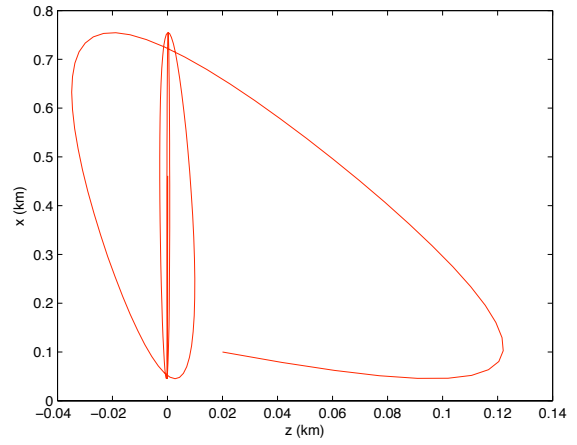
An example of A_z targeting is summarized in Table 29. Initial motion in the cross-track direction is added to the initial conditions. The initial value for A_z is 0.1904 km, and the targeted value for A_z is zero. Figure 30(a) shows a 20,000 s propagation of the unforced motion in the xy plane. Figure 30(b) shows the effect of APF control using A_z targeting. It is seen that the control forces nullify the cross-track motion. The value of A_z as a function of time is shown in Figure 30(c). Maneuver magnitudes as a function of time are shown in Figure 31. The total ΔV expended for trajectory control during the 20,000 s simulation is 0.261 m/s.

Table 29: APF control example, targeting ROE A_z .

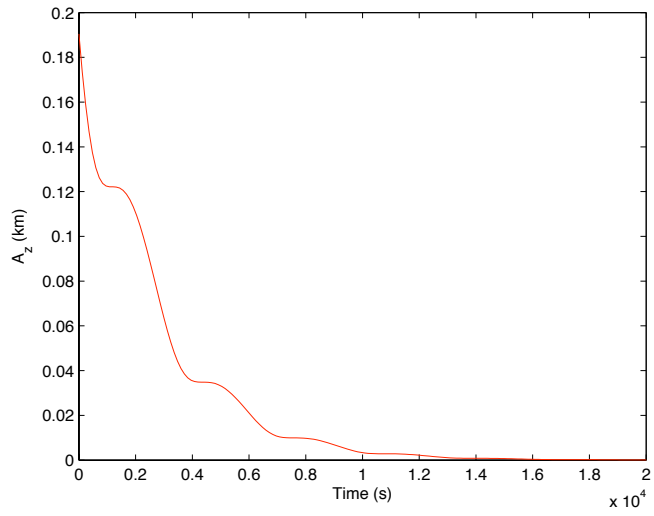
Initial Conditions	Cartesian	$x = 0.100$ km $\dot{x} = -0.0002$ km/s $y = -0.100$ km $\dot{y} = 0.0000$ km/s $z = 0.000$ km $\dot{z} = 0.0002$ km/s
	ROEs	$x_r = 0.4000$ km $E_r = 5.7199$ rad $y_r = 0.2789$ km $A_z = 0.1905$ km $a_r = 0.7096$ km $\psi = 0.1052$ rad
Target ROEs		$A_z = 0.0000$ km
APF Parameters		$k_a = 1E - 07$ $\bar{\bar{Q}}_a = \bar{\bar{I}}_{1 \times 1}$



(a)



(b)



(c)

Figure 30: APF targeting of single ROE A_z . (a) Unforced motion, 20,000 s propagation from initial conditions, (b) APF targeting of $A_z = 0$, $\hat{z} - \hat{x}$ projection, (c) Value of A_z as a function of time.

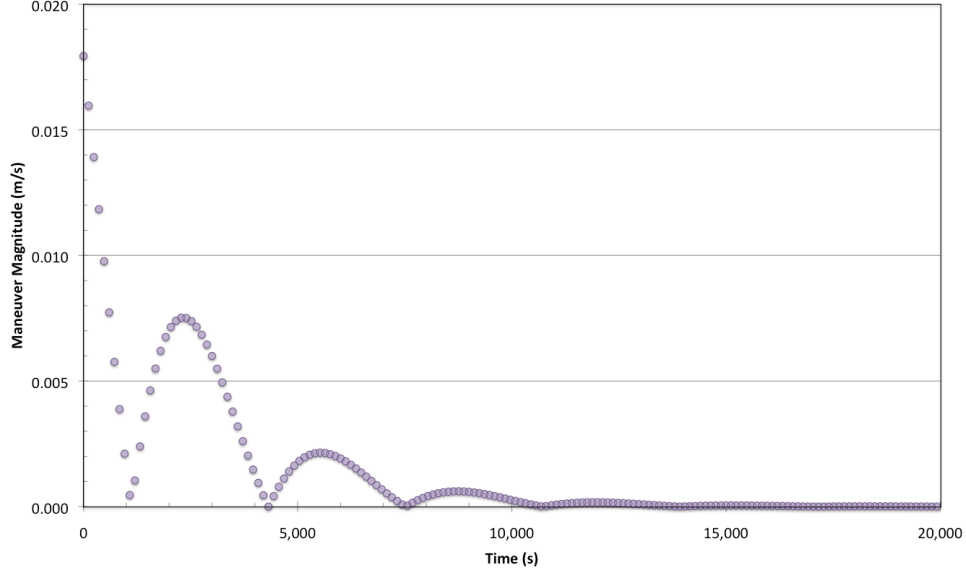


Figure 31: APF A_z targeting maneuver magnitudes.

3.2.5 Targeting Multiple Relative Orbital Elements: x_r , y_r , a_r , and A_z

In targeting multiple ROEs, x_r , y_r , a_r , and A_z , the ROE vector becomes:

$$\bar{\tau} = [x_r, y_r, a_r, A_z]^T \quad (276)$$

and the vector difference of the ROEs with respect to the ROE target vector is:

$$\bar{T} = \begin{bmatrix} x_r - x_{r_{tgt}} \\ y_r - y_{r_{tgt}} \\ a_r - a_{r_{tgt}} \\ A_z - A_{z_{tgt}} \end{bmatrix} = \begin{bmatrix} T_1 \\ T_2 \\ T_3 \\ T_4 \end{bmatrix} \quad (277)$$

Using Eqs. (239), (251), (262) and (270), the vector \bar{T} may be written as:

$$\bar{T} = \begin{bmatrix} 4x + \frac{2\dot{y}}{n} - x_{r_{igt}} \\ y - \frac{2\dot{x}}{n} - y_{r_{igt}} \\ \left[\left(6x + \frac{4\dot{y}}{n} \right)^2 + \left(\frac{2\dot{x}}{n} \right)^2 \right] - a_{r_{igt}} \\ \left[z^2 + \left(\frac{\dot{z}}{n} \right)^2 \right] - A_{z_{r_{igt}}} \end{bmatrix} \quad (278)$$

Expanding Eq. (233) with four ROEs in the targeted set yields:

$$\begin{aligned} \phi_a = \frac{1}{2} k_a \left[q_{11} T_1^2 + (q_{12} + q_{21}) T_1 T_2 + (q_{13} + q_{31}) T_1 T_3 + (q_{14} + q_{41}) T_1 T_4 + \right. \\ \left. q_{22} T_2^2 + (q_{23} + q_{32}) T_2 T_3 + (q_{24} + q_{42}) T_2 T_4 + q_{33} T_3^2 + \right. \\ \left. (q_{34} + q_{43}) T_3 T_4 + q_{44} T_4^2 \right] \end{aligned} \quad (279)$$

where q_{ij} represents the row i , column j element of the matrix \bar{Q}_a . If \bar{Q}_a is assumed to be a symmetric matrix, Eq. (279) simplifies to:

$$\begin{aligned} \phi_a = \frac{1}{2} k_a \left[q_{11} T_1^2 + 2q_{12} T_1 T_2 + 2q_{13} T_1 T_3 + 2q_{14} T_1 T_4 + q_{22} T_2^2 + 2q_{23} T_2 T_3 + 2q_{24} T_2 T_4 + \right. \\ \left. q_{33} T_3^2 + 2q_{34} T_3 T_4 + q_{44} T_4^2 \right] \end{aligned} \quad (280)$$

Taking the partial derivative of ϕ_a with respect to \dot{x} gives:

$$\begin{aligned}
\frac{\partial \phi_a}{\partial \dot{x}} = & k_a \left[q_{11} T_1 \frac{\partial T_1}{\partial \dot{x}} + q_{12} \left(T_2 \frac{\partial T_1}{\partial \dot{x}} + T_1 \frac{\partial T_2}{\partial \dot{x}} \right) + q_{13} \left(T_3 \frac{\partial T_1}{\partial \dot{x}} + T_1 \frac{\partial T_3}{\partial \dot{x}} \right) + \right. \\
& q_{14} \left(T_4 \frac{\partial T_1}{\partial \dot{x}} + T_1 \frac{\partial T_4}{\partial \dot{x}} \right) + q_{22} T_2 \frac{\partial T_2}{\partial \dot{x}} + q_{23} \left(T_3 \frac{\partial T_2}{\partial \dot{x}} + T_2 \frac{\partial T_3}{\partial \dot{x}} \right) + \\
& \left. q_{24} \left(T_4 \frac{\partial T_2}{\partial \dot{x}} + T_2 \frac{\partial T_4}{\partial \dot{x}} \right) + q_{33} T_3 \frac{\partial T_3}{\partial \dot{x}} + q_{34} \left(T_4 \frac{\partial T_3}{\partial \dot{x}} + T_3 \frac{\partial T_4}{\partial \dot{x}} \right) + q_{44} T_4 \frac{\partial T_4}{\partial \dot{x}} \right]
\end{aligned} \tag{281}$$

Taking the partial derivative of ϕ_a with respect to \dot{y} gives:

$$\begin{aligned}
\frac{\partial \phi_a}{\partial \dot{y}} = & k_a \left[q_{11} T_1 \frac{\partial T_1}{\partial \dot{y}} + q_{12} \left(T_2 \frac{\partial T_1}{\partial \dot{y}} + T_1 \frac{\partial T_2}{\partial \dot{y}} \right) + q_{13} \left(T_3 \frac{\partial T_1}{\partial \dot{y}} + T_1 \frac{\partial T_3}{\partial \dot{y}} \right) + \right. \\
& q_{14} \left(T_4 \frac{\partial T_1}{\partial \dot{y}} + T_1 \frac{\partial T_4}{\partial \dot{y}} \right) + q_{22} T_2 \frac{\partial T_2}{\partial \dot{y}} + q_{23} \left(T_3 \frac{\partial T_2}{\partial \dot{y}} + T_2 \frac{\partial T_3}{\partial \dot{y}} \right) + \\
& \left. q_{24} \left(T_4 \frac{\partial T_2}{\partial \dot{y}} + T_2 \frac{\partial T_4}{\partial \dot{y}} \right) + q_{33} T_3 \frac{\partial T_3}{\partial \dot{y}} + q_{34} \left(T_4 \frac{\partial T_3}{\partial \dot{y}} + T_3 \frac{\partial T_4}{\partial \dot{y}} \right) + q_{44} T_4 \frac{\partial T_4}{\partial \dot{y}} \right]
\end{aligned} \tag{282}$$

Taking the partial derivative of ϕ_a with respect to \dot{z} gives:

$$\begin{aligned}
\frac{\partial \phi_a}{\partial \dot{z}} = & k_a \left[q_{11} T_1 \frac{\partial T_1}{\partial \dot{z}} + q_{12} \left(T_2 \frac{\partial T_1}{\partial \dot{z}} + T_1 \frac{\partial T_2}{\partial \dot{z}} \right) + q_{13} \left(T_3 \frac{\partial T_1}{\partial \dot{z}} + T_1 \frac{\partial T_3}{\partial \dot{z}} \right) + \right. \\
& q_{14} \left(T_4 \frac{\partial T_1}{\partial \dot{z}} + T_1 \frac{\partial T_4}{\partial \dot{z}} \right) + q_{22} T_2 \frac{\partial T_2}{\partial \dot{z}} + q_{23} \left(T_3 \frac{\partial T_2}{\partial \dot{z}} + T_2 \frac{\partial T_3}{\partial \dot{z}} \right) + \\
& \left. q_{24} \left(T_4 \frac{\partial T_2}{\partial \dot{z}} + T_2 \frac{\partial T_4}{\partial \dot{z}} \right) + q_{33} T_3 \frac{\partial T_3}{\partial \dot{z}} + q_{34} \left(T_4 \frac{\partial T_3}{\partial \dot{z}} + T_3 \frac{\partial T_4}{\partial \dot{z}} \right) + q_{44} T_4 \frac{\partial T_4}{\partial \dot{z}} \right]
\end{aligned} \tag{283}$$

Evaluating the partial derivatives of the components of the \bar{T} vector with respect to each component of the relative velocity gives:

$$\frac{\partial T_1}{\partial \dot{x}} = 0 \tag{284}$$

$$\frac{\partial T_1}{\partial \dot{y}} = \frac{2}{n} \tag{285}$$

$$\frac{\partial T_1}{\partial \dot{z}} = 0 \tag{286}$$

$$\frac{\partial T_2}{\partial \dot{x}} = -\frac{2}{n} \tag{287}$$

$$\frac{\partial T_2}{\partial \dot{y}} = 0 \tag{288}$$

$$\frac{\partial T_2}{\partial \dot{z}} = 0 \tag{289}$$

$$\frac{\partial T_3}{\partial \dot{x}} = \frac{4\dot{x}/n}{\left[\left(6x + \frac{4\dot{y}}{n} \right)^2 + \left(\frac{2\dot{x}}{n} \right)^2 \right]^{1/2}} \quad (290)$$

$$\frac{\partial T_3}{\partial \dot{y}} = \frac{24x + 16\dot{y}/n}{n \left[\left(6x + \frac{4\dot{y}}{n} \right)^2 + \left(\frac{2\dot{x}}{n} \right)^2 \right]^{1/2}} \quad (291)$$

$$\frac{\partial T_3}{\partial \dot{z}} = 0 \quad (292)$$

$$\frac{\partial T_4}{\partial \dot{x}} = 0 \quad (293)$$

$$\frac{\partial T_4}{\partial \dot{y}} = 0 \quad (294)$$

$$\frac{\partial T_4}{\partial \dot{z}} = \frac{\dot{z}/n}{\left[z^2 + \left(\frac{\dot{z}}{n} \right)^2 \right]^{1/2}} \quad (295)$$

The gradient of the potential function with respect to the relative velocity vector is given by:

$$\nabla_{\rho} \phi_a = \begin{bmatrix} \frac{\partial \phi_a}{\partial \dot{x}} \\ \frac{\partial \phi_a}{\partial \dot{y}} \\ \frac{\partial \phi_a}{\partial \dot{z}} \end{bmatrix} \quad (296)$$

The total derivative of the potential function in Eq. (280) is:

$$\begin{aligned}
\dot{\phi}_a = k_a & \left[q_{11}T_1\dot{T}_1 + q_{12}(\dot{T}_1T_2 + T_1\dot{T}_2) + q_{13}(\dot{T}_1T_3 + T_1\dot{T}_3) + q_{14}(\dot{T}_1T_4 + T_1\dot{T}_4) + \right. \\
& q_{22}T_2\dot{T}_2 + q_{23}(\dot{T}_2T_3 + T_2\dot{T}_3) + q_{24}(\dot{T}_2T_4 + T_2\dot{T}_4) + q_{33}T_3\dot{T}_3 + \\
& \left. q_{34}(\dot{T}_3T_4 + T_3\dot{T}_4) + q_{44}T_4\dot{T}_4 \right] \tag{297}
\end{aligned}$$

The time derivatives of the \bar{T} vector components are:

$$\dot{T}_1 = 0 \tag{298}$$

$$\dot{T}_2 = -3\dot{y} - 6nx \tag{299}$$

$$\dot{T}_3 = 0 \tag{300}$$

$$\dot{T}_4 = 0 \tag{301}$$

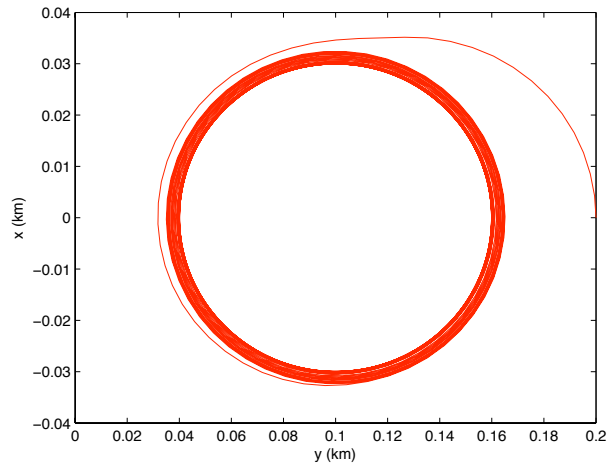
For unforced motion, only the y_r element of the error matrix, T_2 , is changing with time. Tables 7, 8, and 13 may be utilized to determine the locations in the relative orbit where an impulsive maneuver may drive the ROEs in the direction of the target values.

An example of the simultaneous targeting of x_r , y_r , a_r , and A_z is summarized in Table 30. At $t = 0$, the deputy is at a position 200 m ahead of the chief in the along-track direction, with an initial velocity of 0.020 m/s in the radial direction, and 0.020 m/s in the cross-track direction. The target conditions are expressed in terms of ROEs as $x_r = 0$, $y_r = 100$ m, $a_r = 60$ m, and $A_z = 20$ m.

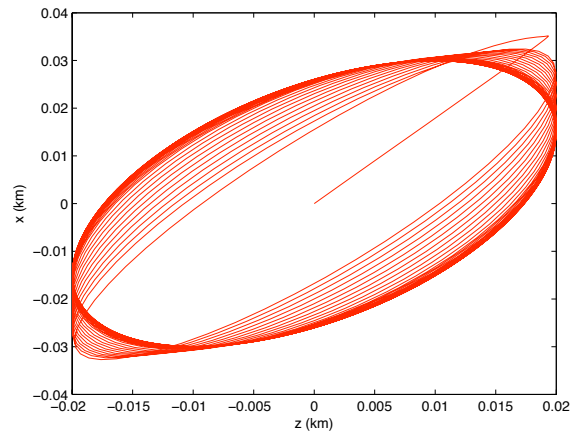
Table 30: APF control example, targeting ROEs x_r, y_r, a_r, A_z .

Initial Conditions	Cartesian	$x = 0.000 \text{ km}$ $\dot{x} = 2E - 05 \text{ km/s}$ $y = 0.200 \text{ km}$ $\dot{y} = 0 \text{ km/s}$ $z = 0.000 \text{ km}$ $\dot{z} = 2E - 05 \text{ km/s}$
	ROEs	$x_r = 0.0000 \text{ km}$ $E_r = 1.5707 \text{ rad}$ $y_r = 0.1621 \text{ km}$ $A_z = 0.0189 \text{ km}$ $a_r = 0.0379 \text{ km}$ $\psi = 0.0000 \text{ rad}$
Target ROEs		$x_r = 0.0000 \text{ km}$ $y_r = 0.1000 \text{ km}$ $a_r = 0.0600 \text{ km}$ $A_z = 0.0200 \text{ km}$
APF Parameters		$k_a = 1E - 07$ $\bar{\bar{Q}}_a = \bar{\bar{I}}_{4 \times 4}$

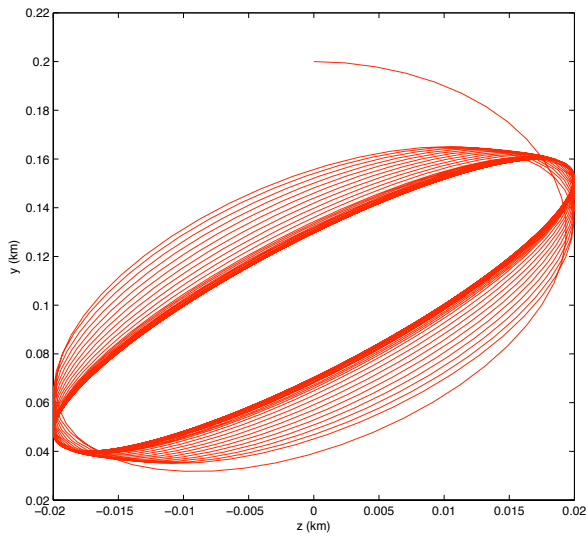
The resulting trajectory is shown in Figure 32. For this example, the trajectory is propagated for 250,000 s. At the completion of that time period, the following ROEs have been reached: $x_r = -0.001 \text{ m}$, $y_r = 100.001 \text{ m}$, $a_r = 60.005 \text{ m}$, $A_z = 20.000 \text{ m}$. The time histories of the ROEs x_d, y_d, a_r, A_z are shown in Figure 33. Maneuver components as a function of time are shown in Figure 34. The total ΔV expended for trajectory control during the simulation is 0.045 m/s.



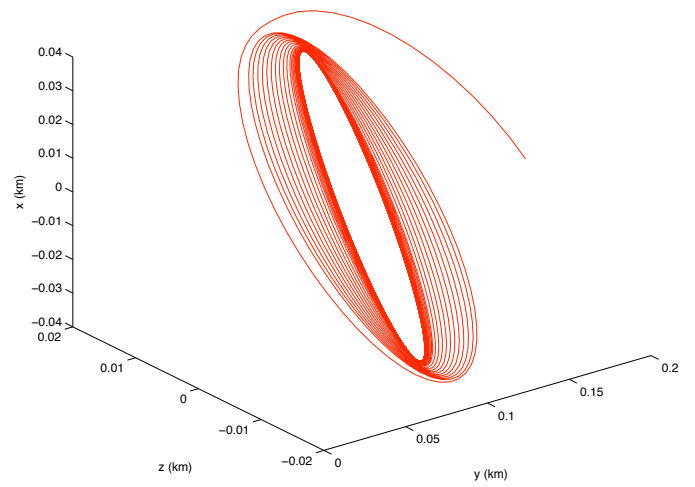
(a)



(b)

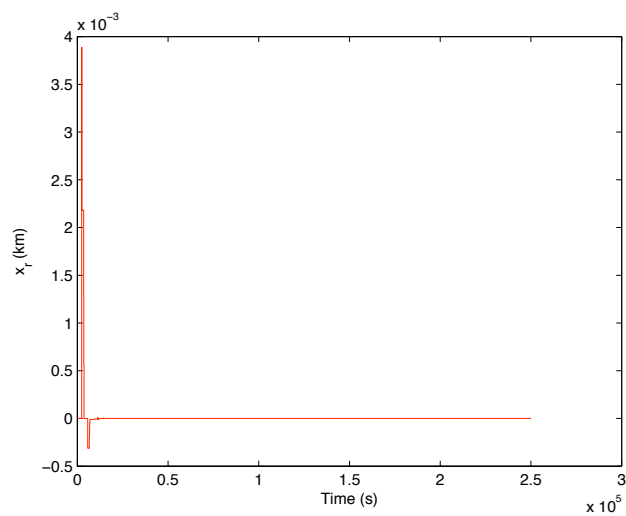


(c)

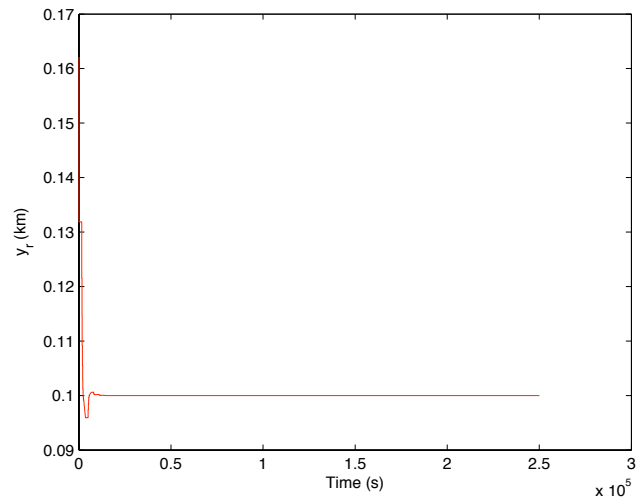


(d)

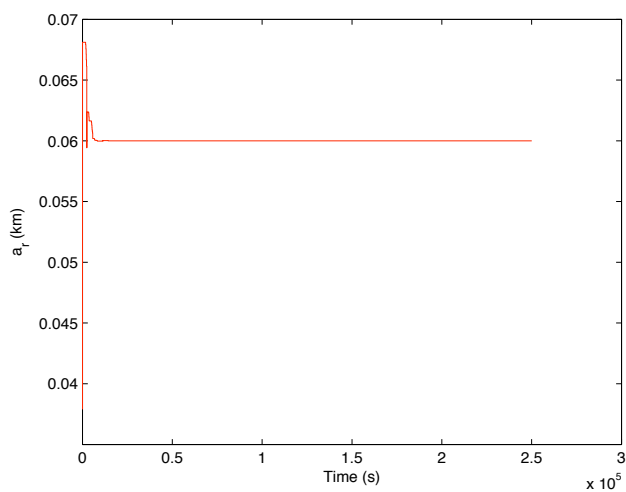
Figure 32: APF targeting of ROEs x_d , y_d , a_r , and A_z , 250,000 sec propagation. (a) $\hat{y} - \hat{x}$ projection, (b) $\hat{z} - \hat{x}$ projection, (c) $\hat{z} - \hat{y}$ projection, (d) 3D trajectory plot.



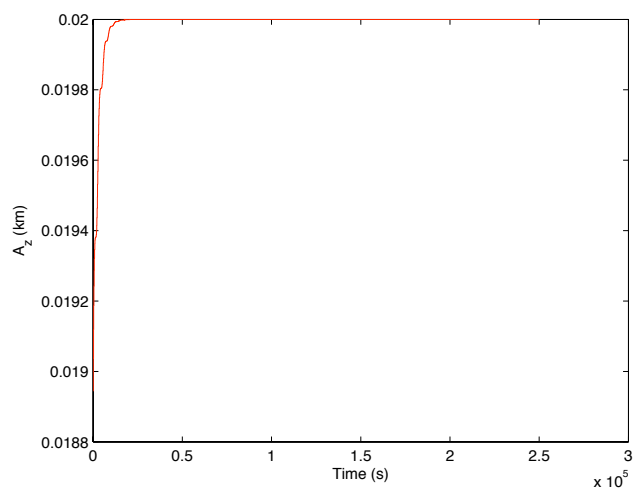
(a)



(b)



(c)



(d)

Figure 33: APF targeting of ROEs x_d , y_d , a_r , and A_z , 25,000 sec propagation. (a) x_r time history, (b) y_r time history, (c) a_r time history, (d) A_z time history.

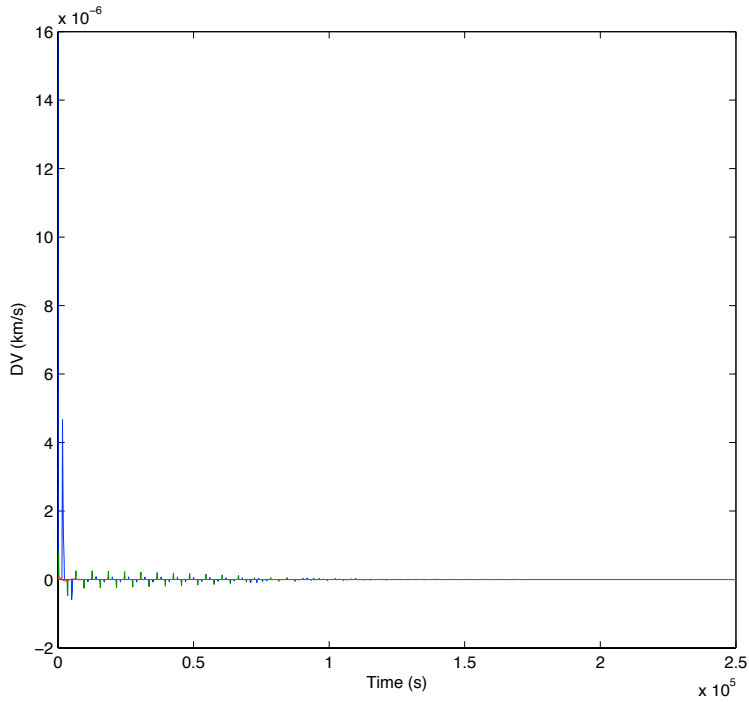


Figure 34: Maneuver components as a function of time for APF targeting of ROEs x_d , y_d , a_r , and A_z . Blue: ΔV_x , Green: ΔV_y , Red: ΔV_z .

3.2.6 Combining Attractive and Repulsive Potentials

The ROE-based approach utilizing APFs allows the targeting of a desired relative orbit. Repulsive potentials are established for obstacle avoidance, where obstacles are defined at fixed relative positions in the LVLH coordinate system. Combination of the attractive ROE targeting with repulsive obstacle avoidance will therefore utilize the attractive potentials described above in Section 3.2, along with the repulsive potentials as described in Section 3.1. However, there is a difference between the maneuver calculations for ROE targeting using an attractive APF and repulsive maneuvers for obstacle avoidance. The attractive maneuvers are based upon the negative gradient of the attractive potential function taken with respect to the relative velocity vector. Repulsive

maneuvers are defined such that the post-maneuver velocity vector is in the direction of the negative gradient of the repulsive potential taken with respect to the relative position vector. We cannot simply superpose the attractive and repulsive potentials and take the gradient as was done in Section 3.1. Alternatively, the attractive and repulsive maneuvers will be calculated separately at each time step, and combined to give a total maneuver that is responsive to both the attractive and repulsive potentials. In addition, a new parameter, r_{obs_soi} , is defined that limits the sphere of influence of the repulsive potential; when the distance between the obstacle and the chaser spacecraft is greater than r_{obs_soi} , the repulsive maneuver is set equal to zero.

The formulation for the combined attractive and repulsive potentials is summarized as follows. The attractive artificial potential function is defined in Eq. (233) as:

$$\phi_a = \frac{1}{2} k_a (\bar{\tau} - \bar{\tau}_{tgt})^T \bar{Q}_a (\bar{\tau} - \bar{\tau}_{tgt}) \quad (302)$$

The attractive control equation is defined in Eq. (236) as:

$$\Delta \bar{V}_a = -\nabla_{\rho} \phi_a \quad (303)$$

The attractive control action is initiated based upon the maneuver constraints shown in Tables 7, 8, and 13, so that an attractive maneuver is implemented only when a maneuver exists that can drive each of the ROEs contained within the target vector toward their targeted values.

The repulsive potential is defined in Eq. (220) as:

$$\phi_r = k_r \exp \left[-\frac{(\bar{\rho} - \bar{\rho}_{obs})^T \bar{Q}_r (\bar{\rho} - \bar{\rho}_{obs})}{\sigma} \right] \quad (304)$$

The repulsive control action is initiated whenever the repulsive potential is increasing and the deputy is within the obstacle sphere of influence. The repulsive control action is expressed as:

$$\Delta \bar{V}_r = \begin{cases} 0 & , \phi_r \leq 0 \text{ or } |\bar{\rho} - \bar{\rho}_{obs}| > r_{obs_soi} \\ -\nabla_{\rho} \phi_r - \dot{\bar{\rho}} & , \phi_r > 0 \text{ and } |\bar{\rho} - \bar{\rho}_{obs}| \leq r_{obs_soi} \end{cases} \quad (305)$$

The total maneuver is calculated at each time step as:

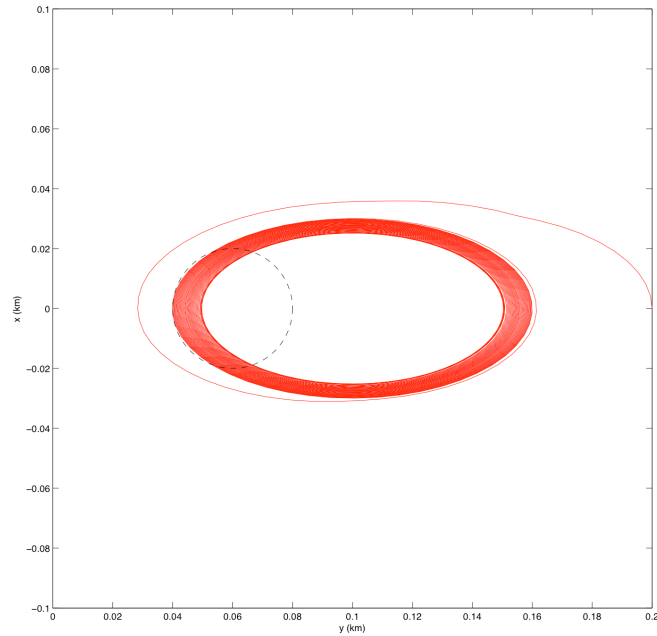
$$\Delta \bar{V}_{TOTAL} = \Delta \bar{V}_a + \Delta \bar{V}_r \quad (306)$$

An example is now considered with the addition of an obstacle and repulsive potential, as described in Table 31. The initial conditions in the $\hat{x} - \hat{y}$ plane are the same as in the previous example, however in this case there is no cross-track motion in order to simplify visualization. The target ROE conditions are unchanged from the previous example. An obstacle is placed at $[x, y, z] = [0, 0.060, 0]$ km, with a sphere of influence of 0.020 km. This is a challenging case, because the targeted ROEs will result in motion that passes through the obstacle position every orbit. The trajectory acting only under the attractive potential is shown in Figure 35(a); the obstacle sphere of influence is shown only for reference. The trajectory including both attractive and repulsive potentials is shown in Figure 35(b). It is seen that when the deputy enters the obstacle sphere of influence, the repulsive potential diverts the trajectory away from the obstacle. Outside of the obstacle sphere of influence, the attractive potential shapes the orbit to the desired

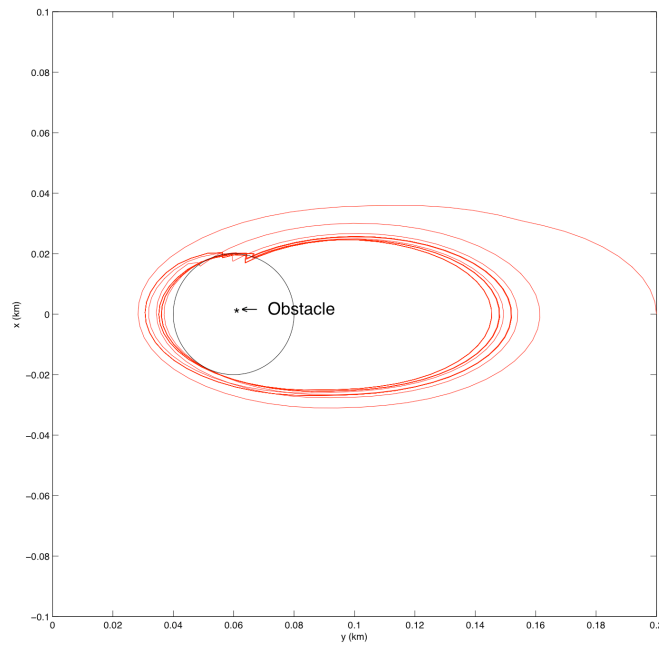
parameters. The time histories of the targeted ROEs are shown in Figure 36. The perturbation of the obstacle to the trajectory prevents the APF guidance from converging to the targeted value of a_r , however, the trajectory converges to the ROE condition $[x_r, y_r, a_r] = [0, 0.100, 0.070]$ km. With these ROE values, the relative orbit is centered on the desired x_r and y_r coordinates, and the converged value of a_r is such that the orbit passes at the boundary of the obstacle sphere of influence. Figure 36 shows the attractive and repulsive maneuver magnitudes as a function of time. This example has high ΔV utilization due to the placement of the obstacle in the nominal orbital path. As shown in Figure 37, when repulsive maneuvers are performed for obstacle avoidance, subsequent attractive maneuvers are performed to correct the trajectory toward the desired ROEs. Overall, the attractive ΔV utilized is 3.43 m/s, the repulsive ΔV is 2.43 m/s, and the total ΔV is 5.86 m/s. A closer look at the effect of the repulsive maneuvers is provided in Figure 37. Figure 38(a) shows the deputy's distance from the obstacle as a function of time when no repulsive maneuvers are performed. Figure 38(b) shows the trajectory once the repulsive maneuvers are enabled. In this case, the repulsive maneuvers shape the trajectory to avoid the obstacle sphere of influence of 20 m.

Table 31: APF control example, targeting ROEs x_r, y_r, a_r, A_z with repulsive obstacle.

Initial Conditions	Cartesian	$x = 0.000 \text{ km}$ $\dot{x} = 2E - 05 \text{ km/s}$ $y = 0.200 \text{ km}$ $\dot{y} = 0 \text{ km/s}$ $z = 0.000 \text{ km}$ $\dot{z} = 0 \text{ km/s}$
	ROEs	$x_r = 0.0000 \text{ km}$ $E_r = 1.5707 \text{ rad}$ $y_r = 0.1621 \text{ km}$ $A_z = 0.0000 \text{ rad}$ $a_r = 0.0379 \text{ km}$ $\psi = 0.0000 \text{ rad}$
Target ROEs		$x_r = 0.0000 \text{ km}$ $y_r = 0.1000 \text{ km}$ $a_r = 0.0500 \text{ km}$ $A_z = 0.0000 \text{ km}$
Obstacle Location		$x = 0.000 \text{ km}$ $y = 0.060 \text{ km}$ $z = 0.000 \text{ km}$
APF Parameters		$k_a = 1E - 07$ $\bar{\bar{Q}}_a = \bar{\bar{I}}_{4 \times 4}$ $k_r = 1E - 06$ $\bar{\bar{Q}}_r = \bar{\bar{I}}_{3 \times 3}$ $\sigma = 1E - 04$ $r_{obs_soi} = 0.020 \text{ km}$

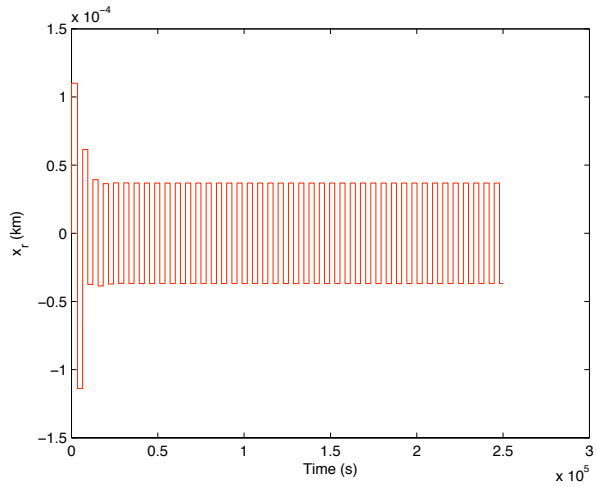


(a)

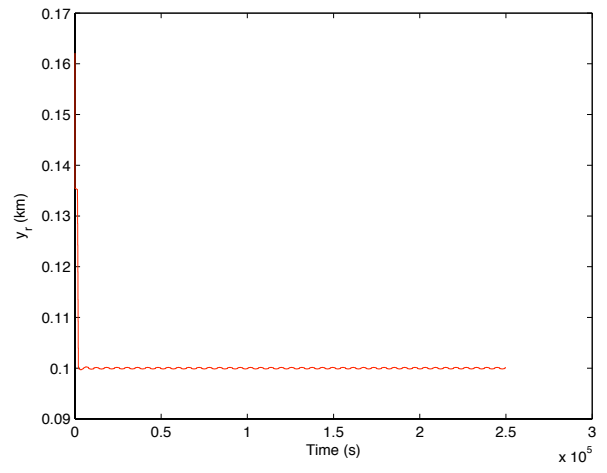


(b)

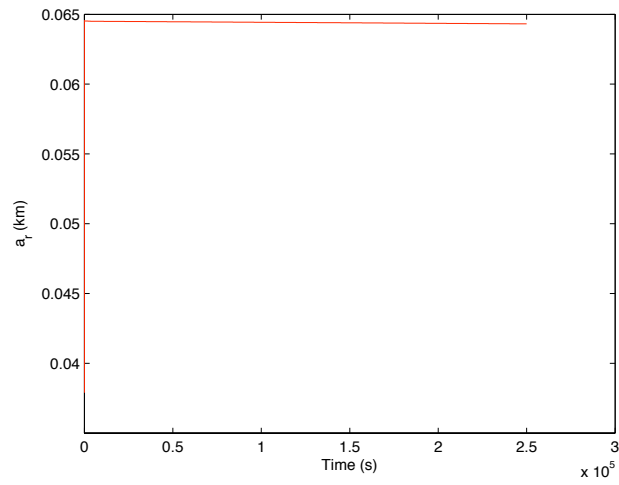
Figure 35: APF targeting of ROEs x_r, y_r , and a_r , 250,000 sec propagation, (a) Trajectory with no obstacle, attractive potential only, $\hat{y} - \hat{x}$ projection, (b) Trajectory with obstacle, attractive and repulsive potentials, $\hat{y} - \hat{x}$ projection.



(a)



(b)



(c)

Figure 36: APF targeting of ROEs x_d , y_d , and a_r , with obstacle, 250,000 sec propagation.

(a) x_r time history, (b) y_r time history, (c) a_r time history.

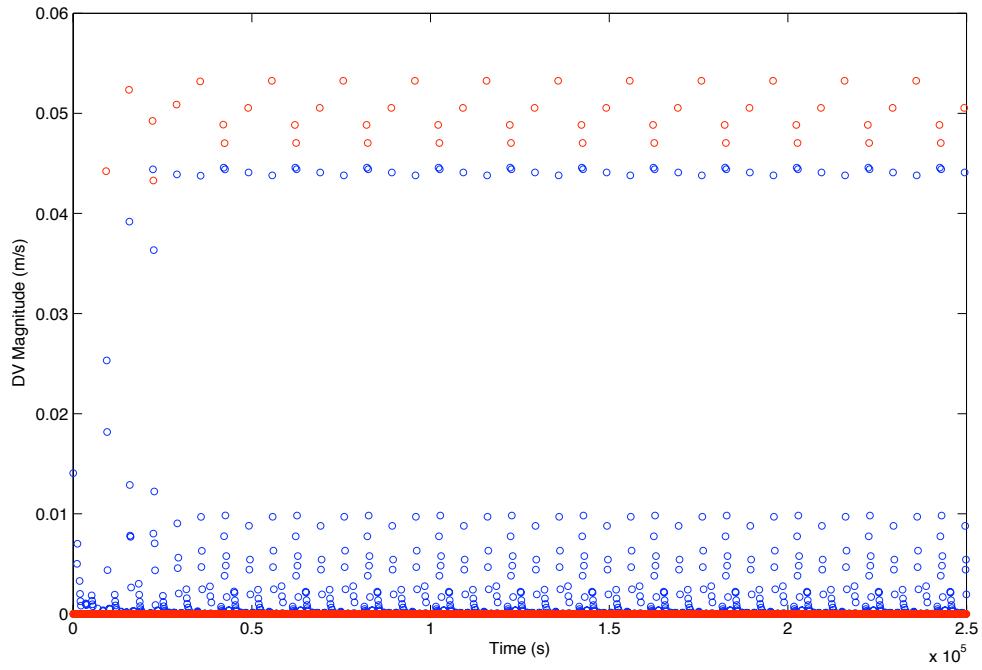
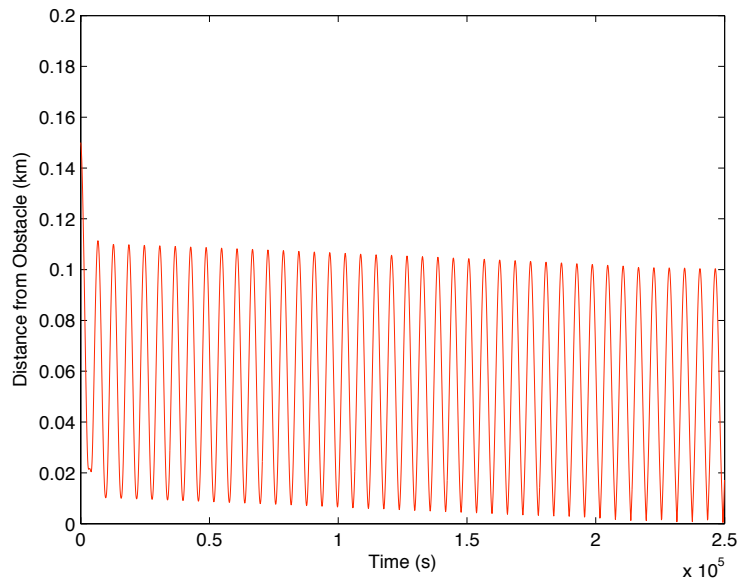
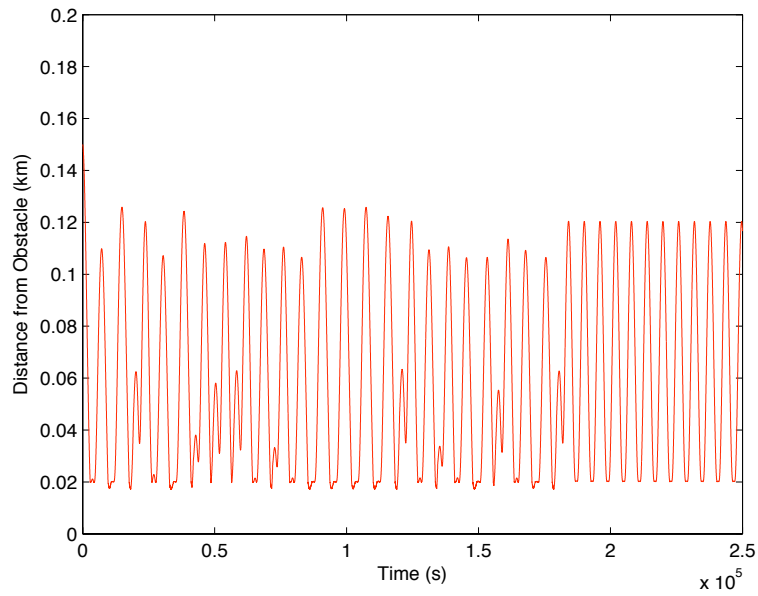


Figure 37: Maneuver magnitudes for attractive ROE targeting (blue) and repulsive obstacle avoidance (red).



(a)



(b)

Figure 38: The effect of repulsive maneuvers is to shape the trajectory to avoid the obstacle sphere of influence. (a) No repulsive maneuvers performed, (b) Repulsive maneuvers performed in response to 20 m obstacle sphere of influence.

3.2.7 Monte Carlo Analysis

Monte Carlo analyses were performed in order to evaluate the reliability of the APF algorithms in converging to the targeted ROE values, and to characterize the ΔV utilization of the ROE-based APF approach versus traditional maneuver design methods. The first scenario evaluates the convergence and ΔV utilization of an attractive APF without obstacles, and the second scenario evaluates the convergence of an attractive APF combined with a repulsive APF associated with a single obstacle. In each scenario, the algorithms resulted in consistent convergence to the targeted ROE values.

Attractive Artificial Potential Function without Obstacles

A 500-case Monte Carlo analysis was performed, targeting the ROE parameters x_r , y_r , a_r , and A_z . The parameters for the Monte Carlo analysis are summarized in Table 32. The initial conditions for the relative Cartesian state were randomly generated, and the resulting initial relative Cartesian states are shown graphically in Figure 39. The minimum and maximum initial values for the ROEs corresponding to the randomly generated population of relative Cartesian states are shown in Table 33, for reference. The ROE target conditions for y_r , a_r , and A_z were randomly generated based upon uniform distributions, however, a fixed value of $x_r = 0$ was targeted in each case.

In each case, the simulation was run for 1E06 s, and the final ROEs were compared to the targeted values. The results are shown in Table 34. A single parameter representing the root-sum-squared (RSS) of the distance of the four final ROE values relative to their targets was calculated as the metric for convergence. A case was considered converged if the RSS distance from the target parameters was less than 1 m.

All 500 cases in the Monte Carlo simulation converged to the targets, based upon this criterion. The worst-case RSS distance was 0.036 m.

Table 32: Attractive APF Monte Carlo evaluation parameters.

Initial Conditions	Cartesian State Sampling Distributions	$x_0 = [-1,1]$ km, uniform $y_0 = [-1,1]$ km, uniform $z_0 = [-1,1]$ km, uniform $\dot{x}_0 = [-0.001,0.001]$ km/s, uniform $\dot{y}_0 = [-0.001,0.001]$ km/s, uniform $\dot{z}_0 = [-0.001,0.001]$ km/s, uniform
	ROE Ranges Resulting from Sampled Monte Carlo Cartesian States	$x_{r_0} = [-5.619,5.884]$ km $y_{r_0} = [-2.759,2.678]$ km $a_{r_0} = [0.200,9.770]$ km $E_{r_0} = [0.006,6.282]$ rad $A_{z_0} = [0.014,1.343]$ km $\psi_0 = [0.001,6.272]$ rad
Target ROEs		$x_r = 0.0000$ km $y_r = [-0.5,0.5]$ km, uniform $a_r = [0,1]$ km, uniform $A_z = [0,1]$ km, uniform
APF Parameters		$k_a = 1E - 07$ $\bar{\bar{Q}}_a = \bar{\bar{I}}_{4 \times 4}$

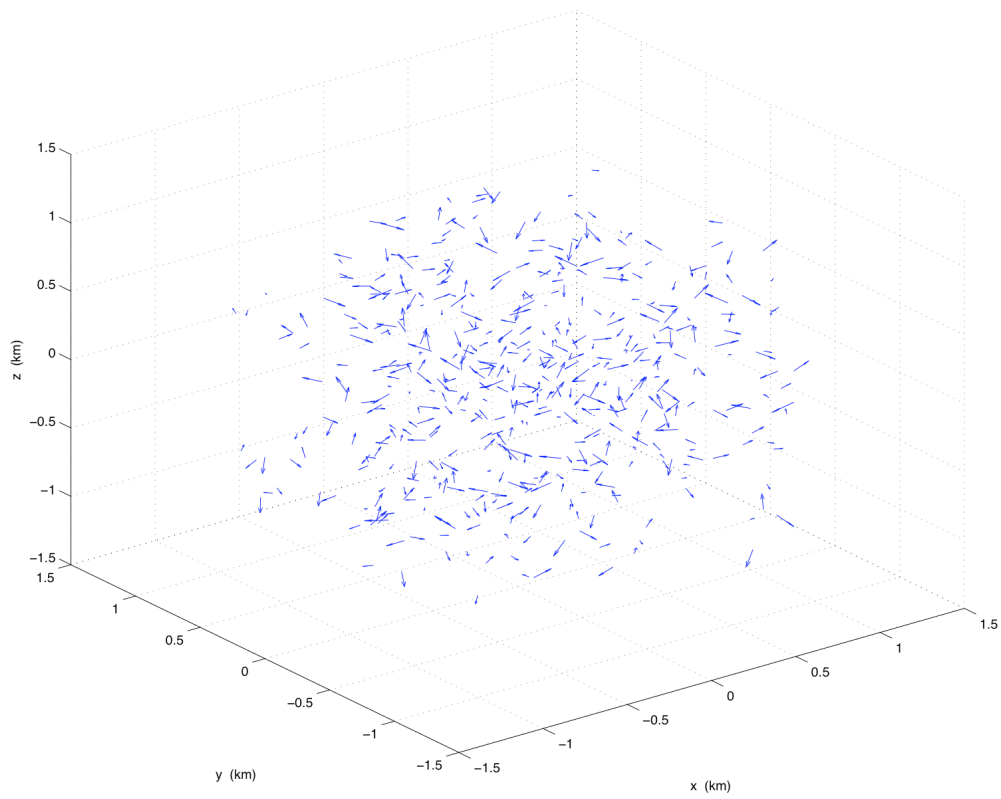


Figure 39: Attractive APF Monte Carlo simulation relative Cartesian state initial conditions.

Table 33: Attractive APF Monte Carlo results.

Final ROE State Relative to the Target	Minimum (km)	Maximum (km)	Average (km)	Standard Deviation (km)
$x_r - x_{r_{tgt}}$	-3.64E-08	1.07E-06	2.28E-09	4.80E-08
$y_r - y_{r_{tgt}}$	-1.14E-08	2.98E-08	-2.72E-09	5.13E-08
$a_r - a_{r_{tgt}}$	-8.14E-14	3.56E-05	8.10E-08	1.59E-06
$A_z - A_{z_{tgt}}$	-1.44E-15	-1.74E-18	-5.54E-16	3.40E-16
RSS	1.57E-16	3.56E-05	8.11E-08	1.59E-06

While there is no expectation of maneuver optimality within the APF approach, it is useful to compare the ΔV utilization resulting from the APFs formulation relative to the maneuver magnitudes calculated using a deterministic method for maneuver design. For this comparison, the state transition matrix (STM) that maps initial conditions to the final states using the solutions to the Clohessy-Wiltshire equations will be applied.

The position and velocity solutions to the Clohessy-Wiltshire equations, Eqs. (49) – (54), can be placed into the form:

$$\begin{bmatrix} \bar{\mathbf{r}} \\ \bar{\mathbf{v}} \end{bmatrix} = \begin{bmatrix} \phi_{rr} & \phi_{rv} \\ \phi_{vr} & \phi_{vv} \end{bmatrix} \begin{bmatrix} \bar{\mathbf{r}}_0 \\ \bar{\mathbf{v}}_0 \end{bmatrix} \quad (307)$$

where

$$\phi_{rr} = \begin{bmatrix} 4 - 3\cos[n(t-t_0)] & 0 & 0 \\ 6\{\sin[n(t-t_0)] - n(t-t_0)\} & 1 & 0 \\ 0 & 0 & \cos[n(t-t_0)] \end{bmatrix} \quad (308)$$

$$\phi_{rv} = \begin{bmatrix} \frac{1}{n}\sin[n(t-t_0)] & \frac{2}{n}\{1 - \cos[n(t-t_0)]\} & 0 \\ \frac{2}{n}\{\cos[n(t-t_0)] - 1\} & \frac{4}{n}\{\sin[n(t-t_0)] - 3(t-t_0)\} & 0 \\ 0 & 0 & \frac{1}{n}\sin[n(t-t_0)] \end{bmatrix} \quad (309)$$

$$\phi_{vr} = \begin{bmatrix} 3n\sin[n(t-t_0)] & 0 & 0 \\ 6n\{\cos[n(t-t_0)] - 1\} & 0 & 0 \\ 0 & 0 & -n\sin[n(t-t_0)] \end{bmatrix} \quad (310)$$

$$\phi_{vv} = \begin{bmatrix} \cos[n(t-t_0)] & 2\sin[n(t-t_0)] & 0 \\ -2\sin[n(t-t_0)] & 4\cos[n(t-t_0)]-3 & 0 \\ 0 & 0 & \cos[n(t-t_0)] \end{bmatrix} \quad (311)$$

For each case in the Monte Carlo simulation, the STM may be utilized to calculate the two-impulse ΔV required to transfer from the randomly dispersed initial LVLH Cartesian state, $\begin{bmatrix} \bar{\mathbf{r}}_i & \bar{\mathbf{v}}_i \end{bmatrix}^T$ to the final converged state resulting from the APF trajectory simulation $\begin{bmatrix} \bar{\mathbf{r}}_f & \bar{\mathbf{v}}_f \end{bmatrix}^T$. Note that the final converged state corresponds to the ROE targets. From Eq. (307),

$$\bar{\mathbf{v}}_0 = \phi_{rv}^{-1}(\bar{\mathbf{r}} - \phi_{rr}\bar{\mathbf{r}}_0) \quad (312)$$

In this scenario, $\bar{\mathbf{r}}_0$ is the initial position equal to $\bar{\mathbf{r}}_i$, $\bar{\mathbf{r}}$ represents the final converged relative position vector equal to $\bar{\mathbf{r}}_f$, and $\bar{\mathbf{v}}_0$ is the velocity vector that targets the final position vector $\bar{\mathbf{r}}_f$ with a time-of-flight given by $t - t_0$. The first maneuver vector, $\Delta\bar{\mathbf{V}}_1$, is calculated as the difference between $\bar{\mathbf{v}}_0$ and the initial velocity vector $\bar{\mathbf{v}}_i$:

$$\Delta\bar{\mathbf{V}}_1 = \bar{\mathbf{v}}_0 - \bar{\mathbf{v}}_i \quad (313)$$

The second maneuver vector represents the impulse required to match the final velocity $\bar{\mathbf{v}}_f$ at the final position, $\bar{\mathbf{r}}_f$:

$$\Delta\bar{\mathbf{V}}_2 = \bar{\mathbf{v}}_f - \bar{\mathbf{v}} \quad (314)$$

The total ΔV utilized in the two-impulse sequence is given by:

$$\Delta\bar{V}_{TOT} = |\Delta\bar{V}_1| + |\Delta\bar{V}_2| \quad (315)$$

The maneuver vectors calculated using the STM approach depend upon the time-of-flight, $t - t_0$. For this analysis, the time-of-flight was varied from 100 to 100,000 s in 100 s time steps, and the time-of-flight was found which minimized \bar{V}_{TOT} for that case.

A comparison of the ΔV utilization from the APF formulation with the two-impulse state transition matrix approach is shown in Table 34. It is seen that, on average, the APF approach results in ΔV utilization that is 50% greater than the two-impulse STM approach, and the APF ΔV standard deviation is significantly greater. This is not unexpected, since the STM approach incorporates an optimization of the transfer time-of-flight to minimize the total ΔV expended. However, it is noted that in some cases the APF ΔV utilization was less than that for the corresponding two-impulse STM solution. It is possible that with additional tuning the APF ΔV utilization could be significantly reduced. Future work regarding the optimization of ΔV utilization is discussed in Section 5.2.

Table 34: Comparison of ΔV utilization between the APF formulation and the two-impulse STM approach.

ΔV Utilization	ROE-Based APF	Two-Impulse STM
Minimum (m/s)	0.554	1.016
Maximum (m/s)	23.689	9.425
Mean (m/s)	5.346	3.547
Standard Deviation (m/s)	4.060	1.461

Attractive Artificial Potential Function Combined with a Single Obstacle

Using the approach described in Section 3.2.6, a 500-case Monte Carlo analysis was performed for a scenario involving a transfer to a specified leading orbit, with an

obstacle at the origin. The parameters for the Monte Carlo analysis are summarized in Table 35. The initial conditions for the relative Cartesian state were randomly generated, using a uniform distribution about the nominal state of $[x, y, z] = [0, 0.2, 0]$ km, $[\dot{x}, \dot{y}, \dot{z}] = [0, 0, 0]$ km/s. The resulting initial relative Cartesian states are shown graphically in Figure 40. The minimum and maximum initial values for the ROEs corresponding to the randomly generated population of relative Cartesian states are shown in Table 36, and the ROE target conditions were fixed at $x_r = 0$, $y_r = 0.1$ km, $a_r = 0$, and $A_z = 0$. The sphere of influence about the obstacle at the origin was fixed at 0.020 km.

In each case, the simulation was run for 1E06 s, and the final ROEs were compared to the targeted values. The results are shown in Table 36. Of the 500 total cases, 151 cases entered the obstacle sphere of influence, resulting in repulsive maneuvers being performed. As before, the RSS convergence criterion of 1 m was evaluated. All 500 cases in the Monte Carlo simulation converged to the targets. The worst-case RSS distance was 6.2E-05 m. Attractive ΔV expended in each case ranged from 0.120 m/s to 10.581 m/s, and repulsive ΔV ranged from 0 to 1.705 m/s.

Table 35: Attractive APF with obstacle Monte Carlo evaluation parameters.

Initial Conditions	Cartesian State Sampling Distributions	$x_0 = [-0.002, 0.002]$ km, uniform $y_0 = [0.198, 0.202]$ km, uniform $z_0 = [-0.002, 0.002]$ km, uniform $\dot{x}_0 = [-0.0001, 0.0001]$ km/s, uniform $\dot{y}_0 = [-0.0001, 0.0001]$ km/s, uniform $\dot{z}_0 = [-0.0001, 0.0001]$ km/s, uniform
	ROE Ranges Resulting from Sampled Monte Carlo Cartesian States	$x_{r_0} = [-0.192, 0.194]$ km $y_{r_0} = [0.014, 0.389]$ km $a_{r_0} = [0.019, 0.427]$ km $E_{r_0} = [0.016, 6.273]$ rad $A_{z_0} = [0.000, 0.094]$ km $\psi_0 = [0.000, 6.283]$ rad
Target ROEs		$x_r = 0.0000$ km $y_r = 0.100$ km $a_r = 0.000$ km $A_z = 0.000$ km
APF Parameters		$k_a = 1E - 07$ $\bar{\bar{Q}}_a = \bar{\bar{I}}_{4 \times 4}$ $k_r = 1E - 06$ $\bar{\bar{Q}}_r = \bar{\bar{I}}_{3 \times 3}$ $\sigma = 1E - 04$ $r_{obs_soi} = 0.020$ km

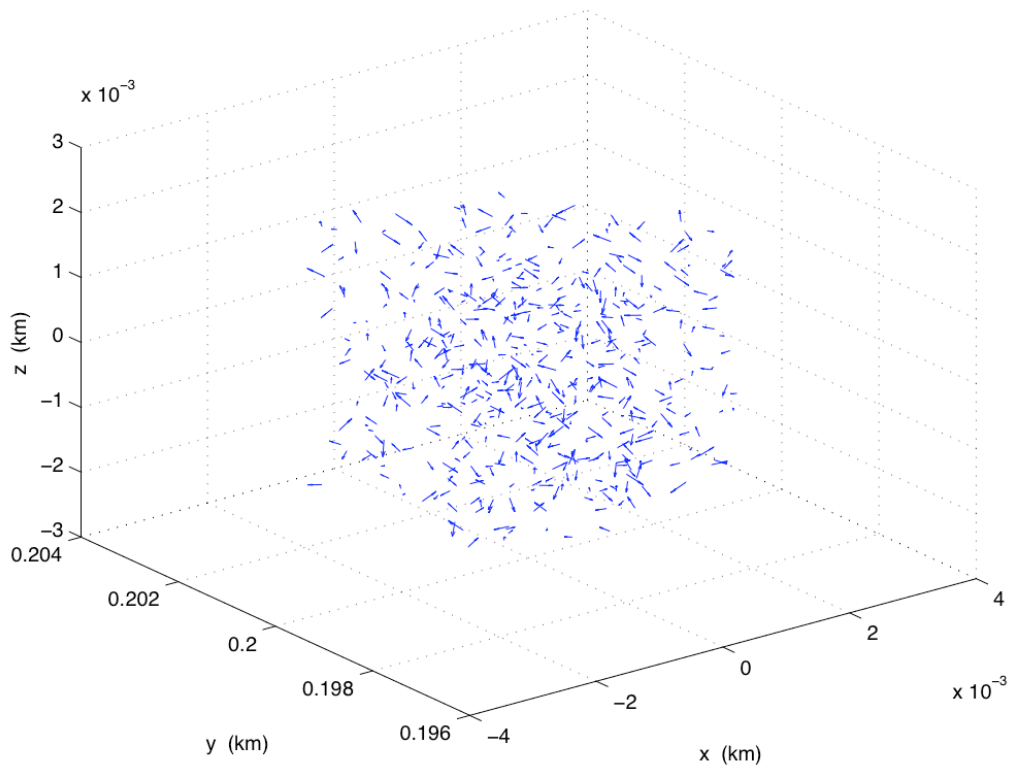


Figure 40: Attractive APF with obstacle Monte Carlo simulation relative Cartesian state initial conditions.

Table 36: Attractive APF with obstacle Monte Carlo results.

Final ROE State Relative to the Target	Minimum (km)	Maximum (km)	Average (km)	Standard Deviation (km)
$x_r - x_{r_{tgt}}$	-3.52E-09	1.10E-09	-1.04E-11	2.00E-10
$y_r - y_{r_{tgt}}$	-6.30E-09	2.14E-09	-2.86E-12	3.34E-10
$a_r - a_{r_{tgt}}$	7.06E-14	6.20E-08	5.36E-10	3.14E-09
$A_z - A_{z_{tgt}}$	1.89E-89	6.48E-83	1.34E-85	2.89E-84
RSS	7.97E-14	6.24E-08	5.43E-10	3.16E-09

CHAPTER 4

AUTOMATED TRAJECTORY CONTROL IN A SIMULATED ENVIRONMENT

In Chapters 2 and 3, trajectory control approaches using relative orbital elements and artificial potential functions are demonstrated within the context of the Clohessy-Wiltshire assumptions, where both the chief and deputy spacecraft orbit in two-body motion about the central body, both spacecraft are treated as point masses, the distance from the chief to deputy is much less than the chief orbit radius, and all perturbations such as third-body effects, drag, and solar radiation pressure are neglected. In this chapter, the performance of the trajectory control algorithms are evaluated within the framework of a flight-like six-degree-of-freedom (6-DOF) guidance, navigation and control (GN&C) simulation environment. The capabilities of the trajectory control algorithms to target the specified relative orbit geometries in the presence of environmental perturbations are assessed. Five scenarios are evaluated: ROE station-keeping; ROE orbit transfer; ROE orbit transfer with APF-based obstacle avoidance; APF targeting of ROEs; and APF targeting of ROEs with obstacle avoidance.

4.1 Guidance, Navigation and Control Six-Degree of Freedom Simulation Environment

The 6-DOF GN&C MATLAB/Simulink simulation framework established for Prox-1 flight software validation [69, 70] is utilized as a realistic test environment for the ROE and APF algorithms developed through this work. As shown in Figure 40, the GN&C simulation includes environmental models for the Sun, Earth and Moon locations, Earth's rotation, magnetic field dipole, Earth's atmosphere, and Earth gravitational field parameters, including the J_2 through J_6 spherical harmonics terms. Environmental

disturbances including third-body gravitational effects from the Sun and Moon, aerodynamic drag, solar radiation pressure, magnetic torque, gravity gradient torque, and higher-order Earth gravitational field are included. Inertial orbit states, attitude and attitude rates for both the chief and deputy are integrated throughout the simulation. Both spacecraft are treated as rigid bodies. Initial state and attitude parameters may be established via an initialization script, along with spacecraft mass properties. The guidance algorithms developed through this work are utilized to control orbital maneuvers by the deputy spacecraft. Finite burn effects are modeled, with a specified constant thrust level applied. A minimum burn time constraint for maneuver execution may be established. Deputy spacecraft slews to the maneuver attitude are modeled. For the scenarios evaluated in this work, spacecraft-specific error sources are not considered, including errors related to relative orbit determination, attitude determination and control, and maneuver execution. These error sources are spacecraft-dependent and vary greatly between missions. A block diagram of the GN&C simulation framework is shown in Figure 41.

For each of the scenarios evaluated in this chapter, the chief is in a circular orbit about the Earth with an orbit radius of 7098.14 km (720 km orbit altitude), and an inclination of 24.0 deg. These are the nominal values for the Prox-1 mission. For this orbit geometry, estimates of the magnitude of accelerations to the deputy spacecraft due to orbit perturbations are shown in Table 37. A deputy spacecraft mass of 60 kg and a frontal area 0.25 m² is assumed in the calculations of the magnitude of accelerations shown in Table 37. It is seen that the spherical harmonic (J_2) oblateness term is the largest perturbation at the 720 km orbit altitude, followed by the sun and moon gravitational perturbations. Accelerations due to solar radiation pressure and drag are modest in comparison with the J_2 , sun and moon gravitational perturbations. It is noted that the relative orbit of the deputy with respect to the chief is most influenced by J_2 when the deputy's relative orbit has cross-track motion resulting from a different inertial orbit

inclination. Solar radiation pressure and atmospheric drag result in differential forces on the deputy and chief spacecraft due to their different frontal areas and masses. The chief spacecraft in each of the scenarios is modeled as a 3-unit CubeSat with a mass of 5 kg.

Table 37: Orbit perturbations for a 720 km circular orbit.

Perturbing Effect	Spacecraft Acceleration (m/s ²)
J ₂ spherical harmonic term (oblateness) [71]	1E-02
Sun's gravity [71]	6E-03
Moon's gravity [71]	3E-05
Solar radiation pressure [43]	4E-08
Atmospheric drag [43]	5E-09

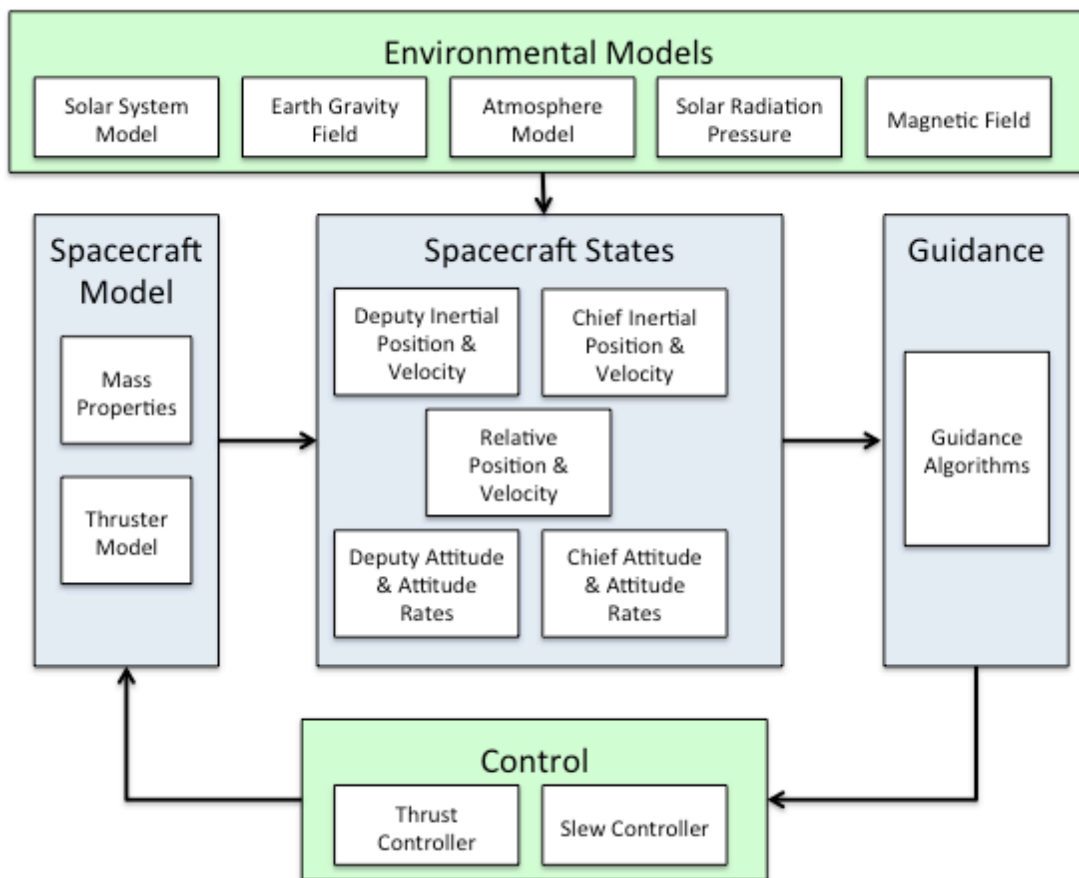


Figure 41: Guidance, navigation and control simulation block diagram.

4.2 Relative Orbital Elements Station-Keeping

The station-keeping strategy described in Section 2.5.3 and summarized in Table 21 is applied to a realistic scenario where there is an initial condition resulting in a secular along-track drift, and the station-keeping maneuver sequence is implemented to return the deputy spacecraft to a desired relative orbit location. The scenario is summarized in Table 38. The station-keeping target location is $[x, y, z] = [0, 50, 0]$. The initial condition $x_r = 2.502$ m results in a secular drift in the negative along-track direction. “Soft constraints” are established at $y_{r_{\min}} = 45$ m and $y_{r_{\max}} = 55$ m; when the value for y_r drifts outside of the soft constraints, a maneuver to set $x_r^+ = 0$ and stop the secular along-track drift is commanded to occur at the next key maneuver point (KMP). Similarly, the cross-track constraint $A_{z_{\max}} = 1$ m is established. Key maneuver points are defined at E_r values of $0, \pi/2, \pi,$ and $3\pi/2$, and at ψ values of 0 and π . Maneuver 1A occurs at $E_r = \pi/2$, as shown in Table 39. The second maneuver in the sequence, Maneuver 2A, is targeted to occur at the next \hat{y} -axis crossing ($x = 0$), to initiate a secular along-track drift returning to the station-keeping target \hat{y} -value one revolution later ($s = 1$). As shown in Table 38, this maneuver actually occurs at $x = 0.068$ m, due to orbit perturbations. Following a drift time of one orbit period, Maneuver 3A is performed to halt the drift at the targeted location. As shown in Table 40, Maneuver 3A is executed at $[x, y] = [0.0662, 50.7571]$ m. Maneuver 3A results in a relative orbit centered on $x_r = 0,$ $y_r = 50$ m, with $a_r = 0.7688$ m. The non-zero value for a_r following maneuver 3A represents the residual error due to orbit perturbations. Maneuver 4A is performed at $\psi = \pi$, to negate the cross-track motion. Following Maneuver 4A, $A_z = 0$.

A second cycle of the station-keeping maneuver sequence is summarized in Tables 41 and 42. The second cycle begins approximately two revs after the first cycle is completed, due to the natural drift of the relative orbit away from the station-keeping

targets. The total ΔV expended during the two cycles of station-keeping is 0.0086 m/s. Following the second station-keeping cycle, the residual error due to orbit perturbations results in $a_r = 0.9861$ m. The station-keeping sequence could be extended indefinitely, with a maneuver frequency of approximately 20 maneuvers per day.

Figure 42 shows the relative position and velocity components as a function of time for this scenario. Figure 43 shows the projections of the trajectory onto the coordinate planes, and the three-dimensional trajectory plot. In the $\hat{y} - \hat{x}$ projection shown in Figure 43(a), it is seen that the second cycle of station-keeping maintains the deputy's orbit within ± 7 m of the target value $y = 50$ m in the along-track direction; this is the expected performance when the initial conditions are established by the natural orbit perturbations. Figure 44 shows the time histories of x_r , y_r , a_r , and A_z . It is noted from Figure 44(d) that once the cross-track motion is nullified by Maneuver 4A, very little cross-track motion is introduced by natural perturbations. Maneuver magnitude as a function of time is shown in Figure 45.

As seen in this scenario, the ROE station-keeping sequence of maneuvers successfully returns the deputy the desired relative orbit. As the station-keeping sequence is repeated sequentially, the algorithm achieves the goal of maintaining a desired leading or trailing relative orbit in an automated fashion, in the presence of orbit perturbations. The residual error due to orbit perturbations following the station-keeping sequence of maneuvers is manifested as an elliptical orbit about the station-keeping target location, with a semi-major axis of less than 1 m.

Table 38: ROE station-keeping scenario.

Initial Conditions	Cartesian	$x = 0.500 \text{ m}$ $\dot{x} = 0.000200 \text{ m/s}$ $y = 50.000 \text{ m}$ $\dot{y} = 0.000265 \text{ m/s}$ $z = -2.000 \text{ m}$ $\dot{z} = 0.000000 \text{ m/s}$
	ROEs	$x_r = 2.502 \text{ m}$ $y_r = 49.621 \text{ m}$ $a_r = 4.022 \text{ m}$ $E_r = 0.094 \text{ rad}$ $A_z = 2.000 \text{ m}$ $\psi = 4.712 \text{ rad}$
Station-Keeping Constraints		$y_{r_{\min}} = 45.0000 \text{ m}$ $y_{r_{\max}} = 55.0000 \text{ m}$ $A_{z_{\max}} = 1.0000 \text{ m}$
Station-Keeping Targets		$x = 0.0000 \text{ m}$ $y = 50.0000 \text{ m}$ $z = 0.0000 \text{ m}$
Station-Keeping Parameter		$s = 1$

Table 39: ROE station-keeping maneuvers 1A, 2A.

Maneuver Number	Maneuver Time (s)	Pre-Maneuver State	$\Delta\bar{V}$ (m/s)	Post-Maneuver State
1A	1,426.7	$x^- = 2.3747$ m $y^- = 48.2642$ m $z^- = -0.1109$ m $\dot{x}^- = 0.002077$ m/s $\dot{y}^- = -0.003761$ m/s $\dot{z}^- = 0.002154$ m/s	$\begin{bmatrix} 0 \\ -0.001254 \\ 0 \end{bmatrix}$	$x^+ = 2.3747$ m $y^+ = 48.2642$ m $z^+ = -0.1109$ m $\dot{x}^+ = 0.002077$ m/s $\dot{y}^+ = -0.004014$ m/s $\dot{z}^+ = 0.002154$ m/s
		$x_r^- = 2.3747$ m $y_r^- = 44.3291$ m $a_r^- = 3.9351$ m $E_r^- = 1.5708$ rad $A_z^- = 2.0437$ m $\psi^- = 6.2289$ rad		$x_r^+ = 0$ m $y_r^+ = 44.3291$ m $a_r^+ = 6.1678$ m $E_r^+ = 2.4497$ rad $A_z^+ = 2.0437$ m $\psi^+ = 6.2289$ rad
2A	3,591.9	$x^- = 0.0680$ m $y^- = 37.8716$ m $z^- = 1.5636$ m $\dot{x}^- = -0.003215$ m/s $\dot{y}^- = -0.000108$ m/s $\dot{z}^- = -0.001309$ m/s	$\begin{bmatrix} 0 \\ -0.000679 \\ 0 \end{bmatrix}$	$x^+ = 0.0680$ m $y^+ = 37.8716$ m $z^+ = 1.5636$ m $\dot{x}^+ = -0.003215$ m/s $\dot{y}^+ = -0.000787$ m/s $\dot{z}^+ = -0.001309$ m/s
		$x_r^- = 0.068$ m $y_r^- = 43.9615$ m $a_r^- = 6.0899$ m $E_r^- = 4.7124$ rad $A_z^- = 1.9955$ m $\psi^- = 2.2412$ rad		$x_r^+ = -1.2189$ m $y_r^+ = 43.9615$ m $a_r^+ = 6.6114$ m $E_r^+ = 4.3125$ rad $A_z^+ = 1.9955$ m $\psi^+ = 2.2412$ rad

Table 40: ROE station-keeping maneuvers 3A, 4A.

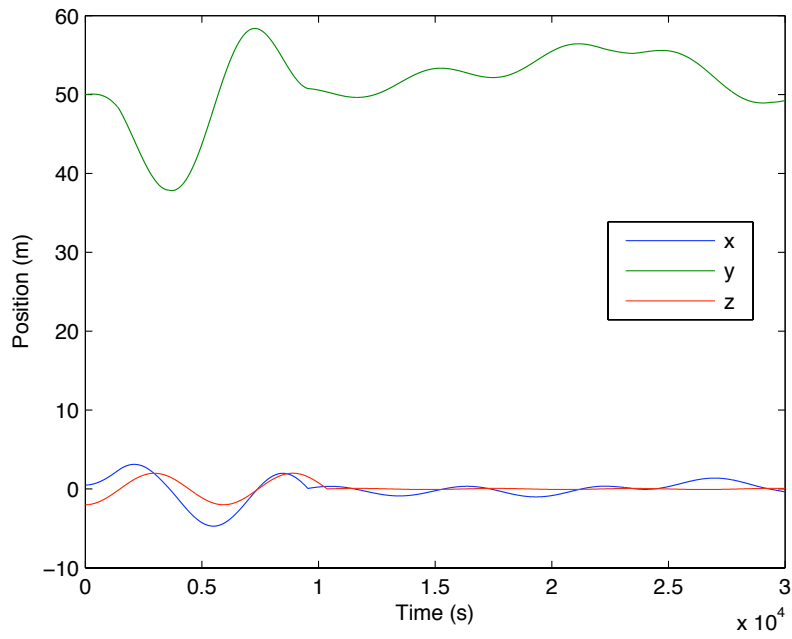
3A	9,543.4	$x^- = 0.0666 \text{ m}$ $y^- = 50.7571 \text{ m}$ $z^- = 1.5414 \text{ m}$ $\dot{x}^- = -0.003210 \text{ m/s}$ $\dot{y}^- = -0.000868 \text{ m/s}$ $\dot{z}^- = -0.001356 \text{ m/s}$	$\begin{bmatrix} 0.0036 \\ 0.0007 \\ 0 \end{bmatrix}$	$x^+ = 0.0662 \text{ m}$ $y^+ = 50.7571 \text{ m}$ $z^+ = 1.5414 \text{ m}$ $\dot{x}^+ = 0.000400 \text{ m/s}$ $\dot{y}^+ = -0.000141 \text{ m/s}$ $\dot{z}^+ = -0.001356 \text{ m/s}$
		$x_r^- = 1.3772 \text{ m}$ $y_r^- = 56.8389 \text{ m}$ $a_r^- = 6.7325 \text{ m}$ $E_r^- = 4.2691 \text{ rad}$ $A_z^- = 2.0061 \text{ m}$ $\psi^- = 2.2653 \text{ rad}$		$x_r^+ = 0.0000 \text{ m}$ $y_r^+ = 50.0000 \text{ m}$ $a_r^+ = 0.7688 \text{ m}$ $E_r^+ = 1.7450 \text{ rad}$ $A_z^+ = 2.0061 \text{ m}$ $\psi^+ = 2.2653 \text{ rad}$
4A	10,371.0	$x^- = 0.3294 \text{ m}$ $y^- = 50.3132 \text{ m}$ $z^- = 0.0000 \text{ m}$ $\dot{x}^- = 0.000127 \text{ m/s}$ $\dot{y}^- = -0.000758 \text{ m/s}$ $\dot{z}^- = -0.002165 \text{ m/s}$	$\begin{bmatrix} 0 \\ 0 \\ 0.002165 \end{bmatrix}$	$x^+ = 0.3294 \text{ m}$ $y^+ = 50.3131 \text{ m}$ $z^+ = 0.0000 \text{ m}$ $\dot{x}^+ = 0.000127 \text{ m/s}$ $\dot{y}^+ = -0.000758 \text{ m/s}$ $\dot{z}^+ = 0.000000 \text{ m/s}$
		$x_r^- = -0.1189 \text{ m}$ $y_r^- = 50.073 \text{ m}$ $a_r^- = 0.9283 \text{ m}$ $E_r^- = 2.8799 \text{ rad}$ $A_z^- = 2.0511 \text{ m}$ $\psi^- = 3.1416 \text{ rad}$		$x_r^+ = -0.1189 \text{ m}$ $y_r^+ = 50.0730 \text{ m}$ $a_r^+ = 0.9283 \text{ m}$ $E_r^+ = 2.8799 \text{ rad}$ $A_z^+ = 0.0000 \text{ m}$ $\psi^+ = 4.7124 \text{ rad}$

Table 41: ROE station-keeping, maneuvers 1B, 2B.

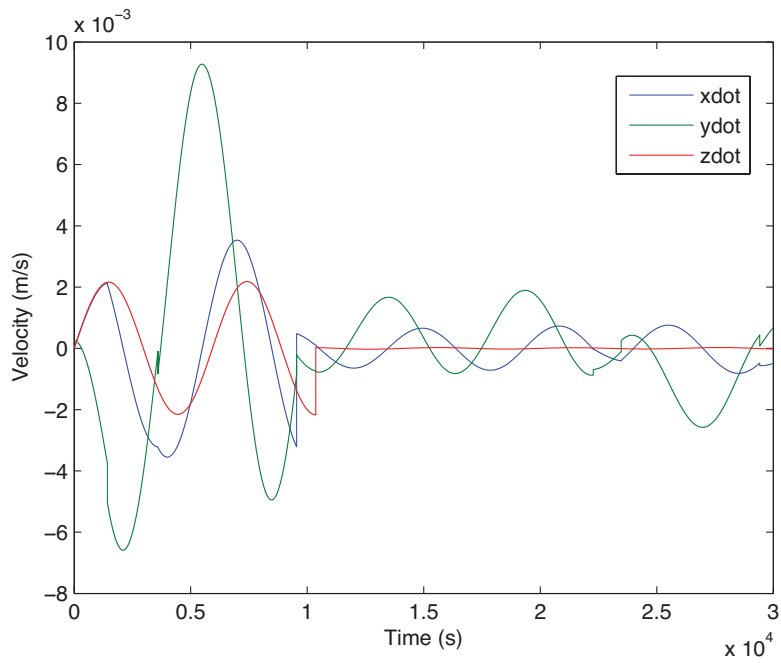
1B	22,279.0	$x^- = 0.3574 \text{ m}$ $y^- = 55.7660 \text{ m}$ $z^- = 0.0000 \text{ m}$ $\dot{x}^- = 0.000009 \text{ m/s}$ $\dot{y}^- = -0.000897 \text{ m/s}$ $\dot{z}^- = 0.000018 \text{ m/s}$	$\begin{bmatrix} 0 \\ 0.000142 \\ 0 \end{bmatrix}$	$x^+ = 0.3574 \text{ m}$ $y^+ = 55.7660 \text{ m}$ $z^+ = 0.0000 \text{ m}$ $\dot{x}^+ = 0.000009 \text{ m/s}$ $\dot{y}^+ = -0.000755 \text{ m/s}$ $\dot{z}^+ = 0.000018 \text{ m/s}$
		$x_r^- = -0.2702 \text{ m}$ $y_r^- = 55.7486 \text{ m}$ $a_r^- = 1.2553 \text{ m}$ $E_r^- = 3.1277 \text{ rad}$ $A_z^- = 0.0166 \text{ m}$ $\psi^- = 6.2832 \text{ rad}$		$x_r^+ = 0 \text{ m}$ $y_r^+ = 55.7486 \text{ m}$ $a_r^+ = 0.7150 \text{ m}$ $E_r^+ = 3.1172 \text{ rad}$ $A_z^+ = 0.0166 \text{ m}$ $\psi^+ = 0.0000 \text{ rad}$
2B	23,471.0	$x^- = 0.0646 \text{ m}$ $y^- = 55.2065 \text{ m}$ $z^- = 0.0593 \text{ m}$ $\dot{x}^- = -0.000370 \text{ m/s}$ $\dot{y}^- = -0.000102 \text{ m/s}$ $\dot{z}^- = -0.000025 \text{ m/s}$	$\begin{bmatrix} 0 \\ 0.000142 \\ 0 \end{bmatrix}$	$x^+ = 0.0646 \text{ m}$ $y^+ = 55.2065 \text{ m}$ $z^+ = 0.0593 \text{ m}$ $\dot{x}^+ = -0.000370 \text{ m/s}$ $\dot{y}^+ = 0.000189 \text{ m/s}$ $\dot{z}^+ = -0.000025 \text{ m/s}$
		$x_r^- = 0.0646 \text{ m}$ $y_r^- = 55.9080 \text{ m}$ $a_r^- = 0.7015 \text{ m}$ $E_r^- = 4.7124 \text{ rad}$ $A_z^- = 0.0638 \text{ m}$ $\psi^- = 1.9466 \text{ rad}$		$x_r^+ = 0.6170 \text{ m}$ $y_r^+ = 55.9080 \text{ m}$ $a_r^+ = 1.3087 \text{ m}$ $E_r^+ = 5.7175 \text{ rad}$ $A_z^+ = 0.0638 \text{ m}$ $\psi^+ = 1.9466 \text{ rad}$

Table 42: ROE station-keeping maneuver 3B.

3B	29,422.0	$x^- = -0.0411 \text{ m}$ $y^- = 49.0173 \text{ m}$ $z^- = 0.0645 \text{ m}$ $\dot{x}^- = -0.000446 \text{ m/s}$ $\dot{y}^- = 0.000444 \text{ m/s}$ $\dot{z}^- = -0.000020 \text{ m/s}$	$\begin{bmatrix} -0.000072 \\ -0.000358 \\ 0 \end{bmatrix}$	$x^+ = -0.0411 \text{ m}$ $y^+ = 49.0173 \text{ m}$ $z^+ = 0.0645 \text{ m}$ $\dot{x}^+ = -0.000519 \text{ m/s}$ $\dot{y}^+ = 0.000087 \text{ m/s}$ $\dot{z}^+ = -0.000020 \text{ m/s}$
		$x_r^- = 0.6782 \text{ m}$ $y_r^- = 49.8629 \text{ m}$ $a_r^- = 1.6687 \text{ m}$ $E_r^- = 5.7518 \text{ rad}$ $A_z^- = 0.0673 \text{ m}$ $\psi^- = 1.8620 \text{ rad}$		$x_r^+ = 0.0000 \text{ m}$ $y_r^+ = 50.0000 \text{ m}$ $a_r^+ = 0.9861 \text{ m}$ $E_r^+ = 4.7958 \text{ rad}$ $A_z^+ = 0.0673 \text{ m}$ $\psi^+ = 1.8620 \text{ rad}$

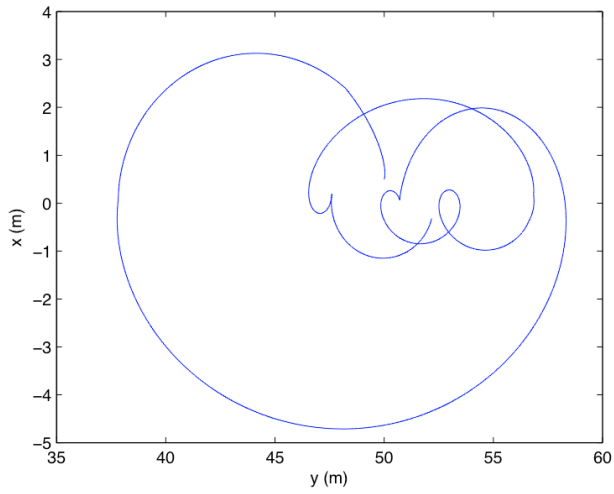


(a)

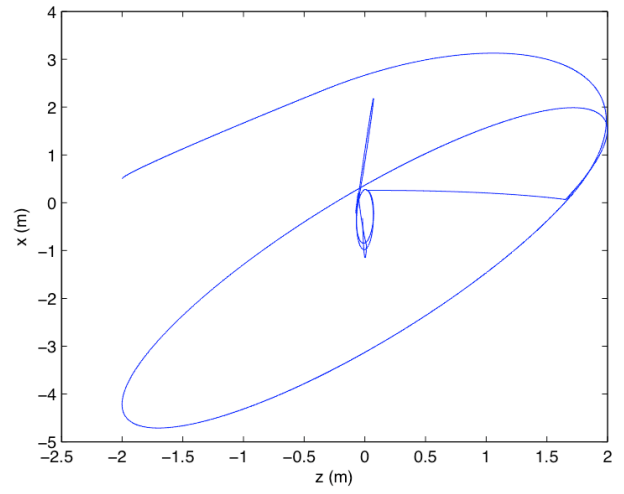


(b)

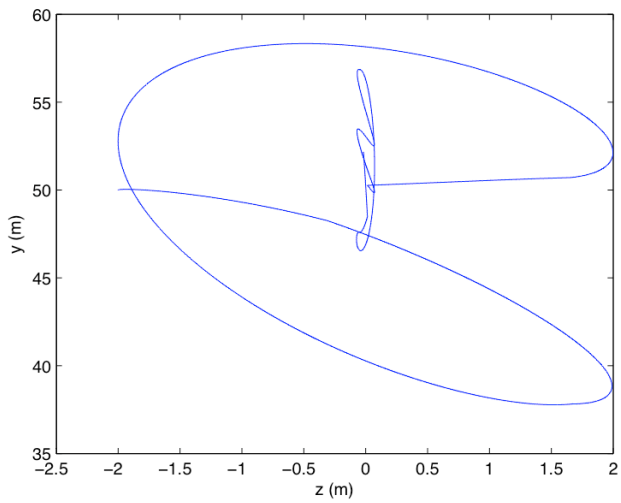
Figure 42: ROE station-keeping scenario, (a) Relative position components as a function of time, (b) Relative velocity components as a function of time.



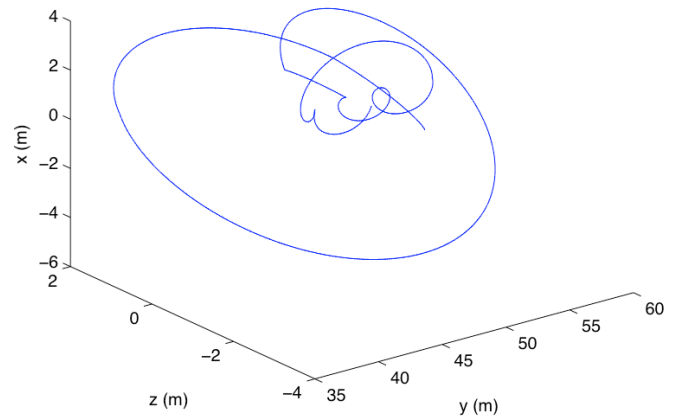
(a)



(b)



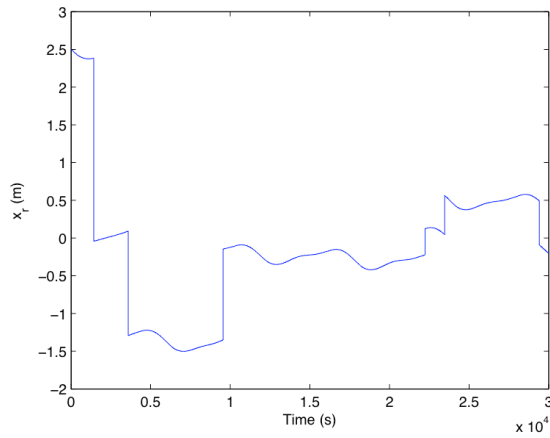
(c)



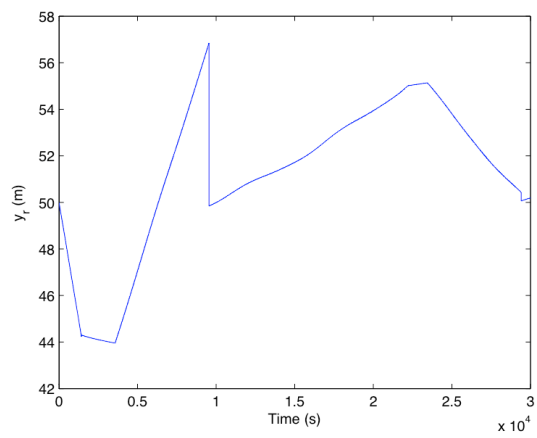
(d)

Figure 43: ROE station-keeping scenario, (a) $\hat{y} - \hat{x}$ projection, (b) $\hat{z} - \hat{x}$ projection, (c)

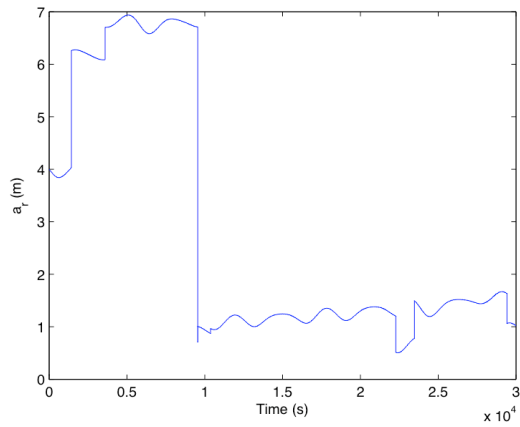
$\hat{z} - \hat{y}$ projection, (d) 3D trajectory plot.



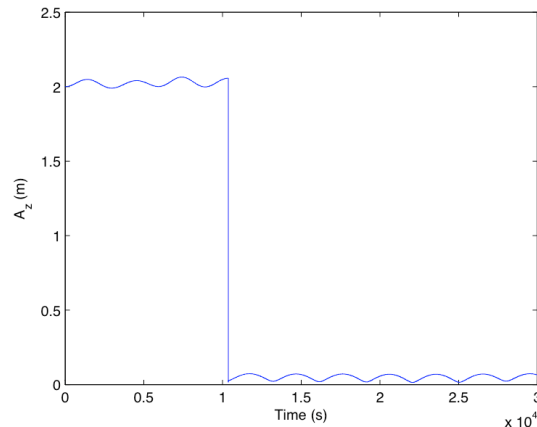
(a)



(b)



(c)



(d)

Figure 44: ROE station-keeping scenario, (a) x_r as a function of time, (b) y_r as a function of time, (c) a_r as a function of time, (d) A_z as a function of time.

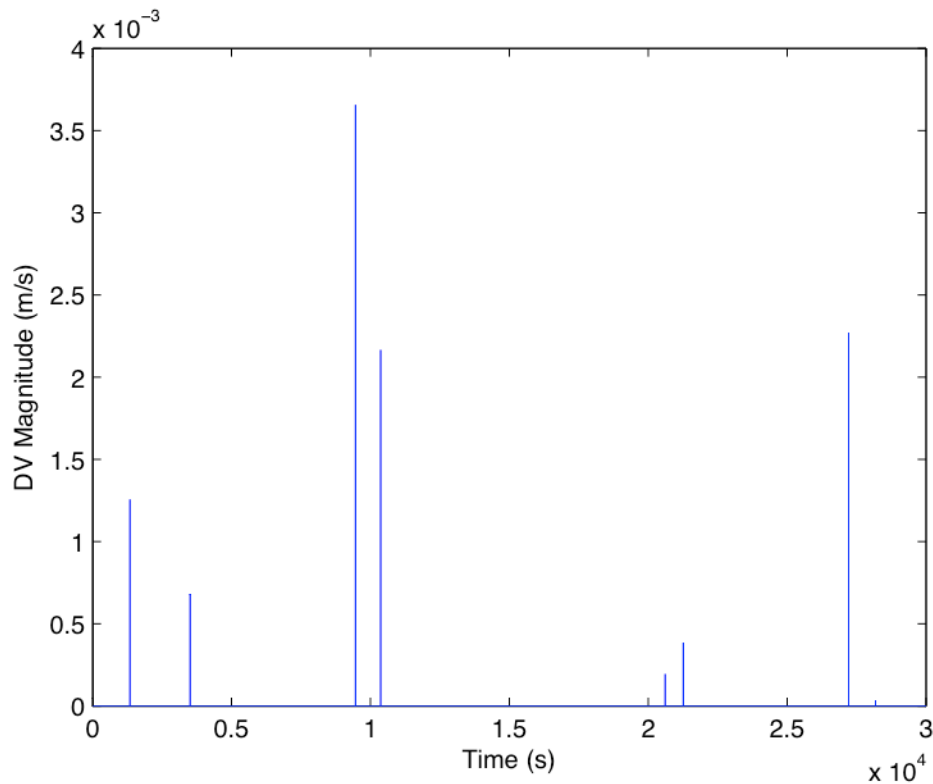


Figure 45: ROE station-keeping scenario, maneuver magnitudes.

4.3 Relative Orbital Elements Transfer

The station-keeping sequence of maneuvers described in Section 2.5.3 and demonstrated in Section 4.2 may also be applied to execute a transfer to a specified leading or trailing orbit, by simply changing the values of the station-keeping constraints and the target location to reflect the desired values upon completion of the orbit transfer. An example of this scenario is summarized in Table 43. The initial conditions are the same as those for the scenario described in Section 4.2, however, in this case the targeted station-keeping location is $[x, y, z] = [0, 100, 0]$ m, and the along-track station-keeping constraints are updated to $y_{\min} = 95$ m and $y_{\max} = 105$ m.

As shown in Table 44, the first two maneuvers in the sequence are performed at the same times as maneuvers 1A and 2A from the previous scenario. Maneuver 1 is

performed to halt the secular along-track drift, and Maneuver 2 is performed at $E_r^- = 3\pi/2$ to initiate a secular along-track drift that will cross the \hat{y} -axis at the desired location of $y = 100$ m one rev later ($s = 1$). As shown in Table 45, Maneuver 3 halts the secular drift and establishes $x_r^+ = 0$ and $y_r^+ = 100$ m. Maneuver 4 nullifies the cross-track motion. Due to the effect of orbit perturbations during the transfer, upon completion of the maneuver sequence there is a relative orbit about the targeted position, with $a_r = 1.5$ m.

Figure 46 shows the relative position and velocity components as a function of time during the transfer. Figure 46 shows the projections of the trajectory onto the coordinate planes, and the three-dimensional trajectory plot. Figure 48 shows the time histories of x_r , y_r , a_r , and A_z , and the maneuver magnitudes as a function of time are shown in Figure 49.

This scenario demonstrates that the station-keeping strategy illustrated in Section 4.2 may also be applied to execute relative orbit transfers to a leading or trailing orbit, by simply updating the target \hat{y} -locations and the along-track station-keeping constraints. The initial condition is arbitrary, and does not need to be on a leading or trailing orbit. Orbit perturbations have a modest, but non-negligible effect on the orbit transfer. Once the transfer is completed, the automated station-keeping scenario is in effect, and residual errors will be corrected through the subsequent station-keeping maneuver sequences.

Table 43: ROE transfer scenario.

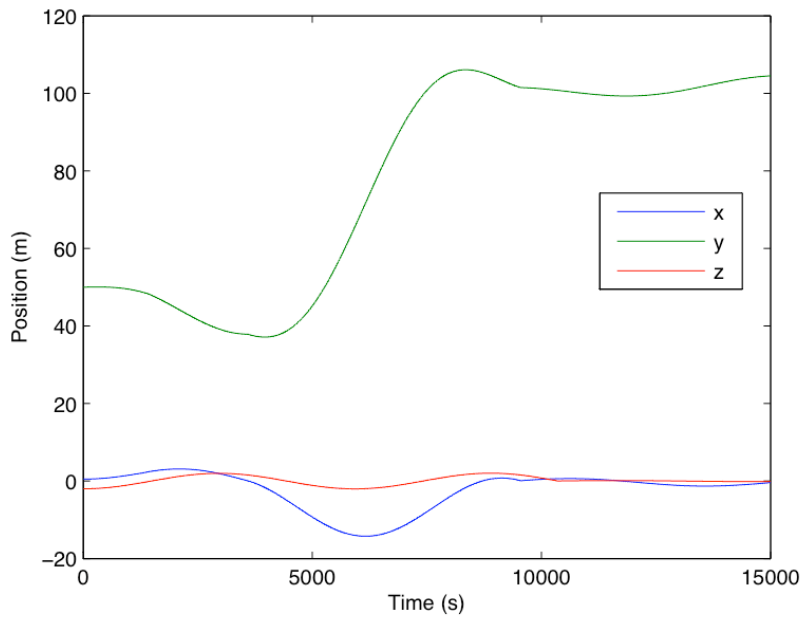
Initial Conditions	Cartesian	$x = 0.500 \text{ m}$ $\dot{x} = 0.000200 \text{ m/s}$ $y = 50.000 \text{ m}$ $\dot{y} = 0.000265 \text{ m/s}$ $z = -2.000 \text{ m}$ $\dot{z} = 0.000000 \text{ m/s}$
	ROEs	$x_r = 2.502 \text{ m}$ $y_r = 49.621 \text{ m}$ $a_r = 4.022 \text{ m}$ $E_r = 0.094 \text{ rad}$ $A_z = 2.000 \text{ m}$ $\psi = 4.712 \text{ rad}$
Station-Keeping Constraints		$y_{r_{\min}} = 95.0000 \text{ m}$ $y_{r_{\max}} = 105.0000 \text{ m}$ $A_{z_{\max}} = 1.0000 \text{ m}$
Station-Keeping Targets		$x = 0.0000 \text{ m}$ $y = 100.0000 \text{ m}$ $z = 0.0000 \text{ m}$
Station-Keeping Parameter		$s = 1$

Table 44: ROE transfer maneuvers 1 and 2.

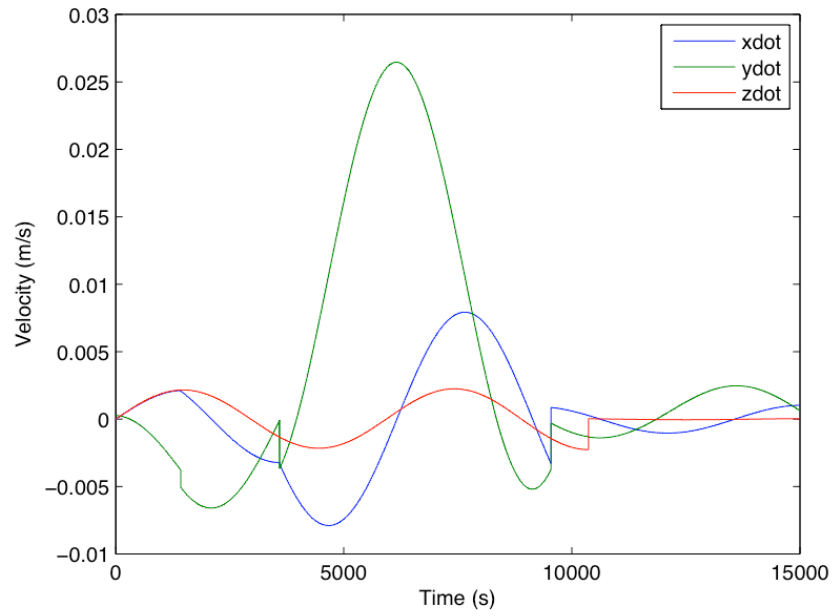
Maneuver Number	Maneuver Time (s)	Pre-Maneuver State	$\Delta\bar{V}$ (m/s)	Post-Maneuver State
1	1,426.7	$x^- = 2.3747$ m $y^- = 48.2642$ m $z^- = -0.1109$ m $\dot{x}^- = 0.002077$ m/s $\dot{y}^- = -0.003761$ m/s $\dot{z}^- = 0.002154$ m/s	$\begin{bmatrix} 0 \\ -0.001254 \\ 0 \end{bmatrix}$	$x^+ = 2.3747$ m $y^+ = 48.2642$ m $z^+ = -0.1109$ m $\dot{x}^+ = 0.002077$ m/s $\dot{y}^+ = -0.004014$ m/s $\dot{z}^+ = 0.002154$ m/s
		$x_r^- = 2.3747$ m $y_r^- = 44.3291$ m $a_r^- = 3.9351$ m $E_r^- = 1.5708$ rad $A_z^- = 2.0437$ m $\psi^- = 6.2289$ rad		$x_r^+ = 0$ m $y_r^+ = 44.3291$ m $a_r^+ = 6.1678$ m $E_r^+ = 2.4497$ rad $A_z^+ = 2.0437$ m $\psi^+ = 6.2289$ rad
2	3,591.9	$x^- = 0.0680$ m $y^- = 37.8716$ m $z^- = 1.5636$ m $\dot{x}^- = -0.003215$ m/s $\dot{y}^- = -0.000108$ m/s $\dot{z}^- = -0.001309$ m/s	$\begin{bmatrix} 0 \\ -0.003480 \\ 0 \end{bmatrix}$	$x^+ = 0.0680$ m $y^+ = 37.8716$ m $z^+ = 1.5636$ m $\dot{x}^+ = -0.003215$ m/s $\dot{y}^+ = -0.003587$ m/s $\dot{z}^+ = -0.001309$ m/s
		$x_r^- = 0.068$ m $y_r^- = 43.9615$ m $a_r^- = 6.0899$ m $E_r^- = 4.7124$ rad $A_z^- = 1.9955$ m $\psi^- = 2.2412$ rad		$x_r^+ = -6.5240$ m $y_r^+ = 43.9615$ m $a_r^+ = 14.5225$ m $E_r^+ = 3.5743$ rad $A_z^+ = 1.9955$ m $\psi^+ = 2.2412$ rad

Table 45: ROE transfer maneuvers 3 and 4.

3	9,543.4	$x^- = 0.1010 \text{ m}$ $y^- = 101.4825 \text{ m}$ $z^- = 1.5614 \text{ m}$ $\dot{x}^- = -0.003276 \text{ m/s}$ $\dot{y}^- = -0.003760 \text{ m/s}$ $\dot{z}^- = -0.001395 \text{ m/s}$	$\begin{bmatrix} 0.0041 \\ 0.0035 \\ 0 \end{bmatrix}$	$x^+ = 0.1010 \text{ m}$ $y^+ = 101.4825 \text{ m}$ $z^+ = 1.5614 \text{ m}$ $\dot{x}^+ = 0.000783 \text{ m/s}$ $\dot{y}^+ = -0.000213 \text{ m/s}$ $\dot{z}^+ = -0.001395 \text{ m/s}$
		$x_r^- = 6.7183 \text{ m}$ $y_r^- = 107.6881 \text{ m}$ $a_r^- = 14.984 \text{ m}$ $E_r^- = 3.5686 \text{ rad}$ $A_z^- = 2.0454 \text{ m}$ $\psi^- = 2.2731 \text{ rad}$		$x_r^+ = 0.0000 \text{ m}$ $y_r^+ = 100.0000 \text{ m}$ $a_r^+ = 1.4962 \text{ m}$ $E_r^+ = 1.7062 \text{ rad}$ $A_z^+ = 2.0454 \text{ m}$ $\psi^+ = 2.2731 \text{ rad}$
4	10,364.0	$x^- = 0.6110 \text{ m}$ $y^- = 100.7523 \text{ m}$ $z^- = 0.0000 \text{ m}$ $\dot{x}^- = 0.000333 \text{ m/s}$ $\dot{y}^- = -0.001342 \text{ m/s}$ $\dot{z}^- = -0.002247 \text{ m/s}$	$\begin{bmatrix} 0 \\ 0 \\ 0.002247 \end{bmatrix}$	$x^+ = 0.6110 \text{ m}$ $y^+ = 100.7523 \text{ m}$ $z^+ = 0.0000 \text{ m}$ $\dot{x}^+ = 0.000333 \text{ m/s}$ $\dot{y}^+ = -0.001342 \text{ m/s}$ $\dot{z}^+ = 0.000000 \text{ m/s}$
		$x_r^- = -0.0985 \text{ m}$ $y_r^- = 100.1213 \text{ m}$ $a_r^- = 1.5530 \text{ m}$ $E_r^- = 2.7232 \text{ rad}$ $A_z^- = 2.1285 \text{ m}$ $\psi^- = 3.1416 \text{ rad}$		$x_r^+ = -0.0985 \text{ m}$ $y_r^+ = 100.1213 \text{ m}$ $a_r^+ = 1.5330 \text{ m}$ $E_r^+ = 2.7232 \text{ rad}$ $A_z^+ = 0.0000 \text{ m}$ $\psi^+ = 4.7124 \text{ rad}$



(a)



(b)

Figure 46: ROE transfer scenario, (a) Relative position components as a function of time, (b) Relative velocity components as a function of time.

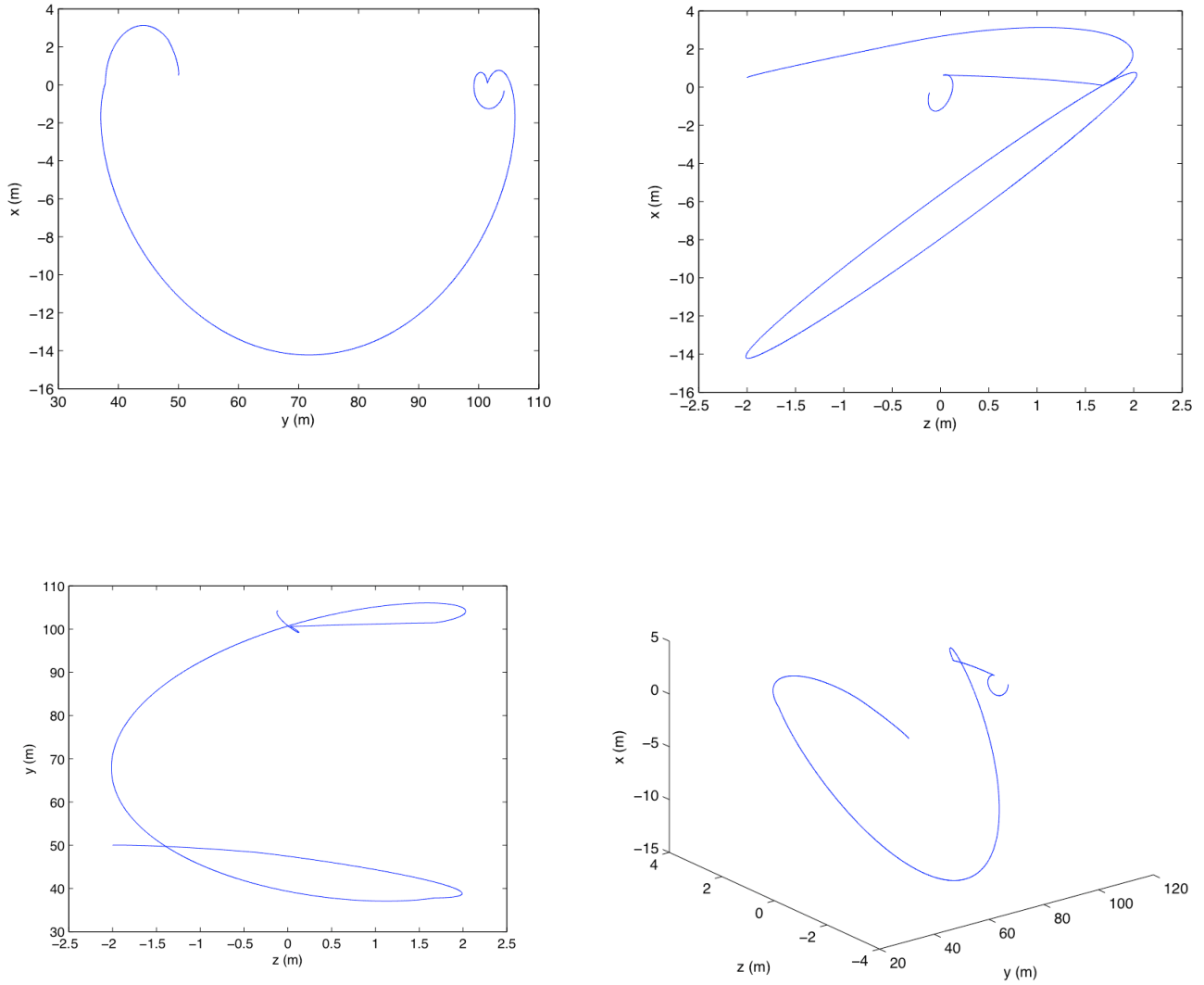
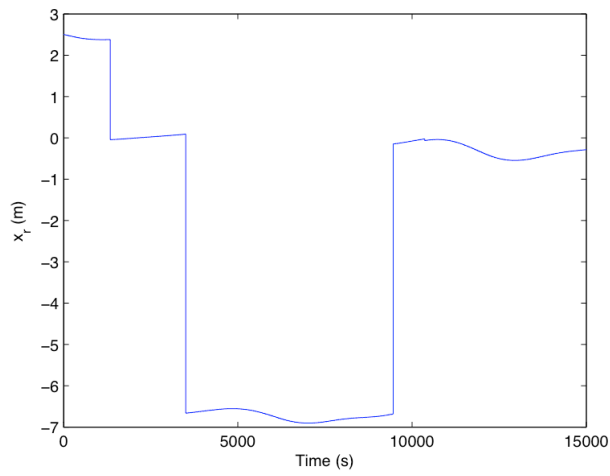
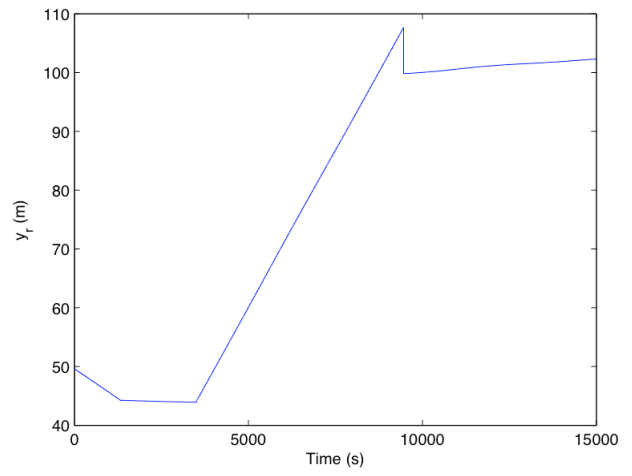


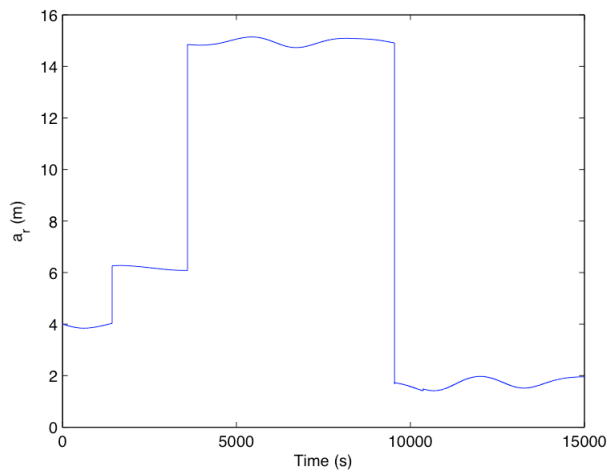
Figure 47: ROE transfer scenario, (a) $\hat{y} - \hat{x}$ projection, (b) $\hat{z} - \hat{x}$ projection, (c) $\hat{z} - \hat{y}$ projection, (d) 3D trajectory plot.



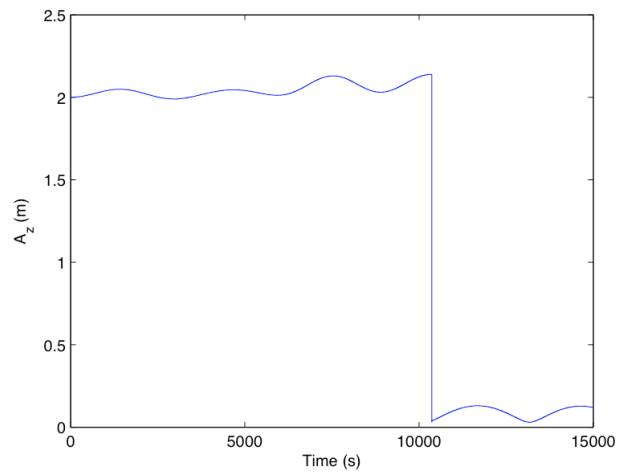
(a)



(b)



(c)



(d)

Figure 48: ROE transfer scenario, (a) x_r as a function of time, (b) y_r as a function of time, (c) a_r as a function of time, (d) A_z as a function of time.

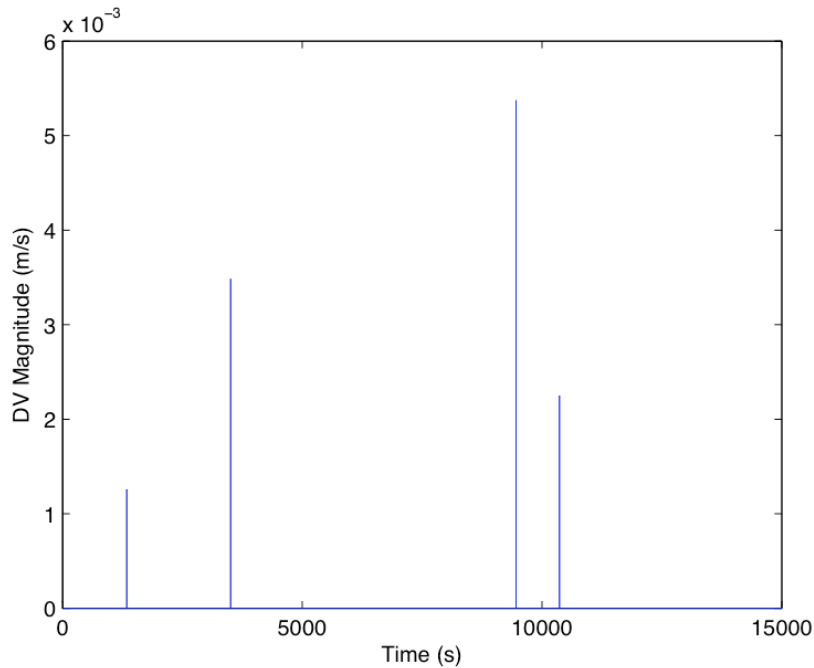


Figure 49: ROE transfer scenario, maneuver magnitudes.

4.4 Relative Orbital Elements Transfer with Artificial Potential Function

Obstacle Avoidance

In this scenario, the ROE station-keeping maneuver sequence is applied to complete a transfer from a leading orbit to a trailing orbit, while a repulsive APF (as described in Section 3.1) is used to ensure collision avoidance with the chief, represented as an obstacle located at the origin of the LVLH coordinate system. This scenario is constructed to ensure that the repulsive APF is encountered. As shown in Table 46, the transfer is from a leading orbit with $y_r = 50$ m to a trailing orbit with target $y = -50$ m. The ROE station-keeping parameter $s = 2$ results in a drift phase that, if left unabated, would pass very close to the origin.

As shown in Table 47, station-keeping Maneuver 1A sets $x_r^+ = 0$, and Maneuver 2A initiates a secular drift in the negative along-track direction. The drifting trajectory encounters the artificial potential field at a distance of 20 m from the origin, and the repulsive Maneuver 3-APF (Table 48) is performed which directs the post-maneuver relative velocity vector away from the origin. The application of the APF-based maneuver truncates the station-keeping sequence of maneuvers. Following the APF maneuver, station-keeping is re-initialized, and a series of three station-keeping maneuvers, 1B, 2B and 3B, are implemented as shown in Tables 48 and 49. Upon the completion of Maneuver 3B, the relative orbit is centered on the desired location, $[x_r, y_r] = [0, 50]$ m, with $a_r = 3.3$ m. No cross-track maneuvers are needed during this sequence.

Figure 50 shows the relative position and velocity components as a function of time during the transfer. Figure 51 shows the projections of the trajectory onto the coordinate planes, and the three-dimensional trajectory plot. The repulsive maneuver introduces a large semi-major axis of the relative motion, $a_r^+ = 90$ m. However, the subsequent station-keeping sequence of maneuvers is able to re-target the trajectory to the desired location. Figure 52 shows the time histories of x_r , y_r , a_r , and A_z . The maneuver magnitudes as a function of time are shown in Figure 53. The largest maneuver is the repulsive Maneuver 3-APF, with a magnitude of 0.077 m/s. The total ΔV utilization is 0.145 m/s.

This scenario shows that ROE station-keeping and a repulsive APF may be used together to ensure collision avoidance while targeting a desired leading or trailing orbit. Even in this worst-case scenario, where the deputy is placed on a direct impact trajectory with the obstacle, the automated control algorithms are able to divert the trajectory away from the obstacle and continue on to reach the targeted location.

Table 46: ROE transfer with APF obstacle avoidance scenario.

Initial Conditions	Cartesian	$x = -1.8660 \text{ m}$ $\dot{x} = -0.0005279 \text{ m/s}$ $y = 49.0000 \text{ m}$ $\dot{y} = 0.0034122 \text{ m/s}$ $z = 0.7071 \text{ m}$ $\dot{z} = 0.0007465 \text{ m/s}$
	ROEs	$x_r = -0.9985 \text{ m}$ $y_r = 50.0001 \text{ m}$ $a_r = 2.0003 \text{ m}$ $E_r = -0.5236 \text{ rad}$ $A_z = 1.0000 \text{ m}$ $\psi = 0.7854 \text{ rad}$
Station-Keeping Constraints		$y_{r_{\min}} = 95.0000 \text{ m}$ $y_{r_{\max}} = 105.0000 \text{ m}$ $A_{z_{\max}} = 1.0000 \text{ m}$
Station-Keeping Targets		$x = 0.0000 \text{ m}$ $y = -50.0000 \text{ m}$ $z = 0.0000 \text{ m}$
Obstacle Location		$x = 0.0000 \text{ m}$ $y = 0.0000 \text{ m}$ $z = 0.0000 \text{ m}$
APF Parameters		$k_r = 1$ $\bar{\mathbf{Q}}_r = \bar{\mathbf{I}}_{3 \times 3}$ $\sigma = 100$ $r_{obs_soi} = 20 \text{ m}$

Table 47: ROE transfer with APF obstacle avoidance, maneuvers 1A and 2A.

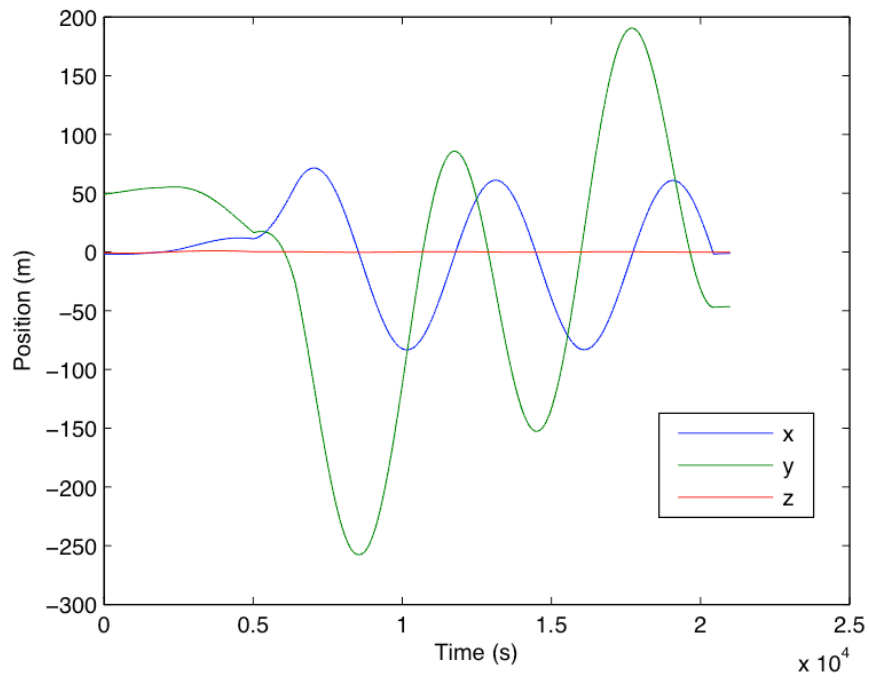
Maneuver Number	Maneuver Time (s)	Pre-Maneuver State	$\Delta\bar{V}$ (m/s)	Post-Maneuver State
1A	508.8	$x^- = -2.0022$ m $y^- = 50.8249$ m $z^- = -0.9657$ m $\dot{x}^- = 0.000000$ m/s $\dot{y}^- = 0.003679$ m/s $\dot{z}^- = -0.000248$ m/s	$\begin{bmatrix} 0 \\ 0.000548 \\ 0 \end{bmatrix}$	$x^+ = -2.0022$ m $y^+ = 50.8249$ m $z^+ = -0.9657$ m $\dot{x}^+ = 0.000000$ m/s $\dot{y}^+ = 0.004227$ m/s $\dot{z}^+ = -0.000248$ m/s
		$x_r^- = -1.0381$ m $y_r^- = 50.8249$ m $a_r^- = 1.9281$ m $E_r^- = 0.0000$ rad $A_z^- = 0.9939$ m $\psi^- = 4.4737$ rad		$x_r^+ = 0.0000$ m $y_r^+ = 50.8249$ m $a_r^+ = 4.0043$ m $E_r^+ = 0.0000$ rad $A_z^+ = 0.9939$ m $\psi^+ = 4.4737$ rad
2A	1937.5	$x^- = -0.0548$ m $y^- = 54.6618$ m $z^- = -0.2823$ m $\dot{x}^- = 0.002135$ m/s $\dot{y}^- = 0.000009$ m/s $\dot{z}^- = 0.001062$ m/s	$\begin{bmatrix} 0 \\ 0.002704 \\ 0 \end{bmatrix}$	$x^+ = -0.0548$ m $y^+ = 54.6618$ m $z^+ = -0.2823$ m $\dot{x}^+ = 0.002135$ m/s $\dot{y}^+ = 0.002791$ m/s $\dot{z}^+ = 0.001062$ m/s
		$x_r^- = -0.0548$ m $y_r^- = 50.6169$ m $a_r^- = 4.0449$ m $E_r^- = 1.5708$ rad $A_z^- = 1.0446$ m $\psi^- = 6.0095$ rad		$x_r^+ = 5.0685$ m $y_r^+ = 50.6169$ m $a_r^+ = 11.0160$ m $E_r^+ = 0.3760$ rad $A_z^+ = 1.0446$ m $\psi^+ = 6.0095$ rad

Table 48: ROE transfer with APF obstacle avoidance, maneuvers 3-APF and 1B.

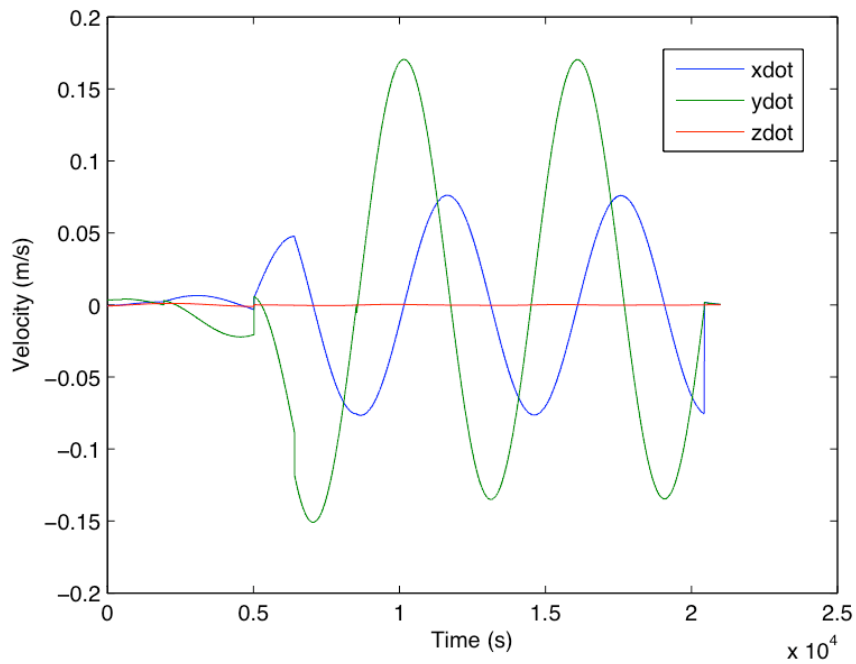
Maneuver Number	Maneuver Time (s)	Pre-Maneuver State	$\Delta\bar{V}$ (m/s)	Post-Maneuver State
3-APF	5,021.2	$x^- = 11.1709$ m $y^- = 16.4691$ m $z^- = 0.1587$ m $\dot{x}^- = -0.003089$ m/s $\dot{y}^- = -0.020586$ m/s $\dot{z}^- = -0.001040$ m/s	$\begin{bmatrix} 0.0071 \\ 0.0267 \\ 0.0011 \end{bmatrix}$	$x^+ = 11.1709$ m $y^+ = 16.4691$ m $z^+ = 0.1587$ m $\dot{x}^+ = 0.004011$ m/s $\dot{y}^+ = 0.006114$ m/s $\dot{z}^+ = 0.000006$ m/s
		$x_r^- = 5.6850$ m $y_r^- = 22.3203$ m $a_r^- = 12.4345$ m $E_r^- = 3.6315$ rad $A_z^- = 0.9980$ m $\psi^- = 2.9819$ rad		$x_r^+ = 56.2662$ m $y_r^+ = 8.8699$ m $a_r^+ = 90.5103$ m $E_r^+ = 0.0841$ rad $A_z^+ = 0.1685$ m $\psi^+ = 1.2281$ rad
1B	6,411.1	$x^- = 55.8836$ m $y^- = -25.7734$ m $z^- = 0.1322$ m $\dot{x}^- = 0.047540$ m/s $\dot{y}^- = -0.088497$ m/s $\dot{z}^- = -0.000177$ m/s	$\begin{bmatrix} 0 \\ -0.0295 \\ 0 \end{bmatrix}$	$x^+ = 55.8836$ m $y^+ = -25.7734$ m $z^+ = 0.1322$ m $\dot{x}^+ = 0.047540$ m/s $\dot{y}^+ = -0.117996$ m/s $\dot{z}^+ = -0.000177$ m/s
		$x_r^- = 55.8834$ m $y_r^- = -115.8339$ m $a_r^- = 90.0605$ m $E_r^- = 1.5708$ rad $A_z^- = 0.2132$ m $\psi^- = 2.4729$ rad		$x_r^+ = 0.0000$ m $y_r^+ = -115.8339$ m $a_r^+ = 143.5367$ m $E_r^+ = 2.4633$ rad $A_z^+ = 0.2132$ m $\psi^+ = 2.4729$ rad

Table 49: ROE transfer with APF obstacle avoidance, maneuvers 2B and 3B.

Maneuver Number	Maneuver Time (s)	Pre-Maneuver State	$\Delta\bar{V}$ (m/s)	Post-Maneuver State
2B	8,534.7	$x^- = -0.0971$ m $y^- = -257.4803$ m $z^- = -0.3524$ m $\dot{x}^- = -0.075572$ m/s $\dot{y}^- = 0.000154$ m/s $\dot{z}^- = -0.000171$ m/s	$\begin{bmatrix} 0 \\ -0.00581 \\ 0 \end{bmatrix}$	$x^+ = -0.0971$ m $y^+ = -257.4803$ m $z^+ = -0.3524$ m $\dot{x}^+ = -0.075572$ m/s $\dot{y}^+ = -0.005656$ m/s $\dot{z}^+ = -0.000171$ m/s
		$x_r^- = -0.0963$ m $y_r^- = -114.3149$ m $a_r^- = 143.1654$ m $E_r^- = 4.7124$ rad $A_z^- = 0.3877$ m $\psi^- = 4.2823$ rad		$x_r^+ = -11.1035$ m $y_r^+ = -114.3149$ m $a_r^+ = 144.8478$ m $E_r^+ = 4.5598$ rad $A_z^+ = 0.3877$ m $\psi^+ = 4.2823$ rad
3B	20,438.0	$x^- = -0.2142$ m $y^- = -46.7276$ m $z^- = -0.1071$ m $\dot{x}^- = -0.075298$ m/s $\dot{y}^- = -0.005439$ m/s $\dot{z}^- = -0.000052$ m/s	$\begin{bmatrix} 0.0770 \\ 0.0059 \\ 0 \end{bmatrix}$	$x^+ = -0.2142$ m $y^+ = -46.7276$ m $z^+ = -0.1071$ m $\dot{x}^+ = 0.001727$ m/s $\dot{y}^+ = 0.000452$ m/s $\dot{z}^+ = -0.000052$ m/s
		$x_r^- = -11.1610$ m $y_r^- = 95.9190$ m $a_r^- = 144.3170$ m $E_r^- = 4.5601$ rad $A_z^- = 0.1178$ m $\psi^- = 4.2826$ rad		$x_r^+ = 0.0000$ m $y_r^+ = -50.0000$ m $a_r^+ = 3.30003$ m $E_r^+ = 1.4406$ rad $A_z^+ = 0.1178$ m $\psi^+ = 4.2826$ rad

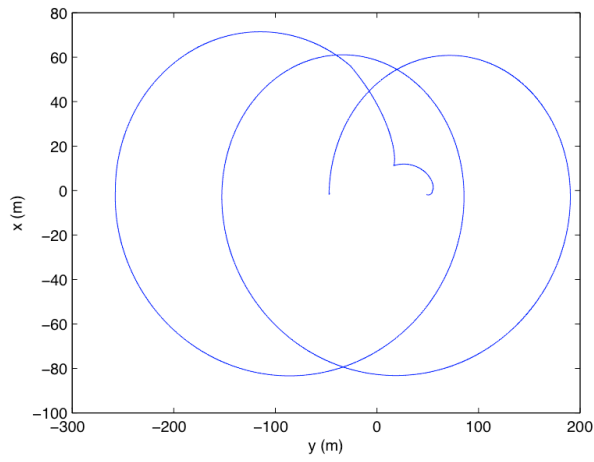


(a)

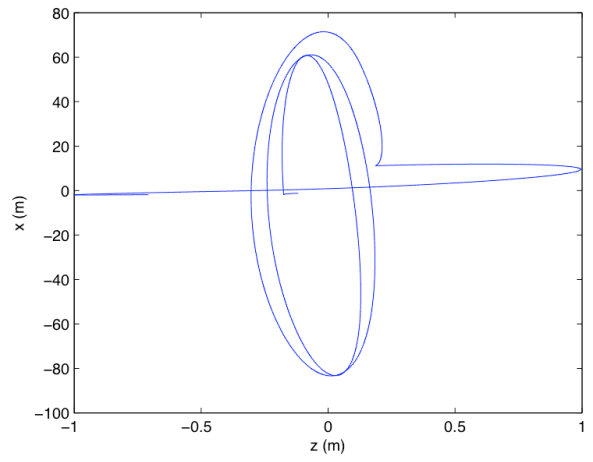


(b)

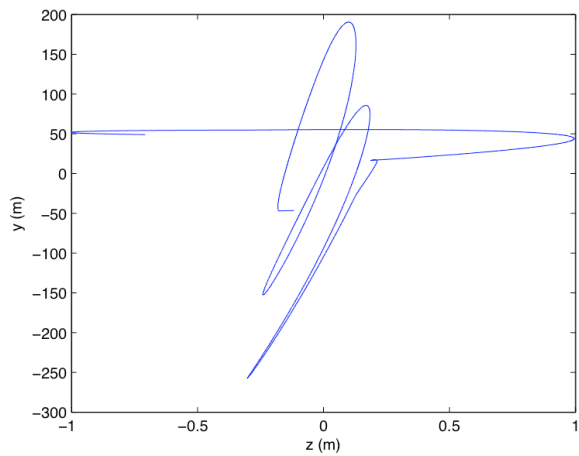
Figure 50: ROE transfer scenario with APF obstacle avoidance, (a) Relative position components as a function of time, (b) Relative velocity components as a function of time.



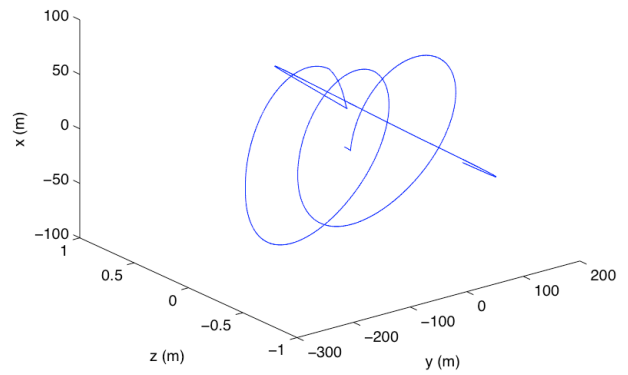
(a)



(b)

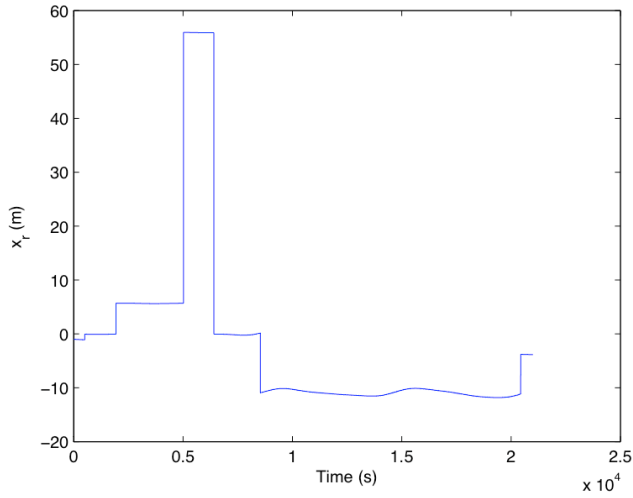


(c)

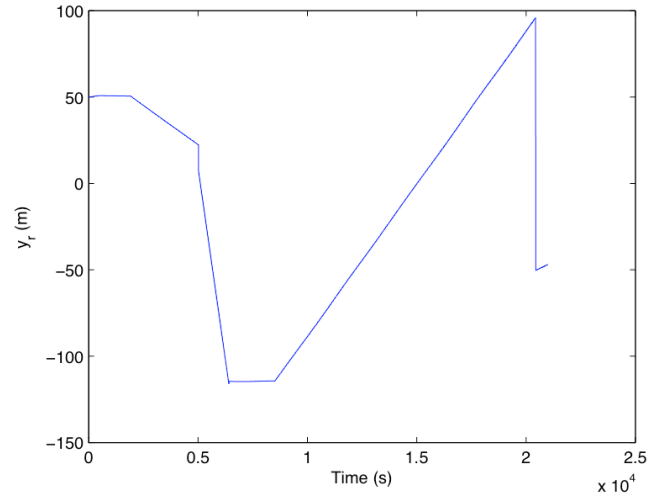


(d)

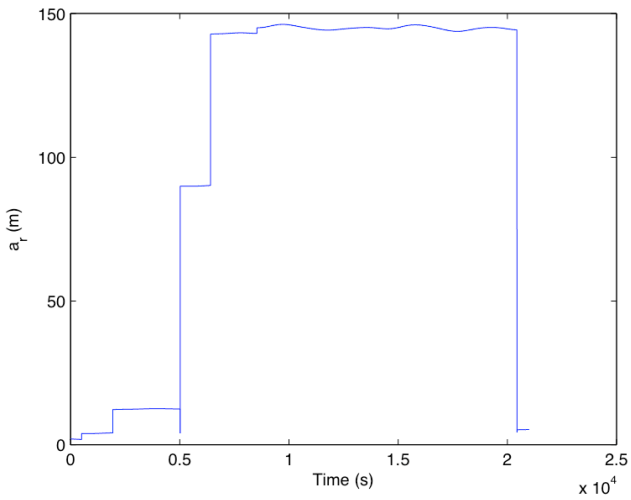
Figure 51: ROE transfer scenario with APF obstacle avoidance, (a) $\hat{y} - \hat{x}$ projection, (b) $\hat{z} - \hat{x}$ projection, (c) $\hat{z} - \hat{y}$ projection, (d) 3D trajectory plot.



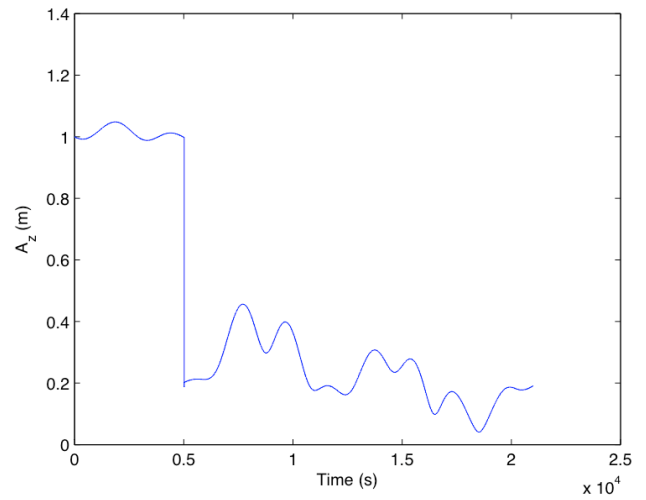
(a)



(b)



(c)



(d)

Figure 52: ROE transfer scenario with APF obstacle avoidance, (a) x_r as a function of time, (b) y_r as a function of time, (c) a_r as a function of time, (d) A_z as a function of time.

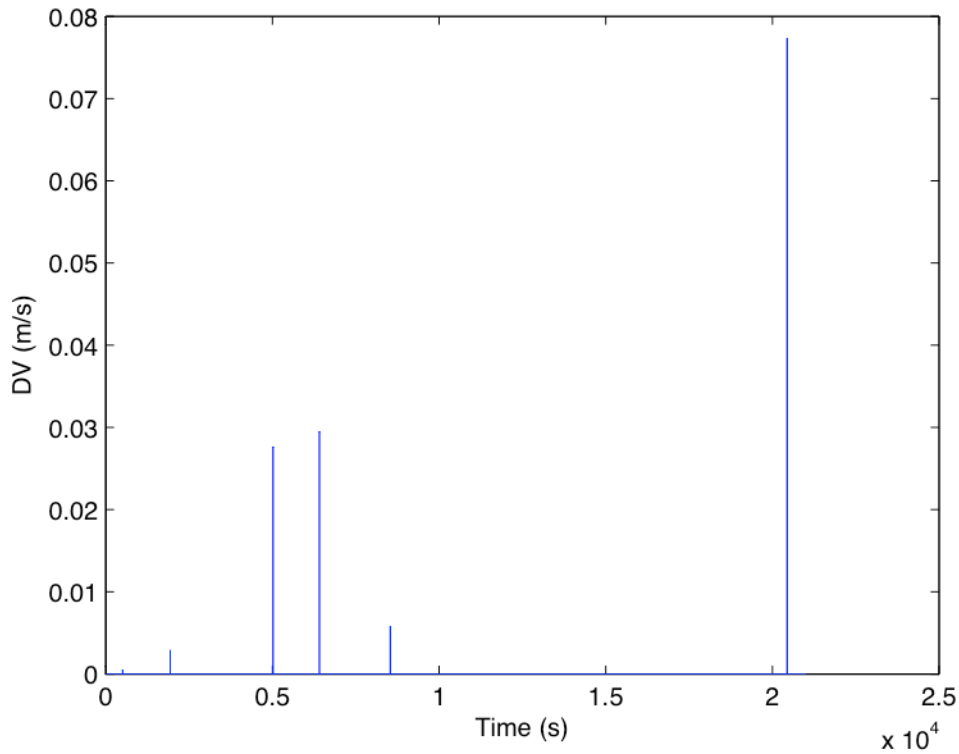


Figure 53: ROE transfer scenario with APF obstacle avoidance, maneuver magnitudes.

4.5 Artificial Potential Function Targeting of Relative Orbital Elements

The APF targeting of a relative orbit geometry specified by a set of ROEs is demonstrated in this scenario. The APF formulation described in Section 3.2.5 is used to target the ROEs x_r , y_r , a_r , and A_z . The scenario is summarized in Table 50. Initially, the deputy spacecraft is in a relative orbit centered on $[x_r, y_r] = [0, 162.111]$ m, with $a_r = 37.888$ m and $A_z = 18.944$ m. The objective is to re-center the relative orbit to $[x_r, y_r] = [0, 120]$ m, with $a_r = 60$ m and $A_z = 20$ m.

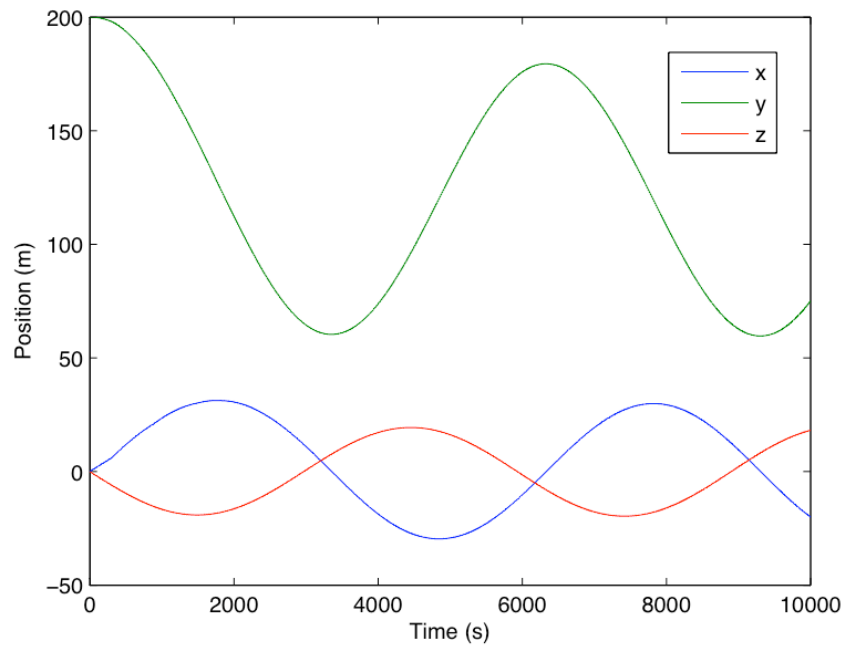
During the 10,000 s simulation, it is seen that the APF is successful in targeting the specified ROEs. Figure 54 shows the relative position and velocity components as a function of time. Figure 55 shows the projection of the trajectory onto the coordinate planes, and the three-dimensional trajectory plot. For comparison purposes, the trajectory

including all orbital perturbations is shown in blue, and the trajectory with no orbital perturbations is shown in red. From Figure 55(a), it is seen that the progression from the initial orbit to the targeted orbit geometry is very smooth, with rapid convergence to the desired orbit. The effect of orbital perturbations is most pronounced early in the trajectory, but once the APF control is exerted and the trajectory approaches the target ROE conditions, the effect of orbit perturbations on the controlled trajectory is minor. Figure 56 shows the time histories of x_r , y_r , a_r , and A_z . The ROE time histories for the trajectory including all orbital perturbations are shown in blue, and for comparison the trajectory without the $J_2 - J_6$ gravitational spherical harmonics (but including all other orbital perturbations) is shown in red. It is clear from Figure 56 that the gravitational spherical harmonics are the primary cause of the “drift” with time of the ROEs x_r , a_r , and A_z , which are constant with time under the Clohessy-Wilshire assumptions. At the conclusion of the 10,000 s simulation, each of the specified ROEs has a value that is within 0.2 m of the target value. The maneuver magnitudes as a function of time are shown in Figure 57. A maneuver is performed roughly every 300 s, with generally decreasing magnitude. A spacing of 300 s between maneuvers is enforced within the simulation framework, to allow time for slews to the specified maneuver attitude. It is noted that a minimum burn duration of 0.01 s is applied in the simulation, corresponding to a minimum ΔV of approximately 1E-04 m/s. The total ΔV utilization in this scenario is 0.030 m/s.

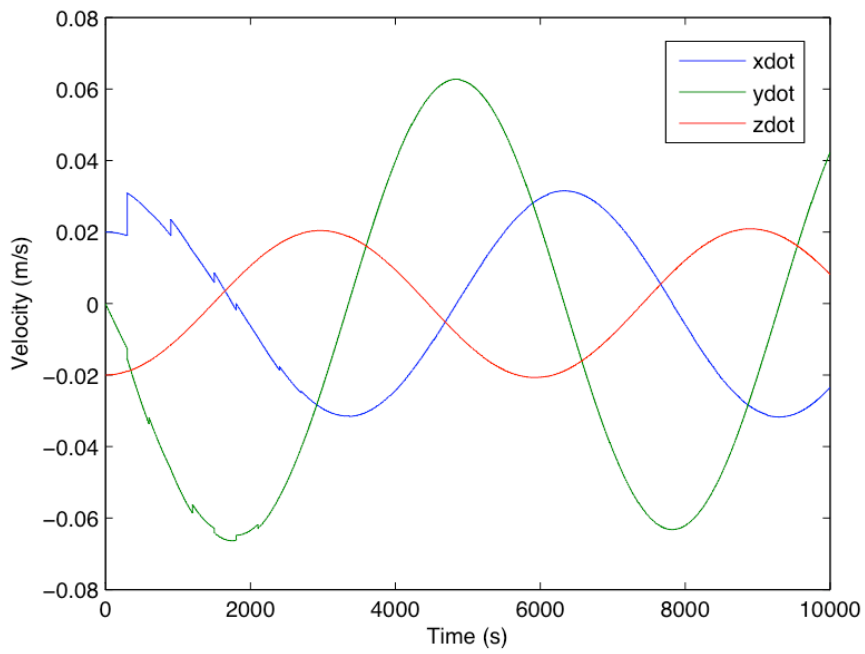
This scenario shows that the APF targeting of ROEs can be successfully performed within an environment that includes orbital perturbations, and with realistic limitations on maneuver timing and maneuver magnitude. Unlike previous APF approaches that target a relative range vector (as described in Section 3.1), this scenario shows that APFs may be used to effectively control the spacecraft to target a specified orbit geometry.

Table 50: APF targeting of ROEs x_d, y_d, a_r, A_z .

Initial Conditions	Cartesian	$x = 0 \text{ m}$ $\dot{x} = 0.020 \text{ m/s}$ $y = 200 \text{ m}$ $\dot{y} = 0.000 \text{ m/s}$ $z = 0 \text{ m}$ $\dot{z} = 0.020 \text{ m/s}$
	ROEs	$x_r = 0 \text{ m}$ $y_r = 162.111 \text{ m}$ $a_r = 37.888 \text{ m}$ $E_r = 1.5708 \text{ rad}$ $A_z = 18.944 \text{ m}$ $\psi = 0 \text{ rad}$
Target ROEs		$x_r = 0 \text{ m}$ $y_r = 120 \text{ m}$ $a_r = 60 \text{ m}$ $A_z = 20 \text{ m}$
APF Parameters		$k_a = 1E - 07$ $\bar{\bar{Q}}_a = \bar{\bar{I}}_{4 \times 4}$

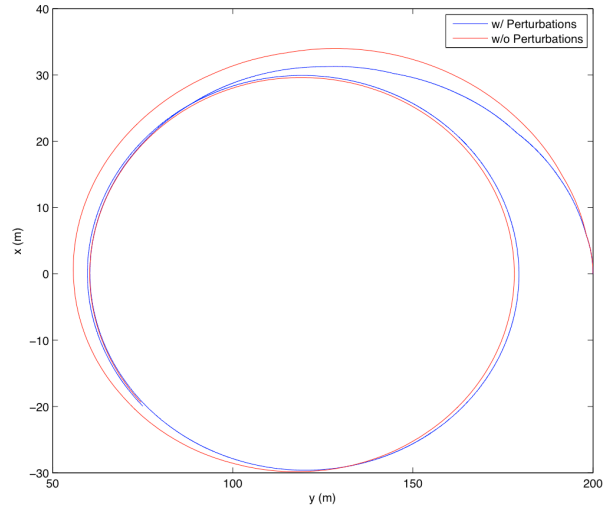


(a)

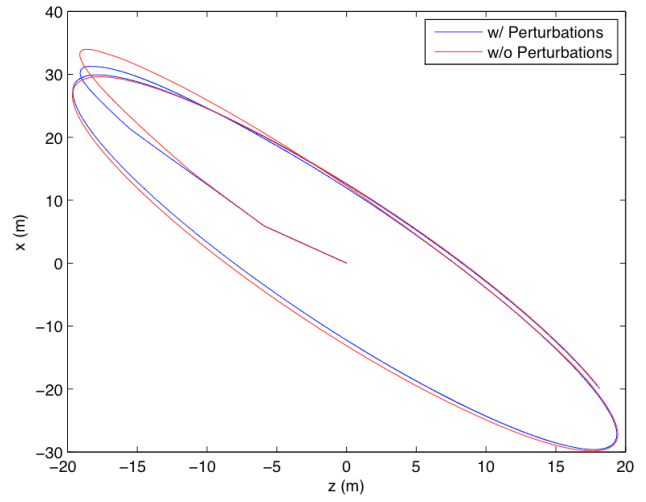


(b)

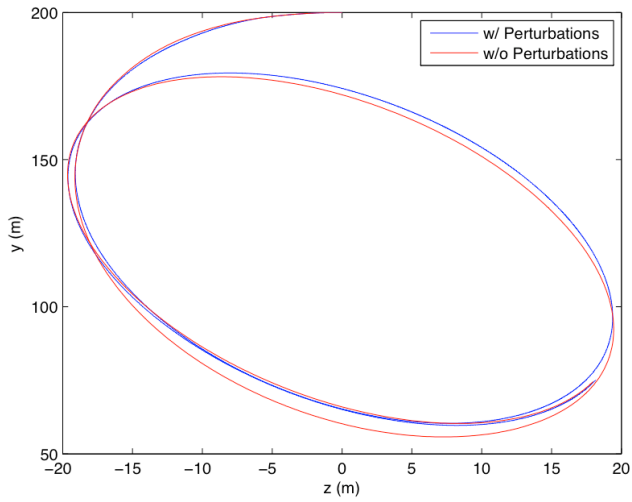
Figure 54: APF targeting of relative orbital elements, (a) Relative position components as a function of time, (b) Relative velocity components as a function of time.



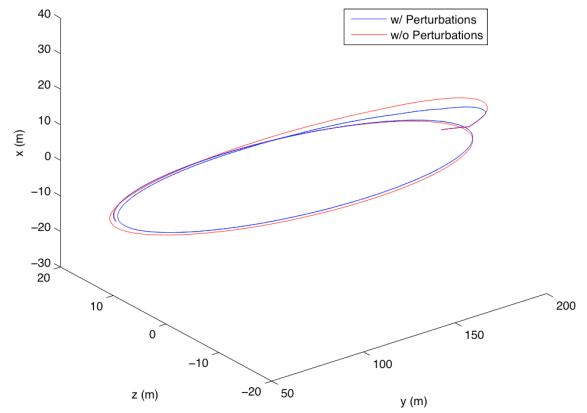
(a)



(b)

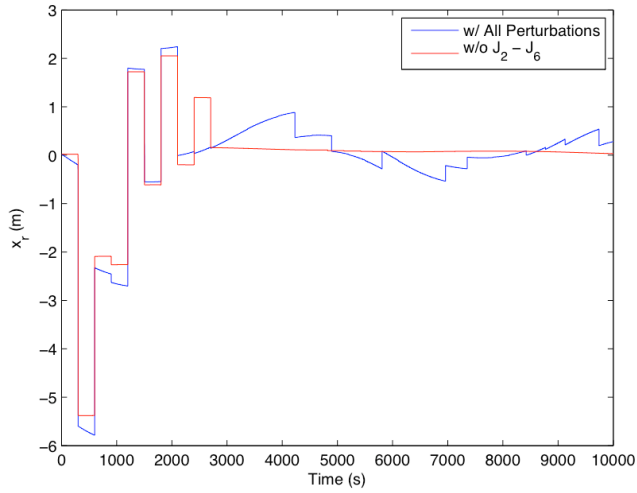


(c)

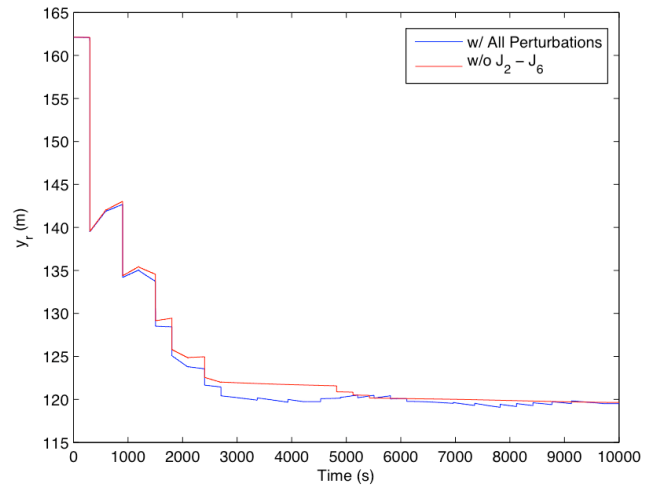


(d)

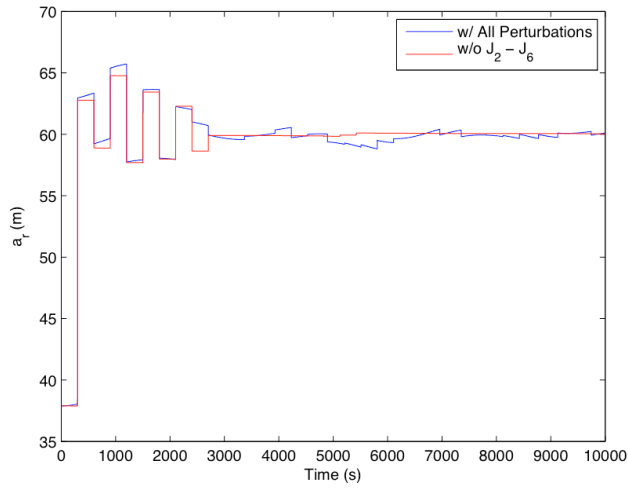
Figure 55: APF targeting of relative orbital elements, (a) $\hat{y} - \hat{x}$ projection, (b) $\hat{z} - \hat{x}$ projection, (c) $\hat{z} - \hat{y}$ projection, (d) 3D trajectory plot.



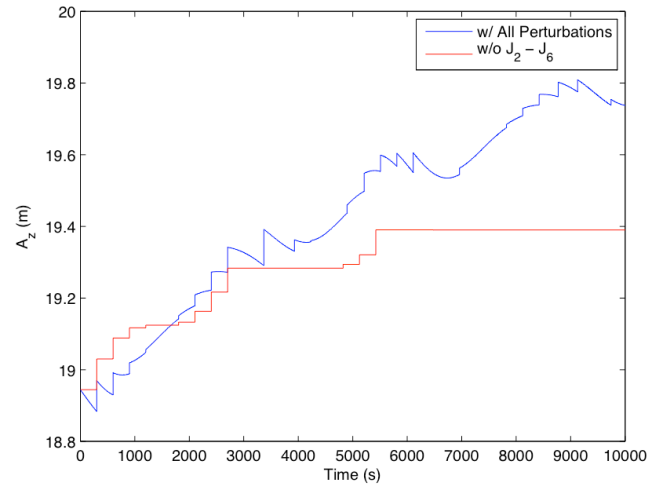
(a)



(b)



(c)



(d)

Figure 56: APF targeting of relative orbital elements, (a) x_r as a function of time, (b) y_r as a function of time, (c) a_r as a function of time, (d) A_z as a function of time.

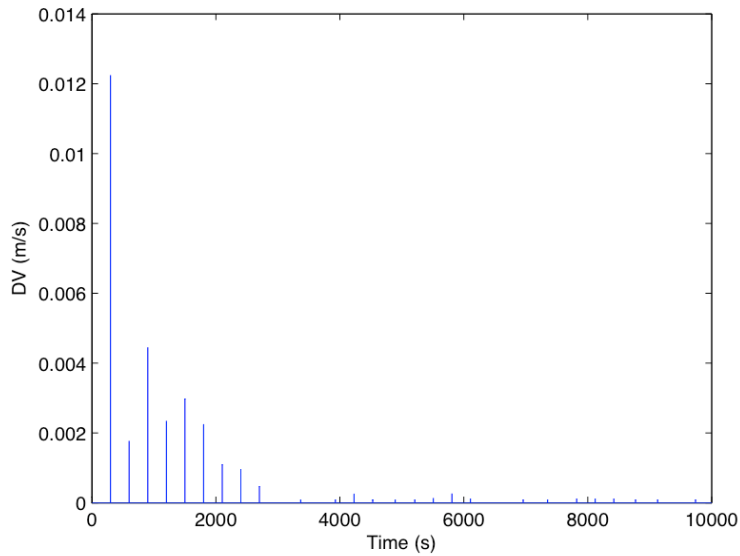


Figure 57: APF targeting of relative orbital elements, maneuver magnitudes.

4.6 Artificial Potential Function Targeting of Relative Orbital Elements with Obstacle Avoidance

In this scenario, the same ROE targets are used as in Section 4.5, however an obstacle is inserted directly in the desired orbital path. A repulsive APF is utilized to ensure obstacle avoidance, and the attractive APF restores the trajectory to the desired parameters. To simplify visualization, no cross-track motion is modeled in this scenario. The obstacle is placed at $[x, y, z] = [0, 60, 0]$ m. The scenario is summarized in Table 51.

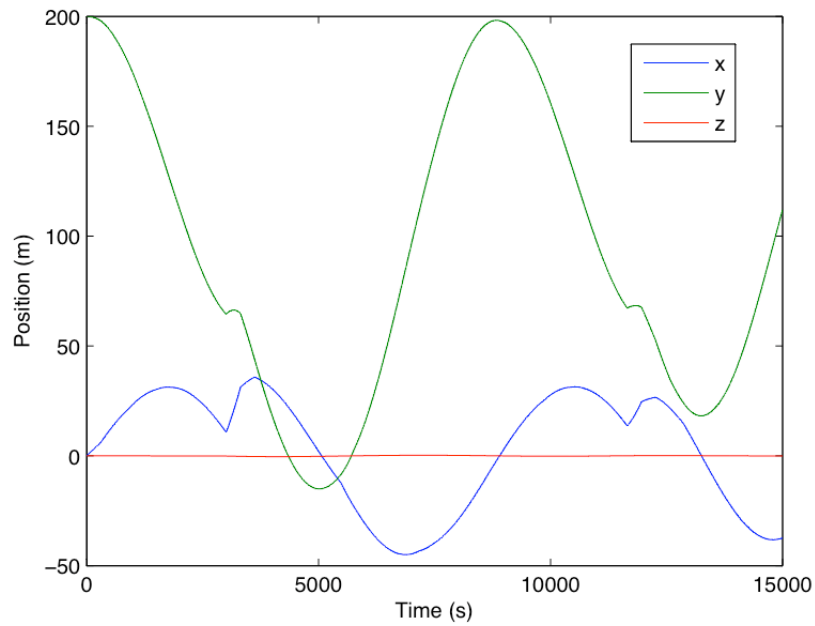
The relative position and velocity components as a function of time are shown in Figure 58, and the trajectory in the $\hat{x} - \hat{y}$ plane is shown in Figure 59. The effect of the repulsive potential is clearly apparent in Figure 59; repulsive maneuvers are performed twice during the simulation to control the trajectory away from the obstacle. However, the attractive APF is able to restore the trajectory toward the targeted ROE values, as shown in Figure 60. Because the obstacle is directly in the path of the desired orbit, the targeted ROEs cannot be precisely attained, however, the attractive APF persistently

controls the orbit in the direction of the desired ROE values. The maneuver magnitudes are shown in Figure 61. The largest maneuvers are the repulsive maneuvers, and each repulsive maneuver is followed by a large attractive maneuver to restore the trajectory toward the ROE targets. The total ΔV utilization in this scenario is 0.415 m/s.

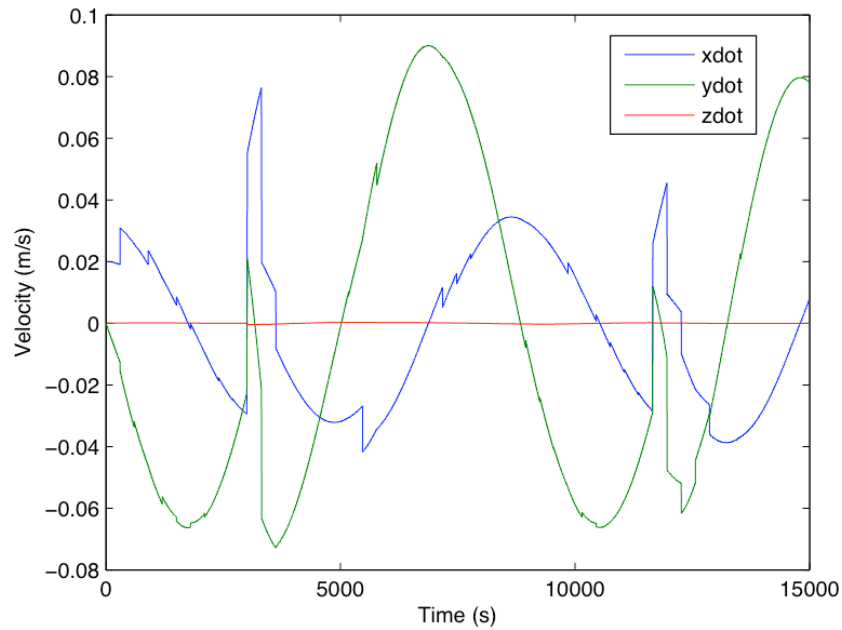
This scenario shows that attractive and repulsive APFs may be utilized together in a realistic environment to target a desired orbit geometry while providing persistent obstacle avoidance in an automated fashion. Even in the worst-case scenario where the obstacle is placed directly in the desired orbit path, the control formulation provides bounded orbital motion that trends toward the goal.

Table 51: APF targeting of ROEs x_d, y_d, a_r, A_z , with obstacle avoidance.

Initial Conditions	Cartesian	$x = 0.0000 \text{ m}$ $\dot{x} = 0.020000 \text{ m/s}$ $y = 200.0000 \text{ m}$ $\dot{y} = 0.000000 \text{ m/s}$ $z = 0.0000 \text{ m}$ $\dot{z} = 0.000000 \text{ m/s}$
	ROEs	$x_r = 0.0000 \text{ m}$ $y_r = 162.1114 \text{ m}$ $a_r = 37.8886 \text{ m}$ $E_r = 1.5708 \text{ rad}$ $A_z = 0.0000 \text{ m}$ $\psi = 0.0000 \text{ rad}$
Target ROEs		$x_r = 0.0000 \text{ m}$ $y_r = 120.0000 \text{ m}$ $a_r = 60.0000 \text{ m}$ $A_z = 0.0000 \text{ m}$
Obstacle Location		$x = 0.0000 \text{ m}$ $y = 60.0000 \text{ m}$ $z = 0.0000 \text{ m}$
APF Parameters		$k_a = 1E - 07$ $\bar{\bar{Q}}_a = \bar{\bar{I}}_{4 \times 4}$ $k_r = 1$ $\bar{\bar{Q}}_r = \bar{\bar{I}}_{3 \times 3}$ $\sigma = 100$ $r_{obs_soi} = 20 \text{ m}$



(a)



(b)

Figure 58: APF targeting of ROEs x_d, y_d, a_r, A_z , with obstacle avoidance, (a) Relative position components as a function of time, (b) Relative velocity components as a function of time.

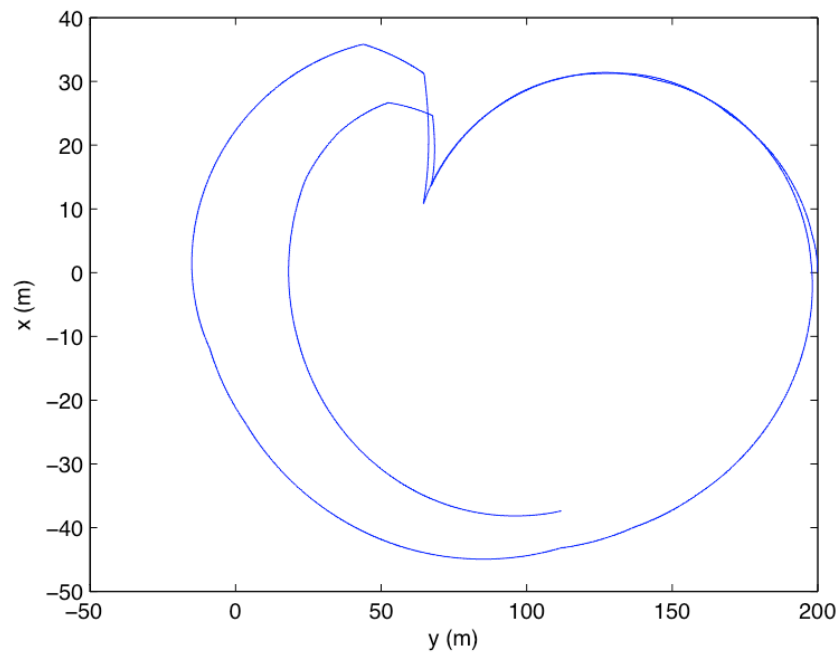
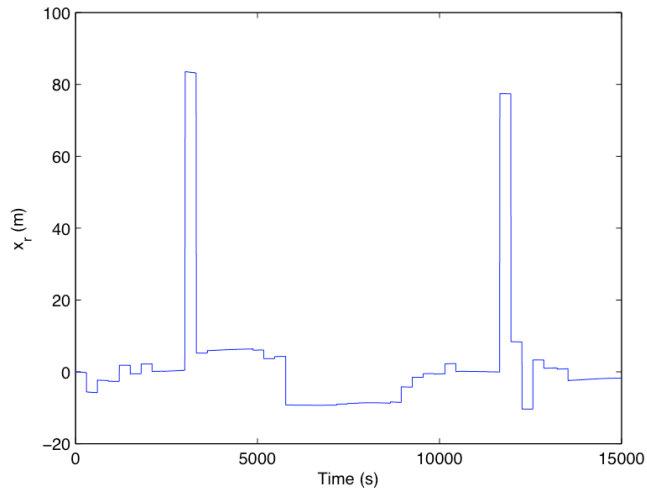
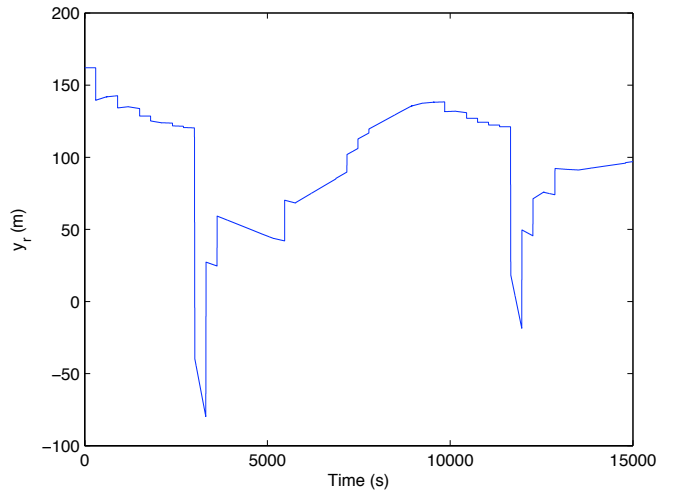


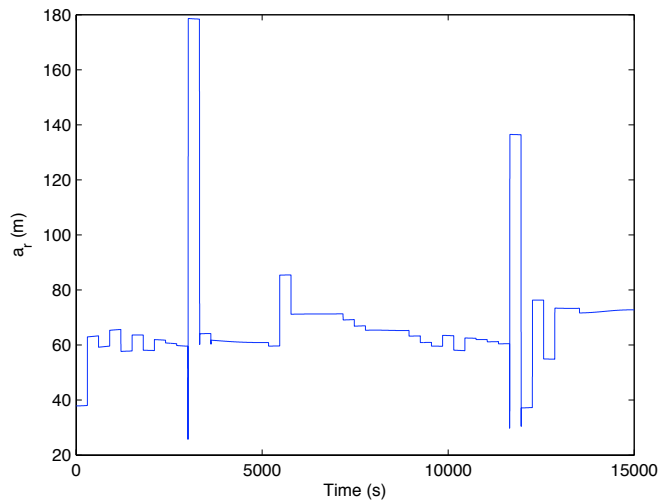
Figure 59: APF targeting of ROEs x_d, y_d, a_r, A_z , with obstacle avoidance, $\hat{y} - \hat{x}$ projection.



(a)



(b)



(c)

Figure 60: APF targeting of ROEs x_d, y_d, a_r, A_z , with obstacle avoidance, (a) x_r as a function of time, (b) y_r as a function of time, (c) a_r as a function of time.

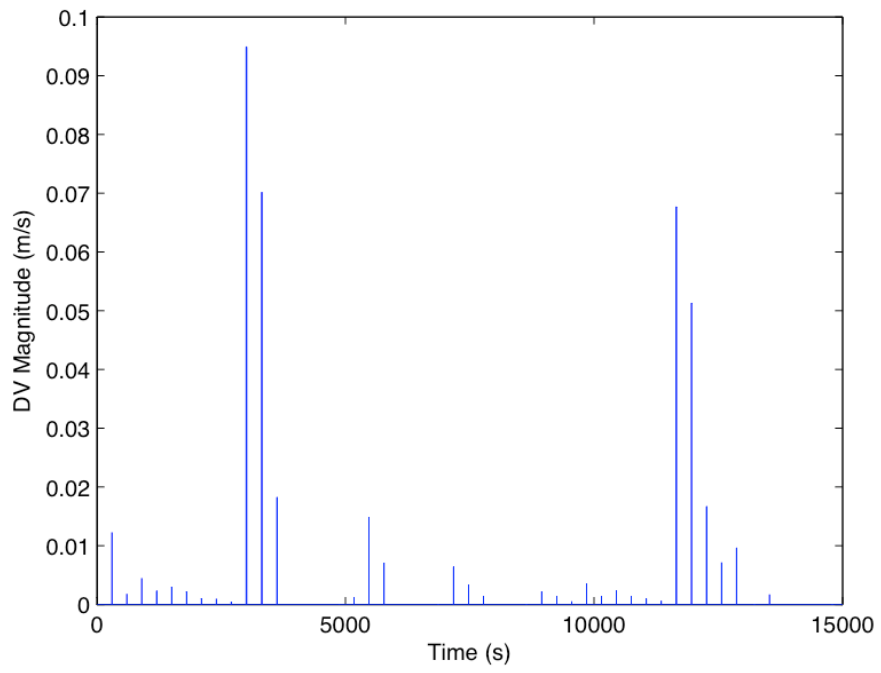


Figure 61: APF targeting of ROEs x_d, y_d, a_r, A_z , with obstacle avoidance, maneuver magnitudes.

CHAPTER 5

CONCLUSIONS AND FUTURE WORK

5.1 Conclusions

This work has presented a new methodology for automated trajectory control for relative proximity operations. The methodology combines the geometric representation of relative orbits that is inherent to the relative orbital elements formulation with artificial potential functions to allow specified orbit geometries to be targeted in an automated fashion.

A complete derivation of the relative orbital elements formulation is provided for the first time. Geometric interpretation of the angular ROEs, E_r , and ψ , are developed, advancing the ROE formulation. Key parameters related to ROEs are defined, including the new parameters relative true anomaly and relative inclination; introduction of these parameters strengthens the analogy between relative orbital elements and classical orbital elements. Transformations between ROEs and the LVLH Cartesian state elements are derived, and expressions for the evolution of ROEs with time are presented. The unforced relative motion trajectory is characterized in terms of ROEs. Three primary modes of the motion are described in terms of the values for ROEs x_r , a_r , and A_z . The changes in ROEs due to a single impulsive maneuver are presented, and an evaluation of ROE variation based upon impulsive maneuver components is provided. ROE-based control strategies are developed, and scenarios are presented including rendezvous, natural motion circumnavigation, and station-keeping in a leading or trailing orbit.

This work develops a new formulation for artificial potential functions that are expressed in terms of ROEs, in order to shape the trajectory along paths that utilize the natural motion established by the relative orbit dynamics, while targeting the desired relative orbit. While previous approaches allowed targeting of a relative position, the ROE-based approach allows the targeting of an orbit geometry while retaining the computational simplicity of the APF approach. Formulations for the APF targeting of individual ROEs, as well as simultaneous targeting of a set of ROEs, are established. An approach for combining ROE targeting using APFs with obstacle avoidance is presented. Convergence of the APF algorithms to the targeted ROE values is evaluated using a Monte Carlo analysis, and convergence is consistently shown for attractive APFs, as well as attractive APFs combined with repulsive APFs for obstacle avoidance. Maneuver magnitudes using the APF approach were evaluated relative to an optimized two-impulse transfer scheme using Clohessy-Wiltshire state transition matrices. While there is no expectation of optimality for the APF-based approach, it is shown that, on average, the APF approach utilizes fifty percent more ΔV than the optimized Clohessy-Wiltshire state transition matrix approach.

The performance of the trajectory control algorithms were evaluated using a realistic guidance, navigation and control simulation environment, including orbital perturbations such as third body effects, aerodynamic drag, and finite burn effects. Scenarios were evaluated, including ROE station-keeping, ROE transfers to leading or trailing orbits, ROE transfers with APF-based obstacle avoidance, and APF targeting of ROEs with and without APF-based obstacle avoidance. In each scenario, the behavior of the trajectory control algorithm is consistent with expectations and the desired orbit

characteristics are met. The control algorithms are shown to be capable of correcting for environmental disturbances to the trajectory.

In summary, ROEs are shown to provide fundamental insight into the relative orbit geometry, providing a useful framework for mission planning and maneuver design. Artificial potential functions, formulated to target ROEs, provide a computationally efficient approach for controlling the spacecraft trajectory to the desired relative orbit geometry in an automated fashion.

5.2 Suggestions for Future Work

As discussed in Chapter 1, there are several different parameter sets for relative motion that have been developed previously, with various applications to orbital mission design. A survey of relative motion formulations would be extremely useful, including transformations between relative motion parameter sets, where applicable. In particular, a comparison of the ROE formulation presented in this work and classical orbital element approaches would be of interest.

The ROE re-parameterization of the Clohessy-Wiltshire solution provides fundamental insight into the relative motion within the context of the underlying assumptions that the chief's two-body orbit is circular, and the relative distance between the chief and deputy is much less than the chief's orbit radius about the central body. Using a similar approach for the case where the chief is on an elliptical two-body orbit about the central body, a set of ROEs may be constructed that yield geometric insight into the relative motion. The Tschauner-Hempel equations are a set of linearized equations expressed in the LVLH frame, representing the relative motion of a deputy about a chief on an elliptical orbit with arbitrary eccentricity [72]. The analytical solution of the

Tschauner-Hempel equations produces six independent fundamental solutions. Sinclair et al provide a geometric interpretation of these solutions and define a set of constant parameters to characterize the relative motion [73]. Similarly, it may be possible to construct a set of ROEs for the parabolic chief problem that yields fundamental insight into the relative motion, with application for deep space and interstellar missions. The analytical guidance methodologies presented in Chapter 2 may be compared with other similar approaches, including the constant-thrust impulse-shaping approach developed by Bevilacqua et al [49].

The approach for APF targeting of ROEs presented in this work may be advanced to yield faster convergence to the desired orbit geometry. In cases where targeting $x_r = 0$ simultaneously with y_r , convergence may be slowed because as x_r approaches zero, the rate of change of y_r approaches zero. As a result, it takes longer for y_r to reach its targeted value. An approach for “relaxation” of the x_r target value, initially targeting non-zero values for x_r and recursively reducing the magnitude of the x_r target value as y_r approaches the target, may yield significantly improved convergence times.

Approaches to optimize the ΔV utilization for APF-based targeting of ROEs may be pursued. The ROE maneuver logic structure may be utilized to further constrain the maneuver locations such that the partial derivatives of the change in the ROEs with respect to the maneuver magnitudes are maximized. Alternate formulations of the APFs to minimize maneuver magnitudes may be explored.

A promising application for the APF-based targeting of ROEs is the formation control of multiple spacecraft in orbit about a chief (or relative to a “virtual” chief). In this work, the angular ROEs E_r and ψ have not been explicitly targeted. However, for

formation control, establishing and maintaining differences between the angular ROEs of the various spacecraft in the network may be necessary for establishing the desired formation orbit. An approach for the APF-based collaborative control of a network of spacecraft in relative motion is a logical next step in this formulation.

As discussed in Chapter 4, this work evaluated effect of environmental disturbances on the performance of the automated trajectory control algorithms. To extend the performance assessment, spacecraft-specific error sources should be included. Relative orbit determination error, attitude determination error, attitude control error, and maneuver execution errors may have a significant effect on the trajectory control performance. Also, reaction wheel desaturation events may affect the timing of planned maneuvers. Finally, robustness testing (e.g., “break it” testing) would be useful to determine how much margin is inherent to the control formulations presented herein. A determination of the limitations of the trajectory control algorithms’ capability to correct for spacecraft error sources and environmental perturbations due to different orbit geometries would be highly useful prior to flight implementation.

APPENDIX A

APPLICATION OF THE HARMONIC ADDITION THEOREM TO THE SOLUTION OF THE CLOHESSY-WILTSHIRE EQUATIONS

A.1 Harmonic Addition Theorem

The Harmonic Addition Theorem states that a sum of sinusoidal functions of the form:

$$f(\theta) = A \cos \theta + B \sin \theta \quad (\text{A.1})$$

can be written as a single sinusoid of the form:

$$f(\theta) = C \cos(\theta + \delta) \quad (\text{A.2})$$

where

$$C = \text{sgn}(A) \sqrt{A^2 + B^2} \quad (\text{A.3})$$

and

$$\delta = \tan^{-1} \left(-\frac{B}{A} \right) \quad (\text{A.4})$$

This can be shown as follows. Expanding Eq. (A.2) using trigonometric addition formulas:

$$f(\theta) = C \cos \theta \cos \delta - C \sin \theta \sin \delta \quad (\text{A.5})$$

Equating the coefficients of Eqs. (A.1) and (A.5) gives:

$$A = C \cos \delta \quad (\text{A.6})$$

$$B = -C \sin \delta \quad (\text{A.7})$$

Combining Eqs. (A.6) and (A.7),

$$\tan \delta = \frac{\sin \delta}{\cos \delta} = -\frac{B/C}{A/C} = -\frac{B}{A}, \quad A \neq 0 \quad (\text{A.8})$$

so

$$\delta = \tan^{-1} \left(-\frac{B}{A} \right) \quad (\text{A.9})$$

Also, from Eqs. (A.6) and (A.7),

$$A^2 + B^2 = (C \cos \delta)^2 + (-C \sin \delta)^2 = C^2 \quad (\text{A.10})$$

Therefore,

$$C = \pm \sqrt{A^2 + B^2} \quad (\text{A.11})$$

To remove the sign ambiguity for C, from Eq. (A.6) it is seen that:

$$C = \frac{A}{\cos \delta} \quad (\text{A.12})$$

From the inverse tangent function in Eq. (A.4), it is evident that $-\frac{\pi}{2} < \delta < \frac{\pi}{2}$, so

$\cos \delta > 0$. Therefore, if $A > 0$, then $C > 0$, and the positive root is taken in Eq. (A.11).

Similarly, if $A < 0$, then $C < 0$, and the negative root is taken. Thus, Eq. (A.11) can be refined to:

$$C = \text{sgn}(A) \sqrt{A^2 + B^2}, \quad A \neq 0 \quad (\text{A.13})$$

Combining Eqs. (A.1) and (A.2), and substituting in Eqs. (A.9), (A.13) and (A.14) gives:

$$f(\theta) = A \cos \theta + B \sin \theta = \text{sgn}(A) \sqrt{A^2 + B^2} \cos \left[\theta + \tan^{-1} \left(-\frac{B}{A} \right) \right], \quad A \neq 0$$

(A.14)

From Eq. (A.1):

$$f(\theta) = B \sin \theta, \quad A = 0 \quad (\text{A.15})$$

A.2 Application of the Harmonic Addition Theorem to the Solution to the Clohessy-Wiltshire Equations

The position solution to the Clohessy-Wiltshire equations is given by Eqs. (49) through (51) as:

$$x = \frac{\dot{x}_0}{n} \sin[n(t-t_0)] - \left(3x_0 + \frac{2\dot{y}_0}{n}\right) \cos[n(t-t_0)] + 4x_0 + \frac{2\dot{y}_0}{n} \quad (\text{A.16})$$

$$y = \frac{2\dot{x}_0}{n} \cos[n(t-t_0)] + \left(6x_0 + \frac{4\dot{y}_0}{n}\right) \sin[n(t-t_0)] - (6nx_0 + 3\dot{y}_0)(t-t_0) - \frac{2\dot{x}_0}{n} + y_0 \quad (\text{A.17})$$

$$z = \frac{\dot{z}_0}{n} \sin[n(t-t_0)] + z_0 \cos[n(t-t_0)] \quad (\text{A.18})$$

The Harmonic Addition Theorem, as stated in Eqs. (A.14) and (A.15), may be applied to Eqs. (A.16) through (A.18), in order to simplify the expressions and derive the standard form for the LVLH Cartesian states in terms of ROEs.

A.2.1 Application of the Harmonic Addition Theorem to the x-Component of the Clohessy-Wiltshire Solution

The x-component of the Clohessy-Wiltshire solution expressed in Eq. (A.16) can be rewritten as:

$$x(t) = x_r + A \cos \theta + B \sin \theta \quad (\text{A.19})$$

where, from Eq. (61):

$$x_r = 4x_0 + \frac{2\dot{y}_0}{n} \quad (\text{A.20})$$

and the coefficients and phase angle are defined using the form of Eq. (A.1) as:

$$A = -\left(3x_0 + \frac{2\dot{y}_0}{n}\right) \quad (\text{A.21})$$

$$B = \frac{\dot{x}_0}{n} \quad (\text{A.22})$$

$$\theta = n(t - t_0) \quad (\text{A.23})$$

Equation (65) defines a_r as:

$$a_r = \sqrt{\left(6x_0 + \frac{4\dot{y}_0}{n}\right)^2 + \left(\frac{2\dot{x}_0}{n}\right)^2} \quad (\text{A.24})$$

By inspection, it is clear from Eqs. (A.21), (A.22) and (A.24) that

$$\frac{a_r}{2} = \sqrt{A^2 + B^2} \quad (\text{A.25})$$

The Harmonic Addition Theorem as expressed in Eq. (A.14) may be applied to Eq. (A.19), resulting in:

$$x(t) = x_r + \text{sgn}(A) \frac{a_r}{2} \cos\left[\theta + \tan^{-1}\left(\frac{B}{-A}\right)\right], \quad A \neq 0 \quad (\text{A.26})$$

and Eq. (A.15) may be applied to Eq. (A.19) to give:

$$x(t) = x_r + B \sin \theta, \quad A = 0 \quad (\text{A.27})$$

Eqs. (A.26) and (A.27) will be evaluated for all combinations of values for A and B . It will be shown that the following expression utilizing the atan2 function encompasses

both Eqs. (A.26) and (A.27), for all combinations of values for A and B except for $A = 0$, $B = 0$:

$$x(t) = x_r - \frac{a_r}{2} \cos[\theta + \text{atan2}(B, -A)] \quad (\text{A.28})$$

For $A = 0$, $B = 0$, it will be shown that

$$x(t) = x_r \quad (\text{A.29})$$

$A > 0, B \geq 0$

For these conditions, $-A < 0$ and the function $\text{atan2}(B, -A)$ is related to the inverse tangent function by:

$$\text{atan2}(B, -A) = \tan^{-1}\left(\frac{B}{-A}\right) + \pi \quad (\text{A.30})$$

Substituting Eq. (A.30) into (A.26) gives:

$$x(t) = x_r + \text{sgn}(A) \frac{a_r}{2} \cos[\theta + \text{atan2}(B, -A) - \pi] \quad (\text{A.31})$$

Noting that:

$$\cos[\theta + \text{atan2}(B, -A) - \pi] = -\cos[\theta + \text{atan2}(B, -A)] \quad (\text{A.32})$$

and since for these conditions $\text{sgn}(A) = 1$, substitution into Eq. (A.31) gives

$$x(t) = x_r - \frac{a_r}{2} \cos[\theta + \text{atan2}(B, -A)] \quad (\text{A.33})$$

$A > 0, B < 0$

For these conditions, $-A < 0$ and the function $\text{atan2}(B, -A)$ is related to the inverse tangent function by:

$$\text{atan2}(B, -A) = \tan^{-1}\left(\frac{B}{-A}\right) - \pi \quad (\text{A.34})$$

Substituting Eq. (A.34) into (A.26) gives:

$$x(t) = x_r + \text{sgn}(A) \frac{a_r}{2} \cos[\theta + \text{atan2}(B, -A) + \pi] \quad (\text{A.35})$$

Noting that:

$$\cos[\theta + \text{atan2}(B, -A) + \pi] = -\cos[\theta + \text{atan2}(B, -A)] \quad (\text{A.36})$$

and since for these conditions $\text{sgn}(A) = 1$, substitution into Eq. (A.35) gives:

$$x(t) = x_r - \frac{a_r}{2} \cos[\theta + \text{atan2}(B, -A)] \quad (\text{A.37})$$

$A < 0, B$ unconstrained

For these conditions, $-A > 0$ and the function $\text{atan2}(B, -A)$ is related to the inverse tangent function by:

$$\text{atan2}(B, -A) = \tan^{-1}\left(\frac{B}{-A}\right) \quad (\text{A.38})$$

Substituting Eq. (A.38) into (A.26) gives:

$$x(t) = x_r + \text{sgn}(A) \frac{a_r}{2} \cos[\theta + \text{atan2}(B, -A)] \quad (\text{A.39})$$

For these conditions, $\text{sgn}(A) = -1$, and substitution into Eq. (A.39) gives:

$$x(t) = x_r - \frac{a_r}{2} \cos[\theta + \text{atan2}(B, -A)] \quad (\text{A.40})$$

$A = 0, B > 0$

From Eq. (A.19), with $A = 0$,

$$x(t) = x_r + B \sin \theta \quad (\text{A.41})$$

Solving Eq. (A.25) for B with $A = 0$ gives:

$$B = \frac{a_r}{2} \quad (\text{A.42})$$

Also,

$$\sin(\theta) = \cos\left(\theta - \frac{\pi}{2}\right) = -\cos\left(\theta + \frac{\pi}{2}\right) \quad (\text{A.43})$$

Substituting Eqs. (A.42) and (A.43) into (A.41) gives:

$$x(t) = x_r - \frac{a_r}{2} \cos\left(\theta + \frac{\pi}{2}\right) \quad (\text{A.44})$$

For $A = 0, B > 0$, the atan2 function can be evaluated as:

$$\text{atan2}(B, -A) = \frac{\pi}{2} \quad (\text{A.45})$$

Therefore, Eq. (A.44) can be written as:

$$x(t) = x_r - \frac{a_r}{2} \cos[\theta + \text{atan2}(B, -A)] \quad (\text{A.46})$$

$A = 0, B < 0$

From Eq. (A.19), with $A = 0$,

$$x(t) = x_r + B \sin \theta \quad (\text{A.47})$$

Solving Eq. (A.25) for B with $A = 0$ gives:

$$B = \frac{a_r}{2} \quad (\text{A.48})$$

Also,

$$\sin(\theta) = \cos\left(\theta - \frac{\pi}{2}\right) \quad (\text{A.49})$$

Substituting Eqs. (A.48) and (A.49) into (A.47) gives:

$$x(t) = x_r - \frac{a_r}{2} \cos\left(\theta - \frac{\pi}{2}\right) \quad (\text{A.50})$$

For $A = 0, B < 0$, the atan2 function can be evaluated as:

$$\text{atan2}(B, -A) = -\frac{\pi}{2} \quad (\text{A.51})$$

Therefore, Eq. (A.50) can be written as:

$$x(t) = x_r - \frac{a_r}{2} \cos\left[\theta + \text{atan2}(B, -A)\right] \quad (\text{A.52})$$

$A = 0, B = 0$

From Eq. (A.19), with $A = 0, B = 0$, it is seen that:

$$x(t) = x_r \quad (\text{A.53})$$

It is noted that this is the only case where the x -component of the LVLH position vector cannot be represented by Eq. (A.28), since $\text{atan2}(0, 0)$ is generally undefined. However, when coding in MATLAB, the $\text{atan2}(0, 0)$ function is evaluated as zero. Since, from Eq. (A.25), $a_r = 0$ for $A = 0, B = 0$, Eq. (A.28) will evaluate correctly to $x(t) = x_r$ using MATLAB.

A.2.2 Application of the Harmonic Addition Theorem to the y -Component of the Clohessy-Wiltshire Solution

The y -component of the Clohessy-Wiltshire solution expressed in Eq. (A.17) can be rewritten as:

$$y(t) = y_r + A \cos \theta + B \sin \theta \quad (\text{A.54})$$

where, from Eq. (62):

$$y_r = y_0 - \frac{2\dot{x}_0}{n} - (6nx_0 + 3\dot{y}_0)(t - t_0) \quad (\text{A.55})$$

The coefficients and phase angle are defined using the form of Eq. (A.1) as:

$$A = \frac{2\dot{x}_0}{n} \quad (\text{A.56})$$

$$B = 6x_0 + \frac{4\dot{y}_0}{n} \quad (\text{A.57})$$

$$\theta = n(t - t_0) \quad (\text{A.58})$$

Equation (65) defines a_r as:

$$a_r = \sqrt{\left(6x_0 + \frac{4\dot{y}_0}{n}\right)^2 + \left(\frac{2\dot{x}_0}{n}\right)^2} \quad (\text{A.59})$$

By inspection, it is clear from Eqs. (A.56), (A.57) and (A.59) that

$$\frac{a_r}{2} = \sqrt{A^2 + B^2} \quad (\text{A.60})$$

The Harmonic Addition Theorem as expressed in Eq. (A.14) may be applied to Eq. (A.54), resulting in:

$$y(t) = y_r + \text{sgn}(A)a_r \cos\left[\theta + \tan^{-1}\left(-\frac{B}{A}\right)\right], \quad A \neq 0 \quad (\text{A.61})$$

which is equivalent to:

$$y(t) = y_r + \text{sgn}(A)a_r \cos\left[\theta - \tan^{-1}\left(\frac{B}{A}\right)\right], \quad A \neq 0 \quad (\text{A.62})$$

Eq. (A.15) may be applied to Eq. (A.54) to give:

$$y(t) = y_r + B \sin \theta, \quad A = 0 \quad (\text{A.63})$$

Eqs. (A.62) and (A.63) will be evaluated for all combinations of values for A and B . It will be shown that the following expression utilizing the atan2 function encompasses both Eqs. (A.61) and (A.62), for all combinations of values for A and B except for $A = 0$, $B = 0$:

$$y(t) = y_r + a_r \sin[\theta + \text{atan2}(A, B)] \quad (\text{A.64})$$

For $A = 0$, $B = 0$, it will be shown that

$$y(t) = y_r \quad (\text{A.65})$$

$A > 0, B > 0$

For these conditions, with $A > 0$, $B > 0$,

$$\tan^{-1}\left(\frac{B}{A}\right) = \frac{\pi}{2} - \tan^{-1}\left(\frac{A}{B}\right) \quad (\text{A.66})$$

The function $\text{atan2}(A, B)$ is related to the inverse tangent function by:

$$\text{atan2}(A, B) = \tan^{-1}\left(\frac{A}{B}\right) \quad (\text{A.67})$$

Substituting Eqs. (A.66) and (A.67) into (A.62) gives:

$$y(t) = y_r + \text{sgn}(A) a_r \cos\left[\theta - \frac{\pi}{2} + \text{atan2}(A, B)\right] \quad (\text{A.68})$$

Noting that:

$$\cos\left[\theta - \frac{\pi}{2} + \text{atan2}(A, B)\right] = \sin[\theta + \text{atan2}(A, B)] \quad (\text{A.69})$$

and since for these conditions $\text{sgn}(A) = 1$, substitution into Eq. (A.68) gives:

$$y(t) = y_r + a_r \sin[\theta + \text{atan2}(A, B)] \quad (\text{A.70})$$

$A > 0, B = 0$

For these conditions, with $A > 0, B = 0$, from Eq. (A.54) we can write:

$$y(t) = y_r + A \cos(\theta) \quad (\text{A.71})$$

The function $\text{atan2}(A, B)$ with $A > 0$ and $B = 0$ is evaluated as:

$$\text{atan2}(A, B) = \frac{\pi}{2} \quad (\text{A.72})$$

From Eq. (A.60),

$$a_r = A \quad (\text{A.73})$$

Substituting Eqs. (A.72) and (A.73) into (A.71) gives:

$$y(t) = y_r + a_r \cos\left[\theta + \text{atan2}(A, B) - \frac{\pi}{2}\right] \quad (\text{A.74})$$

Also,

$$\cos\left[\theta + \text{atan2}(A, B) - \frac{\pi}{2}\right] = \sin[\theta + \text{atan2}(A, B)] \quad (\text{A.75})$$

Substituting Eq. (A.75) into (A.74) with $\text{sgn}(A) = 1$ gives:

$$y(t) = y_r + a_r \sin[\theta + \text{atan2}(A, B)] \quad (\text{A.76})$$

$A > 0, B < 0$

For these conditions, with $A > 0, B < 0$,

$$\tan^{-1}\left(\frac{B}{A}\right) = -\frac{\pi}{2} - \tan^{-1}\left(\frac{A}{B}\right) \quad (\text{A.77})$$

The function $\text{atan2}(A, B)$ is related to the inverse tangent function by:

$$\text{atan2}(A, B) = \tan^{-1}\left(\frac{A}{B}\right) + \pi \quad (\text{A.78})$$

Substituting Eqs. (A.77) and (A.78) into (A.62) gives:

$$y(t) = y_r + \operatorname{sgn}(A) a_r \cos \left[\theta + \operatorname{atan2}(A, B) - \frac{\pi}{2} \right] \quad (\text{A.79})$$

Also,

$$\cos \left[\theta + \operatorname{atan2}(A, B) - \frac{\pi}{2} \right] = \sin \left[\theta + \operatorname{atan2}(A, B) \right] \quad (\text{A.80})$$

Substituting Eq. (A.80) into (A.79) with $\operatorname{sgn}(A) = 1$ gives:

$$y(t) = y_r + a_r \sin \left[\theta + \operatorname{atan2}(A, B) \right] \quad (\text{A.81})$$

$A < 0, B > 0$

For these conditions, with $A < 0, B > 0$,

$$\tan^{-1} \left(\frac{B}{A} \right) = -\frac{\pi}{2} - \tan^{-1} \left(\frac{A}{B} \right) \quad (\text{A.82})$$

The function $\operatorname{atan2}(A, B)$ is related to the inverse tangent function by:

$$\operatorname{atan2}(A, B) = \tan^{-1} \left(\frac{A}{B} \right) \quad (\text{A.83})$$

Substituting Eqs. (A.82) and (A.83) into (A.62) gives:

$$y(t) = y_r + \operatorname{sgn}(A) a_r \cos \left[\theta + \operatorname{atan2}(A, B) + \frac{\pi}{2} \right] \quad (\text{A.84})$$

Also,

$$\cos \left[\theta + \operatorname{atan2}(A, B) + \frac{\pi}{2} \right] = -\sin \left[\theta + \operatorname{atan2}(A, B) \right] \quad (\text{A.85})$$

Substituting Eq. (A.85) into (A.84) with $\operatorname{sgn}(A) = -1$ gives:

$$y(t) = y_r + a_r \sin \left[\theta + \operatorname{atan2}(A, B) \right] \quad (\text{A.86})$$

$A < 0, B = 0$

For these conditions, with $A < 0, B = 0$, from Eq. (A.54) we can write:

$$y(t) = y_r + A \cos \theta \quad (\text{A.87})$$

The function $\text{atan2}(A, B)$ with $A < 0$ and $B = 0$ is evaluated as:

$$\text{atan2}(A, B) = -\frac{\pi}{2} \quad (\text{A.88})$$

From Eq. (A.60),

$$a_r = -A \quad (\text{A.89})$$

Substituting Eqs. (A.88) and (A.89) into (A.87) gives:

$$y(t) = y_r - a_r \cos \left[\theta + \text{atan2}(A, B) + \frac{\pi}{2} \right] \quad (\text{A.90})$$

Also,

$$\cos \left[\theta + \text{atan2}(A, B) + \frac{\pi}{2} \right] = -\sin \left[\theta + \text{atan2}(A, B) \right] \quad (\text{A.91})$$

Substituting Eq. (A.91) into (A.90):

$$y(t) = y_r + a_r \sin \left[\theta + \text{atan2}(A, B) \right] \quad (\text{A.92})$$

$A < 0, B < 0$

For these conditions, with $A < 0, B < 0$,

$$\tan^{-1} \left(\frac{B}{A} \right) = \frac{\pi}{2} - \tan^{-1} \left(\frac{A}{B} \right) \quad (\text{A.93})$$

The function $\text{atan2}(A, B)$ is related to the inverse tangent function by:

$$\text{atan2}(A, B) = \tan^{-1}\left(\frac{A}{B}\right) + \pi \quad (\text{A.94})$$

Substituting Eqs. (A.93) and (A.94) into (A.62) gives:

$$y(t) = y_r + \text{sgn}(A)a_r \cos\left[\theta + \text{atan2}(A, B) - \frac{3\pi}{2}\right] \quad (\text{A.95})$$

Also,

$$\cos\left[\theta + \text{atan2}(A, B) - \frac{3\pi}{2}\right] = -\sin[\theta + \text{atan2}(A, B)] \quad (\text{A.96})$$

Substituting Eq. (A.96) into (A.95) with $\text{sgn}(A) = -1$ gives:

$$y(t) = y_r + a_r \sin[\theta + \text{atan2}(A, B)] \quad (\text{A.97})$$

$A = 0, B > 0$

For these conditions, with $A = 0, B > 0$, from Eq. (A.63),

$$y(t) = y_r + B \sin \theta, \quad A = 0 \quad (\text{A.98})$$

Solving Eq. (A.25) for B with $A = 0$ gives:

$$B = a_r \quad (\text{A.99})$$

The function $\text{atan2}(A, B)$ is related to the inverse tangent function by:

$$\text{atan2}(A, B) = \tan^{-1}\left(\frac{A}{B}\right) = 0 \quad (\text{A.100})$$

Substituting Eqs. (A.99) and (A.100) into (A.98) gives:

$$y(t) = y_r + a_r \sin[\theta + \text{atan2}(A, B)] \quad (\text{A.101})$$

$A = 0, B < 0$

For these conditions, with $A = 0, B < 0$, from Eq. (A.63),

$$y(t) = y_r + B \sin \theta, \quad A = 0 \quad (\text{A.102})$$

Solving Eq. (A.25) for B with $A = 0$ gives:

$$B = -a_r \quad (\text{A.103})$$

The function $\text{atan2}(A, B)$ is related to the inverse tangent function by:

$$\text{atan2}(A, B) = \tan^{-1}\left(\frac{A}{B}\right) + \pi = \pi \quad (\text{A.104})$$

Substituting Eqs. (A.103) and (A.104) into (A.102) gives:

$$y(t) = y_r - a_r \sin[\theta + \text{atan2}(A, B) - \pi] \quad (\text{A.105})$$

Also,

$$\sin[\theta + \text{atan2}(A, B) - \pi] = -\sin[\theta + \text{atan2}(A, B)] \quad (\text{A.106})$$

Substituting Eq. (A.106) into (A.105) gives:

$$y(t) = y_r + a_r \sin[\theta + \text{atan2}(A, B)] \quad (\text{A.107})$$

$A = 0, B = 0$

For these conditions, with $A = 0, B = 0$, from Eq. (A.63),

$$y(t) = y_r \quad (\text{A.108})$$

It is noted that this is the only case where the y -component of the LVLH position vector cannot be represented by Eq. (A.64), since $\text{atan2}(0, 0)$ is generally undefined. However, when coding in MATLAB, the $\text{atan2}(0, 0)$ function is evaluated as zero. Since, from Eq. (A.25) $a_r = 0$ for $A = 0, B = 0$, Eq. (A.64) will evaluate correctly to $y(t) = y_r$ using MATLAB.

A.2.3 Application of the Harmonic Addition Theorem to the z -Component of the Clohessy-Wiltshire Solution

The z -component of the Clohessy-Wiltshire solution expressed in Eq. (A.18) can be rewritten as:

$$z(t) = A \cos \theta + B \sin \theta \quad (\text{A.109})$$

where the coefficients and phase angle are defined using the form of Eq. (A.1) as:

$$A = z_0 \quad (\text{A.110})$$

$$B = \frac{\dot{z}_0}{n} \quad (\text{A.111})$$

$$\theta = n(t - t_0) \quad (\text{A.112})$$

Equation (68) defines A_z as:

$$A_z = \sqrt{z_0^2 + \frac{\dot{z}_0^2}{n^2}} = \sqrt{A^2 + B^2} \quad (\text{A.113})$$

The Harmonic Addition Theorem as expressed in Eq. (A.14) may be applied to Eq. (A.109), resulting in:

$$z(t) = \text{sgn}(A) A_z \cos \left[\theta + \tan^{-1} \left(-\frac{B}{A} \right) \right], \quad A \neq 0 \quad (\text{A.114})$$

which is equivalent to:

$$z(t) = \text{sgn}(A) A_z \cos \left[\theta - \tan^{-1} \left(\frac{B}{A} \right) \right], \quad A \neq 0 \quad (\text{A.115})$$

Eq. (A.15) may be applied to Eq. (A.97) to give:

$$z(t) = B \sin \theta, \quad A = 0 \quad (\text{A.116})$$

Eqs. (A.115) and (A.116) will be evaluated for all combinations of values for A and B . It will be shown that the following expression utilizing the atan2 function encompasses both Eqs. (A.115) and (A.116), for all combinations of values for A and B except for $A = 0, B = 0$:

$$z(t) = A_z \sin[\theta + \text{atan2}(A, B)] \quad (\text{A.117})$$

For $A = 0, B = 0$,

$$z(t) = 0 \quad (\text{A.118})$$

$A > 0, B > 0$

For these conditions, with $A > 0, B > 0$,

$$\tan^{-1}\left(\frac{B}{A}\right) = \frac{\pi}{2} - \tan^{-1}\left(\frac{A}{B}\right) \quad (\text{A.119})$$

The function $\text{atan2}(A, B)$ is related to the inverse tangent function by:

$$\text{atan2}(A, B) = \tan^{-1}\left(\frac{A}{B}\right) \quad (\text{A.120})$$

Substituting Eqs. (A.119) and (A.120) into (A.115) gives:

$$z(t) = \text{sgn}(A) A_z \cos\left[\theta - \frac{\pi}{2} + \text{atan2}(A, B)\right] \quad (\text{A.121})$$

Noting that:

$$\cos\left[\theta - \frac{\pi}{2} + \text{atan2}(A, B)\right] = \sin[\theta + \text{atan2}(A, B)] \quad (\text{A.122})$$

and since for these conditions $\text{sgn}(A) = 1$, substitution into Eq. (A.121) gives:

$$z(t) = A_z \sin[\theta + \text{atan2}(A, B)] \quad (\text{A.123})$$

$$\underline{A > 0, B = 0}$$

For these conditions, with $A > 0, B = 0$, from Eq. (A.109),

$$z(t) = A \cos \theta \quad (\text{A.124})$$

From Eq. (A.113), with $B = 0$,

$$A_z = A \quad (\text{A.125})$$

The function $\text{atan2}(A, B)$ is evaluated as:

$$\text{atan2}(A, B) = \frac{\pi}{2} \quad (\text{A.126})$$

Substituting Eqs. (A.125) and (A.126) into (A.124) gives:

$$z(t) = A_z \cos\left[\theta + \text{atan2}(A, B) - \frac{\pi}{2}\right] \quad (\text{A.127})$$

Also,

$$\cos\left[\theta + \text{atan2}(A, B) - \frac{\pi}{2}\right] = \sin[\theta + \text{atan2}(A, B)] \quad (\text{A.128})$$

Substituting (A.128) into (A.127) gives:

$$z(t) = A_z \sin[\theta + \text{atan2}(A, B)] \quad (\text{A.129})$$

$$\underline{A > 0, B < 0}$$

For these conditions, with $A > 0, B < 0$,

$$\tan^{-1}\left(\frac{B}{A}\right) = -\frac{\pi}{2} - \tan^{-1}\left(\frac{A}{B}\right) \quad (\text{A.130})$$

The function $\text{atan2}(A, B)$ is given by:

$$\text{atan2}(A,B) = \tan^{-1}\left(\frac{A}{B}\right) + \pi \quad (\text{A.131})$$

Substituting Eqs. (A.130) and (A.131) into (A.115) gives:

$$z(t) = \text{sgn}(A)A_z \cos\left[\theta + \text{atan2}(A,B) - \frac{\pi}{2}\right] \quad (\text{A.132})$$

Also,

$$\cos\left[\theta + \text{atan2}(A,B) - \frac{\pi}{2}\right] = \sin[\theta + \text{atan2}(A,B)] \quad (\text{A.133})$$

Substituting Eq. (A.133) into (A.132) with $\text{sgn}(A) = 1$ gives:

$$z(t) = A_z \sin[\theta + \text{atan2}(A,B)] \quad (\text{A.134})$$

$A < 0, B > 0$

For these conditions, with $A < 0, B > 0$,

$$\tan^{-1}\left(\frac{B}{A}\right) = -\frac{\pi}{2} - \tan^{-1}\left(\frac{A}{B}\right) \quad (\text{A.135})$$

The function $\text{atan2}(A,B)$ is given by:

$$\text{atan2}(A,B) = \tan^{-1}\left(\frac{A}{B}\right) \quad (\text{A.136})$$

Substituting Eqs. (A.135) and (A.136) into (A.115) gives:

$$z(t) = \text{sgn}(A)A_z \cos\left[\theta + \text{atan2}(A,B) + \frac{\pi}{2}\right] \quad (\text{A.137})$$

Also,

$$\cos\left[\theta + \text{atan2}(A,B) + \frac{\pi}{2}\right] = -\sin[\theta + \text{atan2}(A,B)] \quad (\text{A.138})$$

Substituting Eq. (A.138) into (A.137) with $\text{sgn}(A) = -1$ gives:

$$z(t) = A_z \sin[\theta + \text{atan2}(A, B)] \quad (\text{A.139})$$

$$\underline{A < 0, B = 0}$$

For these conditions, with $A < 0, B = 0$, from Eq. (A.109),

$$z(t) = A \cos \theta \quad (\text{A.140})$$

From Eq. (A.113), with $B = 0$,

$$A_z = -A \quad (\text{A.141})$$

The function $\text{atan2}(A, B)$ is evaluated as:

$$\text{atan2}(A, B) = -\frac{\pi}{2} \quad (\text{A.142})$$

Substituting Eqs. (A.141) and (A.142) into (A.140) gives:

$$z(t) = -A_z \cos\left[\theta + \text{atan2}(A, B) + \frac{\pi}{2}\right] \quad (\text{A.143})$$

Also,

$$\cos\left[\theta + \text{atan2}(A, B) + \frac{\pi}{2}\right] = -\sin[\theta + \text{atan2}(A, B)] \quad (\text{A.144})$$

Substituting (A.144) into (A.143) gives:

$$z(t) = A_z \sin[\theta + \text{atan2}(A, B)] \quad (\text{A.145})$$

$$\underline{A < 0, B < 0}$$

For these conditions, with $A < 0, B < 0$,

$$\tan^{-1}\left(\frac{B}{A}\right) = \frac{\pi}{2} - \tan^{-1}\left(\frac{A}{B}\right) \quad (\text{A.146})$$

The function $\text{atan2}(A, B)$ is given by:

$$\text{atan2}(A, B) = \tan^{-1}\left(\frac{A}{B}\right) - \pi \quad (\text{A.147})$$

Substituting Eqs. (A.146) and (A.147) into (A.115) gives:

$$z(t) = \text{sgn}(A)A_z \cos\left[\theta + \text{atan2}(A, B) + \frac{\pi}{2}\right] \quad (\text{A.148})$$

Also,

$$\cos\left[\theta + \text{atan2}(A, B) + \frac{\pi}{2}\right] = -\sin[\theta + \text{atan2}(A, B)] \quad (\text{A.149})$$

Substituting Eq. (A.149) into (A.148) with $\text{sgn}(A) = -1$ gives:

$$z(t) = A_z \sin[\theta + \text{atan2}(A, B)] \quad (\text{A.150})$$

$A = 0, B > 0$

For these conditions, with $A = 0, B > 0$, from Eq. (A.109),

$$z(t) = B \sin \theta \quad (\text{A.151})$$

From Eq. (A.112), with $A = 0$,

$$A_z = B \quad (\text{A.152})$$

The function $\text{atan2}(A, B)$ is related to the inverse tangent function by:

$$\text{atan2}(A, B) = \tan^{-1}\left(\frac{A}{B}\right) = 0 \quad (\text{A.153})$$

Substituting Eqs. (A.152) and (A.153) into (A.151) gives:

$$z(t) = A_z \sin[\theta + \text{atan2}(A, B)] \quad (\text{A.154})$$

$A = 0, B < 0$

For these conditions, with $A = 0, B < 0$, from Eq. (A.109),

$$z(t) = B \sin \theta \quad (\text{A.155})$$

From Eq. (A.113), with $A = 0$,

$$A_z = -B \quad (\text{A.156})$$

The function $\text{atan2}(A, B)$ is related to the inverse tangent function by:

$$\text{atan2}(A, B) = \tan^{-1}\left(\frac{A}{B}\right) + \pi \quad (\text{A.157})$$

Since $\tan^{-1}\left(\frac{A}{B}\right) = 0$, from Eq. (A.157) it is seen that:

$$\text{atan2}(A, B) - \pi = 0 \quad (\text{A.158})$$

Substituting Eqs. (A.156) and (A.158) into (A.155) gives:

$$z(t) = -A_z \sin[\theta + \text{atan2}(A, B) - \pi] \quad (\text{A.159})$$

Also,

$$\sin[\theta + \text{atan2}(A, B) - \pi] = -\sin[\theta + \text{atan2}(A, B)] \quad (\text{A.160})$$

Substituting (A.160) into (A.159) gives:

$$z(t) = A_z \sin[\theta + \text{atan2}(A, B)] \quad (\text{A.161})$$

$A = 0, B = 0$

For these conditions, with $A = 0, B = 0$, it is clear from Eq. (A.109) that:

$$z(t) = 0 \quad (\text{A.162})$$

It is noted that this is the only case where the z -component of the LVLH position vector cannot be represented by Eq. (A.117), since $\text{atan2}(0, 0)$ is generally undefined. However, when coding in MATLAB, the $\text{atan2}(0, 0)$ function is evaluated as zero, so, for $A = 0$, $B = 0$, Eq. (A.117) will evaluate correctly to $z(t) = 0$ using MATLAB.

REFERENCES

- [1] Woffinden, D.C., Geller, D., Mosher, T., Kwong, J., “On-Orbit Satellite Rendezvous Inspection: A Concept Study and Design,” *Spaceflight Mechanics 2005, Advances in the Astronautical Sciences*, Vol. 120, Parts 1 & 2, pp. 849-867, 2005.
- [2] Sabol, C., Burns, R., and McLaughlin, C. A., “Satellite Formation Flying Design and Evolution,” *Journal of Spacecraft and Rockets*; Vol. 38, No. 2, 2001, pp. 270-278.
- [3] Fasano, G., and D’Errico, M., “Design of Satellite Formations for Interferometric and Bistatic SAR,” Institute of Electrical and Electronics Engineers Aerospace Conference Paper No. 1064, Mar. 2007.
- [4] Carreau, M., “NASA Approves Orbital Sciences for ISS Commercial Resupply Missions,” *Aviation Week and Space Technology*, October 1, 2013.
- [5] Clark, Stephen. “Satellite In-Space Servicing Demo Mission a Success.” *Spaceflight Now*, July 23, 2007.
- [6] Malik, Tariq. “Prototype Satellites Demonstrate In-Orbit Refueling.” *Space.com*. April 4, 2007.
- [7] Air Force Space Command, “Resiliency and Disaggregated Space Architectures,” White Paper, AFD-130821-034, August 21, 2013.
- [8] Pawlikowski, E., Loverro, D., and Cristler, T., “Space: Disruptive Challenges, New Opportunities, and New Strategies,” *Strategic Studies Quarterly*, Vol. 6, No. 1, Spring 2012.
- [9] Jezewski, D. J., Brazzell, J. P., Prust, E. E., Brown, B. G., Mulder, T. A., and Wissinger, D. B., “A Survey of Rendezvous Trajectory Planning,” American Astronautical Society Paper 91-505, Aug. 1991.
- [10] Gaylor, D.E., and Barbee, B.W., “Algorithms for Safe Spacecraft Proximity Operations,” Conference Proceedings, Space Flight Mechanics 2007, Advances in the Astronautical Sciences, Vol. 127, Parts 1 & 2, pp. 133-152, 2007.

- [11] Holzinger, M., DiMatteo, J., Schwartz, J., and Milam, M., "Passively Safe Receding Horizon Control for Satellite Proximity Operations," Proceedings of the 47th IEEE Conference on Decision and Control, Cancun, Mexico, Dec. 2008.
- [12] Breger, L., and How, J. P., "Safe Trajectories for Autonomous Rendezvous of Spacecraft," *Journal of Guidance, Control, and Dynamics*; Vol. 31, No. 5, 2008, pp. 1478-1489.
- [13] Roger, A. B., and McInnes, C. R., "Safety Constrained Free-Flyer Path Planning at the international Space Station," *Journal of Guidance, Control, and Dynamics*; Vol. 23, No. 6, 2000, pp. 971-979.
- [14] Condurache, D., and Martinuși, V., "Relative Spacecraft Motion in a Central Force Field," *Journal of Guidance, Control, and Dynamics*; Vol. 30, No. 3: Engineering Notes, 2007, pp. 873-876.
- [15] Lovell, T. A., and Tragesser, S. G., "Guidance for Relative Motion of Low Earth Orbit Spacecraft Based on Relative Orbit Elements," AIAA Paper 2004-4988, Aug. 2004.
- [16] Lovell, T. A., Tragesser, S. G., and Tollefson, M. V., "A Practical Guidance Methodology for Relative Motion of LEO Spacecraft Based on the Clohessy-Wiltshire Equations," American Astronautical Society Paper 04-252, Feb. 2004.
- [17] Khatib, O., "Real-Time Obstacle Avoidance for Manipulators and Mobile Robots," *International Journal of Robotics Research*, Vol. 5, No. 1, 1986, pp. 90-99.
- [18] Leonard, N.E., and Fiorelli, E., "Virtual Leaders, Artificial Potentials and Coordinated Control of Groups," Proceedings of the 40th IEEE Conference on Decision and Control, Orlando, FL, Dec. 2001.
- [19] Chait, S., and Spencer, D.A., "Prox-1: Automated Trajectory Control for On-Orbit Inspection," AAS 14-06, 37th Annual American Astronautical Society Guidance and Control Conference, January 2014.
- [20] Woffinden, D.C., and Geller, D. K., "Navigating the Road to Autonomous Orbital Rendezvous," *Journal of Spacecraft and Rockets*; Vol. 44, No. 4, 2007, pp. 898-909.

- [21] Goodman, J.L., "History of Space Shuttle Rendezvous and Proximity Operations," *Journal of Spacecraft and Rockets*, Vol. 43, Iss. 5, pp. 944-959, Sept.-Oct. 2006.
- [22] Choset, H., "Path Planning and Control for Free-Flying Inspection Robot in Space," *Journal of Aerospace Engineering*, Vol. 12, Iss. 2, pp. 74-81, April 1999.
- [23] Ohkami, Y., and Kawano, I., "Autonomous Rendezvous and Docking by Engineering Test Satellite VII: A Challenge of Japan in Guidance, Navigation and Control—Breakwell Memorial Lecture," *Acta Astronautica*; Vol. 53, No. 1, 2003, pp. 1-8.
- [24] Oda, M., Inaba, N., Fukushima, Y., "Space Robot Technology Experiments on NASDA's ETS-VII Satellite," *Advanced Robotics*, Vol. 13, Iss. 3, pp. 335-336, 1999.
- [25] Davis, T.M. and Melanson, D. "XSS-10 Micro-Satellite Flight Demonstration Program Results." *Proceedings of SPIE Conference on Spacecraft Platforms and Infrastructure*, SPIE Vol. 5419, 2004.
- [26] Croomes, "Overview of the DART Mishap Investigation Results," DART Mishap Investigation Board, www.nasa.gov/pdf/148072main_DART_mishap_overview.pdf (Accessed December 17, 2014).
- [27] NASA Marshall Space Flight Center, "DART Demonstrator to Test Future Autonomous Rendezvous Technologies in Orbit." *NASA Facts*. September 2004.
- [28] Howard, R.T. and Bryan, T.C. "DART AVGS Performance." *NASA Marshall Space Flight Center Technical Report*. April 9, 2007.
- [29] Evans, J. W., Piñon, E., and Mulder, T. A., "Autonomous Rendezvous Guidance and Navigation for Orbital Express and Beyond," American Astronautical Society Paper 06-194, Jan. 2006.
- [30] Weismuller, T., and Leinz, M., "GN&C Technology Demonstrated by the Orbital Express Autonomous Rendezvous and Capture Sensor System," American Astronautical Society Paper 06-616, Feb. 2006.

- [31] McCamish, S.B., Romano, Nolet, S., Edwards, C.M., and Miller, D.W., “Flight Testing of Multiple-Spacecraft Control on SPHERES During Close-Proximity Operations,” *Journal of Spacecraft and Rockets*, Vol. 46, No. 6, Nov. – Dec. 2009.
- [32] McCamish, S.B., Romano, M., Yun, X., “Autonomous Distributed Control of Simultaneous Multiple Spacecraft Proximity Maneuvers.” *IEEE Transactions on Automation Science and Engineering*, Vol. 7, No. 3. July 2010.
- [33] Cornier, D., Berthelie, D., Requiston, H., Zekri, E., and Chase, R., “Automated Transfer Vehicle Proximity Flight Safety Overview,” *Proceedings of the First IAASS Conference on Space Safety*, ESA Special Publications, Vol. 599, pp. 89-95, 2005.
- [34] D’Amico, S., Gill, E., and Montenbruck, O., “Relative Orbit Control Design for the PRISMA Formation Flying Mission,” AIAA Paper 2006-6067, Aug. 2006.
- [35] D’Amico, S., Ardaens, J.-S., and Larsson, R., “Spaceborne Autonomous Formation-Flying Experiment on the PRISMA Mission,” *Journal of Guidance, Control, and Dynamics*, Vol. 35, No. 3, May-June 2012.
- [36] Walker, L., “Automated Proximity Operations Using Image-Based Relative Navigation,” AIAA/Utah State University Small Satellite Conference, Paper No. SSC12-VIII-3, Logan UT, 2012.
- [37] NASA Ames Research Center, “Edison Small Satellite Flight Demonstration Missions,” Solicitation Number NNA12ZD0001K, January 8, 2012.
- [38] United States Air Force Chief Scientist, “Report on Technology Horizons, A Vision for Air Force Science and Technology During 2010-2030,” Vol. 1, AF/ST-TR-10-01-PR, May 2010.
- [39] United States Air Force Space Command, “Resiliency and Disaggregated Space Architectures,” White Paper, AFD-130821-034, August 21, 2013.
- [40] Hill, G. W., “Researches in the Lunar Theory,” *American Journal of Mathematics*; Vol. 1, No. 1, 1878.

- [41] Clohessy, W. H., and Wiltshire, R. S., "Terminal Guidance System for Satellite Rendezvous," *Journal of the Aerospace Sciences*; Vol. 27, Sept. 1960, pp. 653-658, 674.
- [42] Schaub, H., and Junkins, J. L., *Analytical Mechanics of Space Systems*, AIAA, Reston, 2003.
- [43] Vallado, D. A., *Fundamentals of Astrodynamics and Applications*, 2nd ed., Microcosm Press, El Segundo, 2004.
- [44] Vaddi, S. S., Alfriend, K. T., Vadali, S. R., and Sengupta, P., "Formation Establishment and Reconfiguration Using Impulsive Control," *Journal of Guidance, Control, and Dynamics*, Vol. 28, No. 2, 2005, pp. 262-268.
- [45] D'Amico, S., and Montenbruck, O., "Proximity Operations of Formation-Flying Spacecraft Using an Eccentricity/Inclination Vector Separation," *Journal of Guidance, Control, and Dynamics*, Vol. 29, No. 3, 2006, pp. 554-563.
- [46] Gill, E., Montenbruck, O., and D'Amico, S., "Autonomous Formation Flying for the PRISMA Mission," *Journal of Spacecraft and Rockets*, Vol. 44, No. 3, 2007, pp. 671-681.
- [47] D'Amico, S., Ardaens, J.-S., Gaias, G., Benninghoff, H., Schlepp, B., and Jorgensen, J. L., "Noncooperative Rendezvous Using Angles-Only Optical Navigation: System Design and Flight Results," *Journal of Guidance, Control, and Dynamics*, Vol. 36, No. 6, 2013, pp. 1576-1595.
- [48] Han, C. and Yin, J., "Formation Design in Elliptical Orbit Using Relative Orbital Elements," *Acta Astronautica*, Vol. 77, Aug.-Sept. 2012.
- [49] Bevilacqua, R., and Lovell, T., A., "Analytical Guidance for Spacecraft Relative Motion Under Constant Thrust using Relative Orbit Elements", *Acta Astronautica*, Vol. 102, Sept.-Oct. 2014, pp. 47-61.
- [50] Phillips, M., "Spacecraft Collision Probability Estimation for Rendezvous and Proximity Operations," Master of Science Thesis, Utah State University, Logan, Utah, 2012.

- [51] Aubin, B.S., "Optimization of Relative Orbit Transfers Via Particle Swarm and Primer Vector Theory," Master of Science Thesis, University of Illinois at Urbana-Champaign, 2011.
- [52] Schwartz, J., Krenzke, T., Hur-Diaz, S., Ruschmann, M., and Schmidt, J., "Error-Contracting Impulse Controller for Satellite Cluster Flight Formation," AIAA 2013-4541, AIAA Guidance, Navigation and Control Conference, Boston, MA, August 2013.
- [53] Schwartz, J., Krenzke, T., Hur-Diaz, S., Ruschmann, M., and Schmidt, J., "The Flocking Controller: A Novel Cluster Control Strategy for Space Vehicles," AIAA 2013-4543, AIAA Guidance, Navigation and Control Conference, Boston, MA, August 2013.
- [54] Doolittle, C. M., Chavez, F. R., and Lovell, T. A., "Relative Orbit Element Estimation for Satellite Navigation," AIAA Paper 2005-6462, Aug. 2005.
- [55] Johnson, K. W., "Relative Orbit Elements for Satellites in Elliptical Orbits," Master of Science Thesis, Air Force Institute of Technology, March 2010.
- [56] Chait, S., and Spencer, D. A., "Prox-1: Automated Trajectory Control for On-Orbit Inspection," AAS 14-066, 37th Annual American Astronautical Society Guidance and Control Conference, Breckenridge, CO, January 2014.
- [57] Rimon, E., and Koditschek, D.E., "Exact Robot Navigation Using Artificial Potential Functions," *Transactions on Robotics and Automation*, Vol. 8, No. 5, 1992, pp. 501-518.
- [58] Newman, W. S., and Hogan, N., "High Speed Robot Control and Obstacle Avoidance Using Dynamic Potential Functions," *Proceedings of the IEEE International Conference on Robotics and Automation*, Vol. 4, March 1987, pp. 14-24.
- [59] Lyapunov, A.M., "The General Problem of the Stability of Motion," Ph.D. Dissertation, University of Kharkov, Ukraine, 1892.
- [60] McInnes, C. R., "Autonomous Proximity Maneuvering Using Artificial Potential Functions," *European Space Agency Journal*, Vol. 17, No. 2, 1993, pp. 159-169.

- [61] McInnes, C. R., "Distributed Control of Maneuvering Vehicles for On-Orbit Assembly," *Journal of Guidance, Control, and Dynamics*, Vol. 18, No. 5, 1995, pp. 1204-1206.
- [62] Lopez, I., and McInnes, C.R., "Autonomous Rendezvous Using Artificial Potential Function Guidance," *Journal of Guidance, Control and Dynamics*, Vol. 18, No. 2, March-April 1995.
- [63] McQuade, F., "Autonomous Control for On-Orbit Assembly Using Artificial Potential Functions," Ph.D. Dissertation, Dept. of Aerospace Engineering, University of Glasgow, Glasgow, Scotland, U.K., 1997.
- [64] Tatsch, A., and Xu, Y., "Nonlinear Controller via Artificial Potential Functions for Spacecraft Attitude Maneuvers," *Advances in the Astronautical Sciences*, Vol. 121, pp. 107-123, 2005.
- [65] Tatsch, A., and Fitz-Coy, N., "Optimized Harmonic Artificial Potential Function Guidance for the Heterogeneous Expert Robots for On-Orbit Servicing (HEROS) Architecture", *Advances in the Astronautical Sciences*, Vol. 128, pp. 1029-1036, 2007.
- [66] Saaj, C.M., Lappas, V., and Gazi, V., "Spacecraft Swarm Navigation and Control Using Artificial Potential Field and Sliding Mode Control," Proceedings of the IEEE International Conference on Industrial Technology, Mumbai, India, Dec. 2006, pp. 2646-2651.
- [67] McCamish, S.B., Romano, Nolet, S., Edwards, C.M., and Miller, D.W., "Flight Testing of Multiple-Spacecraft Control on SPHERES During Close-Proximity Operations," *Journal of Spacecraft and Rockets*, Vol. 46, No. 6, Nov. – Dec. 2009.
- [68] Bevilacqua, R., Lehmann, M., Romano, M., "Development and experimentation of LQR/APF guidance and control for autonomous proximity maneuvers of multiple spacecraft." *Acta Astronautica*, Vol. 68. 2011.
- [69] Schulte, P. and Spencer, D., "Development of an Integrated Guidance, Navigation, and Control Subsystem for Automated Proximity Operations," 65th International Astronautical Congress, Toronto, Ontario, Canada, Sept.-Oct. 2014.

- [70] Zappula, R., "Prox-1 Guidance, Navigation and Control Formulation and Algorithms," Masters Project, Space Systems Design Laboratory, Georgia Institute of Technology, <http://ssdl.gatech.edu/mastersProjects.shtml> (Accessed Jan. 31, 2015).
- [71] Bate, R.R., Mueller, D.D., and White, J.E., *Fundamentals of Astrodynamics*, Dover Publications, Inc., New York, NY, 1971.
- [72] Tschauner, J., Hempel, P., "Rendezvous to a Destination Rotating in an Elliptical Orbit," *Acta Astronautica*, Vol. 11, No. 2, 1965.
- [73] Sinclair, A.J., Sherrill, R.E., and Lovell, T.A., "Geometric Interpretation of the Tschauner-Hempel Solutions for Satellite Relative Motion," *Advances in Space Research*, 2015, doi: 10.1016/j.asr.2015.01.032.